

# **Impact of extremely cold periods on sedimentary systems during the last glacial cycle**

## **Dissertation**

Zur Erlangung des Doktorgrades der Naturwissenschaften

(Dr. rer. nat.)

im Promotionsfach Geowissenschaften

vorgelegt dem Fachbereich 09: Chemie, Pharmazie, Geographie und  
Geowissenschaften der Johannes Gutenberg-Universität Mainz

von

Johannes Joachim Willi Albert

Geb. 12.12.1985 in Landau in der Pfalz

Mainz, den 27.10.2022

Vom Fachbereich Geowissenschaften der Johannes Gutenberg-Universität Mainz angenommen am

\_\_\_\_\_.

Erstgutachter: \_\_\_\_\_

Zweitgutachter: \_\_\_\_\_

Tag der mündlichen Prüfung: \_\_\_\_\_

# Abstract

This thesis deals with two aspects of the impact of extremely cold periods on sedimentary systems during the last European glacial cycle, i.e., the Weichselian glaciation. The first part focuses on spatial and temporal radon degassing patterns in the Quaternary sediments of Schleswig-Holstein (Northern Germany), which were primarily deposited by the Weichselian glaciers advancing from Scandinavia during the Last Glacial Maximum (LGM). In order to obtain information about the spatial heterogeneity of radon exhalation from soil to the atmosphere and its causes, we established radon flux profiles in three research areas, which are located above deep-rooted tectonic faults or salt diapirs (Kleinneudorf, Bad Segeberg and Eckernförde). To gain an understanding about typical radon background levels in this region, we measured radon flux in an area with no tectonic or halokinetic activity, but with steep topography (near Lanker See). Owing to the fact that radon degassing shows strong diurnal and seasonal fluctuations, we measured radon flux of each profile with up to 16 devices simultaneously and absolute flux values from different seasons were normalized for each research area. Areas of increased radon flux appear to be caused by the mineralogical composition of the subsurface (specifically reddish granites and porphyries deposited by the Weichselian glaciers), as well as its grain size (maximum flux values in well-sorted sand / silt strata). Another important factor influencing radon flux is the water content of the subsurface. Radon exhalation intensifies up to a certain degree of moisture content, whereas excessive water reduces the amount of radon released from the soil, because then the water acts as a natural absorber of the kinetic energy. Maximum radon flux, however, occurs above deep-rooted pathways linked to active tectonic and halokinetic fault systems at depth due to an increased concentration of ascending fluids, which are rich in parent isotopes of radon. This suggests that the sediments above salt diapirs and fault structures are very inhomogeneous. Deep-rooted increased permeability and the boundaries between permeable and impermeable sediment strata appear to concentrate radon flux.

In addition to radon flux profiles, we studied the temporal variability of radon outgassing in the research area Kleinneudorf where maximum radon flux was observed during the profile measurements. We continuously monitored radon exhalation for one year in the centre of the Kleinneudorf depression.

Although many factors can influence temporal radon degassing variations, the main drivers in our specific monitoring system are air temperature and atmospheric pressure. We identified four different radon exhalation ‘modes’ representing four different weather regimes: During cold winter months when the temperature gradients between soil and atmosphere are at a minimum, radon exhalation is exclusively driven by changes in air pressure (exhalation mode I). In spring, increased radon exhalation occurs when the air temperature drops below the groundwater temperature, activating the so-called chimney effect (exhalation mode II). During sunny summer months, maximum radon flux was measured in the afternoon when the sun stops heating the soil and the soil is warmer than the surrounding air (exhalation mode III). Exhalation mode IV, which was observed during the autumn season, seems to be an interplay between modes II and III.

The second part of this thesis deals with central European climate variations and their causes during the last glacial cycle, obtained from the sediment records of Holzmaar, Auel infilled maar and several other Pleistocene infilled maar lakes in the Eifel region (Western Germany). The presented near annual-resolution ELSA-20  $C_{org}$ (chlorins) climate proxy record documents multidecadal climate oscillations, which are related to North Atlantic sea surface temperature variations. The ELSA-20 record matches well the North Greenland Ice Core Project (NGRIP)  $\delta^{18}O$  ice core chronology, showing a complete succession of Greenland Stadials (GS) and Interstadials (GI) back to GI17 when the Auel maar lake erupted around 60,000 years ago. This sequence of cold and arid stadials and warm and humid interstadials was also recorded in the sediment records of several other Eifel maar structures, although not with such a high resolution and completeness as in the Auel record. Based on this stratigraphy, time series of flooding and slumping phases from event layers in the sediment cores are presented. Periods of increased flood activity seem to coincide with Heinrich Events in marine sediment records.

Particularly noticeable is a slumped sediment segment during GS12 in all presented sediment cores. Distinct frozen and fractured sediment packages suggest that the region was exposed to deep frost or permafrost conditions around 43,500 years ago. These results are consistent with sediment archives and archeological sites all across Europe that report severely cold and arid climate conditions for this period. This supports the hypothesis that not only Heinrich layer times, but GS12 in particular was one of the coldest intervals of the last glacial cycle. A rapid climate shift towards warmer conditions, probably

caused by the Laschamp geomagnetic excursion, then triggered extreme slumping activity in several maar lakes while the lake floors were still partially frozen. These harsh climate conditions during GS12 accentuate the onset of the Laschamp geomagnetic excursion and must have taken a great toll on regional populations, potentially effecting the Neanderthals inhabiting central Europe and the subsequent predominance of the anatomically modern human.

## **Zusammenfassung**

Diese Arbeit befasst sich mit zwei Aspekten von Auswirkungen extremer Kälteperioden auf Sedimentationssysteme während der letzten europäischen Vereisungsphase, der Weichselvereisung. Der erste Teil beschäftigt sich mit räumlichen und zeitlichen Radonentgasungsmustern in den quartären Sedimenten Schleswig-Holsteins (Norddeutschland), welche primär von den aus Skandinavien vordringenden weichselzeitlichen Gletschern während des Letzten Glazialen Maximums abgelagert wurden. Um Informationen über die räumliche Heterogenität der Radonexhalation vom Boden in die Atmosphäre und deren Ursachen zu erhalten, wurden Radonprofilmessungen in drei Untersuchungsgebieten durchgeführt, die über tiefreichenden tektonischen Verwerfungen oder Salzdiapiren liegen (Kleinneudorf, Bad Segeberg und Eckernförde). Um ein Verständnis für typische Radonhintergrundwerte in dieser Region zu erhalten, wurde der Radonflux in einem Gebiet ohne tektonische oder halokinetische Aktivität, dafür aber mit steiler Topografie untersucht (nahe des Lanker Sees). Da die Radonausgasung starken tages- und jahreszeitlichen Schwankungen unterliegt, maßen wir den Radonflux jedes Profils mit bis zu 16 Geräten gleichzeitig und die in den verschiedenen Jahreszeiten gewonnenen absoluten Fluxwerte wurden für jedes Untersuchungsgebiet normiert. Bereiche mit erhöhtem Radonflux scheinen durch die mineralogische Zusammensetzung des Untergrunds (insbesondere rötliche Granite und Porphyre, die von den Weichselgletschern abgelagert wurden), sowie durch die vorherrschende Korngröße (maximale Fluxwerte in gut sortierten Sand- / Siltschichten) bedingt zu sein. Ein weiterer wichtiger Faktor, welcher den Radonflux beeinflusst, ist der Feuchtigkeitsgehalt des Untergrundes. Bis zu einem bestimmten Wassergehalt wird die Radonexhalation verstärkt, während eine zu hohe Feuchtigkeit die aus dem Boden freigesetzte

Radonmenge reduziert, da das Wasser dann als natürlicher Absorber der kinetischen Energie wirkt. Maximaler Radonflux tritt jedoch über tiefreichenden, aktiven tektonischen und halokinetischen Störungssystemen auf, da es dort zu einer Anreicherung von Radonmutternukliden in aufsteigenden Fluiden kommen kann. Dies deutet darauf hin, dass die Sedimente über Salzdiapiren und Störungsstrukturen sehr inhomogen sind. Eine erhöhte Durchlässigkeit in der Tiefe und die Grenzen zwischen permeablen und impermeablen Sedimentschichten scheinen daher den Radonflux zu konzentrieren.

Zusätzlich zu den Radonfluxprofilen untersuchten wir die zeitliche Variabilität der Radonexhalation im Untersuchungsgebiet Kleinneudorf, wo während den Profilmessungen maximale Fluxwerte beobachtet wurden. Hierzu wurde der Radonflux im Zentrum der Senke in Kleinneudorf für ein Jahr kontinuierlich überwacht. Obwohl viele Faktoren zeitliche Schwankungen der Radonentgasung beeinflussen können, sind die Haupteinflüsse in unserem speziellen Messsystem Lufttemperatur und atmosphärischer Druck. Wir haben vier verschiedene 'Modi' der Radonentgasung identifiziert, die vier verschiedene Wetterregime repräsentieren: In kalten Wintermonaten, wenn die Temperaturgradienten zwischen Boden und Atmosphäre minimal sind, wird die Radonexhalation ausschließlich durch Veränderungen des Luftdrucks bestimmt (Exhalationsmodus I). Im Frühjahr kommt es zu einer verstärkten Radonexhalation, wenn die Lufttemperatur unter die Grundwassertemperatur sinkt, wodurch der so genannte Kamineffekt ausgelöst wird (Exhalationsmodus II). Während der sonnigen Sommermonate wurde maximaler Radonflux am Nachmittag gemessen, wenn die Sonne den Boden nicht mehr aufheizt und die Bodentemperatur wärmer ist als die Temperatur der Umgebungsluft (Exhalationsmodus III). Exhalationsmodus IV, der während der Herbstsaison beobachtet wurde, scheint ein Zusammenspiel zwischen den Modi II und III zu sein.

Der zweite Teil dieser Arbeit befasst sich mit Klimaschwankungen in Mitteleuropa und ihren Ursachen während des letzten glazialen Zyklus. Erkenntnisse hierzu wurden aus Sedimenten des Holzmaares, des Aueler Maares und mehreren anderen Pleistozänen Trockenmaare in der Eifel (Westdeutschland) gewonnen. Der entwickelte ELSA-20  $C_{org}$ (chlorins) Klimaproxydatensatz mit nahezu jährlicher Auflösung dokumentiert multidekadische Klimafluktuationen, welche mit Schwankungen der Meeresoberflächentemperatur im Nordatlantik zusammenhängen. Der ELSA-20 Datensatz stimmt gut

mit der „North Greenland Ice Core Project“ (NGRIP)  $\delta^{18}\text{O}$ -Eiskernchronologie überein und zeigt eine vollständige Abfolge Grönländischer Stadiale (GS) und Interstadiale (GI) bis GI17 vor etwa 60.000 Jahren, als das Auel-Maar ausbrach. Diese Abfolge von kalten und trockenen Stadien sowie warmen und feuchten Interstadien wurde auch in den Sedimenten mehrerer anderer Trockenmaare der Eifel aufgezeichnet, wenn auch nicht mit einer so hohen Auflösung und Vollständigkeit wie im Auel Trockenmaar. Auf der Grundlage dieser Stratigraphie wurden Zeitreihen von Überflutungs- und Rutschungsphasen aus Eventlagen in diesen Sedimentkernen kontruiert. Perioden erhöhter Flutaktivität scheinen mit Heinrich-Ereignissen in marinen Sedimentaufzeichnungen zu korrelieren.

Besonders auffällig ist ein Rutschungssegment während GS12 in allen vorgestellten Sedimentkernen. Gefrorene und zerklüftete Sedimentpakete deuten darauf hin, dass die Region vor etwa 43.500 Jahren tiefreichendem Frost oder Permafrost ausgesetzt war. Diese Ergebnisse sind konsistent mit Sedimentarchiven und archäologischen Fundstellen in ganz Europa, die für diesen Zeitraum sehr kalte und trockene Klimabedingungen beschreiben. Dies unterstützt die Hypothese, dass nicht nur Heinrich-Ereignisse, sondern auch GS12 eine der kältesten Perioden des letzten glazialen Zyklus war. Eine rasche Klimaerwärmung, welche wahrscheinlich durch die Laschamp geomagnetische Exkursion verursacht wurde, löste dann in mehreren Maaren extreme Rutschungen aus, während die Seeböden noch teilweise gefroren waren. Diese rauen Klimabedingungen während GS12 akzentuieren den Beginn der Laschamp-Exkursion und müssen einen hohen Tribut von der regionalen Population gefordert haben, was potentiell Auswirkungen auf die in Mitteleuropa ansässigen Neandertaler hatte und anschließend zur Vorherrschaft des anatomisch modernen Menschen führte.





# Table of Contents

List of Figures .....	II
List of Tables.....	IV
Preface .....	V
1. Introduction.....	1
2. Radon flux measurements in the glacial sediment deposits of Schleswig-Holstein .....	3
2.1. Background information .....	3
2.1.1. Scientific applications of radon.....	5
2.1.2. Radon and health risks .....	6
2.2. Radon profile measurements.....	9
2.3. Radon time series and exhalation modes .....	32
3. Climate variations and main flooding and slumping phases during the last glacial cycle from laminated Eifel maar sediments .....	40
3.1. Background information .....	40
3.1.1. Flooding layers.....	41
3.1.2. Turbidites and slumping layers .....	42
3.2. The ELSA-20 record – Multidecadal climate variations in continental Europe during the last glacial cycle.....	44
3.3. The Auel Cooling Event (ACE) – Evidence for a severely cold period during Greenland Stadial 12 .....	77
4. Conclusion .....	94
5. Acknowledgements.....	96
6. References.....	97
7. Supplements.....	129

Eidesstaatliche Erklärung (statutory declaration)

Curriculum vitae

# List of Figures

Fig. 2.1 Simplified scheme of uranium ( $^{238}\text{U}$ ) decay chain .....	4
Fig. 2.2 Simplified overview of Schleswig-Holstein including the locations of the four research areas .....	12
Fig. 2.3 Illustration of sampling setup .....	17
Fig. 2.4 Study site Lanker See .....	20
Fig. 2.5 Study site Kleinneudorf .....	21
Fig. 2.6 Study site Bad Segeberg .....	22
Fig. 2.7 Study site Eckernförde.....	23
Fig. 2.8 Measured radon flux compared to physical properties of soil samples .....	24
Fig. 2.9 Radon emanation power of typical tillitic material occurring in Schleswig-Holstein and various other natural substances.....	26
Fig. 2.10 Radon emanation power of the Leitgeschiebe (indicator stone) “Götömar-granite” (from Sweden) at various grain sizes and water contents.....	27
Fig. 2.11 Schematic description of possible sources for different types of Local Radon Flux Maxima (LRFM).....	28
Fig. 2.12 Schematic description of radon monitoring above the Kleinneudorf drilling well.....	34
Fig. 2.13 Radon exhalation mode I .....	35
Fig. 2.14 Radon exhalation mode II.....	36
Fig. 2.15 Radon exhalation mode III .....	37
Fig. 2.16 Radon exhalation mode IV .....	38
Fig. 3.1 Idealized characteristics of event layers .....	43
Fig. 3.2 Location of the Auel Maar with respect to modern climatology .....	46
Fig. 3.3 The AU3 / AU4 drilling site .....	47
Fig. 3.4 Maar lake sediment cores SMf2, HM4 and AU4 .....	49
Fig. 3.5 The ISRS method.....	51
Fig. 3.6 Temperature changes in Greenland and central Europe over the past 60,000 years .....	53
Fig. 3.7 Reduced high-frequency climate variability in central Europe during the coldest parts of the last ice age.....	55
Fig. 3.8 Age-depth relation .....	57
Fig. 3.9 Ice core tuning, 23 – 36 ka .....	60
Fig. 3.10 Ice core tuning, 36 – 48 ka .....	62
Fig. 3.11 Ice core tuning, 48 – 59 ka .....	64

Fig. 3.12 Uncertainty determination .....	68
Fig. 3.13 Statistical Analysis .....	70
Fig. 3.14 Evolution of decadal- to centennial-scale climate cycles across the stadial / interstadial events of the last ice age .....	72
Fig. 3.15 Lomb–Scargle spectra for selected times of the Holocene, interstadial GI3 and Heinrich 3 .....	74
Fig. 3.16 Location of coring sites .....	80
Fig. 3.17 Establishing the ELSA-20 stratigraphy .....	82
Fig. 3.18 <i>Picea</i> and <i>Carpinus</i> pollen percentages versus age .....	84
Fig. 3.19 $C_{org}$ (chlorins) records versus age .....	85
Fig. 3.20 Phases of increased slumping and flood activity in sediment cores with the ACE .....	86
Fig. 3.21 The Auel Cooling Event (ACE) .....	89
Fig. 3.22 The Middle-Upper Paleolithic transition .....	92

## List of Tables

Table 2.1 Overview of surveys carried out including prevailing meteorological condition during time of sampling .....	16
Table 2.2 Extracted time intervals with identified exhalation modes .....	34
Table 3.1 Overview of coring sites included in this study .....	79
Table 3.2 Stratigraphic tie-points of presented cores.....	88

# Preface

This thesis is divided into two parts concerning different geoscientific subjects. The first topic deals with radon outgassing anomalies in the Quaternary sediments of Schleswig-Holstein, Northern Germany, and the factors controlling them spatially and temporally. This task was developed within the framework of the ANGUS II (*Auswirkungen der Nutzung des geologischen Untergrundes als thermischer, elektrischer oder stofflicher Speicher* — Impact of the use of the geological subsurface as a thermal, electrical or material storage) project, which was led by the University of Kiel and funded by the German Federal Ministry for Economics and Energy (BMWi). The project's aim was to study the potential of underground storage technologies and their integration into energy systems, using the model area of Schleswig-Holstein. The objective of the workgroup at Mainz University was to detect, characterise and monitor potential fault zones at the surface, which play an important role in the planning and designation of underground storage facilities. For this purpose, the radon flux from the subsurface to the atmosphere was studied in four research areas in Schleswig-Holstein (Lanker See, Kleinneudorf, Bad Segeberg und Eckernförde) with the aim of developing a cost-effective and rapid, yet reliable method to identify near-surface fault systems and thus be able to determine suitable storage sites and potential leakage pathways.

The second subject of this thesis deals with climate reconstructions deriving from several Pleistocene Eifel maar sediments. This work is part of the ELSA (Eifel Laminated Sediment Archive) project of the Institute for Geoscience, Mainz University. Since 1998 the project has systematically drilled many of the 6 open maar lakes and around 60 Pleistocene maar structures of the West Eifel Volcanic Field, Western Germany, with the key objective to reconstruct the region's vegetation and climate and understand the mechanisms controlling them. This thesis focuses on the establishment of a time series of flooding- and slumping frequencies for the past 60,000 years and discusses potential drivers with a closer look at a unique slumping layer that occurred around 43,500 years ago.

This thesis includes chapters that have been published in peer-reviewed journals. At the beginning of the corresponding chapters a brief introduction is given including title, authorship and journal, in which the manuscript was published, as well as my contributions to each publication.

The publications about spatial and temporal radon flux anomalies in the Quaternary sediments of Schleswig-Holstein are as follows:

Albert J, Schärf M, Enzmann F, Waltl M, Sirocko F (2021) Local radon flux maxima in the Quaternary sediments of Schleswig-Holstein (Germany). *Int J Earth Sci* 110:1501–1516.

Mudelsee M, Albert J, Sirocko F (2020) Weather control in radon flux time series from Schleswig-Holstein, Germany. *Int J Geomath* 11:23.

The publications about climate variations during the last glacial cycle from Eifel maar sediments are as follows:

Sirocko F, Martínez-García A, Mudelsee M, Albert J, Britzius S, Christl M et al. (2021) Muted multidecadal climate variability in central Europe during cold stadial periods. *Nat Geosci* 14:651–658.

Albert J, Sirocko F (submitted) Evidence of an extreme cooling event prior to the Laschamp geomagnetic excursion in Eifel maar sediments. Submitted to *Quaternary*

# 1 Introduction

In light of the ever-intensifying global warming, the study of past climate fluctuations and their implications are of enormous importance for future generations. Understanding past climate trends and the mechanisms controlling them, natural and anthropogenic, is the key for predicting and preparing for future tendencies.

Earth's climate of the past 60,000 years has been intensively studied in the last couple of decades (e.g., Grootes et al. 1993; Rasmussen et al. 2014). While the climate of our current epoch, the Holocene, is relatively stable, the last glacial cycle (around 115,000 – 11,700 yr b2k [years before the year 2000]) was marked by an alternation of 26 stadials and interstadials, respectively. Interstadial periods were characterised by warm and humid climate conditions on the European continent due to a strong North Atlantic drift. In contrast, cold and arid environments dominated the landscape during stadial phases. First documented in Greenland ice cores (e.g., North Greenland Ice Core Project Members 2004; Svensson et al. 2008; Rasmussen et al. 2014), this alternating succession has also been found in numerous marine and continental records throughout the Northern Hemisphere (e.g., Sirocko et al. 2005, 2013, 2016, 2021; Van Geel et al. 2010; Moreno et al. 2014; Böhm et al. 2015; Pickarski et al. 2015).

During the last glacial cycle, the vegetation of the Eifel region (Western Germany) gradually changed. Between 60,000 and 49,000 yr b2k a lush spruce (*Picea*) forest covered the region with abundant hornbeam (*Carpinus*) between 55,000 and 49,000 yr b2k (Sirocko et al. 2016). Other present taxa include *Corylus*, *Ulmus*, *Quercus*, *Fraxinus*, *Tilia*, *Abies* and *Alnus*. In the following millennia this dense forest receded stepwise. It first evolved into open woodland dominated by pine and birch trees with abundant spruces during interstadials, then at 36,500 yr b2k into an open steppe landscape with scattered trees, into a grass-dominated tundra at 28,500 yr b2k and finally at 23,000 yr b2k into the cold desert of the Last Glacial Maximum (LGM; Sirocko et al. 2016).

During the last glacial cycle extensive glaciers repeatedly advanced and retreated from Scandinavia into the central European continent. This is known as the Weichselian glaciation (e.g., Ehlers et al. 2004, 2011; Wohlfarth et al. 2008a; Ehlers 2020). While the maximum ice extent, which occurred between

24,000 and 19,000 years, did not quite reach the Elbe River in Northern Germany, the Weichselian glaciers advanced well over 200 km inland in Eastern Germany and further east (e.g., Böse et al. 2012; Woźniak and Czubla 2015). Large quantities of Scandinavian bedrock material were eroded by the ice sheet and redeposited in form of alternating glacial till and glaciofluvial sands sequences. The Weichselian moraines in Northern Germany consist to a large extent of potassium-bearing granitic and porphyritic material (Ehlers 2020). These glacial deposits are characterised by high levels of uranium, which is an important contributor to radon concentrations in the Quaternary strata in Northern Germany due to radioactive decay (Birke et al. 2009).

The Holocene / Pleistocene boundary at 11,700 yr b2k (Walker et al. 2009) marks the end of the last glacial period when the last remnants of the glaciers retreated to the north and extensive, hazel-, oak-, elm- and lime-dominated forests with dense undergrowth evolved again in central Europe (Litt et al. 2001; Sirocko et al. 2016).



## **2 Radon flux measurements in the glacial sediment deposits of Schleswig-Holstein**

The following chapter discusses the impact of glacial sediment deposits and the presence of active fault systems on the spatial variability of radon exhalation from soil to the atmosphere. For this purpose, radon flux was measured along profiles in four study areas in Schleswig-Holstein. Furthermore, laboratory experiments were conducted to determine the influence of grain size and moisture content on radon emanation.

Because radon exhalation not only shows strong spatial variations, but also considerable temporal fluctuations, radon flux was continuously recorded for one year in the research area Kleinneudorf to study the influence of air temperature and atmospheric pressure on radon release from the soil.

### **2.1 Background information**

Radon is ubiquitous in the environment. Being a naturally occurring noble gas, radon is everywhere around us, in the bedrock and soil beneath us, in the water we drink, and in the air we breathe. The most abundant isotope is  $^{222}\text{Rn}$  (henceforth called radon), progeny of  $^{226}\text{Ra}$  and thus part of the  $^{238}\text{U}$  decay series (Fig. 2.1). Radon is of radioactive character, i.e., it emits alpha particles when decaying into its daughter isotope  $^{218}\text{Po}$  with a half-life rate of 3.82 days. Other natural isotopes of radon include thoron ( $^{220}\text{Rn}$ ) and actinon ( $^{219}\text{Rn}$ ). However, thoron and actinon have very short half-lives (55 s and 4 s, respectively) and decay more or less right where they form.

Radon is created through alpha decay of radium within mineral grains that contain uranium and its progenies. The process of radon escaping a grain and entering into the free pore space is called emanation (Semkow 1990). The emanation power is primarily dependent on grain size, although various other parameters like prevailing soil temperature and water content also influence it. Due to the mass

ratio between the produced radon atom and the emitted alpha particle, radon only has a recoil distance of 20 – 70 nm and solely atoms produced near the grain boundary can escape (Monnin and Seidel 1992; Breitner et al. 2010). Accordingly, a smaller grain size enlarges the specific surface area which increases the chance of radon atoms leaving the mineral grain. Another important factor impacting the emanation power is moisture content; since water absorbs kinetic energy and prevents the radon atoms from reaching their maximum recoil distances, therefore decreasing the radon emanation power.

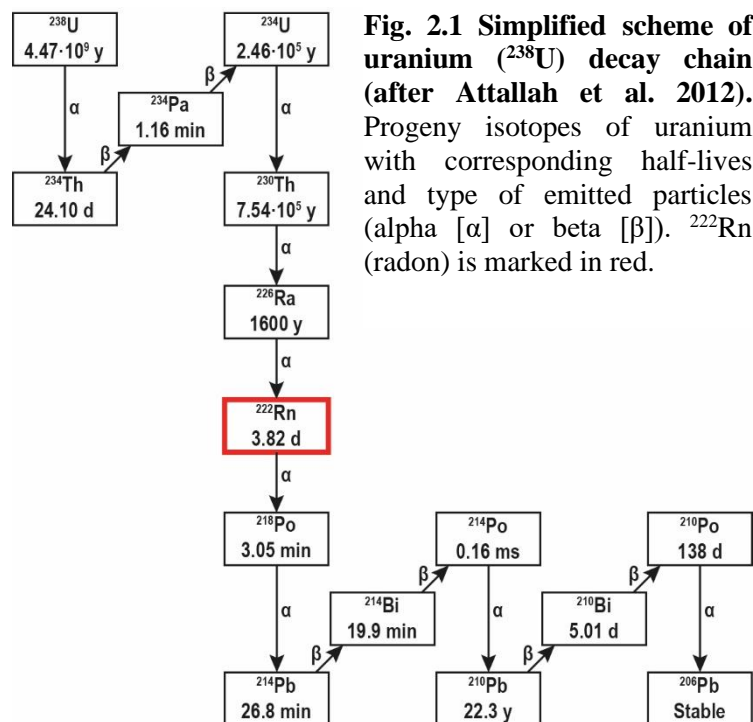


**Fig. 2.1 Simplified scheme of uranium ( $^{238}\text{U}$ ) decay chain (after Attallah et al. 2012).** Progeny isotopes of uranium with corresponding half-lives and type of emitted particles (alpha [ $\alpha$ ] or beta [ $\beta$ ]).  $^{222}\text{Rn}$  (radon) is marked in red.

There are two different mechanisms by which radon moves once in the open pore space, by advection in the pore volume or by diffusion within the pore fluid (Tanner 1964, 1980; Nazaroff 1992). Diffusion, which is driven by concentration gradients, is usually in the order of  $10^{-4}$  to  $10^{-2}$  m per day and is therefore rather insignificant for radon migration. Pressure- and density-driven gas phase flux and buoyant gas bubble movements on the other hand, which strongly depend on soil porosity and permeability, are much greater and can even reach values up to  $10^3$  m per day in fractured rocks and karste (Etiopie and Martinelli 2002). However, because radon is quantitatively too scarce in the subsurface to migrate on its own, it needs the presence of a carrier fluid or gas, usually water,  $\text{CH}_4$  or  $\text{CO}_2$ , to ensure notable migration distances (Etiopie and Lombardi 1995).

Depending on the scientific discipline and objective, radon can be measured in different units. Radon concentrations in soil gas and atmospheric radon are measured per unit volume ( $\text{Bq}/\text{m}^3$ ), whereas radon flux, i.e., the quantity of radon which is being exhaled from the subsurface into the air, is measured per unit surface area and per unit time ( $\text{Bq}/\text{m}^2\text{s}$ ). Radon is being released into the atmosphere from all terrestrial, ice-free surfaces. The main influences on flux quantities are the mineralogical composition of the subsurface, its moisture content, porosity and permeability (e.g., Kemski et al. 2001, 2005; Etiope and Martinelli 2002). Radon exhalation also occurs above open water bodies, although in much smaller quantities than in terrestrial environments (Schery and Huang 2004).

### **2.1.1 Scientific applications of radon**

Radon is used in a range of practical applications in natural sciences and the healthcare sector (Mc Laughlin 2012). For example, spatial radon anomalies can trace soil degassing activities along active fault zones and fractures (e.g., Künze et al. 2012, 2013; Chen et al. 2018, Iovine et al. 2018). Several studies also suggest that radon anomalies in groundwater and soil air are indicative for crustal strain changes and therefore a potential tool to predict imminent earthquakes and volcanic eruptions (e.g., Igarashi et al. 1995; Neri et al. 2016). However, because radon anomalies are not exclusively caused by seismic activities and may have other origins, interpretation about their definite connection should be done with caution (Mc Laughlin 2012; Woith 2015). Nonetheless, using radon as a prediction tool for earthquakes and volcanic eruption is an important research field, because measurements are relatively cost-effective, easy to apply and could potentially save many lives in high-risk areas.

Radon has ideal properties to study vertical mixing processes in atmospheric layers. As the only gaseous member of its decay chain, radon is being constantly exhaled to the atmosphere and its half-life of 3.82 days is optimal to study turbulent atmospheric systems (e.g., Galmarini 2006; Williams et al. 2011; Chambers et al. 2019). Martens et al. (2004) effectively used radon as a tracer to study mass exchange processes between the atmosphere and forest canopies of a tropical rain forest. Radon proved particularly useful during nighttime when  $\text{CO}_2$ -based measurements are too inaccurate for the low nocturnal atmospheric turbulences and long air residence times.

Radon can also be used as a tool in planetary sciences. In 1971 and 1972, the Apollo 15 and 16 lunar missions showed that there are significant spatial variations of radon and its progeny  $^{210}\text{Po}$  on the surface of the moon (Bjorkholm et al. 1973; Gorenstein and Bjorkholm 1973). Additionally, measured  $^{210}\text{Po}$  activities much larger than radon suggested temporal variations of radon exhalation. This led to the conclusion of the existence of an internal lunar activity. These results were later confirmed by the Lunar Prospector space probe, which detected localized radon outgassing events (Lawson et al. 2005).  $^{210}\text{Po}$  has also been detected in Martian dust (Meslin et al. 2006). This indirect evidence of radon on Mars is indicative of a much greater radon exhalation rate on Mars than on the moon.

One application of radon in healthcare was in radiation therapy, where radioisotopes are used to treat various kinds of cancer (e.g., Binkley 1938; Enker 2010; Mc Laughlin 2012). In Brachytherapy, for example, tiny gold tubes or seeds, around 1 mm in diameter and 5 mm in length, containing radioisotopes are inserted into tumour cells as treatment (Brucer 1993). These seeds initially contained a radium solution, also called the “radium cow”, which produced the radon, or “radium milk”. However, due to a build-up of radiation from its decay product  $^{210}\text{Pb}$ , which is harmful for the human body, radon seeds are nowadays replaced by  $^{215}\text{I}$  and  $^{103}\text{Pd}$ .

### **2.1.2 Radon and health risks**

Due to its gaseous character, radon can easily enter the human body through the lungs, where the emitted radiation can seriously damage body cells. This was first discussed in the first half of the last century when 50 percent of the death causes of German and Czechoslovakian miners were attributed to lung cancer (Lorenz 1944). Pitchblende, a highly radioactive mineral containing high amounts of radium, was mined in the mines of Schneeberg (Germany) and Joachimsthal (Czechoslovakia). However, Lorenz (1944) concluded that radon could not be the sole cause for the high death rate among the workers and stated that other factors like high dust levels in the mines or even hereditary susceptibility due to inbreeding must be taken into account.

In the decades following Lorenz's review, comprehensive studies have shown that radon was not only responsible for the high rate of lung cancer among underground workers (e.g., Clement et al. 2010; Tirmarche et al. 2012), but must be considered to be a serious health threat to the general public due to the effects of indoor radon (e.g., World Health Organisation 2009) and contaminated ground- and drinking water (e.g., National Research Council 1999a, 1999b).

Extensive experiments on laboratory animals and cell culture research have inarguably proven that radon and its progenies have a carcinogenic effect on the human lung (International Agency for Research on Cancer [IARC] 2001; Collier et al. 2005). Other discussed types of cancer caused by radon include leukaemia, prostate cancer, and other extra-pulmonary malignancies (e.g., Raaschou-Nielsen 2008; López-Abente et al. 2018). However, the results of these studies are less unequivocal and must be interpreted with caution (Al-Zoughool and Krewski 2009). Radon primarily targets the human lungs through inhalation and is after smoking the second leading cause for lung cancer. It was therefore classified as a class 1 carcinogenic agent by the IARC ([www.iarc.who.int](http://www.iarc.who.int)). The obtained knowledge about the health threats of radon encouraged many countries in Europe and around the world to develop strategies against the impacts of radiation pollution to the public and to systematically map natural- and indoor radon (e.g., Dubois et al. 2010; Griffiths 2010; Tollefsen et al. 2014; Elío et al. 2019; Bundesamt für Strahlenschutz 2020).

With one of the highest aqueous solubilities of all noble gases, radon can easily enter the groundwater system through diffusion from the bedrock. This may present a potential threat to human health in areas where the bedrock type is rich in uranium (e.g., granite) and groundwater is the only available source of drinking water (National Research Council 1999b; Skeppström and Olofsson 2007).

A more prevalent human health risk is radon in indoor air. Building materials of walls, floors and ceilings that contain radium contribute to indoor radon, e.g., concrete, bricks and other masonry materials. However, building materials are only a secondary source for residential radon (Grzywa-Celińska et al. 2020 and references therein). Its primary source comes from the subsurface. Highest radon levels inside a house are always measured on the ground floor, where radon can penetrate building structures from the underground due to pressure differences between inside and outside the house. This happens through

structural defects, such as cracks and cavities in floors and walls (Appleton 2007). The quantity of indoor radon thereby primarily depends on building construction and permeability of the ground material (Iakovleva and Karataev 2005). Radon can penetrate more easily into older houses without proper ground insulation. On the other hand, newly built houses can show higher levels of indoor radon because of lower air exchange due to an improved insulation of modern windows (Dubois et al. 2010). Other factors affecting indoor radon levels are the prevailing season and weather conditions, porosity and permeability of the bedrock and soil, and the nature of carrier fluids (including carbon dioxide gas and surface- and groundwater; e.g., Bossew and Lettner 2007).

## 2.2 Radon profile measurements

This chapter was published as:

Albert J, Schärf M, Enzmann F, Walzl M, Sirocko F (2021) Local radon flux maxima in the Quaternary sediments of Schleswig-Holstein (Germany). *Int J Earth Sci* 110:1501-1516.

### **Author's contribution**

As lead author of this published chapter, I wrote the manuscript and prepared all figures and tables. I co-organized the individual measuring campaigns during student field trips and selected position and orientation of each radon profile with the exception of the research area Eckernförde. Radon profile measurements of research area Eckernförde and laboratory experiments were led by co-author Maximilian Schärf. Further personal contributions include reading out and processing of measurement data, literature research, and conception and calculation of normalized Rn-indices.

### **Abstract**

This paper presents radon flux profiles from four regions in Schleswig-Holstein (Northern Germany). Three of these regions are located over deep-rooted tectonic faults or salt diapirs and one is in an area with no tectonic or halokinetic activity, but with steep topography. Contrary to recently published studies on spatial patterns of soil radon gas concentration we measured flux of radon from soil into the atmosphere. All radon devices of each profile were deployed simultaneously to avoid inconsistencies due to strong diurnal and seasonal variations of radon exhalation. To compare data from different campaigns, values had to be normalized. Observed radon flux patterns are apparently related to the mineralogical composition of the Quaternary strata (particularly to the abundance of reddish granite and porphyry), and its grain size (with a flux maximum in well sorted sand / silt). Minimum radon flux occurs above non permeable, clay-rich soil layers. Small amounts of water content in the pore space

increase radon flux, whereas excessive water content lessen it. Peak flux values, however, are observed over a deep-rooted fault system on the eastern side of Lake Plön, i.e., at the boundary of the Eastholstein Platform and the Eastholstein Trough. Furthermore, high radon flux values are observed in the two regions associated with salt diapirism and near surface halokinetic faults. These regions show frequent “Local Radon Flux Maxima”, which indicate that the uppermost strata above salt diapirs are very inhomogeneous. Deep-rooted increased permeability (effective radon flux depth) or just the boundaries between permeable and impermeable strata appear to concentrate radon flux. In summary, our radon flux profiles are in accordance with the published evidence of low radon concentrations in the “normal” soils of Schleswig-Holstein. However, very high values of radon flux are likely to occur at distinct locations near salt diapirism at depth, boundaries between permeable and impermeable strata, and finally at the tectonically active flanks of the North German Basin.

## **Introduction**

The classification of so-called radon risk areas in Germany based on soil gas radon measurements combined with geological and soil investigations was first introduced by Kemski et al. (e.g., 1996, 2001, 2005). In more recent years the “Bundesamt für Strahlenschutz” (2020) commissioned the establishment of a radon potential map for Germany to determine the health risk posed by radon nationwide based on approximately 5000 measuring points throughout Germany. Due to the passing of a new Radiation Protection Act in July 2017, the federated state of Schleswig-Holstein released a statewide radon potential map at the end of 2020 (Ministerium für Energiewende, Landwirtschaft, Umwelt, Natur und Digitalisierung 2020).

In order to validate the connection between tectonically and halokinetically active structures and locally elevated flux of radon, we studied radon flux and sediment properties in four research areas in Schleswig-Holstein, Northern Germany (Figs. 2.2 – 2.8). The uppermost strata in Northern Germany are mainly characterised by unconsolidated sediments accumulated during the Middle and Late Pleistocene glaciations (Ehlers et al 2004, 2011; Böse et al. 2012). Beneath these Quaternary deposits, Tertiary silts and sands are intruded by rising salt structures with associated fault systems, which extend



under large parts of the state (Geotektonischer Atlas von Nordwestdeutschland und dem deutschen Nordsee Sektor 2001; Fig. 2.2).

The active dynamics of salt diapirism is strongly debated, but at least one of our research areas (Kleinneudorf, east of Lake Plön; Figs. 2.2, 2.5) underwent a strong local subsidence even during the last 50 years (Sirocko et al. 2002; Lehné and Sirocko 2005, 2010). Furthermore, we present radon flux measurements from two other active halokinetic structures, near the Segeberg Sülberg salt wall close to the city of Bad Segeberg (Figs. 2.2, 2.6) and along the southern shoreline of the Eckernförde Bay (Figs. 2.2, 2.7). In order to obtain data at radon background levels, a location with no tectonic or halokinetic activity, but steep topography, has been chosen near Lake Lanker (Figs. 2.2, 2.4). Additionally, laboratory experiments explore radon emanation signals of various rock types naturally occurring in Schleswig-Holstein. Finally, analysis of the influence of exhalation depth is designed to support obtained field results.

## **Background information**

### **Radon**

The radioactive noble gas radon has three naturally occurring isotopes. The most common isotope  $^{222}\text{Rn}$  (radon), progeny radionuclide of  $^{226}\text{Ra}$  (radium) and thus part of the  $^{238}\text{U}$  (uranium) decay series has a half-life of 3.82 days.  $^{220}\text{Rn}$  (thoron) is part of the  $^{232}\text{Th}$  (thorium) decay chain, and  $^{219}\text{Rn}$  (actinon) is part of the  $^{235}\text{U}$  series. Both have a very short half-life (55 s and 4 s respectively) and are thus of less importance for total radon flux. Because of its main source being bedrock and soil (Turekian and Graustein 2003), radon is ubiquitous in the environment and therefore of great interest to understand its behavior in soil / air exchange processes.

Radon is a known cause for lung cancer and is responsible for thousands of deaths in Germany per year (Menzler et al. 2008; Beck 2017). It has been the subject of many scientific studies in many parts of Europe (UNSCEAR 1982; Kreienbrock et al. 2001; George 2008; Bundesamt für Strahlenschutz 2019), and radon risk maps have been established for many countries, including Germany (e.g., Kemski et al.

1996, 2001, 2005; Bundesamt für Strahlenschutz 2020), Spain (Sainz Fernández et al. 2017), and Switzerland (Kropat et al. 2017). Furthermore, radon is used as a footprint for natural phenomena associated to soil degassing along active faults and fractures (e.g., Künze et al. 2012, 2013; Chen et al. 2018; Iovine et al. 2018; Sciarra et al. 2018), and as a precursor for volcanic activities (e.g., Giammanco et al. 2009; Neri et al. 2016) and earthquakes (e.g., Richon et al. 2003; Steinitz et al. 2003; Woith 2015).

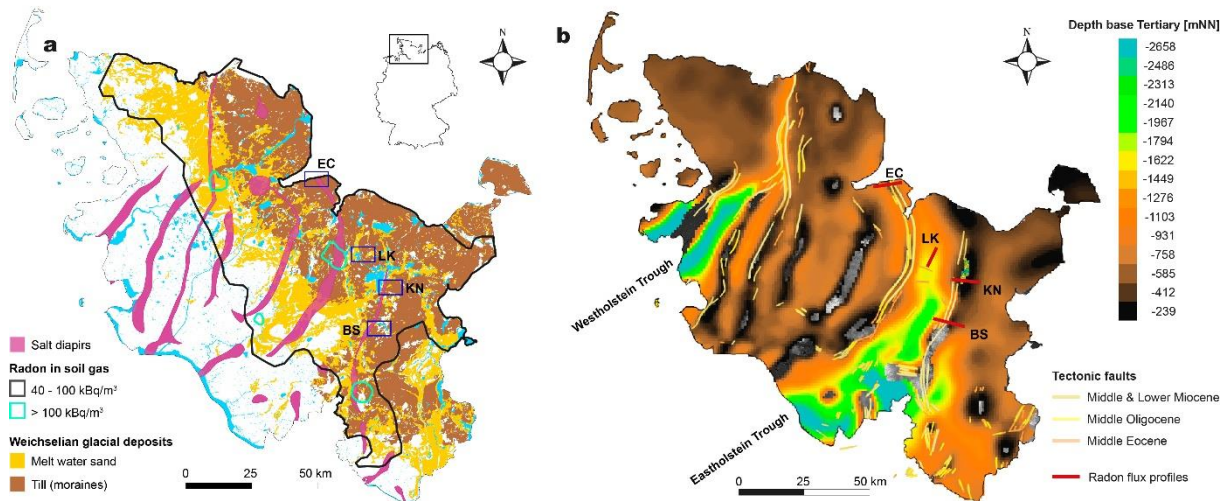


**Fig. 2.2 Simplified overview of Schleswig-Holstein including the locations of the four research areas (BS = Bad Segeberg (N53°58'11.9" E10°23'45.6"), EC = Eckernförde (N54°28'21.1" E10°05'04.6"), KN = Kleinneudorf (N54°06'24.1" E10°27'10.2"), LK = Lanker See (N54°12'38.4" E10°19'06.9")). a) Spatial patterns of salt diapirs, distribution of Weichselian glacial deposits ([www.umweltdaten.landsh.de/nuis/upool/gesamt/geologie/guek250\\_gesamt.pdf](http://www.umweltdaten.landsh.de/nuis/upool/gesamt/geologie/guek250_gesamt.pdf) Accessed 27 October 2022) and elevated radon in soil gas levels ([www.bfs.de/DE/themen/ion/umwelt/radon/karten/boden](http://www.bfs.de/DE/themen/ion/umwelt/radon/karten/boden) Accessed 27 October 2022). b) Depth of base Tertiary along with alignment of Tertiary tectonic faults and orientation of sampled radon profiles (after Geotektonischer Atlas von Nordwestdeutschland und dem deutschen Nordsee Sektor 2001).**

Radon gas is produced through alpha decay of radium within a mineral grain, but due to recoil effects only atoms originating near the grain boundary can escape and may emanate into the free pore space (Semkow 1990). Due to its relatively short half-life, radon can only migrate up to a few meters in the geosphere. So generally, its primary sources are the radium nuclides present in the surrounding bedrock, ground water and soil. Furthermore, the emanation power is strongly dependent on grain size because of its short recoil range of around 20 - 70 nm (Monnin and Seidel 1992; Breitner et al. 2010). A smaller grain size increases the specific surface area and therefore amplifies the chance of radon atoms leaving the mineral grain. A further influence on radon emanation is moisture content, as water is a natural

absorber of kinetic energy and impedes radon atoms from reaching their maximum recoil distances. Several studies revealed that, up to a certain water content, radon emanation enhances with increasing moisture on the grain surface (e.g., Strong et al. 1982; Hassan et al. 2009; Yang et al. 2019), but radon is kept in groundwater until released by a temperature rise or drop of air pressure.

After leaving the mineral grain the gas migrates via two mechanisms, either through diffusion within the pore fluid or advection in the open pore space (Tanner 1964, 1980; Nazaroff 1992). These processes are dependent on concentration gradients and pressure gradients, respectively. Diffusive mechanisms are usually in the order of  $10^{-4} - 10^{-2}$  m per day and are therefore negligible for radon migration. Pressure- and density-driven gas phase flux and buoyant gas bubble movements on the other hand, which strongly depend on soil porosity and permeability, can reach much greater migration distances, even up to  $10^3$  m per day in fractured rocks and karste (Etiopie and Martinelli 2002). However, the quantity of radon in the subsurface is too insignificant to migrate by convection on its own, but radon atoms can be transported by a carrier, either in gaseous or liquid form, to ensure greater transport distances (Etiopie and Lombardi 1995). The most common carriers in the subsurface are  $\text{CH}_4$  and  $\text{CO}_2$ , whose migration behaviors along tectonically active pathways are well understood (Irwin and Barnes 1980; Sciarra et al. 2018). With a half-life of less than four days and short migration distances, most of the radon produced decays near its formation. Thus, only radon atoms which originate near-surface, or are transported in permeable strata by a carrier gas from greater depths can reach the geosphere / atmosphere boundary and exhale into the atmosphere and disperse (Hassan et al. 2009), or accumulate indoors in inhabited areas (Finne et al. 2019).

Radon exhalation can vary greatly depending on time of day (Schubert et al. 2002; Tareen et al. 2019), season (Winkler et al. 2001), or even greater timescales. Yan et al. (2017) found a distinct connection between quasi decadal (8 – 11 years) fluctuations of radon concentration sampled at a hot spring site in Southwestern China and variations in the spring's discharge rate and water temperature. Mudelsee et al. (2020) present a first radon flux time series from our research site Kleinneudorf and document different modes of radon release from the subsurface, predominantly dependent on atmospheric pressure and air temperature variations.

## **Regional geology**

Schleswig-Holstein is the northernmost federal state of Germany (Fig. 2.2). It borders Denmark to the north and the North Sea to the west. To the south, the Elbe River marks the borderline to the adjacent federated states of Niedersachsen and Hamburg. To the east, Mecklenburg-Vorpommern as well as the Baltic Sea border the state.

Geologically, the research areas belong to the North German Basin which itself is part of the much larger central European Basin System, a NW-SE trending tectonic structure stretching from Norway to Central Germany and from the North Sea to Poland (Bayer et al. 1999; Maystrenko et al. 2008). Hundreds of meters of salt were deposited in this basin during the Permian and are today overlain by up to 10 km of Mesozoic and Cenozoic strata. This results in a massive overload causing the salt to react ductile, leading to the rise of salt diapirs and associated fault systems that can reach up to the surface (Fig. 2.2). The salt can even penetrate to the surface, as in Bad Segeberg.

The initial salt movement started during the Triassic, although two other major phases of diapirism occurred during the Jurassic and Cenozoic (Maystrenko 2005). Several studies even show that these halokinetic processes are still active until present day (Sirocko et al. 2002, 2008; Lehné and Sirocko 2005, 2010; Al Hseinat et al. 2016; Al Hseinat and Hübscher 2017).

The topography of Schleswig-Holstein was shaped by three glacial advances (Saalian, Elsterian, and Weichselian glaciations) which transported moraine material from Scandinavia and deposited it in Northern Germany in form of alternating sequences of glacial till and glaciofluvial sands, which form a landscape with elevated moraines, valleys and abundant lakes (Ehlers et al. 2004, 2011; Böse et al. 2012).

## **Research Areas**

The areas for our radon flux sampling were chosen according to the pattern of salt diapirs and known halokinetic faults, documented in the "Geotektonischer Atlas von Nordwestdeutschland und dem deutschen Nordsee Sektor" (2001; Fig. 2.2). We chose research areas where information about the deeper strata is accessible from seismic surveys, that reveal tectonic structures in the topmost 500 m to

ensure the presence of permeable faults which extend into the Quaternary sediments with a potential to reach the surface (Wiederhold et al. 2003; Al Hseinat et al. 2016). The modern topography of Schleswig-Holstein is available as a GIS computed grid ([www.schleswig-holstein.de/DE/landesregierung/ministerien-behoerden/LVERMGEOISH/Service/serviceGeobasisdaten/geodatenService\\_Geobasisdaten\\_Dienste](http://www.schleswig-holstein.de/DE/landesregierung/ministerien-behoerden/LVERMGEOISH/Service/serviceGeobasisdaten/geodatenService_Geobasisdaten_Dienste) Accessed 27 October 2022).

The research area Lanker See (LK) is located in direct proximity east of Lake Lanker and extends in N-S direction across several, partially forested or farmed ridges and valleys (Fig. 2.4). The region lies between two salt walls where the "Geotektonischer Atlas von Nordwestdeutschland und dem deutschen Nordsee Sektor" (2001) documents a complete absence of faults at depth (Fig. 2.2b). This area was chosen to study the influence of topography on radon flux and to gain information about typical radon background levels in Schleswig-Holstein.

The sampling area Kleinneudorf (KN) lies two kilometers east of Lake Plön (Figs. 2.2, 2.5a). The tectonic feature specific to this location is an actively subsiding depression on the lake's eastern shore near the village of Kleinneudorf located on the flank of a salt diapir. Its topographic changes have been described by Lehné & Sirocko (2005, 2010) and Sirocko et al. (2002, 2008). Several independent eyewitnesses reported visual changes to the characteristic landscape of the site over the last 50 years. The area is located directly above the contact zone between the Eastholstein Platform to the east and the flank of the Eastholstein Trough beneath the lake (Fig. 2.5c). The associated faults strike in N-S direction parallel to the lake's shoreline (Geotektonischer Atlas von Nordwestdeutschland und dem deutschen Nordsee Sektor 2001) and appear to cause local subsidence of cm/year, which is unusually high for Northern Germany, but still comparable to local subsidence rates, for example in the city of Lüneburg, southeast of Hamburg (Sirocko 2012).

The third research area is Bad Segeberg (BS), located around 6.2 km northeast of the Kalkberg, a prominent salt dome in the city of Bad Segeberg (Figs. 2.2, 2.6a). In the vicinity to the chosen sampling profiles lies the Segeberg Sülberg salt wall, a N-S striking, around 50 km long salt structure mainly consisting of Zechstein salt. Ross (1998) reports recent uplift rates for the Kalkberg of around 0.5 mm/a, whereas other authors suggest uplift rates of up to 1.2 mm/a (Meier et al. 2003). The sampling site is

near the village of Wardersee directly south of Lake Warder and crosses a suspected border fault outcrop (Fig. 2.6b; Wiederhold et al. 2003). The measured profiles roughly include sampling points of Künze et al. (2013) who also conducted part of their research on radon concentrations in soil gas in this area.

The fourth sampling area (EC) stretches along the Eckernförde Bay shoreline, around 15 km east of the city of Eckernförde (Figs. 2.2, 2.7a). The measured sections extend from the village of Lindhöft in the west to Dänisch-Nienhof in the east. A salt structure and several associated deep-rooted faults extend in N-S direction perpendicular to the shoreline (Fig. 2.7c; Al Hseinat et al. 2016).

Name	Date	Profile length	Sampl. points	Sampl. time [h]	Mean $^{222}\text{Rn}$ flux [mBq/m <sup>2</sup> s]	Highest $^{222}\text{Rn}$ -Idx	Temp. [°C]	Atm. press. [hPa]	Air moist. [%]
<i>Bad Segeberg</i>									
BS 1	4 Apr 2019	3.37 km	13	2	1.71	2.24	13.9	997.7	60
BS 2	16 July 2019	3.69 km	13	2	2.58	2.32	19.5	1012.0	60
BS 3	16 July 2019	3.69 km	11	2	2.04	1.78	17.5	1013.0	67
BS 4	17 July 2019	3.69 km	13	2	2.09	2.00	15.7	1013.9	77
BS 5	14 Aug 2018	495 m	14	1	1.03	2.35	23.2	1007.0	65
BS 6	3 Apr 2019	495 m	16	2	2.39	1.52	10.8	1002.5	89
<i>Eckernförde</i>									
EC 1	8 Apr 2019	11.76 km	16	2	2.00	3.93	8.1	1011.8	65
EC 2	9 Apr 2019	4.70 km	16	2	2.02	3.89	5.5	1015.7	51
EC 3	17 July 2019	11.76 km	14	2	1.89	2.45	18.6	1010.9	72
EC 4	18 July 2019	4.89 km	14	2	1.48	2.13	18.2	1009.4	77
EC 5	18 July 2019	2.79 km	14	2	1.50	2.50	19.1	1007.9	77
EC 6	19 July 2019	10.17 km	14	2	2.12	2.07	19.9	1009.4	78
EC 7	19 July 2019	263 m	14	2	1.56	5.05	20.3	1010.5	71
EC 8	20 July 2019	263 m	14	2	1.51	3.69	22.9	1008.9	56
<i>Kleinneudorf</i>									
KN 1	23 Mar 2018	2.45 km	11	1	0.65	5.32	3.1	1007.0	85
KN 2	5 Apr 2019	2.35 km	16	2	2.71	2.90	9.9	1005.6	81
KN 3	6 & 10 Apr 2019	2.91 km	19	1	4.01	3.91	12.8	1008.4	69
KN 4	21 Mar 2018	198 m	13	1	0.72	5.20	4.9	1023.7	75
KN 5	22 Mar 2018	161 m	13	1	1.18	6.36	5.6	1008.2	89
KN 6	7 Apr 2019	103 m	16	2	2.73	2.88	9.5	1009.6	73
<i>Lanker See</i>									
LK1	7 & 8 Aug 2019	2.57 km	25	2	1.41	2.73	18.8	1004.9	81
LK 2	9 Aug 2019	221 m	14	2	2.87	2.67	20.3	1011.2	69

**Table 2.1 Overview of surveys carried out including prevailing meteorological condition during time of sampling.**

## Methods

All data were generated during field campaigns in 2018 and 2019 (Table 2.1). We measured radon with up to 16 devices simultaneously. This setup does not measure soil radon content but monitors the flux from the soil into the air, providing composite information on processes related not only to the primary

radon content of the soil, but also its permeability, and thus depth of active radon convection in the ground water unsaturated zone of the surface strata, i.e., its potential depth.

### Sampling strategy to measure radon flux

Sampling was performed with a commercial radon concentration measuring device (Radona Expert+, modified by RadonTec GmbH). The display of the instrument was modified to show concentration values of radon every ten minutes. In addition to measuring radon concentration and temperature, the instrument was modified to record the prevailing humidity and atmospheric pressure.

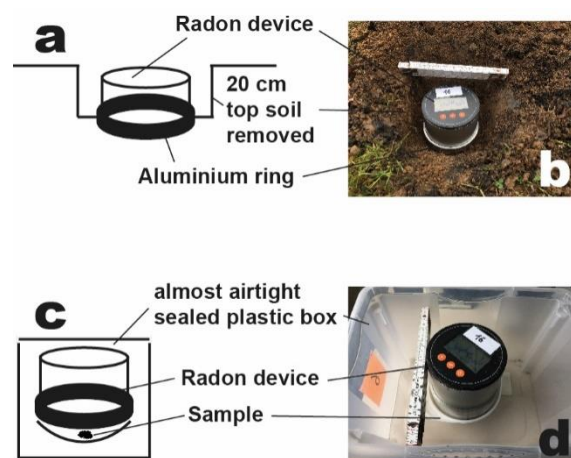


**Fig. 2.3 Illustration of sampling setup.** a) Schematic description and b) picture of radon flux field sampling. c) Schematic description and d) picture of radon sampling under laboratory conditions. Figure d shows setup prior to attachment of lid.

The Radona system was mounted on an aluminum ring of 14 cm in diameter. Before measurement, the topmost soil layer 0 – 20 cm was removed. The aluminum ring of the device was pushed around 2 cm into the soil to allow gas from the subsurface to migrate through, but minimize the effects of wind entering the detection chamber (Fig. 2.3a, b). Initial and end concentrations after two hours, expressed as  $\text{Bq m}^{-3}$ , were determined and the differences between the readings are presented as flux values. If values were significant already after one hour, we stopped measurements to not exceed the detection limit of the devices (see Table 2.1). In consideration of daily variability of radon activity (Schubert et al. 2002; Tareen et al. 2019; Mudelsee et al. 2020), all sampling points of a single profile were measured

with as little time offset as possible, depending on number of research assistants and distances between individual sampling points. According to Tuccimei and Soligo (2008), high CO<sub>2</sub> concentrations can interfere with radon flux signals. However, ongoing studies show that CO<sub>2</sub> levels in Schleswig-Holstein lie well below these critical levels and we therefore did not include a correction factor for interfering CO<sub>2</sub> into our data. In addition to radon flux values, the prevailing meteorological conditions were recorded (Table 2.1) and sediment physical properties were calculated (Fig. 2.8).

Measured radon data were converted into conventional flux values (mBq m<sup>-2</sup> s<sup>-1</sup>) using the formula described by Perrier et al. (2009). Our flux values cannot be used to define "Radon Risk Areas" ([www.bfs.de](http://www.bfs.de)), but facilitate to distinguish regional and local anomalies in the flow of radon from soil into the air. The advantage of this method is to detect the strength of degassing without any drilling effort. To ensure comparability between our own profiles measured at different days and seasons, radon values were normalized through division to mean radon flux of respective profiles to obtain synthesized <sup>222</sup>Rn indices. We chose this approach because absolute values are arbitrary and depend on time of measurement. Normalized values, however, are comparable to each other and provide a fast and easy approach to detect local gas exhalation anomalies over large regions at different times.

### **Radon Devices**

The measurement principle of the Radona device is based on an ionization chamber, where an electric field is applied between an enclosure (cathode) and an inner electrode needle (anode). The positively charged alpha particles, which are formed within the chamber during the decay of radon and its progeny isotope polonium, ionize the air in the measuring chamber. This charged air is accelerated towards the anode or cathode and causes minimal temporal changes to the electrical field, which are detected and evaluated as radioactive decay. As humidity and vibrations of the electrode needle cause similar changes within the electric field, very high humidity or increased vibrations disturb the signal and can lead to failure of the sensor. The Radona device has an application range of 0.2 – 3700 Bq m<sup>-3</sup> and a measuring error range of ±5 – 10%, depending on weather conditions. The efficiency for radon sampling specified by the manufacturer is 0.5 counts per minute (cpm) at 1pCi/l, or, equivalently, a "harmonized" efficiency of 81 cph at 100 Bq m<sup>-3</sup>. The operating range of the device chamber is 10 – 40 °C. However, the



chamber is still functional at 0 °C, because temperature is not a primary factor for the reliability of the chamber. Although temperatures below 10 °C might slightly increase the measurement error, the impact of this effect is minimal and neglectable for our specific sampling strategy.

### **Radon flux transects**

Gas flux profiles consist of up to 16 single sampling points (16 Radona devices) on transects perpendicular to faults visible in seismic profiles or the "Geotektonischer Atlas von Nordwestdeutschland und dem deutschen Nordsee-Sektor" (2001). Fault lines were projected vertically to the earth's surface using the information of the "Geotektonischer Atlas" (Figs. 2.5 – 2.7). For profiles with more than 16 sampling points (see Table 2.1), sampling was performed on two separate days and measured radon flux values of the second day were normalized to the results of the first day at two points of sampling. Transects were of 1 – 2 km length to guarantee a sufficient distance to the center area above fault outcrops. To ensure higher resolution in zones of elevated radon exhalation, sampling distance was reduced near points of apparent high radon activity. Additionally, we conducted more detailed surveys in areas of interest with lengths of a few hundred meters. Individual sampling points were selected after accessibility to the area and soil cover.

### **Soil samples**

Soil samples were collected along selected profiles using a steel tube of known volume. Samples were taken exactly beneath the location of the radon instruments and weighted to calculate wet bulk density. Subsequently, samples were dried in an oven at 55 °C for several hours to remove moisture content without altering soil chemistry (e.g., organic carbon or sulfur content) and, after cooling, weighted again to determine water content and dry bulk density. Mean grain sizes were identified using a Camsizer particle analyzer by "Retsch Technology". Permeability coefficients ( $k_f$ ) were calculated using the empirical formulas of Beyer (1964) and Seiler (1973), which are based on grain size compositions of samples. To isolate the clay fraction from the silt fraction, the Atterberg experimental method was used (Stein 1985). The loss-on-ignition (LOI) method was applied to determine organic carbon content (Dean 1974). For this purpose, specimens were weighted, heated at 550 °C for four hours inside a "Nabertherm" muffle furnace and weighted again to obtain LOI values, which mainly represent organic

carbon. Carbonate content was analyzed using the gas volumetric Scheibler method described by Tatzber et al. (2007).

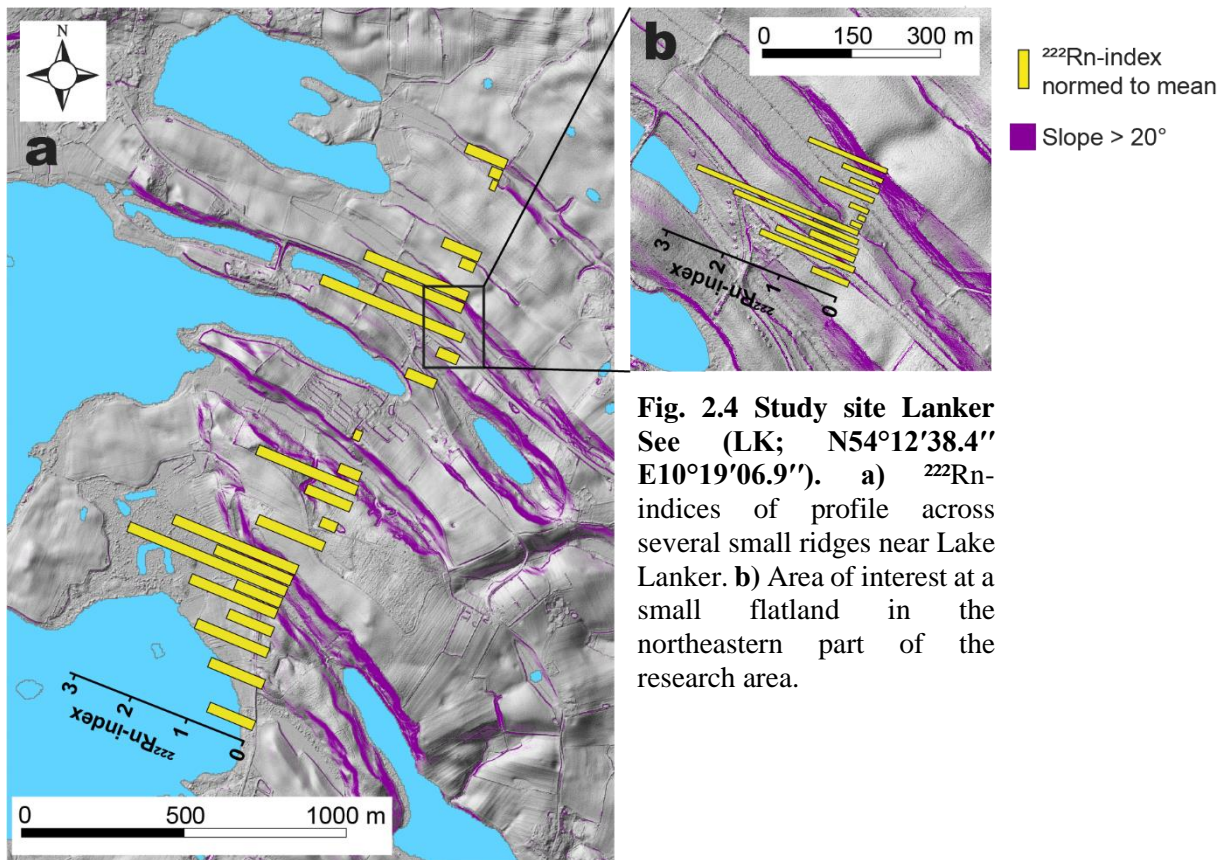


**Fig. 2.4 Study site Lanker See (LK; N54°12'38.4'' E10°19'06.9'').** a)  $^{222}\text{Rn}$ -indices of profile across several small ridges near Lake Lanker. b) Area of interest at a small flatland in the northeastern part of the research area.

## Results

### Radon flux transects

From March 2018 till August 2019 a total of 22 radon profiles (323 sampling points) were measured. Profiles for all research areas are summarized in Table 2.1 and Fig. 2.8. The temperature ranged from 3.1 °C in March to 23.2 °C in August. Atmospheric pressure varied between 997.7 and 1023.7 hPa and relative humidity between 51 and 89%. Water content of soil samples varies between 2.49 and 50.97 wt% (Fig. 2.8a). Bulk density wet and bulk density dry range from 0.75 to 1.93 g/cm<sup>3</sup> (Fig. 2.8b) and from 0.53 and 1.66 g/cm<sup>3</sup> (Fig. 2.8c), respectively. Mean grain sizes vary between 145 and 729 μm (Fig. 2.8d) and permeability coefficients ( $k_f$ ) range from 1.83E-06 to 7.12E-04 m/s (Seiler; Fig. 2.8e)

and from  $1.47\text{E-}06$  to  $2.48\text{E-}04$  m/s (Beyer; Fig. 2.8f). LOI varies between 0.67 and 18.67 wt% (Fig. 2.8g) and calcium carbonate content between 0 and 1.15 wt% (Fig. 2.8h).

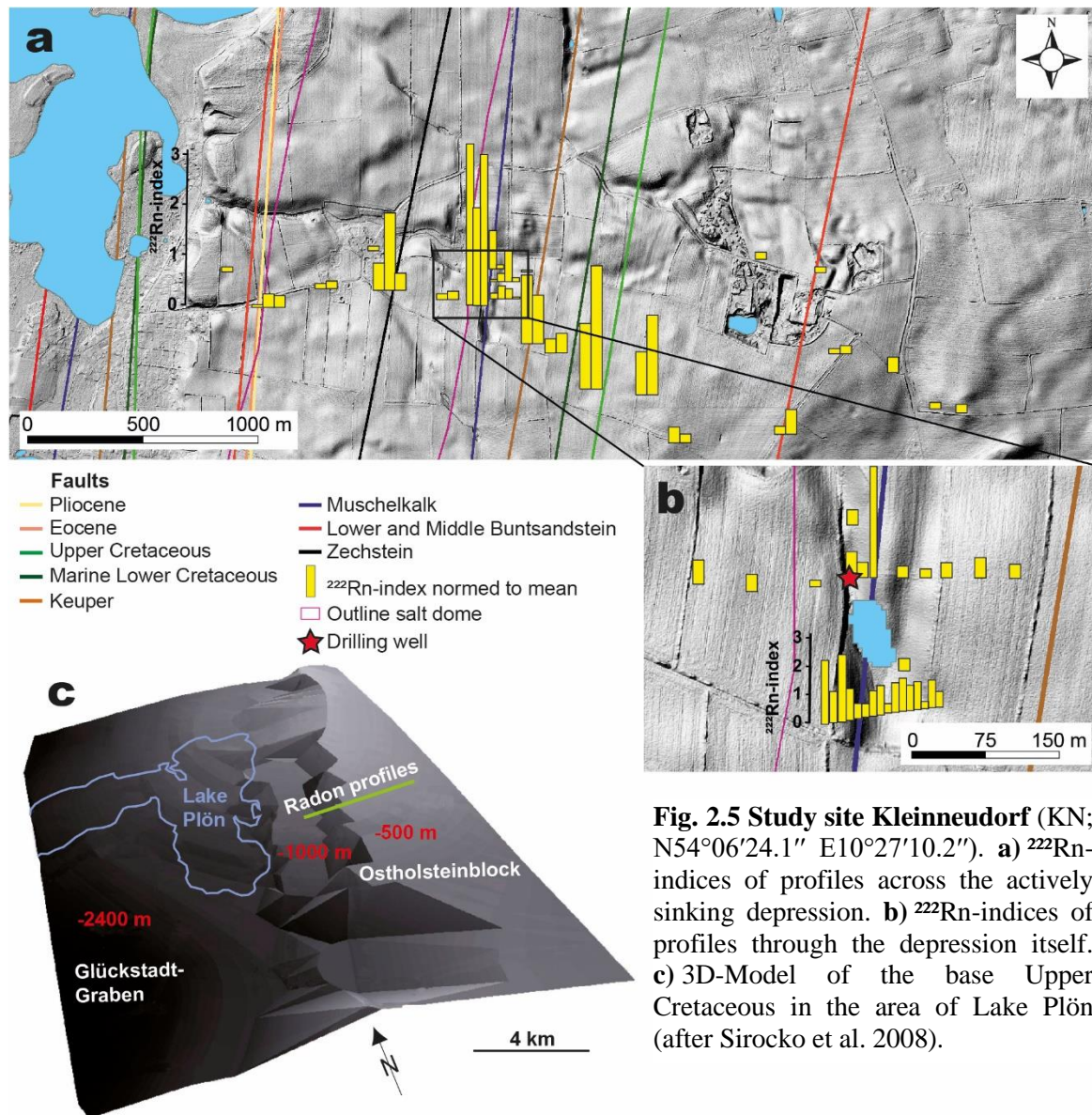


**Fig. 2.5** Study site Kleinneudorf (KN; N54°06'24.1" E10°27'10.2"). **a)**  $^{222}\text{Rn}$ -indices of profiles across the actively sinking depression. **b)**  $^{222}\text{Rn}$ -indices of profiles through the depression itself. **c)** 3D-Model of the base Upper Cretaceous in the area of Lake Plön (after Sirocko et al. 2008).

In the research area Lanker See (LK) mean radon flux was  $2.77 \text{ mBq m}^{-2} \text{ s}^{-1}$  for profile LK1 (Table 2.1). Maximum radon exhalation occurred at two sites, which are at the slope toe of the southernmost margin ( $^{222}\text{Rn}$  indices between 2.14 and 2.73) and at the slopes bordering a small flatland in the northern part of the section ( $^{222}\text{Rn}$  index between 1.36 and 2.46; Fig. 2.4a). A more detailed profile (LK2) was sampled across the flatland and showed mean radon flux of  $5.63 \text{ mBq m}^{-2} \text{ s}^{-1}$ . Maximum radon flux was observed

at the southern, rather smooth slope ( $^{222}\text{Rn}$  indices between 1.91 and 2.67) and minimal radon exhalation occurred at the lowermost part of the flatland ( $^{222}\text{Rn}$ -indices between 0.11 and 0.21; Fig. 2.4b).

In the research area Kleinneudorf (KN) mean radon flux ranged from 1.27 to 7.88  $\text{mBq m}^{-2} \text{s}^{-1}$  for all profiles (Table 2.1). Maximum radon exhalation was detected within the sinking depression and on the neighbouring farmlands (maximum  $^{222}\text{Rn}$ -indices between 2.90 and 5.32; Fig. 2.5a). At higher spatial resolution through the depression peak radon flux occurred at the steep flanks of the trough (maximum  $^{222}\text{Rn}$ -indices between 2.88 and 6.63; Fig. 2.5b).

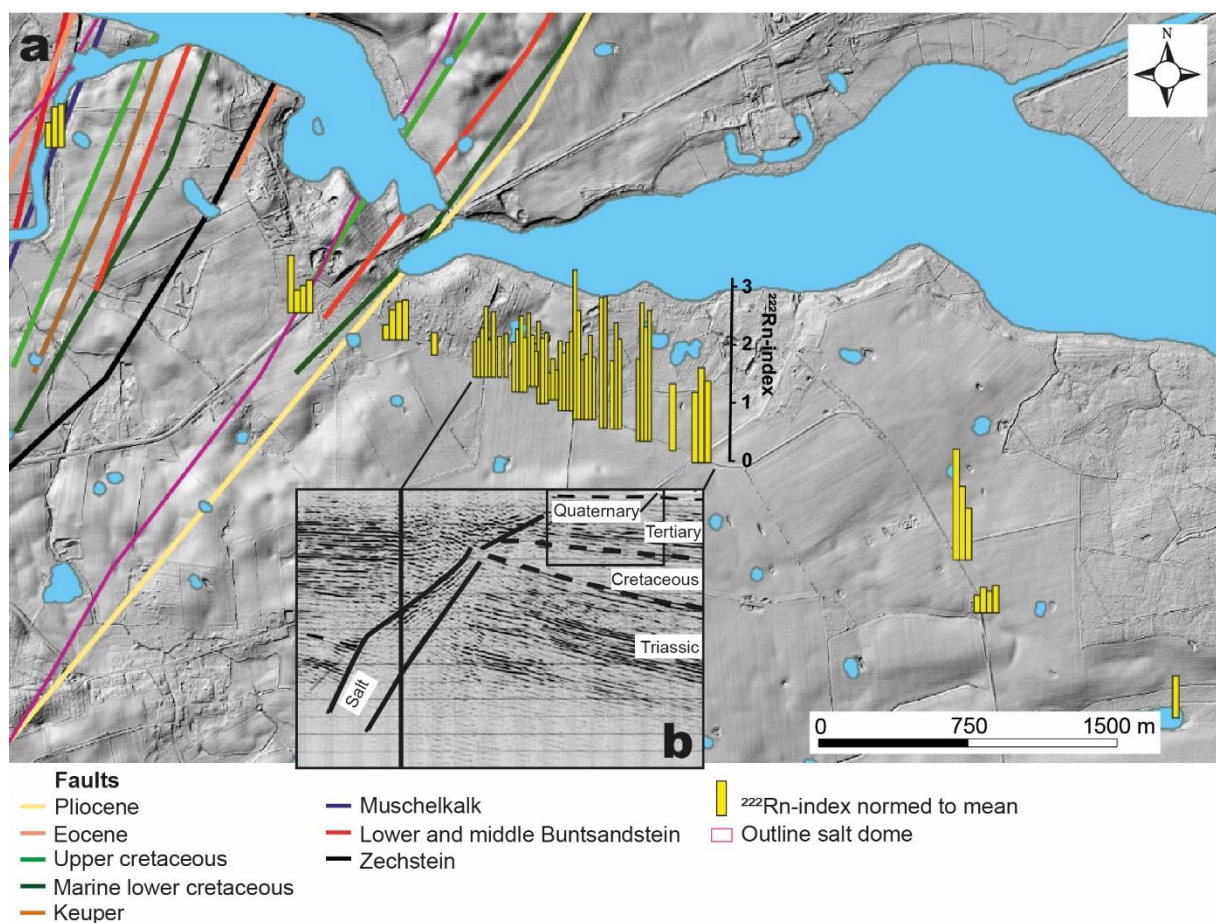


**Fig. 2.6 Study site Bad Segeberg (BS; N53°58'11.9" E10°23'45.6"). a)**  $^{222}\text{Rn}$ -Indices of profiles across border fault outcrop. **b)** Seismic profile adapted from Wiederhold et al. (2003).

In Bad Segeberg (BS) mean radon flux was between 2.02 and 5.07  $\text{mBq m}^{-2} \text{s}^{-1}$  (Table 2.1). Maximum radon activity was recorded around 0.93 to 1.15 km east of the salt dome above a suspected border fault outcrop (maximum  $^{222}\text{Rn}$ -indices between 1.52 and 2.35; Fig. 2.6a). The tectonic faults above the salt

dip with an angle of  $35^\circ$ . We have plotted these faults at the depth of Tertiary strata. The extension to the surface will shift their position to the east into the region of the radon flux maxima (Fig. 2.6b).

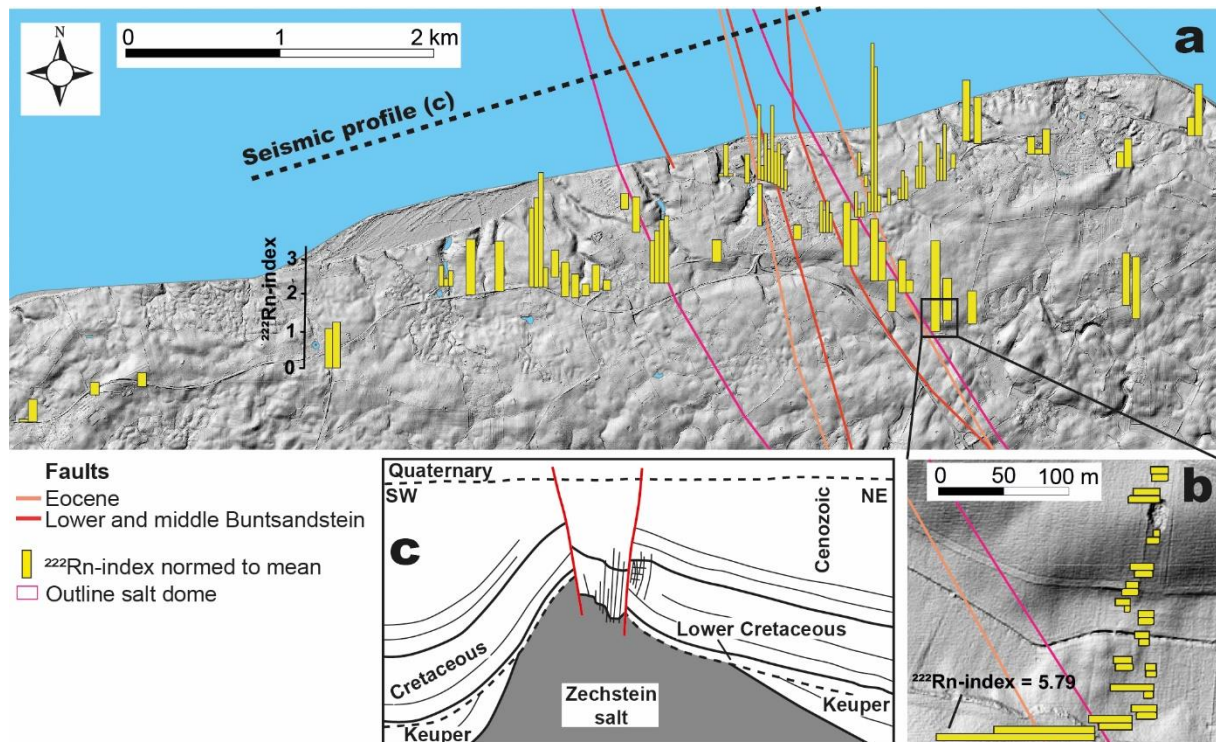


**Fig. 2.7 Study site Eckernförde** (EC; N54°28'21.1" E10°05'04.6"). **a)**  $^{222}\text{Rn}$ -indices of profiles across the fault zone parallel to the Eckernförde Bay. **b)** Area of interest through a small trough in the southern part of the research area. **c)** Schematic description of the subsurface, adapted from Al Hseinat (2016).

In Eckernförde (EC) mean flux values ranged from  $2.90$  to  $4.16 \text{ mBq m}^{-2} \text{ s}^{-1}$  for all profiles (Table 2.1). We measured increased radon flux levels in the vicinity to the fault zone (maximum  $^{222}\text{Rn}$ -indices between  $2.07$  and  $3.93$ ; Fig. 2.7a). Two detailed traverses at the fault zone's eastern margin showed maximum radon exhalation at the southern, steep slope with  $^{222}\text{Rn}$ -indices of  $5.05$  (EC7) and  $3.69$  (EC8), quite contrary to the trough base and at its northern flank (Fig. 2.7b).

### Exhalation depth

Due to radon concentrations being significantly higher between  $0.7$  and  $1 \text{ m}$  than in shallower depths (Rose et al. 1990; Künze et al. 2013), we compared the radon flux signal at the surface and from a  $1 \text{ m}$  deep drilling hole for our specific sampling strategy at seven sampling points. We used the setup described in the methods section to measure radon flux at the surface. To obtain information about flux

levels at 1 m depth, we drilled boreholes using a hand-operated drilling implement. We then inserted a 1 m long plastic filter pipe with slits along its complete length into each borehole, which increases the effective soil area, refilled the space between the pipe and the drill hole wall with the excavation material and connected the pipe to the measuring device.

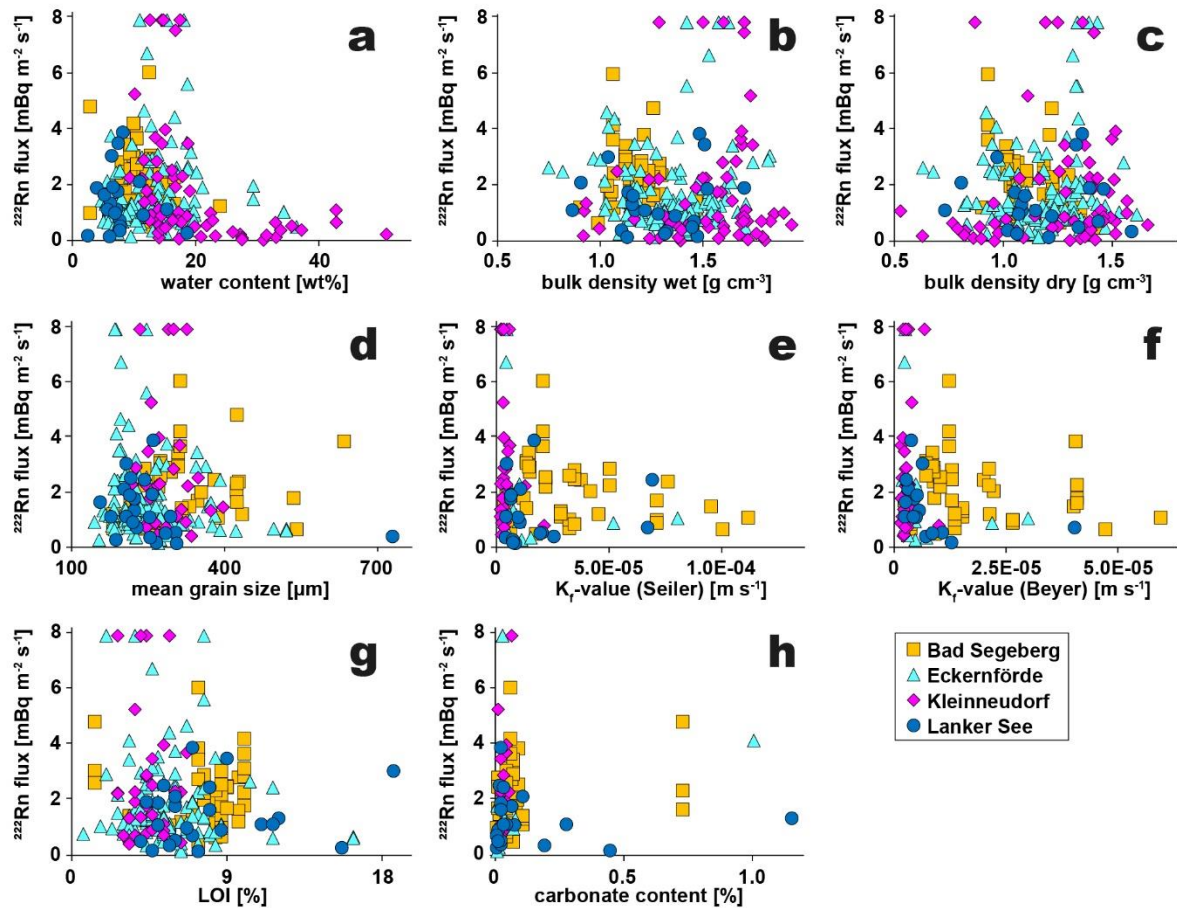


**Fig. 2.8 Measured radon flux** compared to physical properties of soil samples **a)** water content, **b)** bulk density wet, **c)** bulk density dry, **d)** mean grain size, **e)** permeability coefficient after Seiler (1973), **f)** permeability coefficient after Beyer (1964), **g)** Loss on Ignition (LOI), and **h)** carbonate content of soil samples. Shown sample points may exceed detection limit of  $7.85 \text{ mBq m}^{-2} \text{ s}^{-1}$ .

Although absolute values are not comparable between the surface and 1 m depth for our sampling strategy, which is due to an increased soil area inside the borehole, radon flux was two / three times higher for the 1 m depth measurements. It is most likely the enlargement of actively degassing soil volume that causes an increase of flux out of the borehole. Therefore, active exhalation depth is an important factor to determine radon flux. This appears to us as the most probable explanation for

increased radon flux above faults. Exhalation above permeable faults most likely transports gas from greater depths to the surface.

However, it is significantly labour-consuming to drill an adequate number of boreholes for an interpretable profile. For identifying anomalies of enhanced radon flux, it is sufficient to remove only the top soil, as long as all sampling points are prepared uniformly and grain size distribution of soils and soil types are comparable between measurement sites. A method to determine the precise influence of the exhalation depth has not yet been developed, but will be the subject of a future, systematic study.

### **Laboratory experiments**

We measured radon emanation powers of selected samples in the laboratory for **i)** typical tillitic material occurring in Schleswig-Holstein and **ii)** various other natural substances to support our acquired field results (Fig. 2.9). In total, radon emanation power for 52 sediment samples (silt / sand fraction) of uniform weight (100 g) were analysed using the Radona system in almost airtight sealed plastic boxes, to still allow air to enter and gently disperse the accumulating radon (Fig. 2.3c, d). Sampling time for all specimens was one hour. The technical error of the device is  $\pm 10\%$ . To minimize additional reproduction errors, we have considered an error of  $\pm 40\%$  to be significant. It was found that differences in emanation values greater than 50% for the various materials were indeed reproducible. However, obtained absolute values depend on our specific sampling setup (measured quantities, time of sampling) and are thus not comparable to other studies. The results show very high radon production for primary red-coloured, feldspar rich granitic, porphyritic and gneissic material (Fig. 2.9). All other samples show none to slightly increased elevated emanation levels compared to the surrounding air.

In order to gain information about grain size- and water content dependence of radon emanation, we further measured radon emanation powers for a specific type of granite, the Göttemar-granite (originally from Sweden), at various grain sizes and moisture contents (Fig. 2.10). After being crushed and grinded, the material was separated into gravel, sand, silt, and clay fractions, which were measured at different water contents using the above-mentioned sampling setup. The results present a maximum production for the silt fraction. The sand and gravel fractions certainly have a high permeability, but the total specific surface area ( $\text{m}^2 \text{g}^{-1}$ ) of gravel grains is much lower than for silt, which combines high emanation

power from a large specific surface with high permeability. If water is added to the variable system, radon release is significantly higher for wet samples compared to dry samples for fractions smaller than 2 mm. Maximum radon emanation is reached for the silt fraction at 2 wt% water content.

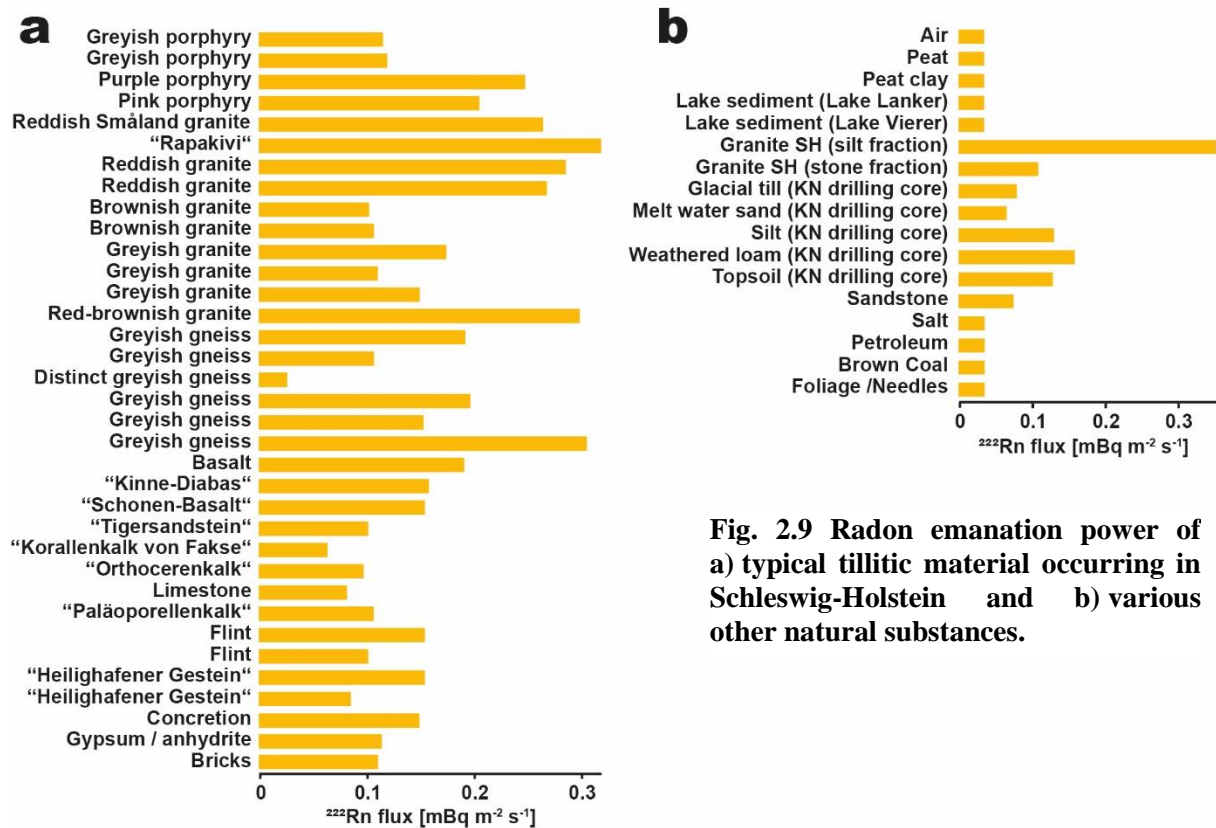


**Fig. 2.9 Radon emanation power of a) typical tillitic material occurring in Schleswig-Holstein and b) various other natural substances.**

Increased permeability in well sorted sand and silt may generally allow for a high gas flow in glacial melt water sands. A slight wetness of the strata could even intensify the radon flux when these water films evaporate (Fig. 2.10). Water coatings of mineral grains slow down emanating radon atoms preventing them from entering adjacent grains and keeping them in the covering pore water. Ongoing studies are designed to show that this proportion could then be released if the sediment is heated or if changes in air pressure modify the storing capacity of the water "film". These convective processes operate only in the unsaturated zone, but not when the pore space is filled with pore water (saturated zone). Apparently, radon is more effectively released if the open pore space facilitates gas flux. Contrarily, excessive moisture content would be conducive to the compaction of the soil due to water surface tension and thereby lessen the emanation power (Tanner 1980).



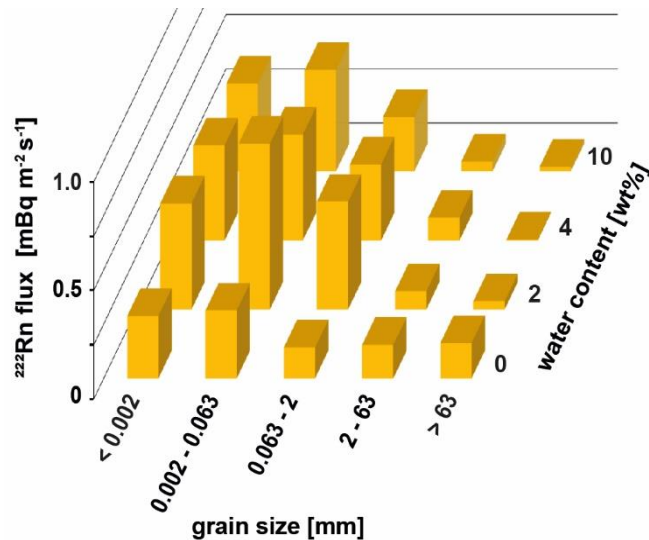


**Fig. 2.10 Radon emanation power of the Leitgeschiebe (indicator stone) “Göttemar-granite” (from Sweden) at various grain sizes and water contents.**

### Local Radon Flux Maxima (LRFM)

We could not identify any strong connection between increased radon flux and physical properties of the soil samples (Fig. 2.8). Radon anomalies cannot be explained by sediment properties directly beneath single points of sampling and must therefore be of different origin. We identified various processes, which can cause Local Radon Flux Maxima (LRFM). Fig. 2.11 presents a schematic model of potential sources for anomalously high radon flux.

We found in experiments under laboratory conditions elevated emanation levels for feldspar-rich, reddish granites, porphyria and gneisses compared to other samples (Fig. 2.9). Sedimentary structures of radium-rich sands / silts can lead to an increased radon emanation potential compared to the surrounding areas (Mineralogical LRFM; Fig. 2.11).

Near Lake Lanker, we measured radon activity in soil gas in an area with no known active fault system, i.e., an area where we can expect typical background radon flux in Schleswig-Holstein, which is strongly influenced by the radium-rich sediments of Weichselian tills (see above). However, the radon flux was not homogenous. Increased exhalation appears to occur at sampling points near contact zones to water-oversaturated, clay-rich, impermeable sediment deposits (Sedimentary LRFM; Figs. 2.4, 2.11).

Highest flux values were detected above tectonic and halokinetic fault systems and can be regarded as an indicator for actively rising, radon parent-rich fluids at the fault, caused by increased permeability. This deep-rooted flux results in an anomaly linked to structural deformations of the subsurface. Highest radon flux signals are not limited to areas directly above fault outcrops, but may be scattered in the loose sediment packages overlying these fault systems (Structural LRFM; Figs. 2.5 – 2.7, 2.11).

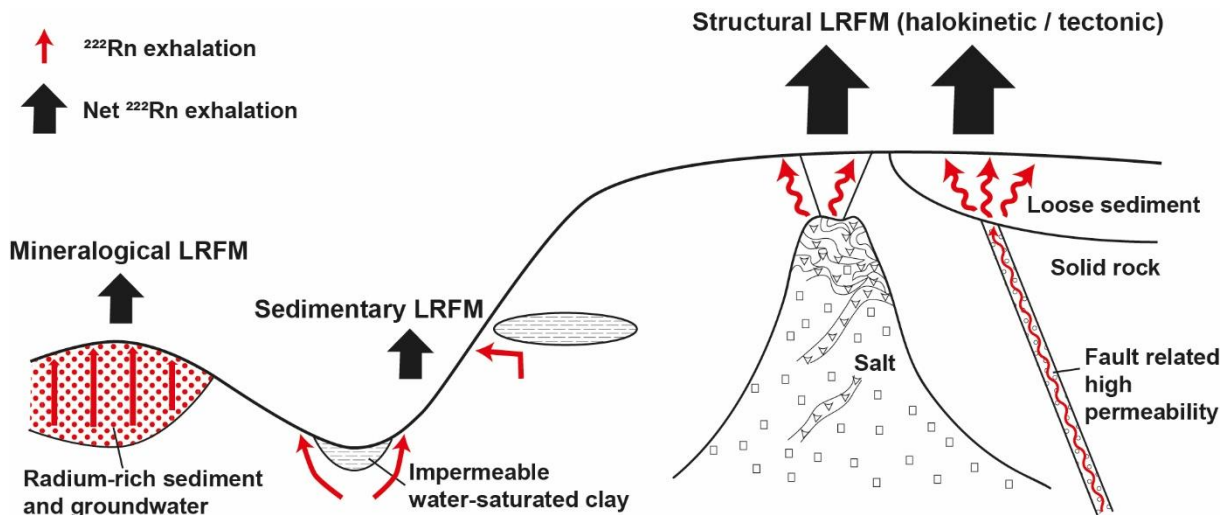


**Fig. 2.11 Schematic description of possible sources for different types of Local Radon Flux Maxima (LRFM).** Size of black arrows indicate relative net quantity of radon exhalation.

In Kleinneudorf, we found maximum radon flux levels in the unconsolidated sediments above a deep-rooted fault system caused by the displacement between the Eastholstein Platform and the Eastholstein Trough (Fig. 2.5). A 40 m deep drilling core and seismic surveys of the Kleinneudorf depression document a loose sediment package below this depression between 30 and 40 m (Köhn et al. 2019; Rabbel et al. in prep; Sirocko et al. in prep.).

Near the Segeberg Sülberg salt dome, we measured a sudden increase in radon flux directly above the outcrop of a border fault (Fig. 2.6a). From there, a halokinetic LRFM with values up to 2.5 times higher than their profiles' respective means stretches for a few hundred meters eastward, explainable by the low angle of faults and thus a shifted penetration point (Fig. 2.6b). These results are coherent with the study of Künze et al. (2013), who conducted soil gas analysis across the same border fault and found a similar distribution of increased radon concentration in soil gas.

We further found zones of maximum radon activity linked to active halokinetic fault structures near the shoreline of the Eckernförde Bay, where halokinetic LRFMs form perpendicular to the shore along the fault's outcrops or in their close vicinity (Fig. 2.7).

## **Discussion**

Gas exhalation varies greatly depending on time of day or season (e.g., Winkler et al. 2001; Tareen et al. 2019) and environmental factors, such as temperature and air pressure, strongly control outgassing cycles (Mudelsee et al. 2020; see chapter 2.3). For the majority of our sampling points, radon flux does not exceed  $5 \text{ mBq m}^{-2} \text{ s}^{-1}$  (Fig. 2.8). We interpret these values as the typical radon background activity in Schleswig-Holstein, which agrees well with the radon flux map of Europe by Karstens et al. (2015), who estimated similar flux levels based on soil properties, uranium content and modelled soil moisture contents derived from two different reanalysis data sets.

By establishing the radon potential map for Germany, Kemski et al. (e.g., 2001, 2005) showed that elevated radon background activity in the eastern part of Schleswig-Holstein is contributed to the mineralogical composition of the subsurface, more precisely to the sediments of the Weichselian glaciers which cover large areas of the state (Fig. 2.2a). This glacial material mainly consists of potassium bearing granitic and porphyry deposits, rich in parent radionuclides, resulting in increased levels of radon emanation (Fig. 2.9). Birke et al. (2009) detected increased uranium concentrations for these glacial sediments and therefore sufficient source material for radioactive decay to occur. As shown in Fig. 2.2a, regions of increased radon background levels coincide with the distribution of radium-rich glacial deposits.

Even if the mineralogical composition of the subsurface is relatively homogenous over large areas, radon flux is characterised by considerable spatial variations. Clay-rich soil layers in valley depths with water-saturated pore space act as a natural plug for soil gas release (Tanner 1980), which deviates the rising radon gas to the flanks of the impermeable strata and cause high radon flux on the boundary of these clay-rich strata (Figs. 2.4b, 2.11).

Maximum radon flux is observed in the vicinity of active fault outcrops (Figs. 2.5, 2.6, 2.7) indicating an enrichment of radon activity in connection with zones of deep reaching high permeability. Areas above active fault systems do not necessarily have to exhibit enhanced radon in soil gas, but are more likely to show increased levels of radon exhalation. This is not only given above open faults associated with thermal wells or CO<sub>2</sub> fumaroles, but also in regions of strong surface subsidence, which leads to a loose sedimentary structure. It is quite likely that the exhalation depth in Kleinneudorf reaches well into these highly permeable cover sands, which are formed by gravitational sinking of the cover sediments above a deep-rooted tectonic fault (Fig. 2.11).

The subsurface of Schleswig-Holstein is characterised by several vast salt walls and accompanying fault structures (Fig. 2.2), along which potential LRFM can form. The influence of this process must depend on the depth and uplift activity of the salt. In Bad Segeberg the salt reaches the surface, whereas in other locations the top of salt diapirs can be several hundred meters deep. If the rise of salt was strong enough to create keystone fault structures (as in Eckernförde), the halokinetic process is sufficient to produce advective pathways for deep-rooted rise of radioisotope-rich fluids.

Increased radon activity in connection with structural pathways can be observed worldwide. Iovine et al. (2018) found a strong connection between increased radon in soil gas and active tectonic structures in the Calabrian Arc in Southern Italy. Künze et al (2012) measured similar anomalous radon signals above both seismically active and inactive fault systems in the Cantabrian Mountains in Northwest Spain. Since it has a half-life of only 3.82 days, radon originating in depths of a few hundred meters or more cannot reach the surface unless it uses the presence of a carrier. Chyi et al. (2010) showed in experimental studies that an induced CO<sub>2</sub> flux leads to anomalously high radon signals. Since CO<sub>2</sub> is an abundant component of soil gases and is able to cover great distances by advection, it can transport radon atoms upwards from a deeper source to the soil cover, along active fault structures (Perrier et al. 2009; Sciarra et al. 2018). Ongoing research is designed to compare the outgassing cycles of radon and CO<sub>2</sub> in Schleswig-Holstein in long time series and study the role of CO<sub>2</sub> as a possible carrier gas for radon in that region.

## Conclusion

In this work we present a rapid, yet reliable method for measuring radon flux from soil to atmosphere. We conducted our research in four geologically unique locations in Schleswig-Holstein and conclude that there is a distinct connection between the presence of active fault structures and increased radon flux. Even though absolute radon values differ considerably between measuring campaigns, so-called LRFM can, but do not have to form in close vicinity to suspected fault outcrops. Furthermore, the mineralogical composition of the subsurface, in particular the abundance of reddish Scandinavian granites, and contact zones between permeable and impermeable soil layers can create radon flux anomalies, although the resulting radon exhalation does not reach quantitative or spatial dimensions like flux levels caused by increased permeability through faulting activity. In summary, the following LRFM types, classified into three geological categories, can be distinguished (Fig. 2.11):

- Mineralogical LRFM, strongly affected by the accumulation of radionuclide-rich sediment deposits,
- Sedimentary LRFM, influenced by diverted migration paths due to clay-rich, impermeable soil layers,
- Structural (tectonic / halokinetic) LRFM, forming in areas of deep-reaching structural pathways due to tectonic and/or halokinetic activity.

## **2.3 Radon time series and exhalation modes**

This chapter contains parts of the results of the publication presented by Mudelsee et al. (2020). The complete article, which is attached to this thesis, was published as:

Mudelsee M, Albert J, Sirocko F (2020) Weather control in radon flux time series from Schleswig-Holstein. *Int J Geomath* 11:23.

### **Author's contribution**

My contributions to this chapter include reading out and processing of the timeseries measurement data and compiling of meteorological data. I prepared the figures showing the radon exhalation modes and contributed to the discussion.

### **Abstract**

Radon flux not only varies spatially due to differing radium contents in the subsurface and the presence of pathways for radon migration along faults and fractures, but also shows substantial temporal variations. In order to better interpret the results of the radon profiles presented in chapter 2.2, we measured the radon flux continuously for one year in the research area Kleinneudorf. The main drivers of radon flux from soil into the atmosphere in our measurement setup are air temperature and atmospheric pressure. However, temporal radon flux patterns were not consistent and varied depending on the prevailing season. We identify four different radon exhalation modes representing four principal weather regimes.

## **Introduction**

Radon exhalation is not only characterised by considerable spatial variations, but also strong temporal fluctuations. Radon flux measured at a single point can vary greatly depending on time of day and outgassing patterns significantly depend on the prevailing season (e.g., Winkler et al. 2001; Tareen et al. 2019). Schubert and Schulz (2002) found strong diurnal variations in the radon concentration in the uppermost soil layers and at the soil / air boundary, which were associated with convective soil gas migration processes due to variations in the soil / air temperature gradient. Siino et al. (2019) identified sub-daily, daily and yearly periodicities in radon exhalation in several monitoring sites across Italy and concluded that short-term fluctuations are mainly dependent on temperature and atmospheric pressure, whereas long-term variations are additionally influenced by parameters like seasonal rainfall. In order to gain a comprehensive picture of radon outgassing patterns, it is therefore crucial to develop long-lasting, high-resolution time series.

## **Methods**

We monitored the radon flux from April 2018 till April 2020 in the research area Kleinneudorf. For this purpose, a flux box measurement system was set up above a groundwater monitoring well in the centre of the Kleinneudorf depression (Fig. 2.5b). In contrast to other radon time series, our specific flux box sampling strategy does not measure the radon concentration in the soil, but rather its changes over time and obtained radon flux values only reflect the boundary conditions at the Kleinneudorf site for this specific setup. Thus, absolute values are arbitrary and not comparable to other studies presenting time series of radon concentrations. However, our sampling method allows a direct analysis of radon outgassing cycles and the factors controlling them, which is quite relevant in context of potential health risks.

The uppermost 40 m of the subsurface comprise alternating strata of highly permeable melt water sands and till (Supplementary Fig. 1). The measuring device is located inside two boxes directly above the well (Fig. 2.12). This allows for protection from direct sunlight, rain and venting effects caused by wind.

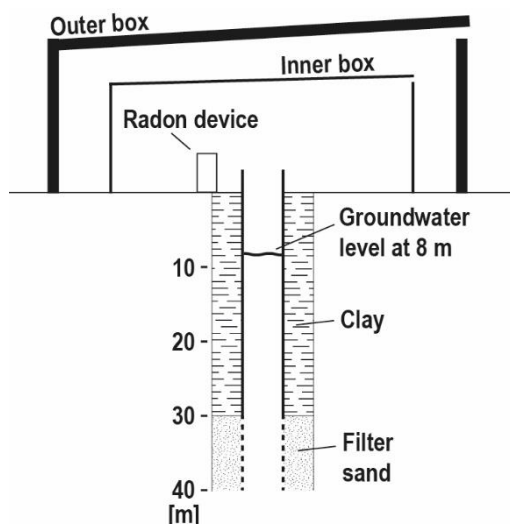


**Fig. 2.12 Schematic description of radon monitoring above the Kleinneudorf drilling well.** The topmost 30 m are encased by impermeable plastic pipes and clay. The lowermost 10 m are embedded in filter sand and allow gas to enter.

The top 30 m of the well are encased by impermeable plastic pipes and clay and only the lowermost 10 m allow gas to enter the well. The groundwater level at the Kleinneudorf site is at 8 m.

Radon was measured with a commercial Canary Pro monitor (by Corentium). The measurement principle is based on a Si photodiode. When  $^{222}\text{Rn}$  and its daughter isotopes  $^{218}\text{Po}$  and  $^{214}\text{Po}$  decay inside the device's chamber, some of the emitted alpha particles hit the open diode. These impacts cause the release of energy, which is counted and interpreted as radioactive decay. Due to the electric charge of its progeny isotopes, only  $^{222}\text{Rn}$  can enter the detection chamber. The Canary device has an application range from 0 – 100,000 Bq/m<sup>3</sup>. The efficiency for radon sampling specified by the manufacturer is one count per hour at a concentration of 33 Bq/m<sup>3</sup>. In addition to measuring the radon concentration every hour, the instrument records the prevailing air temperature and atmospheric pressure.

Exhalation mode	Begin of time interval	End of time interval	Max. radon concentration [Bq/m <sup>3</sup> ]	Temperature range [°C]	Atm. pressure range [hPa]
I	10-02-2019 02:00	22-02-2019 02:00	13412.6	-1.8 – 12.6	979.0 – 1030.0
II	26-04-2018 02:00	06-05-2018 02:00	3102.3	1.9 – 22.4	993.4 – 1027.4
III	18-07-2018 02:00	27-07-2018 02:00	7572.7	14.3 – 39.5	1005.3 – 1015.8
IV	01-09-2018 02:00	11-09-2018 02:00	4333.1	11.0 – 28.4	1003.1 – 1024.9

**Table 2.2 Extracted time intervals with identified exhalation modes.** The table shows the maximum radon concentration, as well as ranges of respective air temperatures and air pressures.



## Radon exhalation modes

Radon flux was measured over a time period of 2 years (April 2018 till April 2020). Temporal patterns of radon outgassing are best visible in time spans of around one week. Four time intervals, which represent four different weather regimes (i.e., exhalation modes), were taken from the time series (Table 2.2, Figs. 2.13 – 2.16). In our monitoring system radon outgassing cycles were primarily driven by surface air pressure and temperature.

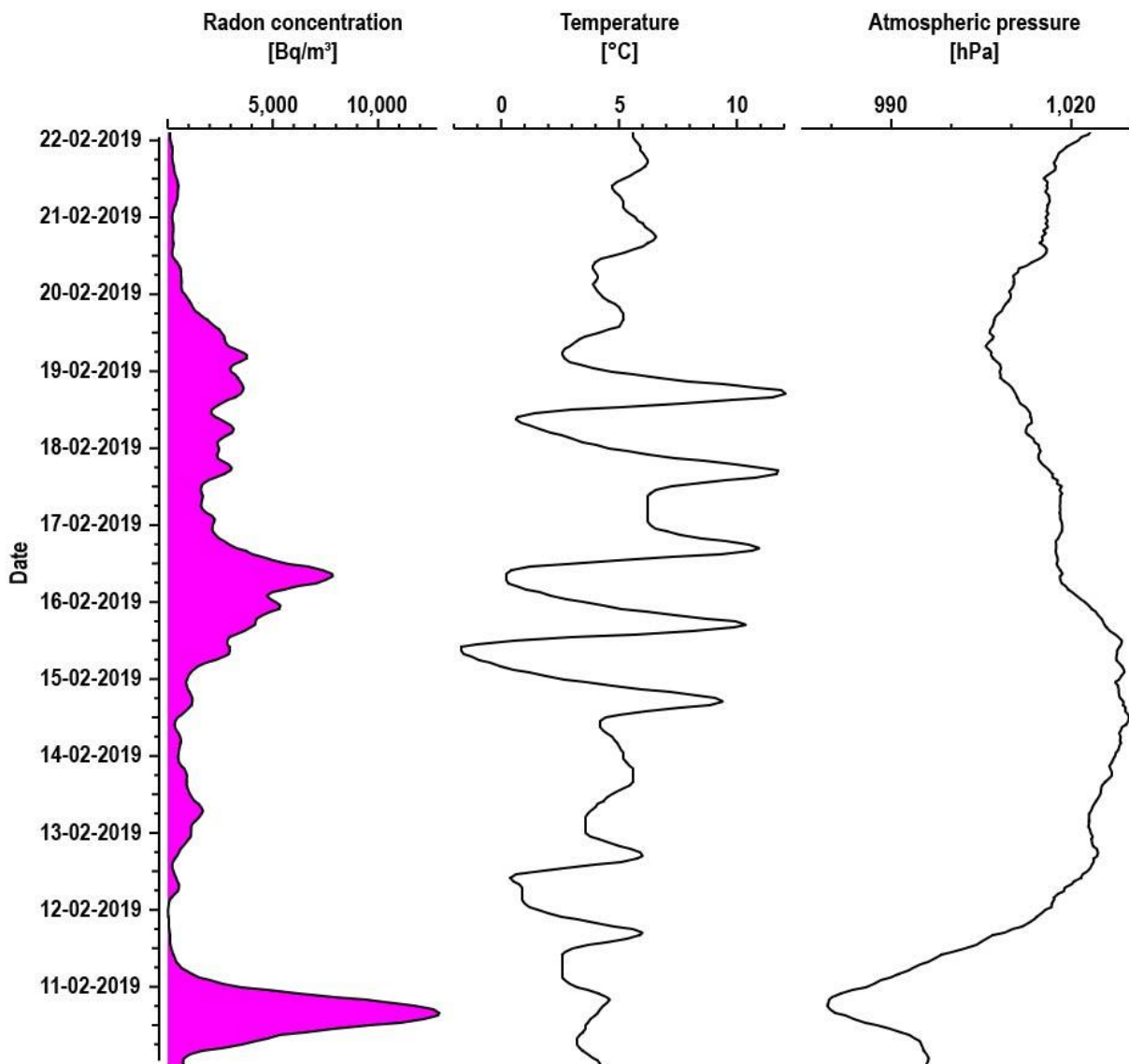


**Fig. 2.13 Radon exhalation mode I.** Time series of radon concentration, air temperature and air pressure from February 10<sup>th</sup> till 22<sup>nd</sup> 2019.

Exhalation mode I spans from February 10<sup>th</sup> till 22<sup>nd</sup> 2019 (Fig. 2.13). No periodic radon flux signal can be observed. This regime reflects the cold winter months, when temperature gradients between day and

night are at a minimum. It is here that the influence of atmospheric pressure on radon outgassing is best observable. Rising air pressure weighs heavily on the ground, pushing the radon back into the strata, whereas venting effects with significantly intensified radon release from the soil occur during periods of decreasing air pressure.

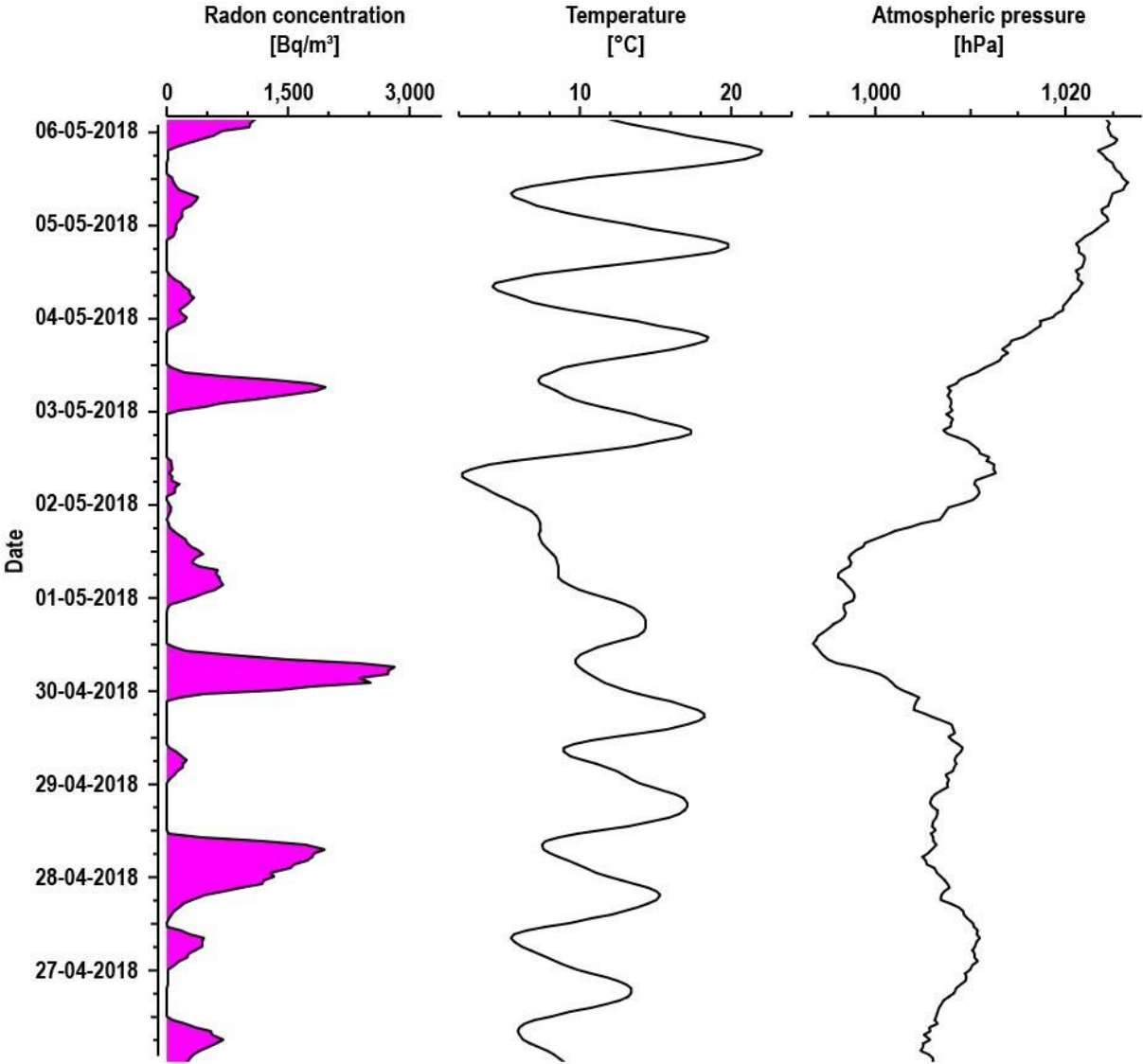


**Fig. 2.14 Radon exhalation mode II.** Time series of radon concentration, air temperature and air pressure from April 26<sup>th</sup> till May 06<sup>th</sup> 2018.

Exhalation mode II covers the period from April 26<sup>th</sup> till May 06<sup>th</sup> 2018 (Fig. 2.14). This mode represents weather conditions in spring time and has a very prominent radon maximum during the night when air temperature drops below groundwater temperature. This activates the so-called “chimney effect”, i.e., when the temperature and moisture difference between the atmosphere and the borehole causes air

density anomalies and literally sucks the gas out of the subsurface. Radon outgassing is significantly greater during nights of dropping air pressure. Although the chimney effect is intensified due to our specific borehole setup, it still affects radon outgassing cycles in “normal” soil / strata (Sirocko et al. in prep.).

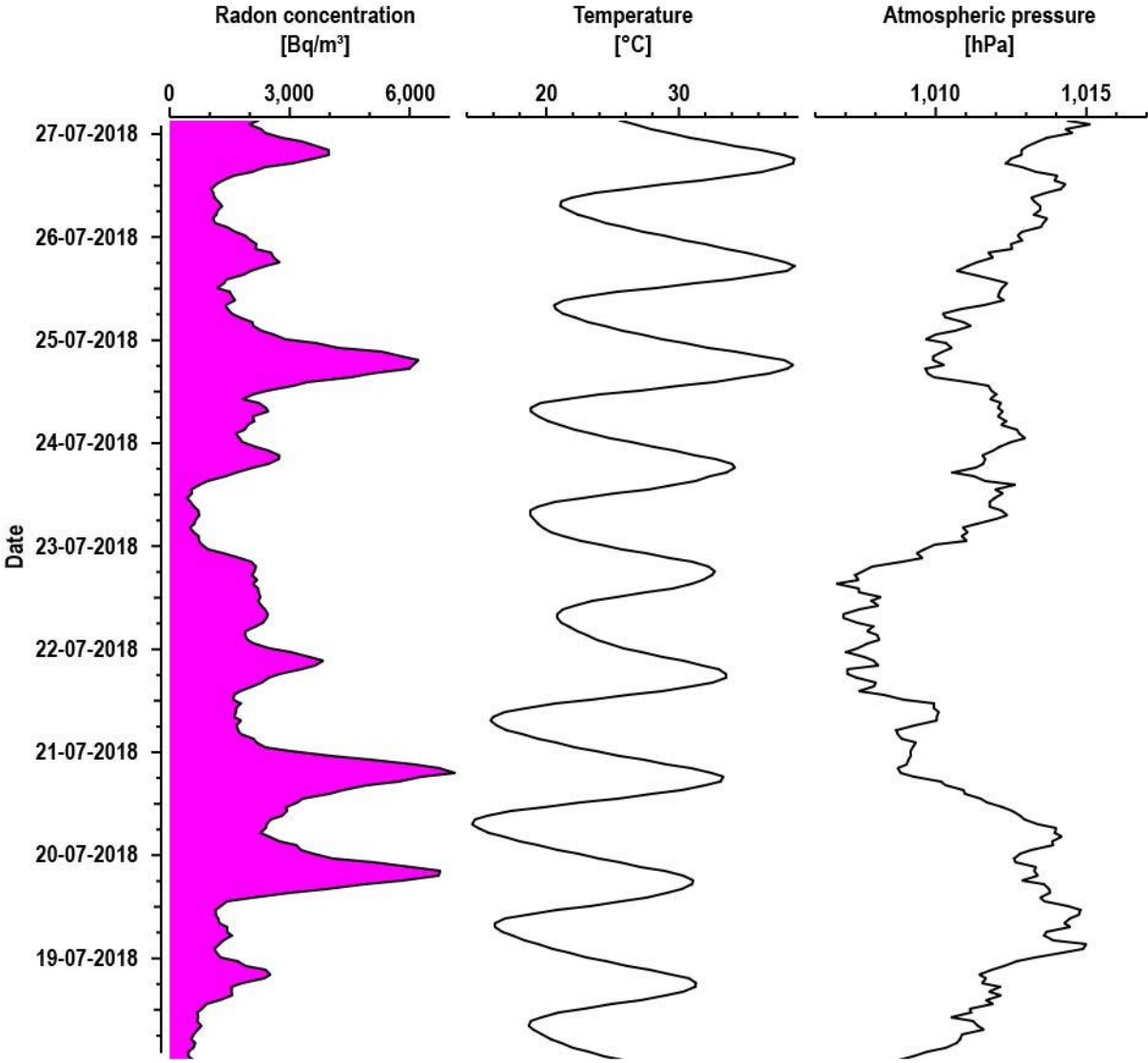


**Fig. 2.15 Radon exhalation mode III.** Time series of radon concentration, air temperature and air pressure of the time interval from July 18<sup>th</sup> till 27<sup>th</sup> 2018.

Exhalation mode III, which represents the time span from July 18<sup>th</sup> till 27<sup>th</sup> 2018, shows a radon outgassing peak during the late afternoon when air temperature starts to decrease (Fig. 2.15). Intense solar radiation heats up the upper subsurface strata during sunny summer days. As soon as direct insolation begins to cease and the soil temperature just below the surface is warmer than the surrounding

air, the onset of thermal convection causes increased radon release from the soil. Radon outgassing is further intensified on days of dropping air pressure.

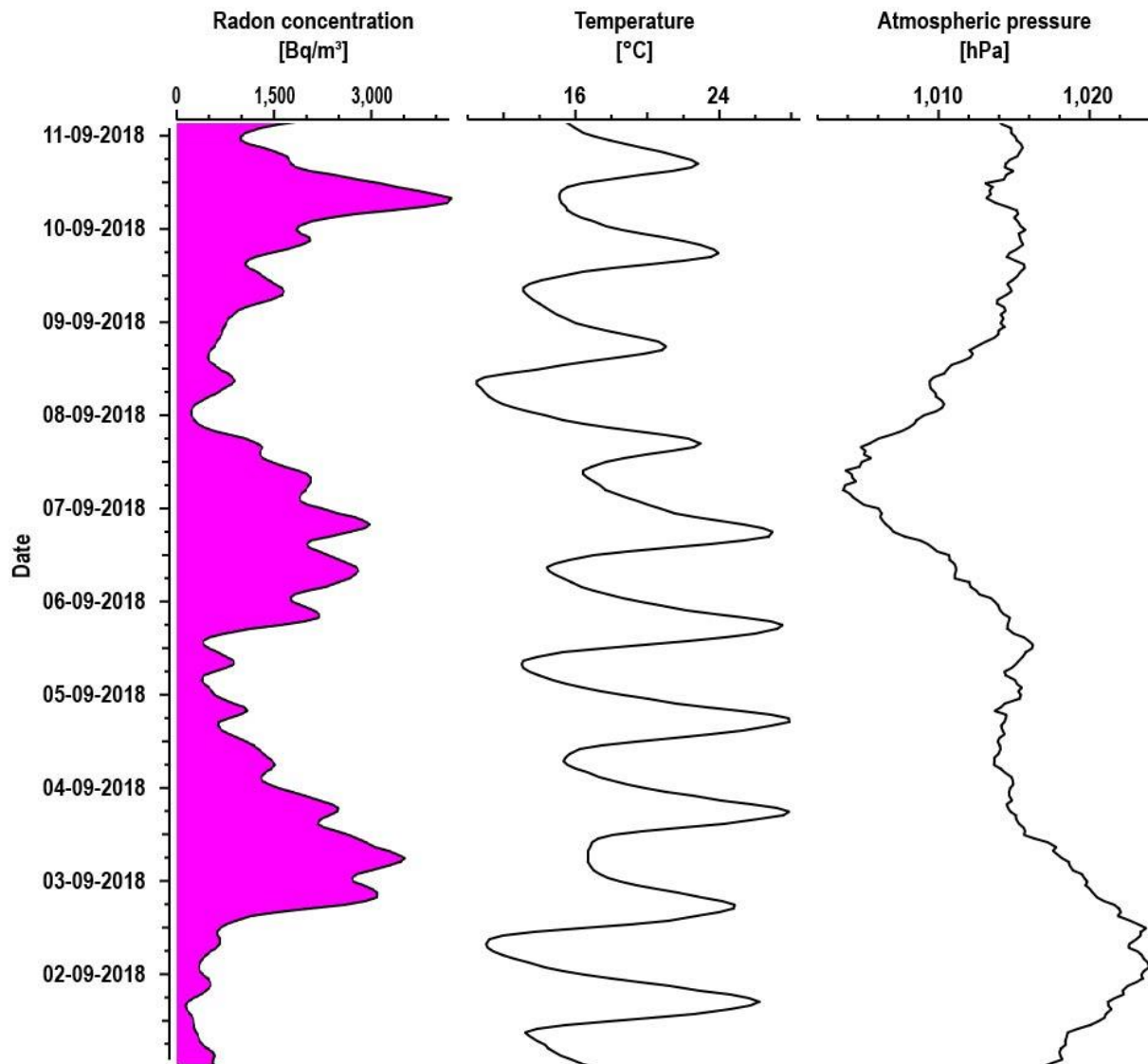


**Fig. 2.16 Radon exhalation mode IV.** Time series of radon concentration, air temperature and air pressure from September 1<sup>st</sup> till 11<sup>th</sup> 2018.

Exhalation mode IV, which ranges from September 01<sup>st</sup> till 11<sup>th</sup> 2018, features a prominent radon outgassing periodicity of around three days following the progression of atmospheric pressure (Fig. 2.16). Within these cycles, secondary radon flux peaks occur every afternoon and night. This regime represents a mixture between Exhalation modes II and III, i.e., the transition period from summer to more temperate weather conditions in autumn.

## Conclusion

We present a high-resolution radon flux time series from a well drilled near the village of Kleinneudorf in Schleswig-Holstein, Northern Germany. The flux of gas into the atmosphere is influenced by many geogenic and exogenic factors. As a result, radon flux shows substantial time-dependent fluctuations during the course of a year and absolute flux quantities and outgassing patterns exhibit strong differences depending on the prevailing season and weather conditions. Because of these significant variations, the time series had to be subdivided into short segments of around ten days in order to reveal clear outgassing cycles and identify the mechanisms controlling them.

The dominant driving forces for daily outgassing cycles in our monitoring system are air temperature and atmospheric pressure. However, other factors such as water level, heavy rainfall as well as strong winds may also influence the release of gas from the soil into the atmosphere (e.g., Gregorič et al. 2014; Ye et al. 2019). We identified four radon exhalation modes representing four different weather regimes / seasons:

- No recurring exhalation pattern during times of minimal temperature gradients between soil and atmosphere (cold winter months) and varying air pressure as the sole influence on soil gas release (exhalation mode I),
- Activation of the chimney effect when air temperature drops below the groundwater temperature during spring nights (exhalation mode II),
- As soon as the sun stops heating the soil in the afternoon on a hot summer day and the soil temperature is warmer than the air temperature (exhalation mode III),
- An interplay between modes II and III during the transition from summer to a more temperate autumn season (exhalation mode IV).

### **3 Climate variations and main flooding and slumping phases during the last glacial cycle from laminated Eifel maar sediments**

This chapter deals with climate variations and major flood and slumping phases in the Eifel region during the last glacial cycle. Sediment records of several infilled maar lakes are being correlated to the Greenland Stadial (GS) and Interstadial (GI) succession of the North Greenland Ice Core Project (NGRIP) ice core stratigraphy (North Greenland Ice Core Project Members 2004; Svensson et al. 2008; Rasmussen et al. 2014) using pollen and organic carbon (chlorins) data. The near annual ELSA-20 climate proxy record shows a complete GI / GS succession back to GI17 around 60,000 years ago and discusses a connection between the intensity of multidecadal climate fluctuations in central Europe and North Atlantic sea-ice cover during particularly cold intervals.

A prominent slumping layer stands out in all presented sediment records. Frozen and fractured sediment packages with a breccia-like texture suggest that the region was exposed to permafrost or deep frost conditions around 43,500 years ago. A rapid climate shift or some other significant geological phenomenon must have caused this major slumping event while the soil was still partially frozen.

#### **3.1 Background information**

Maar lakes are exceptional climate archives due to their unique geological setting. Lake sediments are commonly composed of autochthonous biogenic material (e.g., silicates, carbonates and organic matter) and terrestrially-derived clastic components (Lowe and Walker 2014). Calm sedimentation environments and long water residence times with anoxic bottom waters often promote annually laminated sediment layers, i.e., varves. Event deposits, such as tephra- or flood layers, contrast clearly from the background sedimentation (Lowe 2011). This allows the study of past climate changes in great

detail and lake sediments have been used to great extent to reconstruct past climate and vegetation changes (e.g., Brauer et al. 1999, 2001; Litt et al. 2001; Sirocko et al. 2013, 2016).

Although there are many lacustrine basins in central Europe suitable for Holocene climate reconstructions, lake sediments that allow going further back in time are scarce and limited to a few regions in Europe (e.g., Ampel et al. 2008; Wohlfarth et al. 2008b). One of these regions is the west Eifel volcanic field located in Western Germany, which lies in a homogeneous climate zone stretching across central Europe from Belgium to Poland (Wernli and Pfahl 2009). The Eifel is known for its numerous maar structures. In total, 68 open and infilled maar basins are located in the region. The ELSA (Eifel Laminated Sediment Archive) drilling project of the University of Mainz, founded by Prof. Dr. Frank Sirocko in 1998, set the task to systematically core and study these maar lakes (e.g., Sirocko et al. 2005, 2013, 2016; Seelos et al. 2009).

### **3.1.1 Flooding layers**

Floodings are one of the most common natural disasters, that affect millions of people and are responsible for economic losses of around 50 billion US\$ each year (UNISDR CRED 2015; AON 2016). Extreme flood events will likely become even more frequent and more severe in the next couple of decades due to global warming (e.g., Milly et al. 2002; Huntington 2006; Hirabayashi et al. 2013). Effectively predicting such hazards and evaluating their risk requires knowledge about past flooding events. Palaeoflood hydrology, i.e., the study of frequency and intensity of flood events, makes use of various methods (Baker et al. 2002). Observations and written records from eyewitnesses are utilized to establish flood time series during the historical era (e.g., Bell 1970; Glaser et al. 2010). Going further back in time, geoscientific archives provide a valuable source to track palaeoflood frequencies. These include the growth of tree rings and scars on tree trunks (Ballesteros-Cánovas et al. 2015), water-borne detritus layers on speleothems (Atkinson et al. 1986; Denniston and Lutscher 2017), and flood deposits in lakes (Gilli et al. 2013; Brunck et al. 2016) and fluvial systems (Jones et al. 2010). Rivers are often high-energy systems and information about prior flood events can easily be lost due to erosional processes (Macklin 1999; Thorndycraft et al. 2005). In contrast, lacustrine basins are a much more

reliable source of information due to their usually very slow and constant sedimentation rates (Gilli et al. 2013) and can, potentially, record flood events with a resolution down to the season. The distinct characteristics of flood layers are often easily recognisable in the background sediments and erosion processes are much more uncommon than in river systems.

The increased fluvial input into a lake during a flood event originates from heavy rain fall in its catchment area. Clearly visible detrital laminations occur when sufficient material is delivered during a flood event via the riverine system (Schillereff et al. 2014). Minerogenic and organic detrital particles that are eroded from creeks and their slopes, are consequently transported into the river drainage and lake (Mulder et al. 2003; Wirth et al. 2011). The amount and grain size of the transported material depends on the intensity of the hydrological energy of the river system, caused by heavy rains. The finer the detrital material, the further it is transported from the lakeshore to the centre of the lake and the longer it is held in suspension. Due to the finest particles being deposited several days after the event occurred, flood layers commonly comprise a clay capping layer, or “clay cap”, at the top (Schlölaut et al. 2014).

There are several methods to identify such event layers. Optical approaches like microscopy are used to identify flood layers in thin sections. More severe events can even be detected macroscopically directly on the core (e.g., Brunck et al. 2016). Further investigations based on sedimentological (e.g., grain size analysis) or geochemical (micro-scale X-ray fluorescence [ $\mu$ -XRF]) analyses can then be used to characterise the event layers and distinguish between floods, turbidites and slumps (Fig. 3.1; e.g., Croudace et al. 2006; Gilli et al. 2013). A first continuous flood timeseries for central Europe reaching back to 60,000 yr b2k is presented by Brunck et al. (2016).

### **3.1.2 Turbidites and slumping layers**

Turbidites form during a singular temporal event. This happens through pore water overpressure of the water-saturated particles or destabilization of the grain structure (Sirocko 2009). The material flows down the slope and redeposits at the lake’s bottom. Heavier and denser components sink faster and



accumulate more quickly than the fine-grained, lighter particles, which remain longer in suspension. This results in an often distinct, continuously graded grain size distribution of a turbidite event layer (Fig. 3.1b; e.g., Stow and Shanmugam 1980; Schnellmann et al. 2005).

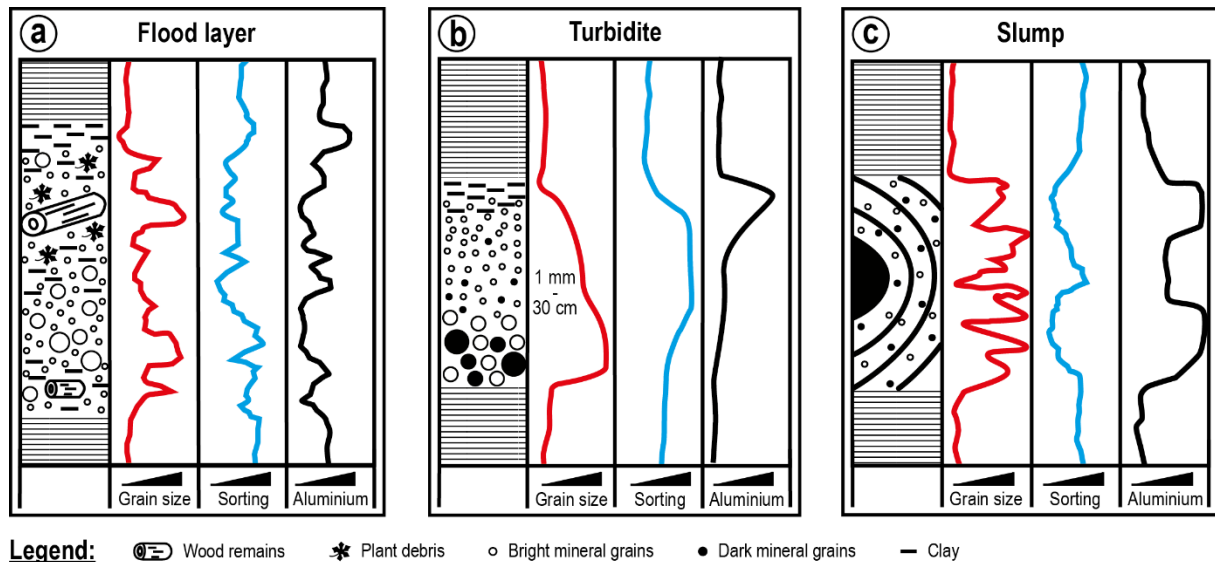


**Fig. 3.1 Idealized characteristics of event layers (Brunck et al. 2016).** Typical grain size distribution, sorting and aluminium content of a) a flooding layer, b) a turbidite, and c) a slumping layer.

Slumping layers are sedimentary rearrangements within a lake. Formerly deposited, unconsolidated material destabilizes as a whole package and is re-deposited as a gravitational slide down a slope (Fig. 3.1c). This mass movement can be caused by an overload of a slope, by seismic shocks due to an earthquake, or through freezing and thawing of the sediment, i.e., solifluction (e.g., Shmuel et al. 1996; Verpaelst et al. 2017; Christiansen et al. 2021). The sediment package rotates around an axis parallel to the slope. Typically, internal lamination structures may be preserved to some extent despite distortion. This results in well-developed folding textures in a scale from millimetres to several metres in the slumped sediment package. In laminated sediment sequences, folds in the order of millimetres or centimetres are clearly visible, whereas larger-scale folds can be detected as tilted or bent layers.

## **3.2 The ELSA-20 record – Multidecadal climate variations in continental Europe during the last glacial cycle**

This chapter was published as:

Sirocko F, Martínez-García A, Mudelsee M, Albert J, Britzius S, Christl M et al. (2021) Muted multidecadal climate variability in central Europe during cold stadial periods. *Nat Geosci* 14:651-658.

### **Author's contribution**

My contributions to this published article include the development of the lithologies and stratigraphies of all presented maar sediment records, the construction of the age/depth models and tuning of the ELSA-20 record to the NGRIP Greenland Stadial / Interstadial succession.

### **Abstract**

During the last ice age, the Northern Hemisphere experienced a series of abrupt millennial-scale changes linked to variations in the strength of the Atlantic Meridional Overturning Circulation and sea-ice extent. However, our understanding of their impacts on decadal-scale climate variability in central Europe has been limited by the lack of high-resolution continental archives. Here, we present a near annual-resolution climate proxy record of central European temperature reconstructed from the Eifel maar lakes of Holzmaar and Auel in Germany, spanning the past 60,000 years. The lake sediments reveal a series of previously undocumented multidecadal climate cycles of around 20 to 150 years that persisted through the last glacial cycle. The periodicity of these cycles suggests that they are related to the Atlantic multidecadal climate oscillations found in the instrumental record and in other climate archives during the Holocene. Our record shows that multidecadal variability in central Europe was strong during all warm interstadials, but was substantially muted during all cold stadial periods. We suggest that this

decrease in multidecadal variability was the result of the atmospheric circulation changes associated with the weakening of the Atlantic Meridional Overturning Circulation and the expansion of North Atlantic sea-ice cover during the coldest parts of the ice age.

## **Introduction**

The last glacial cycle was marked by a series of abrupt climate transitions between cold (stadial) and warm (interstadial) periods, known as Dansgaard-Oeschger (D/O) cycles (North Greenland Ice Core Project Members 2004). Although the ultimate causes of these abrupt climate transitions remain under discussion, there is an emerging consensus that they were linked to changes in the meridional heat transport associated with strong variations in the strength of the Atlantic Meridional Overturning Circulation (AMOC; Rahmstorf 2002; Böhm et al. 2015). However, the strong nonlinear nature of the D/O cycles suggests that they involve complex feedbacks operating across the ocean, atmosphere and cryosphere systems (Rahmstorf 2002; Li and Born 2019). In particular, recent studies suggest that rapid changes in North Atlantic sea-ice cover played a crucial role in amplifying or even instigating ocean circulation changes (Sadatzki et al. 2019).

The influence of these millennial-scale climate oscillations beyond the high-latitude North Atlantic is now well established in different marine (Peterson et al. 2000; Martrat et al. 2007; Deplazes et al. 2013) and terrestrial climate records (Fleitmann et al. 2009; Cheng et al. 2016). However, our understanding of their impact on European decadal- to centennial-scale climate variability has been limited by the lack of continuous and high-resolution continental archives. Understanding the relationship between changes in North Atlantic circulation and European climate on these short timescales seems particularly relevant in the context of the existing debate regarding ongoing changes in the strength of the AMOC over the past decades (Srokosz and Bryden 2015; Caesar et al. 2018; Thornalley et al. 2018).

In this Article, we present a new near annual-resolution climate proxy record from the maar lakes of the west Eifel volcanic field located in the west of Germany, an area that is representative of the climate of central Europe (Fig. 3.2) The drilling site of the sediment core from Auel is shown in Fig. 3.3, and

photographs of cores from Holzmaar and Auel are shown in Fig. 3.4. The cores are logged with 1-mm resolution to determine the organic carbon fraction of chlorins (Fig. 3.5). The temporal resolution of the glacial section of the record (Fig. 3.6 – 3.11) is unprecedented not only for European terrestrial archives but also globally (Fig. 3.8a), and allows us to evaluate the relationship between D/O cycles and decadal climate variability in central Europe (Fig. 3.12, 3.13).

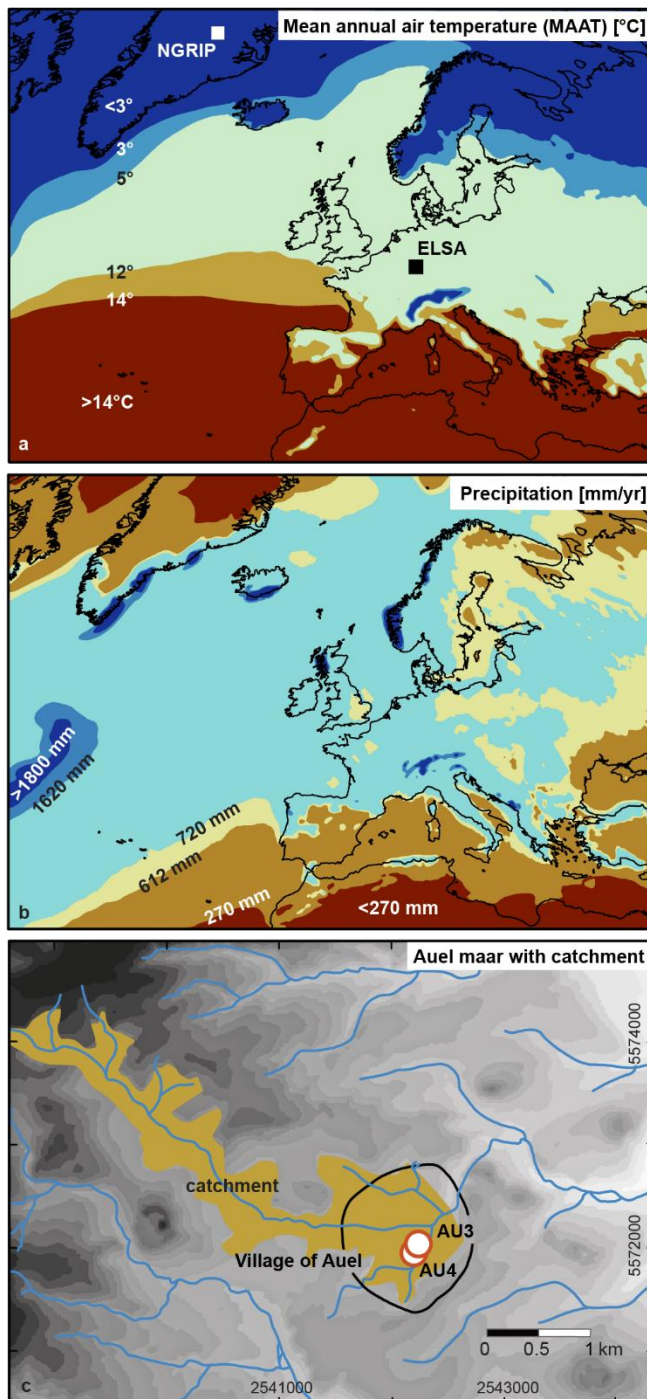


**Fig. 3.2 Location of the Auel Maar with respect to modern climatology.** a) Mean annual air temperature (MAAT). b) Mean annual precipitation. ERA5 reanalysis data for the North Atlantic and Europe is from Hersbach et al. (2020). c) Digital elevation model for the Auel Maar catchment. Solid line indicates the area of the infilled maar lake. Locations of the NGRIP ice core and the area of the ELSA lake sediment cores are shown in the maps.

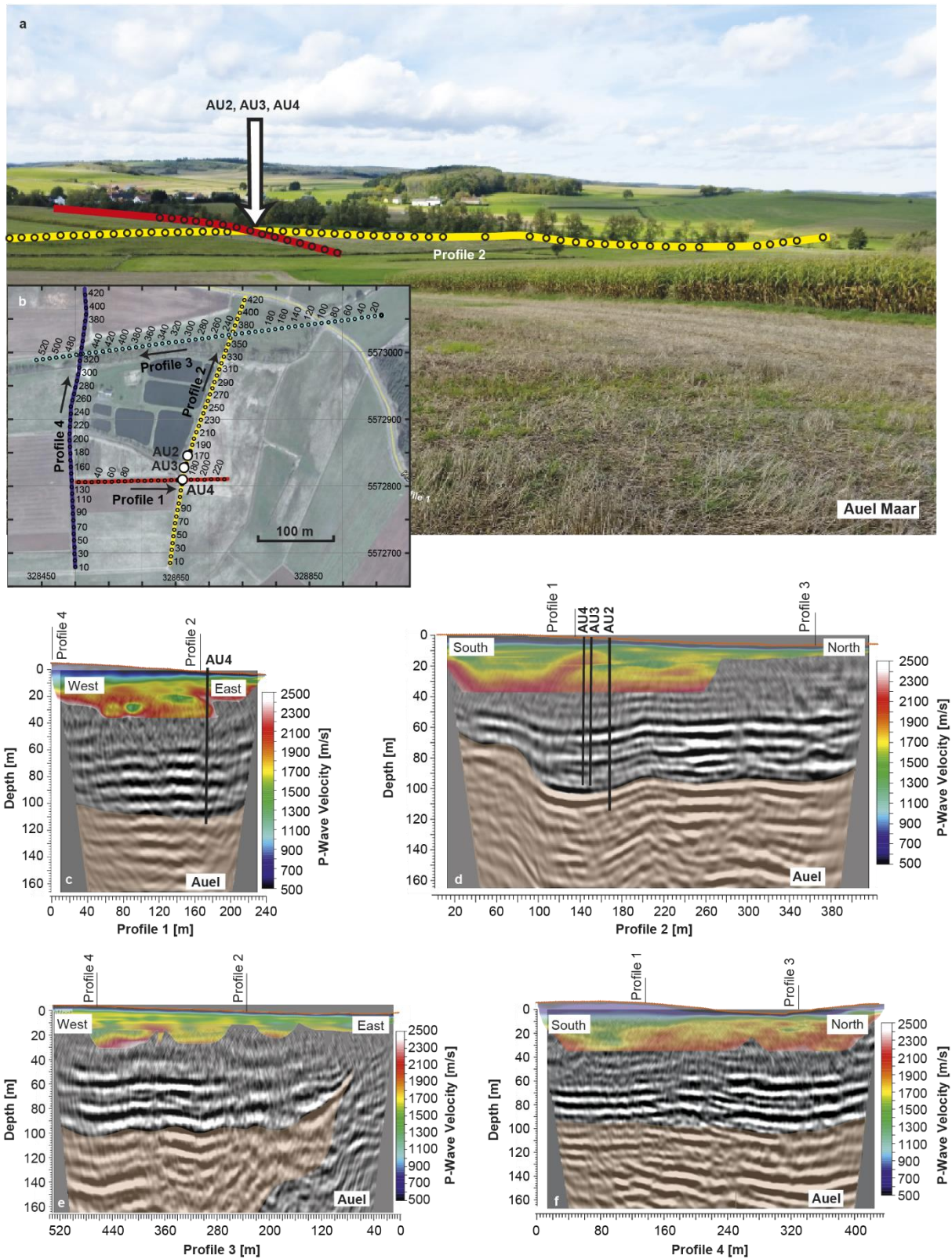


**Fig. 3.3 The AU3 / AU4 drilling site.** a) Photo of the infilled maar lake of Auel with drilling sites and locations of seismic lines. b) Seismic line 1 and core locations. Core AU2 is included in the figures, because this core was studied by Sirocko et al. (2016) for the pioneering work on the Auel Maar.

## The ELSA-20 record

During the past 20 years, the ELSA (Eifel Laminated Sediment Archive) project has drilled more than 50 cores from the 68 open and infilled maar lakes of the west Eifel volcanic field (Sirocko et al. 2013, 2016). In this study, we present new sediment cores from the maar lakes of Schalkenmehren, Holzmaar and Auel, which are combined to generate a continuous near annual-resolution climate record spanning the past 60,000 years, the ELSA-20 stack.

After the eruption of the Auel volcano at 59,130 years before 2000 ce (yr b2k), the Auel lake (diameter, 1.3 km; depth, 105 m) was continuously loaded with fine-grained fluvial suspensions collected from a 5-km-long catchment up to the early Holocene, when it was finally filled with gravel (Figs. 3.3, 3.4). To obtain a continuous record of central European climate variability, the Auel record (14,801 – 59,130 yr b2k) was supplemented with Holocene sections of two nearby lakes, the Schalkenmehren Maar Lake (0 – 700 yr b2k) and late glacial Holzmaar (701 – 14,800 yr b2k; Figs. 3.4, 3.8), both having a catchment structure similar to that of Auel. The sediments are annually layered (varved) during all interstadials and the Holocene. Stadial and glacial sediments are also laminated, but annual varves cannot always be distinguished in the coldest sections (see Methods) due to the absence of a distinct summer layer and possible micro-bioturbation during times of oxygenated deep water.

The elemental composition of the different sediment cores was analysed at 0.5-mm resolution (three months on average) using X-ray fluorescence (XRF) scanning. In addition, the colour reflectivity was measured at 1-mm intervals (six months on average) using the ISRS670 method (Rein and Sirocko 2002). This method detects the changes at 670 nm in the spectra of visible light, which are a function of chlorophyll derivatives (chlorins) and chlorophylls themselves in the bulk sediment. These in turn are linearly linked to organic carbon ( $C_{org}$ ) content (see Methods). Overlapping millimetre-scale  $C_{org}$ (chlorins) datasets for cores AU3 and AU4, which show an identical interstadial succession (Fig. 3.8), were merged into one continuous record, with all drilling disturbances and gaps larger than 2 cm closed by a dynamic time warping of AU3 sections in the AU4 master core (see Methods). The interstadial succession was dated into Marine Isotope Stage (MIS) 3 using 25 radiocarbon measurements

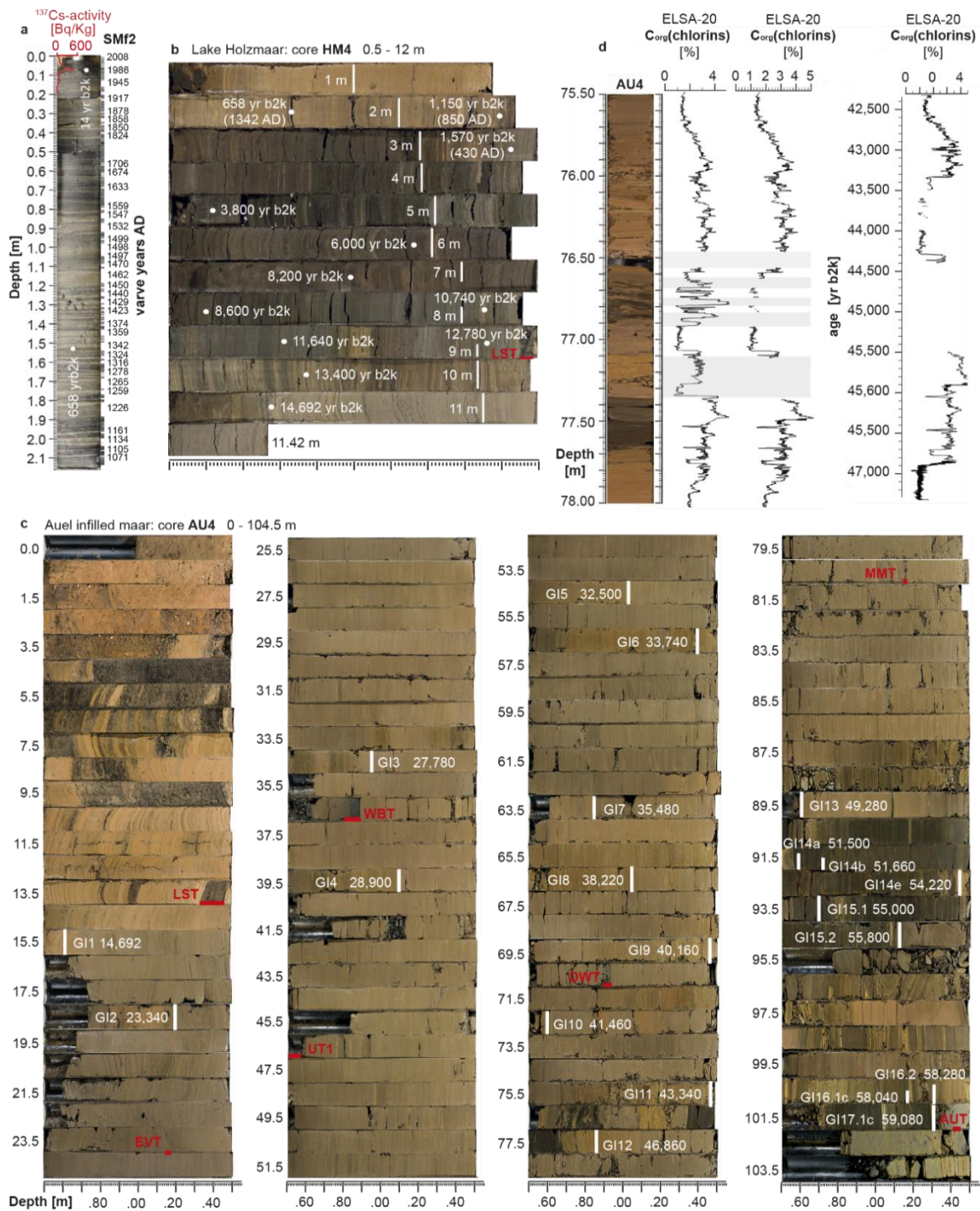


**Fig. 3.4** Maar lake sediment cores SMf2, HM4 and AU4. **a**) Photo of freeze core SMf2 from Schalkenmehrener Maar with  $^{137}\text{Cs}$  profile and varve counts for the last 800 years. **b**) Core photo of sediment core HM4 with depth of palynostratigraphical fix-points for the Bayesian age model of the Holocene section. The ages for the palynological markers are taken from Litt et al. (2009). **c**) Core photo of sediment core AU4 with depth and age (all yr b2k) of interstadials from Rasmussen et al. (2014). **d**) Sedimentary disturbances between 75.5 and 78.0 m in core AU4 (see chapter 3.3). This interval represents GS12 and GI12 for which only selected parts of the  $\text{C}_{\text{org}}(\text{chlorins})$  data have been used. All ages are given in the yr b2k notation.

and  $10^{10}\text{Be}$  analyses at depth of the expected Laschamp  $^{10}\text{Be}$  maximum (Fig. 3.8, 3.14). The time series revealed the entire succession of Greenland interstadials (GIs, Fig. 3.6) and was thus aligned to the North Greenland Ice Core Project (NGRIP) ice core stratigraphy (Rasmussen et al. 2014). We used a Bayesian age model to generate continuous time series of  $C_{\text{org}}$ (chlorins) and Si/Al. The resultant time series were resampled at one-year-resolution, smoothed over three years with a three-point running average, and are denoted herein as ELSA-20  $C_{\text{org}}$ (chlorins) and Si/Al records (Figs. 3.6, 3.7).

Temperature changes play a critical role in controlling both productivity and organic matter preservation in the maar lakes from the Eifel region (Lücke et al. 2003). During summer peak temperatures, the lakes stratify, and the nutrient content and aquatic primary productivity increase in surface waters. At the same time, decreased deep water ventilation causes the development of anoxic conditions at the bottom of the lakes, increasing organic matter preservation in the sediments. Accordingly, the  $C_{\text{org}}$ (chlorins) content of maar lake sediments is sensitive to temperature changes and can be used to reconstruct past climate variability. The Si/Al ratio monitors the content of biogenic silica in the sediment and represents a second indicator of productivity changes by siliceous phytoplankton (diatoms and chrysophytes). Although both productivity indicators can be affected by several complicating factors (see Methods), the covariance of  $C_{\text{org}}$ (chlorins) and Si/Al during all sections with visible diatom layers indicates that both proxies indeed document the primary production of diatoms and chrysophytes. The covariance of both proxies suggests that preservation or diagenetic alteration have not strongly affected the  $C_{\text{org}}$ (chlorins) or Si/Al record.

Diatoms and other siliceous plankton growth is mainly driven by temperature and nutrient changes in the maar lakes (Lücke et al. 2003; Brüchmann and Negendank 2004). Other climate parameters such as wind-driven turbulence of the surface water may also affect phytoplankton growth in the lake, but we see no evidence from the lithology (in particular grain size and botanical macroremains) that they played an important role in the Auel lake.

In fact, the ELSA-20  $C_{\text{org}}$ (chlorins) and Si/Al records reveal a close coupling between lake productivity in central Europe and temperature changes in Greenland and North Atlantic sea surface temperature



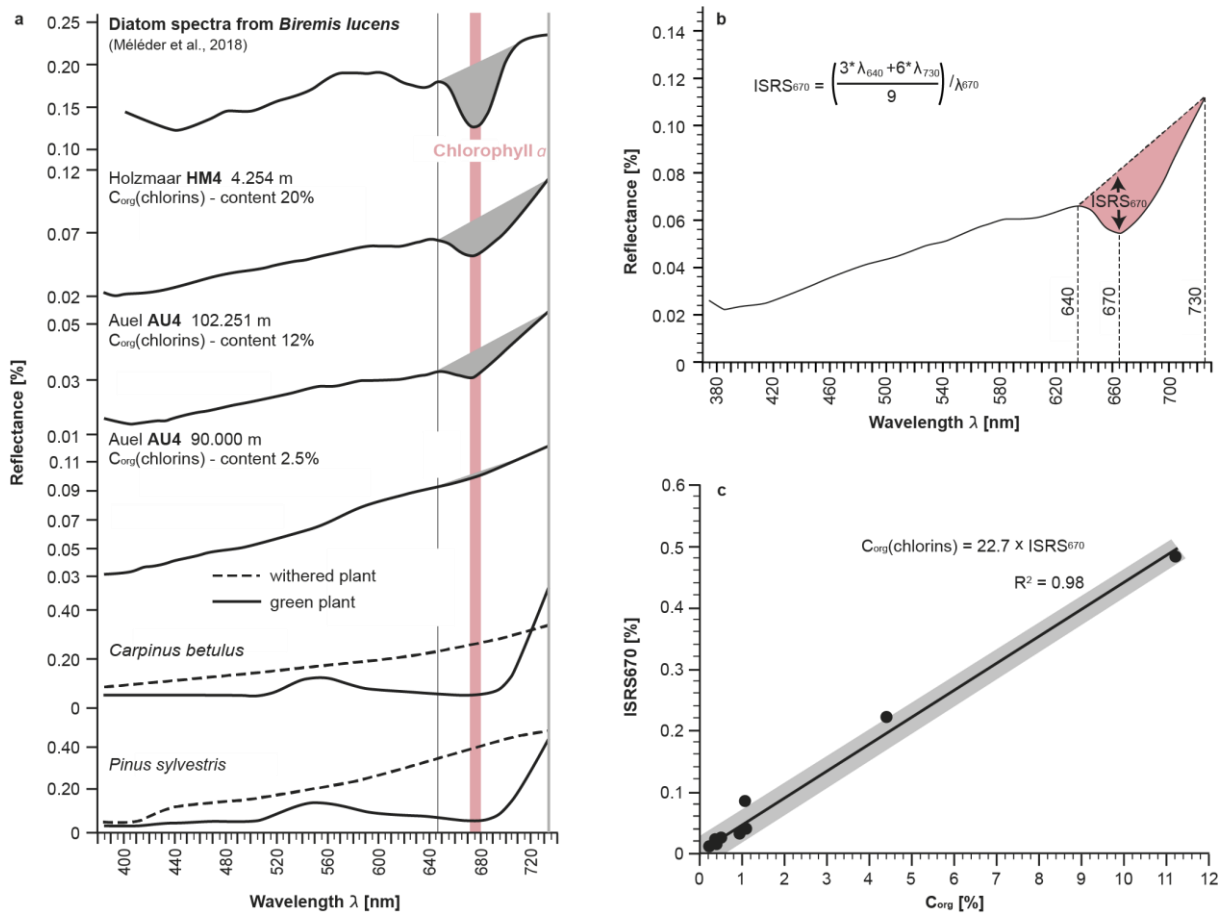


**Fig. 3.5 The ISRS method.** **a)** Reflectance of visible light wavelength, measured with a Gretag Spectrolino at 1 mm step size with 2x2 mm sensor field and spectral resolution of 10 nm. The red line characterises the absorption at 670 nm. Examples are given for three samples: rich, intermediate, low in organic carbon content. Reflectance spectra from fresh and withered plant leaves and needles are given for comparison to the adsorption of organic carbon from diatoms at 670 nm (Rein and Sirocko 2002). **b)** Quantification of the Absorption Depth at wavelength of 670 nm. The approach follows the “In Situ Reflectance Spectroscopy – ISRS” method for chlorophyll derivates (mainly chlorins) in marine sediments off Peru (Rein and Sirocko 2002), but is now adapted to the lake sediments of the Eifel maar lakes. **c)** Organic carbon measurements of 10 discrete samples versus ISRS of the same samples. Each sample represents a homogenized 10 cm long section from core AU2. The homogenized sample was measured 10 times and averaged. The relation between ISRS at 670 nm and C<sub>org</sub> content is linear and can be expressed by the equation C<sub>org</sub> = ISRS<sub>670</sub> x 22.7.

(SST) records on millennial timescales across all stadial and interstadial cycles of the last glacial cycle (Figs. 3.6, 3.7). However, the shape of the D/O cycles does not present the sharp sawtooth pattern characteristic of Greenland ice-core  $\delta^{18}\text{O}$  records, which is typically attributed to the large influence of changes in sea-ice coverage in the Nordic seas and regional changes in precipitation in Greenland climate (Li et al. 2010; Deplazes et al. 2013). Instead, ELSA-20 stadial / interstadial cycles are more symmetrical, as expected from North Atlantic SSTs (Fig. 3.7a), Greenland deuterium excess records and other climate records located in low and mid latitudes, where the influence of sea ice is less

pronounced (Masson-Delmotte 2005; Martrat et al. 2007; Sánchez Goñi et al. 2009; Deplazes et al. 2013; Cheng et al. 2016).

During the last deglaciation, the ELSA-20 records show a sharp increase in lake productivity coinciding with the deglacial warming recorded in North Atlantic SST records (around 14,700 years ago). Similarly, during the period between 48,000 and 60,000 years ago, our tracers indicate high lake production coinciding with warm conditions in the North Atlantic (Fig. 3.7). These observations strongly support that productivity changes in the Eifel maar lakes were indeed driven by temperature changes over the past 60,000 years, and confirm that atmospheric temperatures in central Europe were closely coupled to SST changes in the North Atlantic Ocean and Greenland (Van Kreveld et al. 2004).

## **Methods**

### **The ELSA Project**

During the last 20 years, the ELSA Project at the University of Mainz has drilled more than 50 cores from the 68 open and infilled maar lakes of the west Eifel volcanic field to construct a continuous time series of climate and environmental change, ranging from today back into the Middle Pleistocene. The stratigraphy of all ELSA cores is documented by Sirocko et al. (2013, 2016) and Förster et al. (2019). Sediment cores from the maar lakes of Schalkenmehren, Holzmaar and Auel were chosen for the ELSA-20 stack.

### **The Eifel maar lakes**

The Eifel is located in Germany, west of the Rhine. It experienced 200 – 300 m of uplift during the Cenozoic, leading to the formation of more than 60 Pleistocene maar eruption structures (Büchel 1994). Eight of these maar lakes are today still filled with water, of which six have more than 20-m-deep waters with anoxic conditions at the bottom. All other maar structures are infilled Pleistocene lakes. The largest of these maar lakes were dated by the ELSA Project (Sirocko et al. 2005, 2013, 2016) and erupted during the last 130,000 years (Förster and Sirocko 2016; Förster et al. 2019).

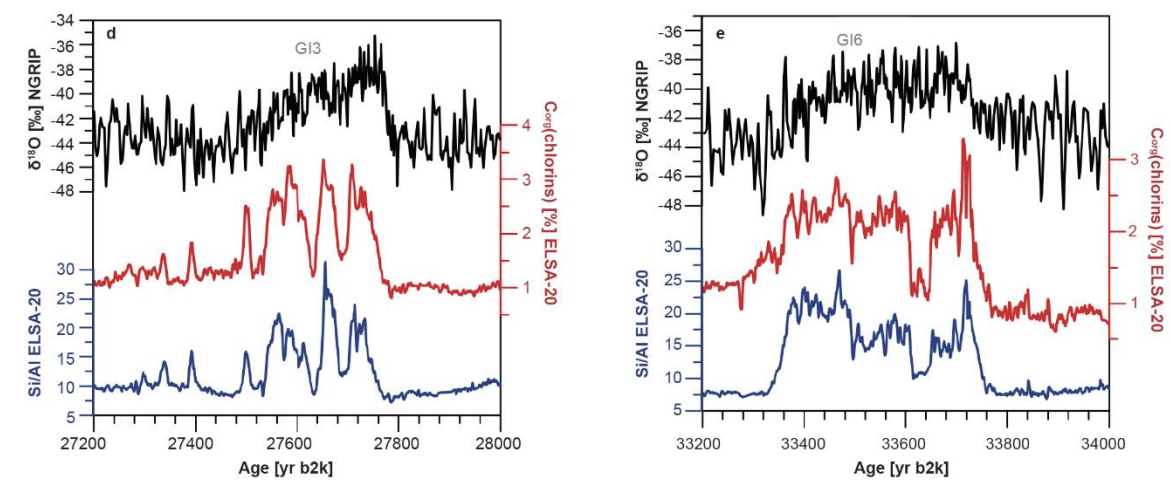
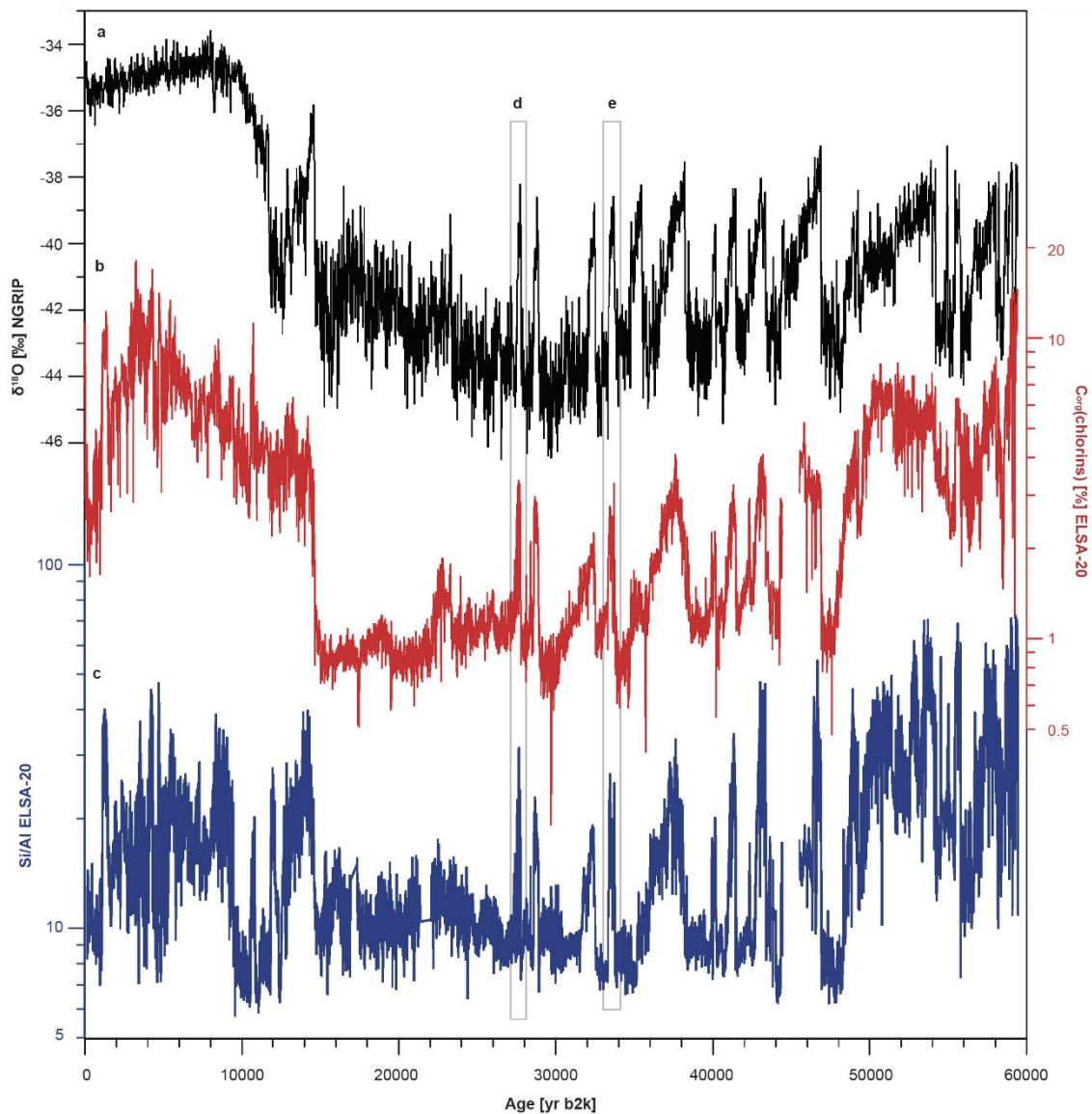


**Fig. 3.6** Temperature changes in Greenland and central Europe over the past 60,000 years. **a)** NGRIP1  $\delta^{18}\text{O}$ , a proxy for temperature changes in Greenland. **b)** ELSA-20  $C_{\text{org}}(\text{chlorins})$  content. **c)** ELSA-20 Si/Al ratio. Both **b)** and **c)** are proxies for lake primary production, primarily driven by changes in lake temperature. **d,e)** Multidecadal climate cycles recorded in the ELSA records during Greenland interstadials (GI) 3 and 6.

The most complete and undisturbed ELSA cores are from Schalkenmehren (the last 658 years, since the megaflood layer of AD 1342), Holzmaar (MIS1) and Auel (MIS2 and 3). The 22-m-deep lake of Schalkenmehren was cored with UWITEC freeze core technology. The uppermost 50 cm clearly show the Chernobyl  $^{137}\text{Cs}$  spike from AD 1986 (Sirocko et al. 2013), which provides a perfect time marker at the top of the ELSA-20 stack. The switch from the Schalkenmehren core to the Holzmaar core is at the AD 1342 megaflood layer (658 yr b2k). The Holocene record of HM4 from Holzmaar is dated by six palynostratigraphy markers (Fig. 3.4) and reaches down to 14,682 yr b2k, the beginning of the present warm interglacial.

The Pleistocene part of the stack is based on the cores from Auel, which is 20 km away from Holzmaar. The Laacher See Tephra (13,056 yr b2k; Reinig et al. 2021) is visible in all cores (AU3, AU4 and HM4), with the same mineralogy (Förster and Sirocko 2016; Förster et al. 2019). The tie point between the Holzmaar and Auel sites is, however, the first deglacial increase of  $C_{\text{org}}$  at 14,692 yr b2k (Förster et al. 2019).

### **Seismic site survey of the Auel Maar structure**

Before drilling cores AU3 and AU4, the commercial company GeoFakt (Bonn) conducted a preliminary survey of the central part of the Auel Maar with four high-resolution seismic profiles (Fig. 3.3) to obtain information on the structure of the maar lake sediments, in particular to detect the deepest location of the sediment infill.

A total of four seismic profiles were carried out at Auel with P-wave reflections. Geophone spacing was 2 m and shot point spacing was 4 m. Acquisition was performed with 96 to 120 active channels. The seismic-wave source consisted of a hand hammer. The data processing was hybrid; that is, first breaks were used for refraction tomography and further reflections were used for seismic profiling. The result of refraction tomography was a two-dimensional (2D) velocity model down to a depth of ~30 m. The final depth migration transforms the stacked time section into a depth section and shifts dipping reflections laterally to the ‘true’ reflector position. The migration velocity was derived from the stacking velocities.

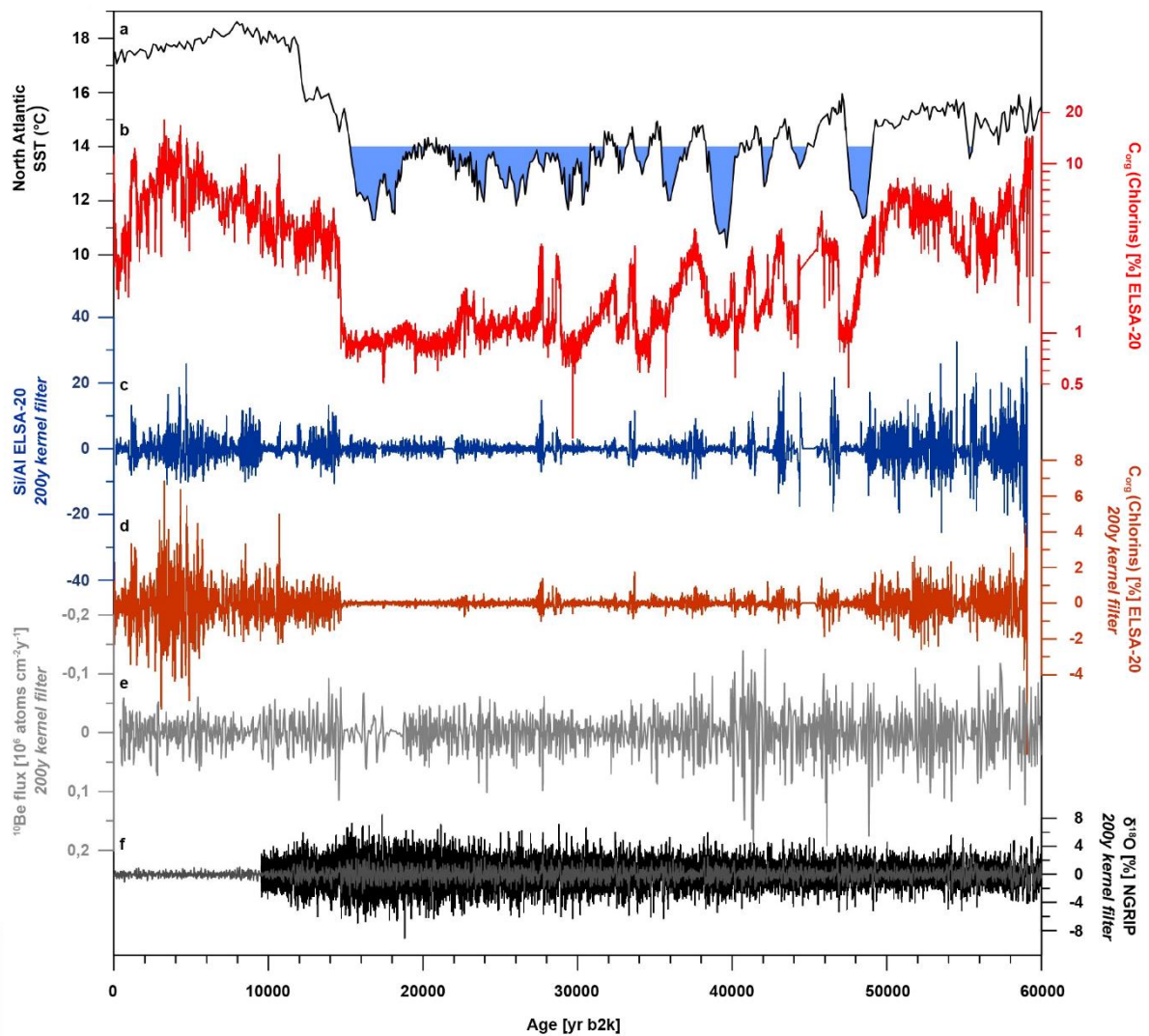


**Fig. 3.7 Reduced high-frequency climate variability in central Europe during the coldest parts of the last ice age.** **a)** North Atlantic SST reconstruction (Martrat et al. 2007). **b)** ELSA-20  $C_{org}$ (chlorins) record. **c)** ELSA-20 Si/Al record after kernel detrending using a 200-year bandwidth (Methods). **d)** ELSA-20  $C_{org}$ (chlorins) record after kernel detrending using a 200-year bandwidth. **e)**  $^{10}\text{Be}$  flux record measured in Greenland ice cores (Muscheler et al. 2005), after kernel detrending using a 200-year bandwidth. **f)** NGRIP1  $\delta^{18}\text{O}$  (black) after kernel detrending using a 200-year bandwidth.

Cores AU2, AU3 and AU4 were plotted onto the seismic profiles (Fig. 3.3). Apparently, the deepest continuous reflector exactly matches the evidence from the lithology to outline the contact between eruption tephra fallback and the deepest lake sediments at 102.5 m.

The survey documented that the deepest part of the Auel Maar was near the intersection of profiles 1 and 2, where AU2 had already been drilled in 2014. The new drillings of AU3 and AU4 are thus within 10 m of AU2, but positioned to reach the exact deepest part of the infilled maar structure (Fig. 3.3).

This exact positioning of the core location was important to sample and preserve the extraordinary quality of the MIS3 sediment. In particular, AU4 reached into a local bathymetric depression, which was apparently at least seasonally anoxic or even developed a monimolimnion (continuous anoxic conditions of the deep water during all seasons of the year). This location and the conditions in the deepest, most anoxic part of the maar basin explain the high content of  $C_{org}$  in the sediments, as well as its excellent preservation.

### **Lithology of ELSA-20 cores**

All cores are laminated, but the Holocene and many interstadial sections are varved; that is, they show seasonal layering. Dark Holocene and interstadial sections are either  $C_{org}$ -rich sapropel, unlaminated gyttja or varved diatom gyttja (Figs. 3.4, 3.8). The glacial section is composed of lithogenic clay, silt and fine sand layers in varying proportions. The glacial section of Auel is mainly fine-grained sand, suggesting that the lake was shallow. MIS3 sediments in Auel are continuously fine-grained because of riverine suspensions that ran into the deep lake with suboxic bottom water, either after seasonal rain or snow melting. The sediments of the early MIS3 are extremely rich in  $C_{org}$  — mostly sapropel and sometimes varved diatom gyttja.

The lithology of the ELSA-20 cores is documented in Fig. 3.8c, which includes a visualization of all sections with a yellow-greenish colour (visible only in the first weeks after drilling). All of these sections consist of seasonal varves with diatom-rich summer layers. These sections match the depth with high ISRS670 (in situ reflectance spectroscopy absorption at 670 nm) values, indicating the presence of chlorins.

### **Organic carbon**

Organic carbon was determined with a Gretag Spectrolino instrument, which measures the reflectance for each wavelength of the visible light as percent relative to a white colour standard (Fig. 3.5). The Spectrolino measured the sediment reflectivity over a 2.5 mm-wide area, and the individual measurements were done in 1-mm increments. The Spectrolino technique was originally developed for marine sediments by Rein and Sirocko (2002). The absorption at 670 nm was calibrated in the first study

versus organic carbon and chlorins content, both of which revealed a linear relation to the ISRS670 value, which is subtracted from the interpolated value between 640 and 730 nm (Fig. 3.5). The ISRS670 accordingly detects chlorophyll *a*, *b* and *c* and bacteriochlorophyll *c* and *d* (green sulfur bacteria) as well as their derivatives, and can be applied to detect trends in total aquatic palaeoproduction in both ocean and

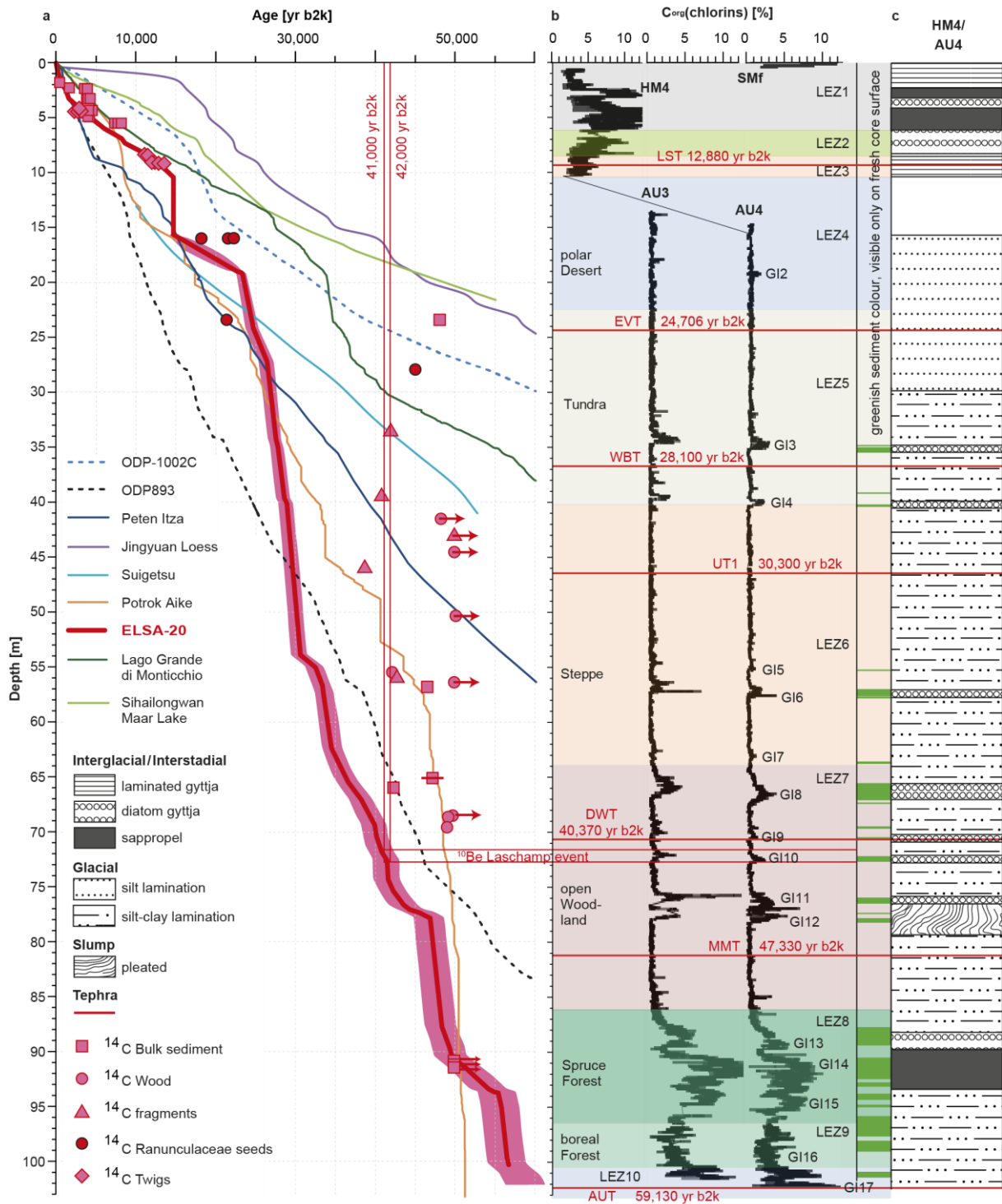


**Fig. 3.8 Age-depth relation.** For figure caption, see next page.

**Fig. 3.8 Age-depth relation. a)** The  $C_{org}$ (chlorins) data for cores SMf, HM4, AU3 and AU4 are shown versus depth to document the basis for the Age-Depth model, calculated according to Fig. 3.9. The ELSA-20 age is plotted together with  $^{14}C$  dates and  $^{10}Be$  data. The error is calculated with a Bayesian approach. The Age-Depth model is compared to other high-resolution marine and terrestrial records. Cariaco Basin: ODP-1002C (Haug et al. 1998); St. Barbara Basin ODP893 (Cannariato et al. 1999); Guatemala: Lake Petén-Itzá (Correa-Metrio et al. 2012); China: Jingyuan loess plateau (Sun et al. 2010); Japan: Lake Suigetsu (Bronk Ramsey et al. 2012); Italy: Lago Grande di Monticchio (Brauer et al. 2007); China: Sihailongwan Maar Lake (Mingram et al. 2018); S-Patagonia: Laguna Potrok Aike (Kliem et al. 2013). The sedimentation rate of the SMf and HM4 cores is similar to other global records, but the sedimentation rate of the Auel cores is globally exceptional during MIS3. **b)** The  $C_{org}$ (chlorins) are shown versus depth for cores AU3 and AU4, which have been drilled with an 0.5 m offset. Both cores reveal an identical interstadial pattern, which allows for the Dynamic Time Warp of short AU3 sections into the AU4 core. Background colors are the pattern of Landscape Evolution Zones (LEZ) as defined by Sirocko et al. (2016). 8 tephra have been observed in the cores of HM (Förster and Sirocko 2016; Förster et al. 2019). The ages for the Eltville Tephra (EVT), Wartgesberg Tephra (WBT), Dreiser Weiher Tephra (DWT) and Meefelder Maar Tephra (MMT) are presented here on the updated ELSA-20 timescale. **c)** The lithology of all ELSA-20 cores is presented with its main characteristics.

lake sediments (Butz et al. 2015; Michelutti and Smol 2016; Sanchini and Grosjean 2020).

Absorption forms a pronounced minimum in the wavelength range of 640–730 nm in cores from both Holzmaar and Auel. Reflectivity in this wavelength band (the I-band, 660–670 nm (Louda and Baker 1986; Rosell-Melé et al. 1997); that is, the red part of the spectrum) was shown to relate to sediment concentrations of chlorophyll *a* and its degradation products (Das et al. 2005; Wolfe et al. 2006; Méléder et al. 2018).

The ISRS670 of AU3 and AU4 was calibrated to  $C_{org}$  (total organic carbon, TOC; Fig. 3.8), which was determined in the laboratories of the Institute of Geography, TU Dresden, using a Total Analyzer system (TOC-VCPN; Shimadzu). Finely ground sample aliquots (200 mg) were suspended in 200 ml of 0.22 M HCl. While carbonate-derived carbon was purged out, the non-purgeable organic carbon was catalytically transformed into  $CO_2$  and measured in replication. For the reference material NIST 1941b (reference TOC value  $2.99 \pm 0.24\%$ ), replicate measurements yielded an overall accuracy and precision of  $2.96 \pm 0.14\%$ . We selected 10 samples for calibration of the ISRS670 signal relative to  $C_{org}$  content. These 10 samples were spaced along the entire cores of HM4 and AU3. Aliquots (10 g) of sediment were homogenized and pressed into a plate for which the surface reflection was measured 10 times with the Spectrolino instrument. The average of the 10 measurements was plotted versus the measured  $C_{org}$  content (Fig. 3.5c). The relation is apparently linear and can be expressed by the simple relation



$C_{\text{org}} (\%) = \text{ISRS670} \times 22.7$ . This equation was used to convert the 200,000 ISRS670 measurements (100,000 each in cores AU3 and AU4) into a final  $C_{\text{org}}$  concentration time series (Fig. 3.6).

The results suggest that the vast majority of organic matter in the Holzmaar lake is autochthonous. This matches the findings of Lücke et al. (2003), who showed with TOC/TN (total nitrogen) ratios and  $\delta^{13}\text{C}$  analysis of the organic matter that organic matter from in situ production within the lake system is indeed the main contribution to sedimentary organic carbon at Holzmaar and Auel. The covariance of  $C_{\text{org}}$ (chlorins) and Si/Al indicates that in situ production is also the main source of organic carbon for the record from Auel. We observe a few sections of deviations from this general structure. These intervals are characterised by high aeolian dust content, which adds silicium from aeolian quartz grains to the total Si content. It is only during the Younger Dryas and well into the early Holocene that the Si/Al record is lower than the respective  $C_{\text{org}}$ (chlorins) record. This could be related to an increase in the water pH of Holzmaar after the Laacher See volcanic eruption at 13,056 yr b2k; ongoing studies will evaluate this in further detail.

### **Micro XRF geochemistry**

Semi-quantitative element analysis was performed on cores HM4 and AU4 with an Avaatech XRF core scanner (Avaatech XRF Technology) at the Max Planck Institute for Chemistry in Mainz. XRF core scanning is a rapid, non-destructive technique to determine the chemical composition in sediments (Richter et al. 2006). Before the measurements, the sediment surface was carefully flattened using a blade to remove irregularities from core slicing, then covered with 4  $\mu\text{m}$ -thin SPEX CertiPrep Ultralene film to avoid contamination and drying during measurements. XRF scans were performed at a tube voltage of 10 kV with a current of 550  $\mu\text{A}$  and counting time of 10 s. The scanner was equipped with an Oxford 100-W X-ray source with a rhodium anode and a silicon drift detector. The measurements were obtained with a down-core resolution of 0.5 mm and a cross-core slit size of 12 mm. Element data are given in counts per second and were used to calculate elemental intensity ratios, thereby reducing noise.

The Si/Al data series shows mostly the same maxima and minima that are visible in the ISRS  $C_{\text{org}}$ (chlorins) analyses (Figs. 3.6, 3.9 – 3.11). Si/Al is an established proxy for the abundance of diatoms and other silicifying organisms. However, silicium is also prominent in lithogenic quartz and feldspar,

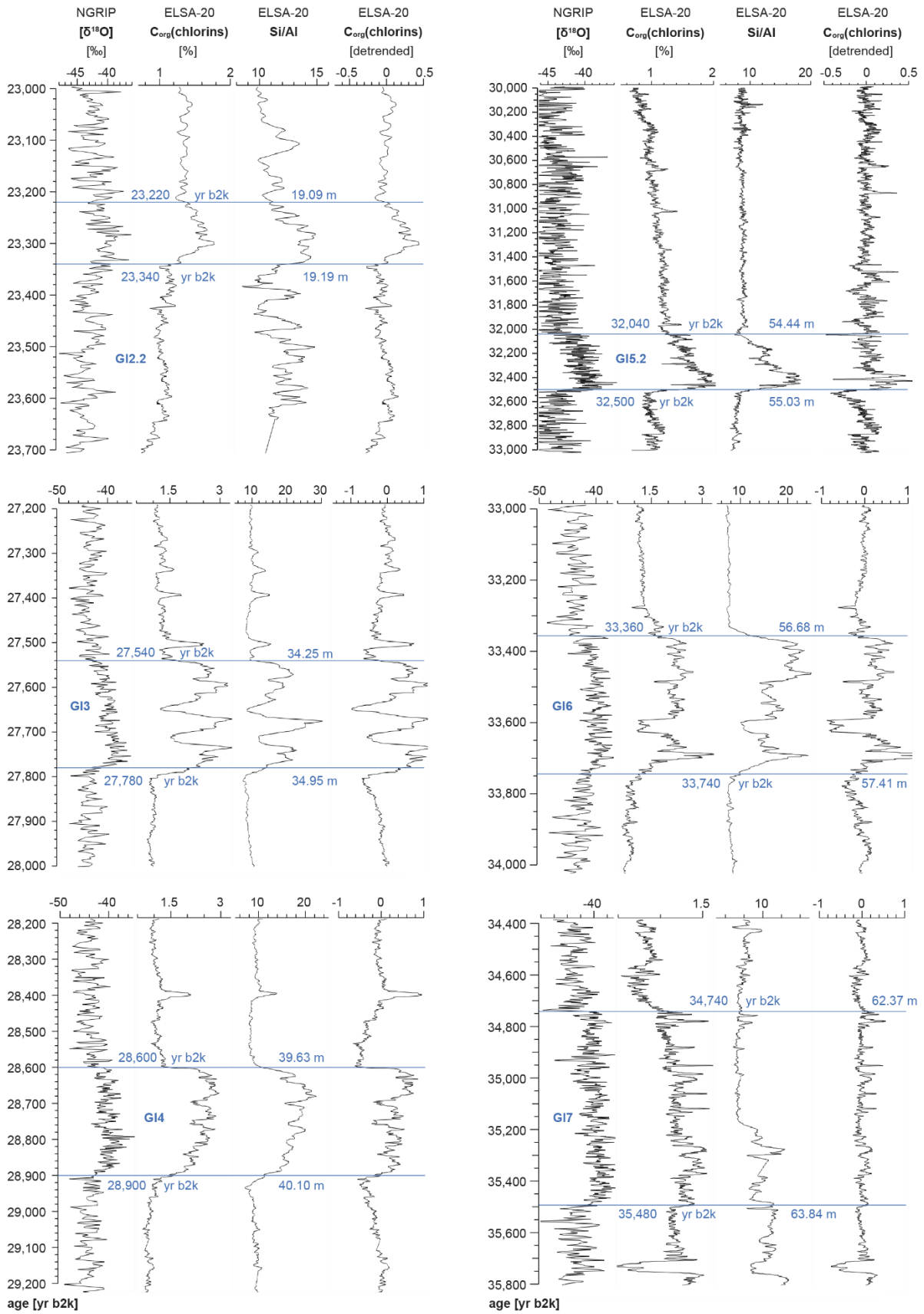


**Fig. 3.9 Ice core tuning, 23 – 36 ka.**  $\delta^{18}\text{O}$  and chronology of the NGRIP ice core (North Greenland Ice Core Project Members 2004; Rasmussen et al. 2006, 2014; Vinther et al. 2006; Andersen et al. 2006; Svensson 2008) in comparison to ELSA-20  $\text{C}_{\text{org}}(\text{chlorins})$  content and Si/Al. The ELSA-20  $\text{C}_{\text{org}}(\text{chlorins})$  data are also shown in the kernel detrended version used for the wavelet and spectra as shown in Figs. 3.7, 3.14, 3.15.

so the Si record has to be normalized to Al to separate inorganic silicates from the diatom silicate. The almost perfect match of Si/Al to the  $C_{org}$  (chlorins) content reinforces the interpretation that the organic carbon in Auel derives from the decomposition of diatoms and other silicifying organisms (see above). These are visible as discrete summer layers in all interstadial sections of the Auel cores, they produce the chlorophyll *a* derivatives that cause the ISRS signal, and their opaline tests can be traced geochemically by the Si/Al ratio.

### **Stratigraphy**

Nine different dating methods have been applied to date the entire suite of ELSA cores (Sirocko et al. 2005, 2013, 2016). Dates from all cores have been synchronized into a consistent stratigraphy. The first age marker is the  $^{137}Cs$  spike in 1986 AD, which is clearly visible in freeze cores from several maar lakes that were dated (Sirocko et al. 2013) by this chronostratigraphic marker from the Chernobyl fallout. The second marker is a flood layer representing the Millennium Flood in July of 1342 AD. This layer is well visible in the upper parts of all Holocene cores, because it contains abundant debris of wood washed into the maar by the flood event. The layer serves as a tie point to link the Schalkenmehrener Maar freeze core with the Holocene Holzmaar core (Fig. 3.4), the latter being continuously varved. However, the Holocene stratigraphy was not based on varve counting, which would have to be anchored by  $^{14}C$  (Hajdas et al. 1995). Instead, we used palynostratigraphy time markers as determined in the high-resolution varved pollen profile from Meerfelder Maar (Litt et al. 2009).

We analysed 54 samples from the Auel and Holzmaar cores in the  $^{14}C$  laboratories of Heidelberg, Kiel and Mannheim. Heidelberg sample IDs start with 'HD', Kiel sample IDs with 'KIA' and at Curt-Engelhorn-Center for Archaeometry, Mannheim, sample IDs start with 'MAMS'. Although the laboratories in Kiel and Mannheim utilize AMS for  $^{14}C$  measurements, the laboratory in Heidelberg performed the analysis by  $^{14}C$  decay counting.

$^{14}C$  samples consist of a collection of various organic materials. Conventional  $^{14}C$  ages are normalized to a  $\delta^{13}C$  of  $-25\%$ . All  $^{14}C$  ages are universally calibrated using the calibration dataset IntCal13 and the calibration software OxCal 4.3. The calibrated date ranges are given in units of years b2k as mean

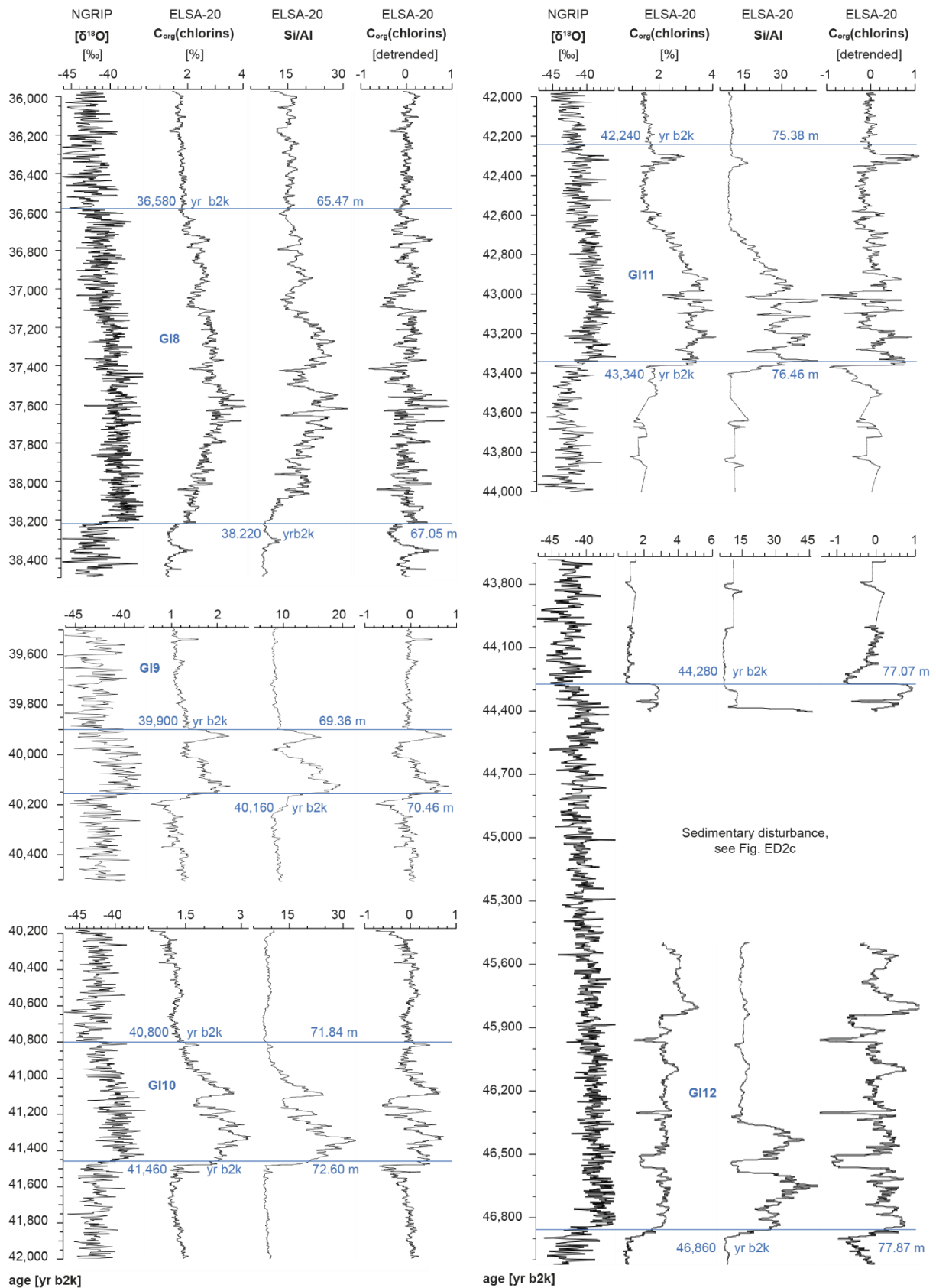


**Fig. 3.10 Ice core tuning, 36 – 48 ka.**  $\delta^{18}\text{O}$  and chronology of the NGRIP ice core (North Greenland Ice Core Project Members 2004; Rasmussen et al. 2006, 2014; Vinther et al. 2006; Andersen et al. 2006; Svensson 2008) in comparison to ELSA-20  $C_{\text{org}}$ (chlorins) content and Si/Al. The ELSA-20  $C_{\text{org}}$ (chlorins) data are also shown in the kernel detrended version used for the wavelet and spectra as shown in Figs. 3.7, 3.14, 3.15.

calibrated values with a 1-sigma uncertainty. To account for the fact that  $^{14}\text{C}$  uncertainties are not normally distributed, the calibrated dates are also given as 1-sigma date ranges.

Because the calibration dataset covers an age range up to 46,400 yr BP, some of the analysed  $^{14}\text{C}$  ages could not be calibrated. Cases where the  $^{14}\text{C}$  ages exceeded the range of the calibration dataset were denoted 'no cal'. These values were nevertheless included in the plot of Fig. 3.8, but are shown with an arrow as a minimum age. This figure shows all ages from terrestrial plant macrofossils, but also from bulk carbon, to be much older than the age of deposition in the maar lake. This is explained by the fact that Schalkenmehren, Holzmaar and Auel were fed by local creeks and thus have comparable sedimentation processes. Such an offset is to be expected, because the three independent processes (i) to (iii) shown below lead to  $^{14}\text{C}$  values that are too old in comparison to the sedimentation ages.

- (i) The creek that runs through Auel Maar even today has a catchment with length of 5 km and erodes old soil particles. Wood fragments in particular, but also seeds, are affected by this process. Sirocko et al. (2013) have demonstrated for the Ulmener Maar that particles up to several thousand years older than the time of deposition are washed into a maar lake by rivers. Holzmaar and Auel sediments have encountered the same process (Hajdas et al. 1995).
- (ii) Glacial loess has a detrital carbonate fraction of up to 10%, which must have caused a hard water effect in the MIS2 lake water.
- (iii) Active fumaroles are very abundant in the Eifel and inject  $\text{CO}_2$  from the deep Earth crust and mantle directly into the lake water column.

All of these processes cause  $^{14}\text{C}$  ages to appear older than the age of deposition (Fig. 3.8). However, we do not observe any  $^{14}\text{C}$  ages younger than the tuned age–depth relation, which is a strong argument for the dominating effect of processes (i) to (iii). Only two dates match the correct deposition age within the error of the MIS3  $^{14}\text{C}$  calibration. As a consequence,  $^{14}\text{C}$  values cannot be used to date the sediment, but the  $^{14}\text{C}$  values corroborate unequivocally that the sediments have been deposited during the last 48,000 years.

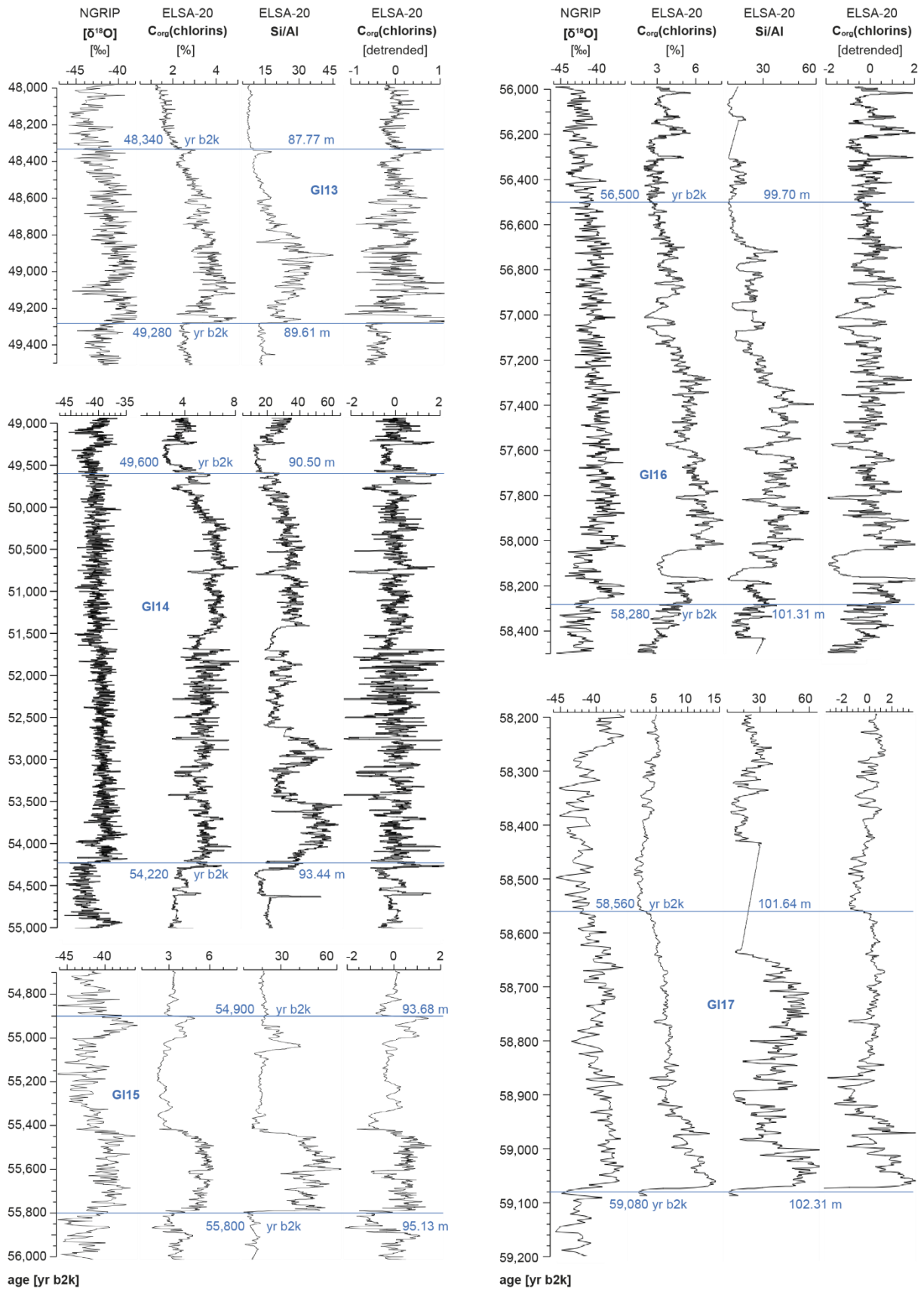


**Fig. 3.11 Ice core tuning, 48 – 59 ka.**  $\delta^{18}\text{O}$  and chronology of the NGRIP ice core (North Greenland Ice Core Project Members 2004; Rasmussen et al. 2006, 2014; Vinther et al. 2006; Andersen et al. 2006; Svensson 2008) in comparison to ELSA-20  $\text{C}_{\text{org}}$ (chlorins) content and Si/Al. The ELSA-20  $\text{C}_{\text{org}}$ (chlorins) data are also shown in the kernel detrended version used for the wavelet and spectra as shown in Figs. 3.7, 3.14, 3.15.

## **Holocene palynostratigraphy**

Holocene European lake sediments are classically dated by radiocarbon dating, or the successive spread of trees. Pollen is a well-established proxy for vegetation and climate change and has also been used to define pollen zones in central Europe. We synchronized the ELSA pollen counts with the pollen profiles for Meerfelder Maar (Litt et al. 2009), which were presented on an annual layer varve chronology. The slight discrepancy when comparing the varve chronology with the b2k ice-core notation comes from the use of varve years, which are often in the BP notation, officially reserved for  $^{14}\text{C}$  dates. The larger problem is, however, that the change from one pollen zone to another is defined from the start of the transition or from the midpoint of the transition, which is not always clear. To take both sources of error into account, we use the ages as presented by Litt et al. (2009) and add a combined error of  $\pm 100$  years for the ELSA-20 Bayesian age model (Fig. 3.12).

## **Ice-core tuning**

The first tuning of a 5-cm-resolution  $C_{\text{total}}$  curve of core AU2 to the GIs was carried out by Sirocko et al. (2016). The annual-resolution  $C_{\text{org}}$ (chlorins) curve matches the older  $C_{\text{total}}$  curve in its general shape, but now shows a resolution that documents every event (beginning and end) of the GI on the GICC05 timescale (Rasmussen et al. 2014) in detail. We present in Figs. 3.6 and 3.7 the  $C_{\text{org}}$  content and Si/Al, next to the Greenland  $\delta^{18}\text{O}$  record (Rasmussen et al. 2014).

The resolution of the NGRIP  $\delta^{18}\text{O}$  record is 5 cm, smoothed to 20 years, and one year for the ELSA-20 stack. The start and end, as well as the internal structure, are most similar for GI3 to GI17. It is only for GI8 that the onset of the interstadial is different—sharp within 20 years at Greenland, but stretched for about a century in ELSA-20. The overall similar structure of the Greenland / North Atlantic climate evolution and the central European response is the basis for our age assignments for the beginning and end of the interstadials, as documented in Figs. 3.9 – 3.11.

## **$^{10}\text{Be}$ analysis**

Bulk samples were selected from the interval of the tuned GI8 – GI12 to be measured for  $^{10}\text{Be}$  content to determine the depth of the Laschamp  $^{10}\text{Be}$  maximum (Muscheler et al. 2005). The  $^{10}\text{Be}/^9\text{Be}$  ratios

were measured at the ETH Zurich AMS facilities and normalized to the ETH Zurich in-house AMS standards S2007N and S2010N with nominal  $^{10}\text{Be}/^9\text{Be}$  ratios of  $28.1 \times 10^{-12}$  and  $3.3 \times 10^{-12}$ , respectively (Christl et al. 2013). Both standards have been calibrated relative to ICN 01-5-1 with a nominal ratio of  $^{10}\text{Be}/^9\text{Be} = 2.709 \times 10^{-11}$  (Nishiizumi et al. 2007), which is associated with a  $^{10}\text{Be}$  half-life of  $1.387 \pm 0.012$  Myr (Chmeleff et al. 2010; Korschinek et al. 2010).

Data for the pronounced  $^{10}\text{Be}$  maximum from 71.95 to 74.75 m are documented in Fig. 3.14 and also included in Fig. 3.8. This depth interval is integrated with ages at 41,000 and 42,000 yr b2k into the ELSA-20 age model and presents a marked fixed point in the Bayesian age model.

### **Bayesian error calculation**

The tuning, as documented above, provides the age control points for our age model. For a comparison of the ELSA-20 age to other records that were dated by other methods, we needed to develop a combined error analysis that includes the ice core error and the error of our synchronization. We achieved this by developing a Bayesian age model for the Holzmaar and Auel cores. This is based on a set of fix points through which a curve is fitted and uncertainty bands are calculated by means of a Bayesian statistical approach.

The majority of fix points stem from mathematical tuning (Fig. 3.12) of  $C_{\text{org}}$ (chlorins) from AU4 to  $\delta^{18}\text{O}$  from NGRIP for selected stadial and interstadial events (Rasmussen et al. 2014). Holocene fix points are from the palynological markers and the Laacher See Tephra layer with its established age of 13,056 yr b2k (Reinig et al. 2021). The 1-sigma uncertainties for the visual tuning are determined by fits of parametric change-point regression models to the  $C_{\text{org}}$ (chlorins) and  $\delta^{18}\text{O}$  time series (Fig. 3.12). The models are the ramp (Mudelsee 2000) and the break (Mudelsee 2009). Estimation is performed by an ordinary least-squares regression combined with a brute-force search for the optimum change points. For the detected change points, the 1-sigma standard errors in depth (AU4) and time (NGRIP) are obtained by means of 2,000-block bootstrap resampling. This approach preserves the distributional shape and autocorrelation in the random components (Mudelsee 2014). In addition to the tuning uncertainty, there is also the counting uncertainty of the NGRIP timescale (Rasmussen et al. 2014). The full fix-point age uncertainties are obtained via error propagation (Mudelsee 2014) from the tuning and



counting uncertainties. The age model (Fig. 3.8) is obtained by fitting a compound Poisson–Gamma model to the accumulation rate for core AU4 in a Bayesian framework (Haslett and Parnell 2008). The employed R software Bchron (by A. Parnell) is a numerical enhancement of the original implementation. The input data for Bchron are the 41 fix points and the depth points for output ( $AU4_{\text{predict}}$ ). The output is the age curve ( $AU4_{\text{agedepth}}$ ) at the depth points, obtained by means of the following Bchron command:

```
AU4_agedepth = Bchronology (ages = NGRIP_age, ageSds = NGRIP_1-σ (age),
positions = AU4_depth, positionThicknesses = 2 * AU4_1-σ (depth),
calCurves = rep('normal', 41), predictPositions = AU4_predict).
```

The output for  $AU4_{\text{agedepth}}$  takes into account the 1-sigma tuning uncertainty,  $NGRIP_{1-\sigma}(\text{age})$ . Bchron outputs the ages together with preselected percentiles as uncertainty estimates. We use the 15.87th and 84.13th percentiles, which correspond to the  $\pm 1$ -sigma uncertainty bounds of a normal distribution (Abramowitz and Stegun 1965). For determination of the full uncertainty, we add the NGRIP counting uncertainty to the  $\pm 1$ -sigma tuning uncertainty by means of error propagation. The resulting age curve for AU4 with  $\pm 1$ -sigma uncertainty bands (tuning or full) is shown in Fig. 3.8.

There are a number of slumps and tephra sections in core AU4 (Fig. 3.8), where, between the top and base of a section, the material is of constant age. These sections are extracted before the Bayesian modelling and inserted manually afterwards. The ELSA-20 stack is thus a synthetic record, which reaches from AD 2000 back to 59,130 yr b2k, the time of eruption of the Auel Maar. The total estimated uncertainties increase with age, as is the case for NGRIP, but the uncertainty relative to the NGRIP chronology is mostly less than 100 years. We also cannot exclude time-transgressive behaviour of chronozones in terrestrial records (Rach et al. 2014; Obrecht et al. 2020).

The Bayesian age model was finally constructed on the basis of four fix points for the younger record of HM4 and the more recent part (Fig. 3.12).

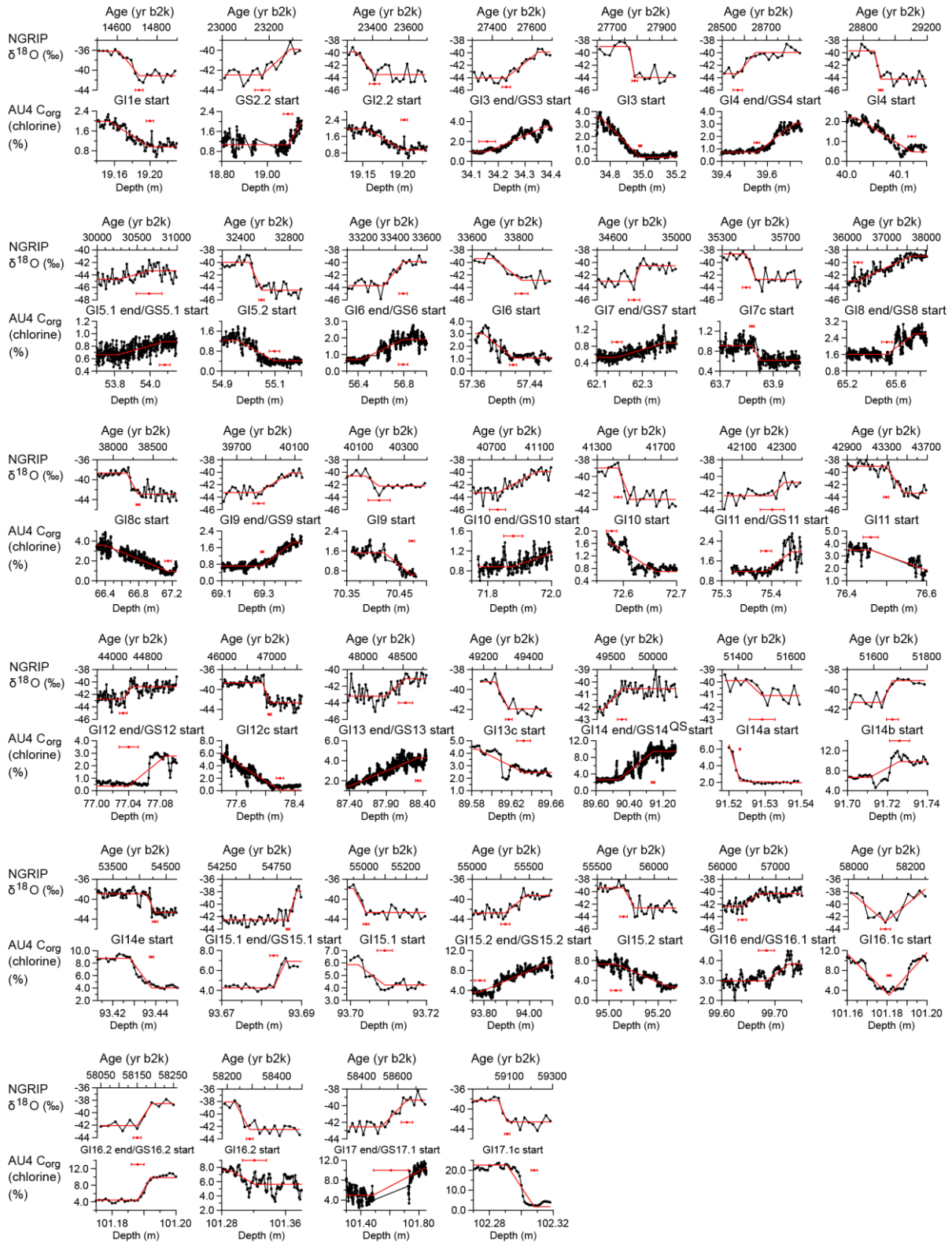


**Fig. 3.12 Uncertainty determination.** Control points for the Bayesian error calculation of the AU4 C<sub>org</sub>(chlorins) to δ<sup>18</sup>O from NGRIP (North Greenland Ice Core Project Members 2004) for selected GI events except the disturbed sections of GI12 – GS12.

### **Statistical analysis of ELSA-20 time series**

The spectra for the various time intervals (Fig. 3.13) were calculated on the detrended time series obtained with a Gasser–Müller kernel trend (Mudelsee 2014) estimated with a bandwidth of 200 yr. The spectral power was determined by means of the Lomb–Scargle Fourier transform combined with Welch’s overlapped segment procedure (Mudelsee 2014), which is implemented in REDFIT software (Schulz and Mudelsee 2002). No bias correction was necessary due to the even spacing of the series. The significances of the spectral peaks were tested against the upper 99% percentile from the chi-squared distribution for the AR(1) red noise alternative. Because an incomplete detrending appears as overestimated redness in a spectrum, we employed a conservative approach and additionally tested the higher-frequency components against white noise.

The sample of peak periods for the warm intervals (Fig. 3.15a–c), calculated without the possibly power-biased longer-period peaks, has 24 data points. The sample for the cold intervals (Fig. 3.15d–i) has 28 data points. Warm intervals tend to show more longer-period peaks (slower variations) and fewer short-period peaks (faster variations) than cold intervals, as an unpaired Student’s t-test (von Storch and Zwiers 2001) revealed ( $P < 0.0034$ ).

Wavelet power spectra for the detrended time series obtained with a Gasser–Müller kernel trend, estimated with a bandwidth of 200 yr, were calculated using the methods proposed by Torrence and Compo (1998). The significances of the different cycles are indicated in Fig. 3.14 by the thick black contours, which enclose regions of greater than 95% confidence for a red noise process with a lag-1 coefficient of 0.72. The NGRIP 5 cm  $\delta^{18}\text{O}$  record (North Greenland Ice Core Project Members 2004; Andersen et al. 2006; Vinther et al. 2006; Svensson 2008; Rasmussen et al. 2014) and the  $^{10}\text{Be}$  record (Muscheler et al. 2005) were linearly interpolated to their respective average sample resolution before the analysis.

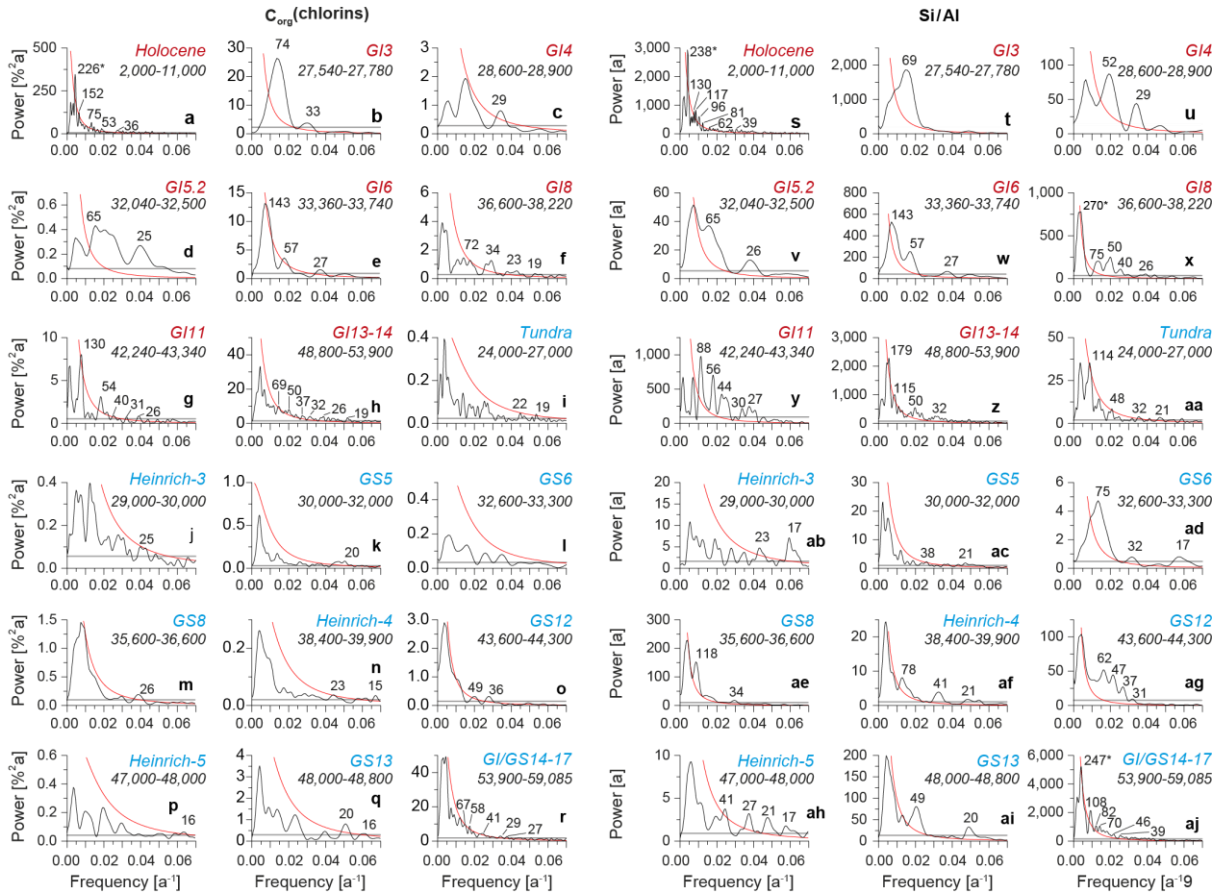


**Fig. 3.13 Statistical Analysis.** **a-r)**  $C_{org}$ (chlorins) Lomb-Scargle spectral power estimation for selected time intervals for the ELSA-20  $C_{org}$ (chlorins) record. Employed were a Welch taper and following estimation parameters: a, number of segments ( $n_{50}$ ) = 10, 6-dB bandwidth (BW) =  $8.0 \times 10^{-4} \text{ yr}^{-1}$ ; b,  $n_{50} = 2$ , BW =  $9.9 \times 10^{-3} \text{ yr}^{-1}$ ; c,  $n_{50} = 2$ , BW =  $8.0 \times 10^{-3} \text{ yr}^{-1}$ ; d,  $n_{50} = 4$ , BW =  $8.6 \times 10^{-3} \text{ yr}^{-1}$ ; e,  $n_{50} = 3$ , BW =  $8.4 \times 10^{-3} \text{ yr}^{-1}$ ; f,  $n_{50} = 5$ , BW =  $2.9 \times 10^{-3} \text{ yr}^{-1}$ ; g,  $n_{50} = 2$ , BW =  $2.2 \times 10^{-3} \text{ yr}^{-1}$ ; h,  $n_{50} = 10$ , BW =  $1.7 \times 10^{-3} \text{ yr}^{-1}$ ; i,  $n_{50} = 6$ , BW =  $1.9 \times 10^{-3} \text{ yr}^{-1}$ ; j,  $n_{50} = 3$ , BW =  $3.2 \times 10^{-3} \text{ yr}^{-1}$ ; k,  $n_{50} = 6$ , BW =  $2.8 \times 10^{-3} \text{ yr}^{-1}$ ; l,  $n_{50} = 3$ , BW =  $8.0 \times 10^{-3} \text{ yr}^{-1}$ ; m,  $n_{50} = 5$ , BW =  $4.8 \times 10^{-3} \text{ yr}^{-1}$ ; n,  $n_{50} = 7$ , BW =  $4.2 \times 10^{-3} \text{ yr}^{-1}$ ; o,  $n_{50} = 4$ , BW =  $5.7 \times 10^{-3} \text{ yr}^{-1}$ ; p,  $n_{50} = 5$ , BW =  $4.8 \times 10^{-3} \text{ yr}^{-1}$ ; q,  $n_{50} = 4$ , BW =  $5.0 \times 10^{-3} \text{ yr}^{-1}$ ; and r,  $n_{50} = 11$ , BW =  $1.8 \times 10^{-3} \text{ yr}^{-1}$ . Each panel indicates (italics) name and time interval (yr b2k) and shows spectral power (black line), AR(1) red noise upper 99% percentile (red line), white noise upper 99% percentile (grey line) and the periods for significant and (within BW) separable spectral peaks. The low-frequency peak marked by an asterisk (a) may have a biased power estimate due to the kernel detrending. The high-frequency spectrum parts (up to  $0.5 \text{ yr}^{-1}$ ) do not exhibit relevant peaks. **s-aj)** Si/Al Lomb-Scargle spectral power estimation for selected time intervals for the ELSA-20 Si/Al record. Employed were a Welch taper and following estimation parameters: s, number of segments ( $n_{50}$ ) = 10, 6-dB bandwidth (BW) =  $8.1 \times 10^{-4} \text{ yr}^{-1}$ ; t,  $n_{50} = 2$ , BW =  $9.9 \times 10^{-3} \text{ yr}^{-1}$ ; u,  $n_{50} = 2$ , BW =  $8.0 \times 10^{-3} \text{ yr}^{-1}$ ; v,  $n_{50} = 4$ , BW =  $8.6 \times 10^{-3} \text{ yr}^{-1}$ ; w,  $n_{50} = 3$ , BW =  $8.4 \times 10^{-3} \text{ yr}^{-1}$ ; x,  $n_{50} = 5$ , BW =  $2.9 \times 10^{-3} \text{ yr}^{-1}$ ; y,  $n_{50} = 2$ , BW =  $2.2 \times 10^{-3} \text{ yr}^{-1}$ ; z,  $n_{50} = 10$ , BW =  $1.7 \times 10^{-3} \text{ yr}^{-1}$ ; aa,  $n_{50} = 6$ , BW =  $1.9 \times 10^{-3} \text{ yr}^{-1}$ ; ab,  $n_{50} = 3$ , BW =  $3.2 \times 10^{-3} \text{ yr}^{-1}$ ; ac,  $n_{50} = 6$ , BW =  $2.8 \times 10^{-3} \text{ yr}^{-1}$ ; ad,  $n_{50} = 3$ , BW =  $8.0 \times 10^{-3} \text{ yr}^{-1}$ ; ae,  $n_{50} = 5$ , BW =  $4.8 \times 10^{-3} \text{ yr}^{-1}$ ; af,  $n_{50} = 7$ , BW =  $4.2 \times 10^{-3} \text{ yr}^{-1}$ ; ag,  $n_{50} = 4$ , BW =  $5.7 \times 10^{-3} \text{ yr}^{-1}$ ; ah,  $n_{50} = 5$ , BW =  $4.8 \times 10^{-3} \text{ yr}^{-1}$ ; ai,  $n_{50} = 4$ , BW =  $5.0 \times 10^{-3} \text{ yr}^{-1}$ ; and aj,  $n_{50} = 11$ , BW =  $1.8 \times 10^{-3} \text{ yr}^{-1}$ . Each panel indicates (italics) name and time interval (yr b2k) and shows spectral power (black line), AR(1) red noise upper 99% percentile (red line), white noise upper 99% percentile (grey line) and the periods for significant and (within BW) separable spectral peaks. The low-frequency peaks marked by an asterisk (a, f, r) may have biased power estimates due to the kernel detrending. The high-frequency spectrum parts (up to  $0.5 \text{ yr}^{-1}$ ) do not exhibit relevant peaks.

### **Stadial and interstadial multidecadal climate variability**

In addition to documenting the entire succession of millennial-scale D/O cycles in central Europe, the unprecedented resolution of our record uncovers a series of decadal-scale climate cycles that persist through the last ice age. These Auel multidecadal cycles can be visually identified in most of the lake interstadials (Figs. 3.6, 3.9 – 3.11), but are not evident in the Greenland ice cores or in the lower-resolution North Atlantic SST records (Figs. 3.6d,e, 3.7a). Although the cycles occur mainly during GIs, they are sometimes accompanied by a series of events before and after the GI (for example, GI3 and GI11, Fig. 3.6b,c) and are substantially reduced or disappear during the coldest parts of the glacial and stadial periods. Our analysis indicates that the reduction / absence of these cycles from the ELSA-20 records during cold periods represents a climatic signal. We cannot fully exclude, that changes in the climate sensitivity of the lake productivity proxies can occur at temperatures near or below freezing point, but based on the undisturbed sedimentary structure we consider this possibility unlikely (see Methods).

To investigate further the nature and periodicity of these cycles, we apply a Gasser–Müller kernel detrending (estimated with a bandwidth of 200 years; Mudelsee 2014) to the ELSA-20 record to subtract the millennial-scale climate variability. The detrended records show that the amplitude of this high-frequency climate oscillations increases during all warm interstadial periods as well as during the Holocene (Fig. 3.7). The evolutive wavelet spectra of the record show that these cycles have different periodicities in the range between ~700 and ~9 years (Fig. 3.14), and illustrate the strong pacing of these high-frequency oscillations by the stadial / interstadial transitions, particularly in the interval between 14,700 and 48,000 yr b2k (Figs. 3.7, 3.14). The spectral analysis of selected intervals using the Lomb–Scargle Fourier transform combined with Welch’s overlapped segment averaging procedure (Mudelsee 2014) reveals that a series of multidecadal cycles in the ranges from ~20 to ~140 years are statistically significant during most of the warm interstadial periods and the Holocene (Figs. 3.13, 3.15). By contrast, during the coldest parts of the stadial periods, the variability above the 20-year band decreases substantially. However, significant periodicities above the 20-year band are still observed in several of the stadial periods, particularly in the Si/Al record (Fig. 3.13, 3.15 and Methods).

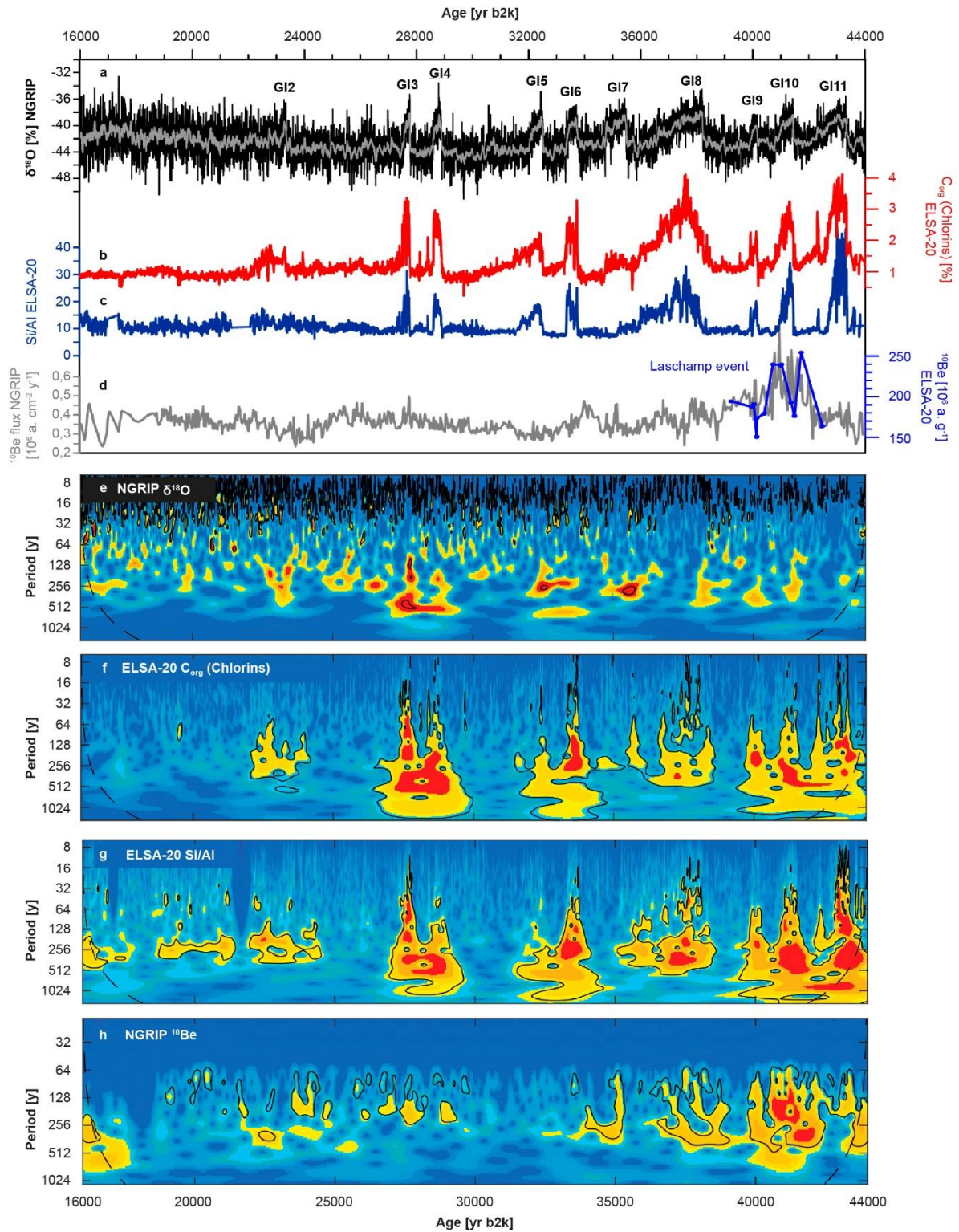


**Fig. 3.14 Evolution of decadal- to centennial-scale climate cycles across the stadial / interstadial events of the last ice age. a–d)** Evolution of NGRIP1  $\delta^{18}\text{O}$  (a), ELSA-20  $C_{\text{org}}$ (chlorins) (b), ELSA-20 Si/Al (c) and  $^{10}\text{Be}$  flux record (d) measured in Greenland ice cores. **e–h)** Wavelet spectra after kernel detrending using a 200-year bandwidth, corresponding to **a–d)**, respectively. Details of the wavelet spectra calculation are provided in the Methods. The thick contour encloses regions of greater than 95% confidence for a red-noise process with a lag-1 coefficient of 0.72. Dashed lines at either end of the figures indicate the ‘cone of influence’, where edge effects become important.

High-frequency climate cycles of similar periodicity have been identified in previous studies during past centuries and across the Holocene period (that is, the past 11,700 years) in multiple climate archives, including tree rings (Schlesinger and Ramankutty 1994; Mann et al. 1995), speleothems (Fleitmann et al., 2003), ice cores (Knudsen et al. 2011) and lake (Hodell et al. 1995) and marine (Haug et al. 2001) sediments. The multidecadal cycles in the band of 30 – 90 years have received particular attention and are thought to be closely related to the Atlantic multidecadal oscillation (AMO; Knudsen et al. 2011). The AMO has been identified as a coherent mode of climate variability that traces the average anomalies of instrumental SST measurements in the North Atlantic basin over the past 150 years (Kerr 2000). These climate oscillations cause profound impacts in a range of global climate phenomena that have important societal and economic relevance, such as temperature and precipitation changes over Europe, North America, Africa and Asia (Sutton and Hodson 2005; Zhang et al. 2019), Atlantic hurricane frequency and intensity (Goldenberg et al. 2001), shifts in the position of the Intertropical Convergence Zone (Knight et al. 2006), El Niño–Southern Oscillation variability (Dong et al. 2006; Levine et al. 2017) or changes in Arctic sea-ice extent (Li et al. 2018). However, its forcing mechanism is not fully understood.

### **Potential drivers of multidecadal climate variability**

Current hypotheses regarding the potential drivers of the AMO during the instrumental period (roughly the last 150 years) as well as in the palaeoclimatic records (through the Holocene) can be grouped into two categories: external radiative forcing linked to solar variability and internal oscillations of the climate system tied to the AMOC. The most well-known mode of solar irradiance variability is the one associated with the reverse in polarity of the solar magnetic field roughly every 11 years. The duration of this cycle is now well constrained by multiple space-based radiometers and historical observations of sunspot activity to approximately 9 to 14 years (Lean 2017). Beyond the instrumental era, cycles of ~88 years (Gleissberg), ~205 years (de Vries or Suess), as well as a series of unnamed longer cycles have been identified in total solar irradiance reconstructions inferred from  $^{14}\text{C}$  and  $^{10}\text{Be}$  measurements in polar ice cores and tree rings across the Holocene period (Steinhilber et al. 2012). Although causal

links between the solar Gleissberg cycle and the AMO have been proposed (Wang et al. 2005; Otterå et al. 2010; Seidenglanz et al. 2012), the exact mechanisms by which the relatively weak solar radiation changes would be transferred into the large climate signals associated with the AMO are still not fully understood (Lean 2017). Alternatively, other authors have concluded that the AMO cycles observed in instrumental and palaeoclimate temperature and precipitation records are not primarily driven by external forcing, but are linked to the internal modes of variability of the AMOC (Schlesinger and Ramankutty 1994; Mann et al. 1995; Knight et al. 2006; Knudsen et al. 2011; Zhang et al. 2019).

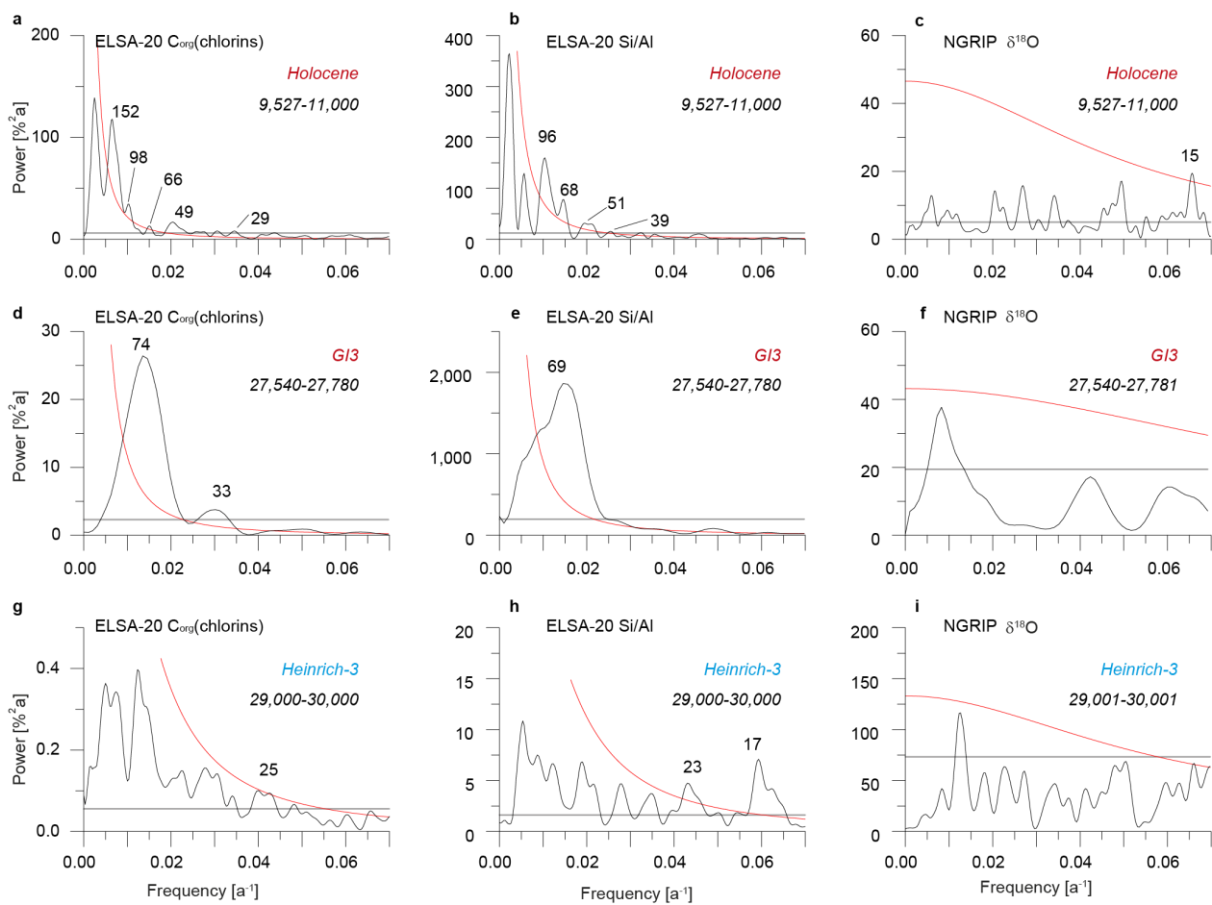


**Fig. 3.15 Lomb–Scargle spectra for selected times of the Holocene, interstadial GI3 and Heinrich 3.** Lomb–Scargle spectral power estimation for selected time intervals (Holocene (a–c), GI3 (d–f), Heinrich 3 (g–i)) for the series of ELSA-20  $C_{org}$ (chlorins) (a,d,g), ELSA-20 Si/Al (b,e,h) and NGRIP  $\delta^{18}O$  (c,f,i). Estimation parameters: number of segments ( $n_{50}$ ) = 3, 6-dB bandwidth (BW) =  $2.2 \times 10^{-3} \text{ yr}^{-1}$  (a–c);  $n_{50}$  = 2, BW =  $9.9 \times 10^{-3} \text{ yr}^{-1}$  (d–f);  $n_{50}$  = 3, BW =  $3.2 \times 10^{-3} \text{ yr}^{-1}$  (g–i). Each panel shows spectral power (black line), AR(1) red noise upper 99% percentile (red line), white noise upper 99% percentile (grey line) and the periods (in years) for significant and (within BW) separable spectral peaks. See Methods for details.



Study of multidecadal cycles during ice ages has been limited, so far, by the temporal resolution of the available records, with only the Greenland ice-core records having the appropriate resolution (North Greenland Ice Core Project Members 2004). However, our analysis of the NGRIP  $\delta^{18}\text{O}$  record indicates that multidecadal cycles were not statistically significant during the Holocene, nor during the stadial / interstadial cycles of the last ice age (Figs. 3.14, 3.15). Our records, however, provide evidence that multidecadal climate variability in the band of the AMO (that is, 30 to 150 years) persisted through the last ice age in central Europe, but was clearly reduced during most of the cold stadial periods.

So far, there are no indications from ice-core records suggesting that solar intensity changed substantially on multidecadal to centennial timescales between glacials and interglacials and/or between stadial and interstadials (Muscheler et al. 2005). Unfortunately, the resolution of the available  $^{10}\text{Be}$  ice-core record (~35 years) hampers a complete evaluation of a potential solar origin of these glacial multidecadal cycles, but no clear stadial–interstadial structure is evident in the power spectra of centennial-scale cycles (Fig. 3.14e; Wagner et al. 2001; Muscheler and Beer 2006). This contrasts with the clear stadial / interstadial pattern found in our records and suggests that the reduction of centennial-scale climate variability during cold periods was unlikely to be caused directly by solar variability changes.

Although the specific mechanism suppressing or decreasing high-frequency climate variability in central Europe during stadial periods remains to be fully evaluated, existing climate model simulations suggest that it may be linked to the combined effect of the Laurentide and Scandinavian ice sheets, increased sea-ice extent and reduced strength of the AMOC on atmospheric circulation patterns (Justino and Peltier 2005; Pausata et al. 2011). Glacial model simulations tend to show that, as a consequence of ice-sheet topographic forcing and ice albedo feedbacks, the surface pressure field of the North Atlantic was characterised by the existence of four distinct centres of action (over the Labrador Sea, Siberia, the Iberian Peninsula and the Aleutian Islands), in contrast with the north–south dipole structure that is characteristic of the present-day North Atlantic oscillation (NAO). This glacial configuration was associated with meridional wind anomalies over the North Atlantic instead of the more zonal winds characteristic of the modern NAO. Interestingly, these changes in the structure of North Atlantic

atmospheric circulation patterns during glacial maxima boundary conditions resulted in suppression of the multidecadal variability of sea-level pressure, SST and AMOC strength in the model simulation (Justino and Peltier 2005), which is consistent with our observations.

In summary, the ELSA-20 records reported here reveal that multidecadal cycles are a characteristic feature of warm interglacial periods as well as of all interstadial peaks of the last ice age. In addition, they indicate a reduction in multidecadal climate variability in central Europe during the coldest parts of the last ice age (the stadial periods and the LGM). We suggest that this decrease in the strength of multidecadal oscillations was the result of the dramatic changes in atmospheric circulation patterns in the North Atlantic associated with the weakening of the AMOC and the increase in sea-ice extent during these periods of extremely cold climate conditions.

### **3.3 The Auel Cooling Event (ACE) – Evidence for a severely cold period during Greenland Stadial 12**

This chapter is unpublished as of the submission of this thesis. It was submitted to *Quaternary* as:

Albert J, Sirocko F (submitted) Evidence for an extreme slumping event prior to the Laschamp geomagnetic excursion in Eifel maar sediments.

#### **Author's contribution**

I am lead author of this manuscript and prepared all figures and tables. My further contributions include the development of the stratigraphies and lithologies of all presented sediment records, as well as literature research and data interpretation. I constructed the age/depth models of the sediment records and age-tuned the organic carbon (chlorins) data to the NGRIP ice core stratigraphy.

#### **Abstract**

We present a timeseries of flood and slumping phases in central Europe from event layers in sediment cores from infilled Eifel maar basins (Germany). Palynological, petrographic and organic carbon (chlorins) records are used to understand the precise timings of these events. Periods of increased flood activity seem to coincide with Heinrich Events in marine sediment records, which are associated with more arid climate conditions, indicating a vegetation response within the maars' catchment areas. This multi-proxy correlation reveals a slumped sediment segment in all cores during Greenland Stadial (GS) 12. Frozen and fractured sediment packages suggest deep frost or permafrost conditions for the region at around 43,500 yr b2k. The results agree well with sediment archives and archeological sites across Europe that report severely cold and arid conditions for the stadial. This supports the assumption, that not only Heinrich layer times, but in particular GS12 was indeed a severely cold period. Furthermore, a

rapid climate shift or a major geological phenomenon, probably linked to the Laschamp geomagnetic excursion, triggered extreme slumping activity in several maar lakes while the sediments were partially frozen. The harsh climatic conditions during GS12 accentuate the onset of the Laschamp geomagnetic event and mark the beginning of the transition from Neanderthals to modern humans as the dominant species in central Europe.

## **Introduction**

During the last glacial cycle, the northern hemisphere underwent a series of climate fluctuations, also known as Dansgaard-Oeschger (D/O) cycles (North Greenland Ice Core Project Members 2004; Svensson et al. 2008; Rasmussen et al. 2014). Cold and arid stadials were interposed with warm and humid interstadials. While steppe biomes were wide-spread throughout Europe during stadial periods, forests evolved during interstadials (Fletcher et al. 2010). Throughout early Marine Isotope Stage (MIS) 3 (60,000 – 49,000 yr b2k), a spruce-dominated forest with hornbeams and other thermophilous tree taxa was present in the Eifel region (Sirocko et al. 2016). This lush forest receded near the end of Greenland Interstadial (GI) 13 and open woodland expanded during subsequent Greenland Stadials (GS). The landscape further evolved at the end of GI8 (36,500 yr b2k) into a steppe with scattered birch and pine trees, into a tundra environment with abundant Ranunculaceae 28,500 yr b2k ago, and finally at 23,000 yr b2k into the polar desert of the LGM (Sirocko et al. 2016).

The climate and environmental deteriorations after GI13 are thought to be at least partly responsible for European Neanderthal depopulation and subsequent territorial expansion of anatomically modern humans (Conard et al. 2006; Conard and Bolus 2008; Nigst et al. 2014; Obrecht et al. 2017; Staubwasser et al. 2018). This cultural transition is known as the Middle-Upper Paleolithic transition and it is documented across Europe as a severe drop in population density (Morin 2008), as well as shifts in hunted species (Discamps et al. 2011) and distinct artefact assemblages at archaeological sites (Conard et al. 2006; Hoffecker 2009; Hublin 2015).

The stadial / interstadial succession was accompanied by repeated volcanic activity across the Eifel which caused the formation of numerous maar lakes in the region and the deposition of distinctive tephra layers in their sediments (e.g., Büchel 1994; Förster and Sirocko 2016; Förster et al. 2019). The ELSA (Eifel Laminated Sediment Archive) project at the University of Mainz has systematically drilled and studied more than 50 sediment cores from the open maar lakes and Pleistocene infilled maar structures of the West Eifel Volcanic Field (e.g., Sirocko et al. 2005, 2013, 2016; Seelos and Sirocko 2007; Fuhrmann et al. 2020). The near annual-resolution ELSA-20 climate proxy record shows striking structural similarities to the NGRIP  $\delta^{18}\text{O}$  ice core chronology (Rasmussen et al. 2014), showing a complete succession back to GI17 (Sirocko et al. 2021; see chapter 3.2). The ELSA-Flood-Stack (Brunck et al. 2016) reconstructs main flood phases in the Eifel of the past 60,000 years and the ELSA-Tephra-Stack (Förster and Sirocko 2016; Förster et al. 2019) contains the region’s volcanic history from the Laacher See volcanic eruption 13,000 years ago (Brauer et al. 1999; Reinig et al. 2021) back to 500,000 years.

## Methods

### Coring sites

This study includes sediment records from the Pleistocene maar basins of Auel Maar, Dehner Maar, Merscheider Maar, Oberwinkler Maar and Rother Maar (Fig. 3.16). Cores have been recovered using ‘Seilkern’ coring technology. A detailed overview for all coring sites is given in Table 3.1.

Maar lake	Diameter [m]	Core	Height above sea level [m]	Time span coverage [yr b2k]	Core depth [m]	UTM coordinates
Auel Maar	1293	AU2	452.90	10,000 – 59,130	123.0	32 N 328668.00 5572850.00
		AU3	452.40	10,000 – 59,120	102.0	32 N 328686.00 5572859.00
		AU4	451.50	10,000 – 59,130	104.5	32 N 328732.00 5572977.00
Dehner Maar	931	DE3	565.37	12,000 – 76,250	88.0	32 N 322384.42 5574206.47
Merscheider Maar	771	MS1	528.00	28,600 – 65,700	69.0	32 N 324823.03 5574125.16
Oberwinkler Maar	800	OW1	385.00	25,800 – 72,000	49.0	32 N 352719.74 5556393.10
Rother Maar	823	RM2	453.00	7700 – 66,400	65.0	32 N 330075.77 5570533.04

**Table 3.1 Overview of coring sites included in this study.**

The Auel infilled maar with a diameter of 1325 m is one of the larger maar structures of the Eifel (Seib et al. 2013; Brunck et al. 2016). Today, the Tieferbach, which has a catchment area of 12,187 km<sup>2</sup>, flows through its former centre from west to east. Cores AU2, AU3 and AU4 have respective lengths of 123 m, 102 m and 104.5 m (Supplementary Figs. 4 – 6). Of these, AU2 and AU4 reach well into the maar's eruption sequence. Due to its abundant fluvial input, the Auel cores have the highest average sedimentation rate (2 mm/year) of all ELSA cores and AU3 and AU4 were used for the near annual-resolution C<sub>org</sub>(chlorins) record presented by Sirocko et al. (2021; see chapter 3.2).

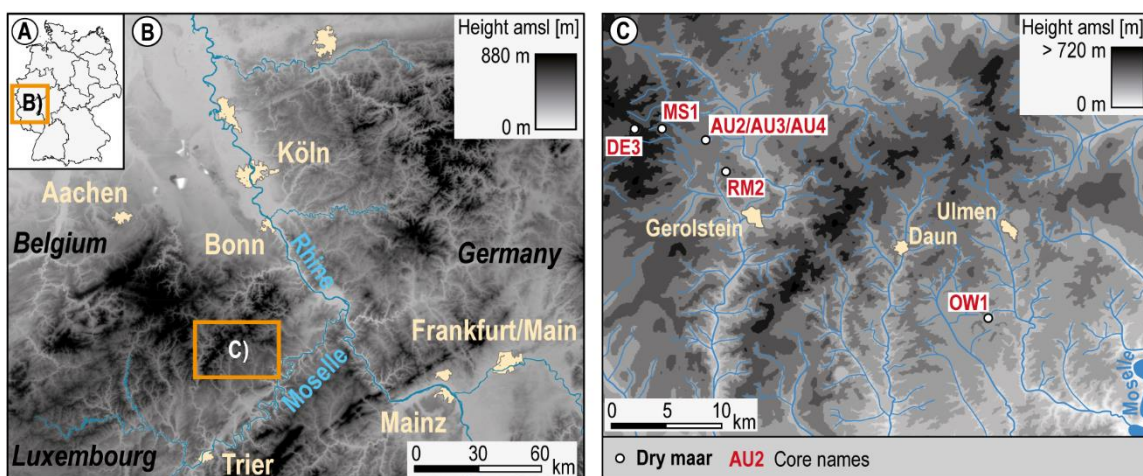


**Fig. 3.16 Location of coring sites.** a) Overview of Germany. Digital elevation maps of b) West Germany and c) the West Eifel Volcanic Field with drainage system and maar locations (after Büchel 1994).

The Dehner Maar with a diameter of 950 m and a near circular basin is still very recognizable in the landscape. Although there are no traces of a past inflow, there is an outflow to the west (Sirocko et al. 2013). Core DE3 is 88 m long and reaches the basis of the lake sediments (Supplementary Fig. 9). The sediment record shows annual layer preservations over large parts and is therefore varve counted from the Laacher See tephra layer (13,056 yr b2k; Reinig et al. 2021) back to 26,770 yr b2k, almost reaching GI3 (Sirocko et al. 2016).

The Merscheider Maar and the Rother Maar have diameters of 771 m and 823 m, respectively (Seib et al. 2013). Today, the Mannebacher creek (Merscheider Maar — catchment area of 1.78 km<sup>2</sup>) and the Rother creek (Rother Maar — catchment area of 2.33 km<sup>2</sup>) flow through the former maar basins. The

69 m (MS1) and 65 m (RM2) long sediment records, which were drilled near the maars' centres, both reach into their respective eruption sequence (Supplementary Figs. 12, 18).

Located approximately 25 km east of the other maars (Fig. 3.16), the Oberwinkler Maar has a diameter of around 800 m (Seib et al. 2013) and is embedded in a smooth valley with two small creeks flowing through its basin. Core OW1 has a length of 48 m (Supplementary Fig. 15) and although it does not reach the basis of the lake sediments, it extends into MIS 4 (Engels et al. 2008).

### **Establishing the ELSA-20 stratigraphy**

The ELSA-20 chronology (Sirocko et al. 2021; see chapter 3.2) consists of sediment records from Holocene maar lakes of Schalkenmehren (SMf) and Holzmaar (HM4) and the Pleistocene maar basin of Auel (AU3 and AU4; Fig. 3.17).

To decrease the number of gaps in the Auel record, AU3 and AU4 were cored with an offset of 0.5 m and drilling positions were only 5 m apart (Sirocko et al. 2021). A dynamic time warp algorithm was applied to the organic carbon (chlorins) data of both cores to determine structural similarities (Fig. 3.17a,b). Gaps in the AU4 data were then filled with available data points in the AU3 core's corresponding segments. In the resulting AUcomp record (Fig. 3.17c), events such as tephra layers, slumps and drilling artefacts were given zero time in the age/depth model. Slumps and drilling artefacts were determined visually on the sediment cores, while tephra layers were identified by their petrographic composition (Förster and Sirocko 2016). The result is the ELSA-20 climate proxy record (Fig. 3.17d), which was then age-tuned to the stadial / interstadial succession of the NGRIP ice cores (Fig. 3.17e; North Greenland Ice Core Project Members 2004; Svensson et al. 2008; Rasmussen et al. 2014) using a Bayesian age model.

### **Tephrochronology**

Most discrete tephra layers are characterised by distinct coarse-grained, greyish to black event deposits in contrast to the yellowish to brown finer-grained background sediments. The volcanic layer succession in the Eifel cores was sampled and processed by Förster and Sirocko (2016) and Förster et al. (2019). Six known tephra layers were identified based on their specific petrographic signature in the sediments

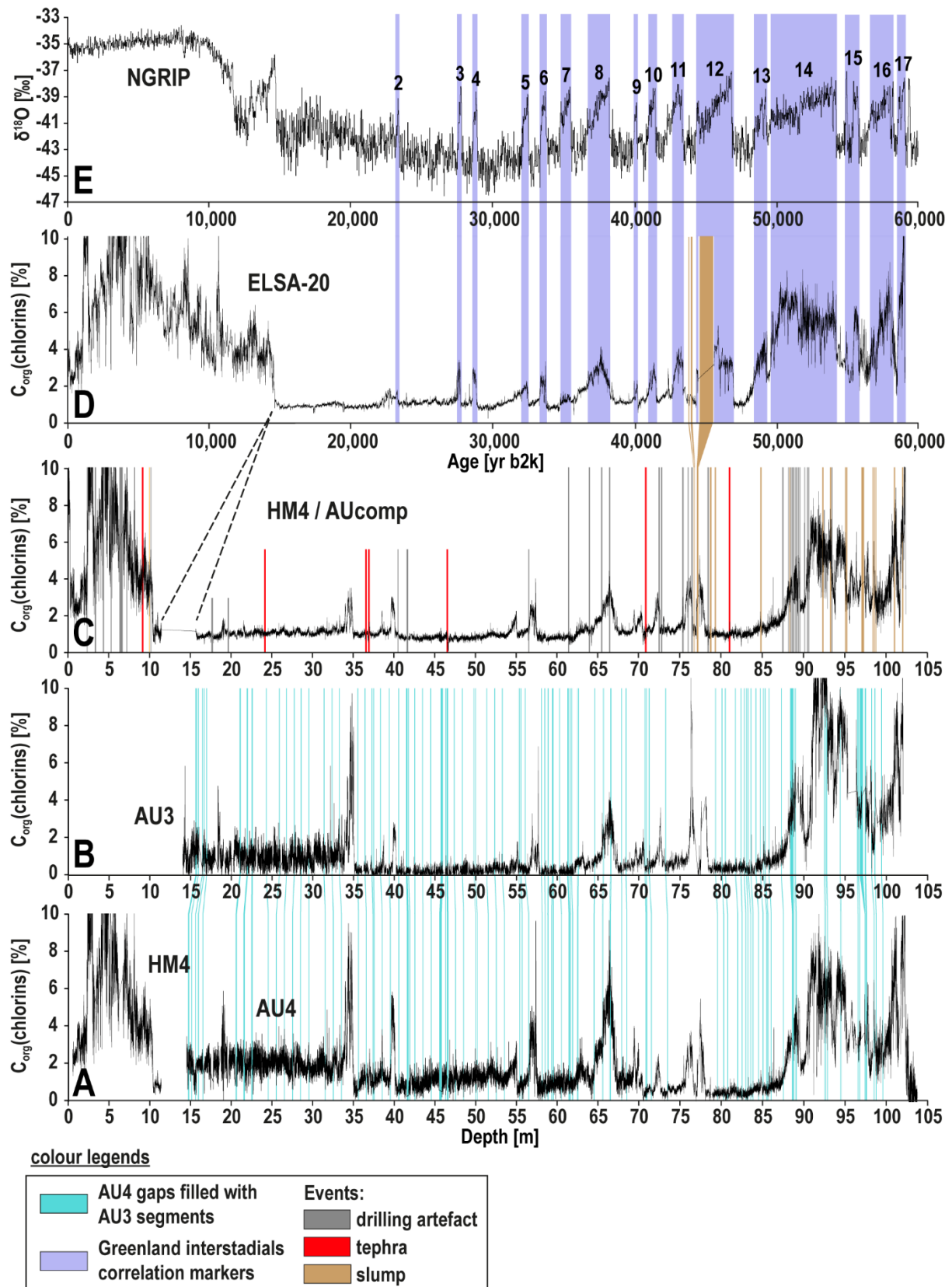


**Fig. 3.17 Establishing the ELSA-20 stratigraphy.**  $C_{org}(\text{chlorins})$  data of cores **a)** AU4 and HM4 and **b)** AU3. Gaps in AU4 data were filled with available data points in AU3 corresponding segments. **c)** In the resulting  $AU_{comp}$  dataset, events such as tephra layers, slumps and drilling artefacts were given a time period of formation equal to zero. **d)** The result is the ELSA-20 climate proxy record (Sirocko et al. 2021), which was then age-tuned to **e)** Greenland Interstadials (GI) 2 - 17 of the NGRIP ice cores (Rasmussen et al. 2014).



of the five presented sites (Table 3.2; Supplementary Fig. 2), i.e., the Laacher See Tephra (LST — 13,056 yr b2k; Reinig et al. 2021), the Eltville Tephra (EVT — 24,620 yr b2k), the Wartgesberg Tephra (WBT — 28,100 yr b2k), the Dreiser Weiher Tephra (DWT — 40,370 yr b2k), the Meerfelder Maar Tephra (MMT — 47,340 yr b2k), and the Aueler Maar Tephra (AUT — 59,130 yr b2k). Furthermore, one tephra of unknown origin (UT1 [Unknown Tephra 1] — 30,300 yr b2k) was found in the sediments. Accordingly, deposits of the Laacher See and Eltville eruptions were found in Aueler Maar and Dehner Maar. The WBT and the UT1 are visible in Aueler Maar, Dehner Maar and Rother Maar. The UT1 was additionally deposited in core MS1. The DWT was deposited in the Aueler Maar, Merscheider Maar and Rother Maar and the MMT was deposited in all presented cores. The AUT is clearly visible in all presented records, except core AU3, which does not reach down to the eruption sequence. Age of the EVT derives from varve counting done on core DE3 (Sirocko et al. 2016). Ages of all other marker tephra layers except LST are based on the ELSA-20 stratigraphy (Sirocko et al. 2021).

#### **Pollen and organic carbon (chlorins) data**

Pollen preparation was done according to the techniques of Berglund and Ralska-Jasiewiczowa (1986) and Faegri and Iversen (1989). Sediment samples of 1 cm<sup>3</sup> volume were treated with potassium hydroxide solution (KOH), hydrochloric acid (HCl) and hydrofluoric acid (HF). Acetic acid (C<sub>2</sub>H<sub>4</sub>O<sub>2</sub>) and a mixture (9:1) of acetic anhydride (C<sub>4</sub>H<sub>6</sub>O<sub>3</sub>) and sulphuric acid (H<sub>2</sub>SO<sub>4</sub>) was used for acetolysis. Samples were centrifugated at 3000 – 3500 rpm for 5 minutes and then sieved at 200 µm and filtered at 10 µm. To calibrate absolute pollen concentration per cm<sup>3</sup>, *Lycopodium*-spore tablets were added. Samples were mounted using liquid, anhydrous glycerol (C<sub>3</sub>H<sub>8</sub>O<sub>3</sub>). Pollen counting was performed using a six hundred-fold magnification and a minimum of 300 pollen grains were counted for each sample. Because pollen analysis was intended for correlating the sediment cores to the early MIS 3 warm phase forest (Sirocko et al. 2016), only *Picea* and *Carpinus* percentages are presented in the pollen diagram (Fig. 3.18; Sirocko et al. 2013, 2016, submitted). For complete pollen diagrams of cores versus depth,

see Supplementary Figs. 7, 10, 13, 16, 19. For complete pollen diagrams of cores versus age, see Supplementary Figs. 3, 8, 11, 14, 17, 20.

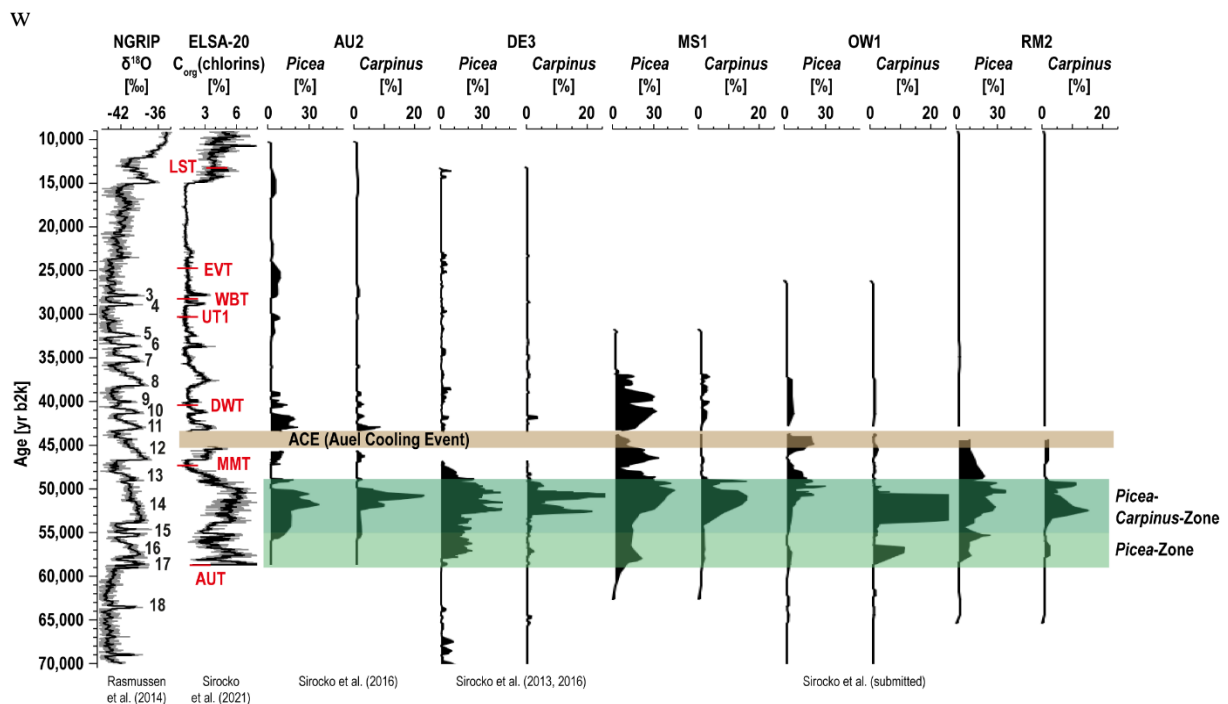


**Fig. 3.18** *Picea* and *Carpinus* pollen percentages versus age (Sirocko et al. 2013, 2016, submitted). Highlighted in green are the *Picea*-Zone and the *Picea-Carpinus*-Zone, which represent the early MIS 3 warm phase forest covering the Eifel. Highlighted in brown is the Auel Cooling Event (ACE), a massive slumping event in the maar records during GS12. Additionally shown are the interstadial succession (GI3 - 19) of NGRIP oxygen isotope time series (Rasmussen et al. 2014) and the ELSA-20  $C_{org}$ (chlorins) record (Sirocko et al. 2021). Ages of marker layers (red abbreviations) derive from ice core tuning of ELSA-20  $C_{org}$ (chlorins) record. Pollen data were smoothed using a three-point running mean. Pollen counts were performed by Frank Dreher.

Organic carbon (chlorins) content was determined with a Gretag Spectrolino. The measurement principle of this method is based on the sediment reflectance of each wavelength relative to a white colour standard over a 2.5-mm-wide area (Rein and Sirocko 2002; Butz et al 2015). A detailed introduction to this method is given by Sirocko et al. (2021; see chapter 3.2). Cores AU3, AU4, that make up the ELSA-20 record (Fig. 3.17), as well as DE3 were measured in 1-mm-wide increments. OW1 was measured in 2-mm-wide and cores MS1 and RM2 in 5-cm-wide increments. Organic carbon (chlorins) contents of all presented cores were age-tuned to the ELSA-20 chronology (Sirocko et al. 2021) and the stadial / interstadial succession back to GI18 (Table 3.2, Fig. 3.19) using identified marker tephra layers (Förster and Sirocko 2016; Förster et al. 2019) as anchor points.

## Flood and slump event layers

Sediment cores were visually examined to identify slumps and flood layers thicker than 0.7 cm. This method, established by Brunck et al. (2016), analyses the variance of the stadial / interstadial flood and slump frequency in central Europe and does not provide an absolute count of event layers (Fig. 3.20).

Regional discrepancies in frequency and temporal occurrence of slump and flood layers between the maars can be explained by differing geomorphologic settings and magnitudes of inflow, respectively. The Auel infilled maar basin for example has both the highest fluvial input and sedimentation rate (2 mm/a). This results in a greater sensitivity to floods in Auel and thus explains increased flood deposition and thicker flood layers.

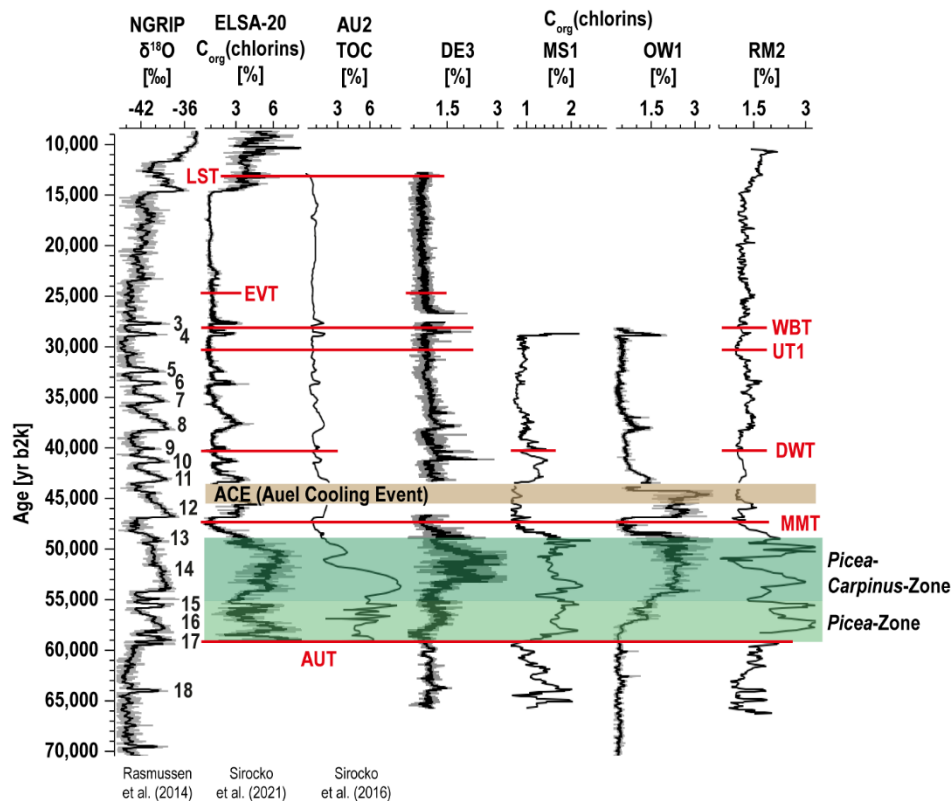


**Fig. 3.19**  $C_{org}$ (chlorins) records versus age. The *Picea*-Zone and the *Picea-Carpinus*-Zone are highlighted in green and red lines represent marker tephra layers in each sediment core. The Auel Cooling Event (ACE) is highlighted in brown. Also shown are Greenland Interstadials 3 – 19 of NGRIP oxygen isotope time series (Rasmussen et al. 2014), the ELSA-20  $C_{org}$ (chlorins) data (Sirocko et al. 2021) and the total organic carbon (TOC) record of core AU2 (Sirocko et al. 2016). AU2, MS1 and RM2 records were smoothed using a three-point running mean. DE3 and OW1 records were smoothed using a 30-point running mean and a 15-point running mean, respectively. For a detailed overview of stadial / interstadial succession and volcanic marker layers, see Table 3.2.

## Results

### Alignment of cores

As illustrated in Fig. 3.18, all cores show a long-lasting maximum of spruce (*Picea*) between GI17 and GI13. During GI14 and GI13, this *Picea*-Zone is further characterised by a prominent peak of hornbeam (*Picea-Carpinus*-Zone). These two phases represent the early MIS 3 warm phase forest covering the Eifel with abundant thermophilous tree pollen (Sirocko et al. 2016).

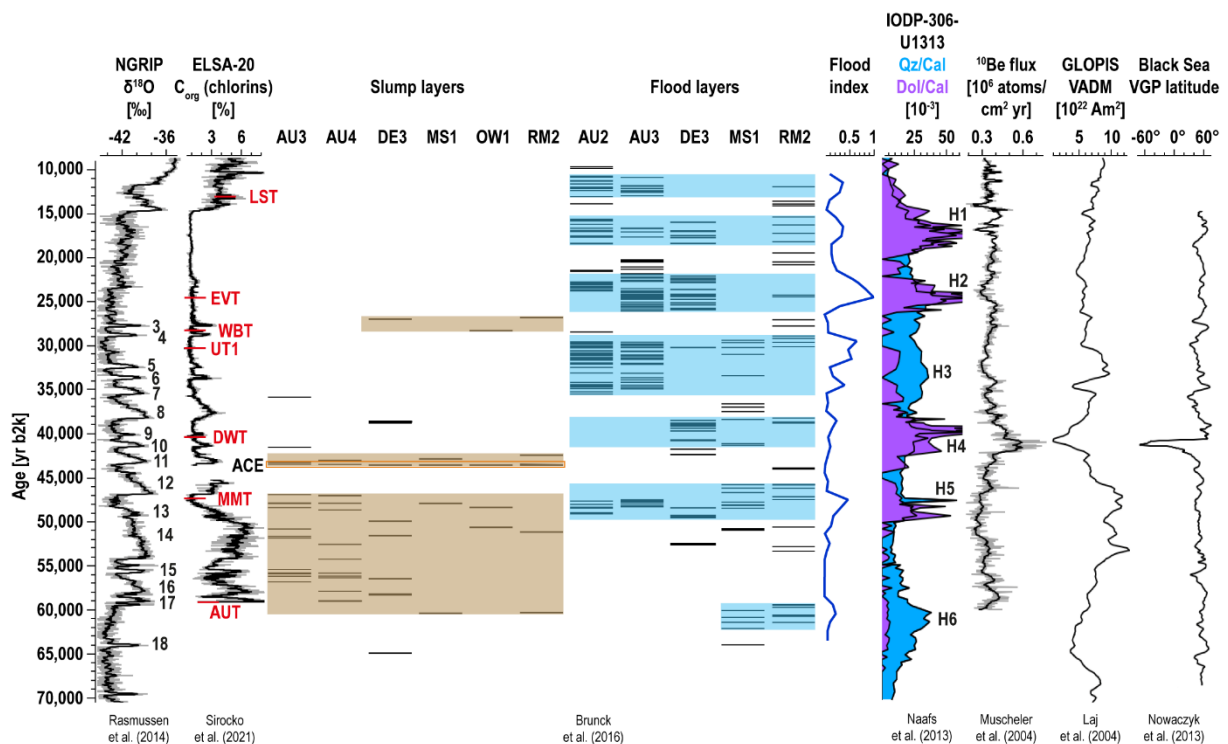


**Fig. 3.20 Phases of increased slumping and flood activity in sediment cores (highlighted in brown and light blue, respectively) and normalized flood index (blue line) with the ACE (Auel Cooling Event).** Additionally shown are Greenland Interstadials 3 - 18 of NGRIP oxygen isotope time series (Rasmussen et al. 2014), the ELSA-20  $C_{org}$ (chlorins) data (Sirocko et al. 2021) with marker tephra layers (red abbreviations), identified Heinrich Events (H1 – 6) in quartz / calcite (blue) and dolomite / calcite (purple) ratios from North Atlantic Site U1313 (Naafs et al. 2013), the composite  $^{10}\text{Be}$  flux record from GRIP and GISP2 ice cores (Muscheler et al. 2004), the GLOPIS-75 relative paleointensity stack (Laj et al. 2004) and virtual geomagnetic pole (VGP) latitudes from Black Sea sediments (Nowaczyk et al. 2013).

Although measured with different resolutions, the overall structures of the presented organic carbon (chlorins) records show clear similarities to the ELSA-20 (Sirocko et al. 2021) and NGRIP ice core chronologies (Fig. 3.19; North Greenland Ice Core Project Members 2004; Svensson et al. 2008;

Rasmussen et al. 2014). This allows direct matching of the records using marker tephra layers (Förster and Sirocko 2016; Förster et al. 2019) as anchor points. In particular, the early MIS 3 warm phase (GI17 – 13) is clearly visible in all cores as a distinct, long-lasting maximum in organic carbon (chlorins) production. Due to the maars' differing characteristics (geomorphologic setting, inflow rate), other interstadial periods are not as prominent as GI17 – 13 and intensities of interstadial signals vary between the cores (Fig. 3.19). However, using the volcanic marker deposits as control points, almost all interstadial periods could be identified in the organic carbon (chlorins) records (Table 3.2).

### **Flood and slump frequency**

Periods of increased slumping as well as flooding frequency could be identified in all sediment records (Fig. 3.20). Intervals of high and supra-local flood activity seem to align with Heinrich Events in marine sediment records (Naafs et al. 2013). Phases of increased slumping activity occurred during the early MIS 3 warm phase (60,000 – 47,000 yr b2k), at 43,500 yr b2k and subsequent to GI3. Slumps between 60,000 and 47,000 yr b2k and after GI3 are characterised by well-developed folding textures within the sediment ranging from several millimetres to tens of centimetres in thickness, quite contrary to the slumping event that occurred at 43,500 yr b2k.

### **Frost at 43,500 yr b2k (The Auel Cooling Event)**

The multi-proxy correlation reveals in all cores a massive slumping event during GS12 (Fig. 3.20). Due to its unique characteristics in the Auel maar sediments (Fig. 3.21a,b), we describe this as the Auel Cooling Event (ACE). At its type locality, the ACE led to the formation of a slump with a fractured, breccia-like sediment texture. Fragments of fine-grained, unconsolidated sediment packages with distinctive edges between individual “blocks” suggest that the sediment was solidified due to deep frost conditions at 43,500 yr b2k. Individual fragments are clearly distinguishable by colour and can reach diameters of several centimeters (Fig. 3.21b), whereby larger blocks accumulate at the slump's base and smaller ones towards its top. Extensive folding textures within visible laminations and rotation of individual blocks suggest that the transported material has lost much of its original structure. In the Auel cores, the ACE thickness varies between 0.32 m (AU4), 0.50 m (AU3) and 0.74 m (AU2; Supplementary Figs. 4 – 6).

LEZ	Time marker	Age [yr b2k]	AU2 [m]	AU3 [m]	AU4 [m]	DE3 [m]	MS1 [m]	OW1 [m]	RM2 [m]
LEZ 3 Boreal coniferous forest	LST top		13.80	13.59	14.40	3.40			
	LST base	<b>13,056</b>	13.95	13.69	14.50	3.48			
	Onset GI1	<b>14,692</b>	14.65	14.68	15.61	10.00			7.70
LEZ 4 Polar desert	End GI2	<b>23,220</b>		18.31	19.09				20.30
	Onset GI2	<b>23,340</b>		18.39	19.19	27.16			20.80
	EVT top			24.36	24.15	30.48			
	EVT base	<b>24,620</b>		24.44	24.16	30.57			
LEZ 5 Tundra	End GI3	<b>27,540</b>	34.15	34.45	34.25				28.15
	Onset GI3	<b>27,780</b>	34.75	35.04	34.95	36.73			28.55
	WBT top		36.66	36.80	36.83	37.80			28.80
	WBT base	<b>28,100</b>	36.90	37.02	36.89	37.92			28.92
	End GI4	<b>28,600</b>	39.55	39.82	39.63	39.88		9.19	29.10
	Onset GI4	<b>28,900</b>	39.95	40.17	40.10	40.18	3.30	9.49	29.90
	UT1 top		46.43	46.55	46.50	42.76	8.72		31.36
	UT1 base	<b>30,300</b>	46.59	46.68	46.59	42.91	8.80		31.41
LEZ 6 Steppe	End GI5.2	<b>32,040</b>	54.25	54.31	54.44	43.92	10.35	18.30	33.35
	Onset GI5.2	<b>32,500</b>	55.40	55.15	55.03	44.27	10.70	19.00	33.90
	End GI6	<b>33,360</b>	56.65	56.83	56.68	44.57	11.65	19.65	35.10
	Onset GI6	<b>33,740</b>	57.70	57.73	57.41		12.55	20.03	35.60
	End GI7	<b>34,740</b>	61.95	62.11	62.37			21.36	36.40
	Onset GI7c	<b>35,480</b>	63.15	63.32	63.84			22.22	36.85
LEZ 7 Open woodland	End GI8	<b>36,580</b>	65.35	65.43	65.47	46.26	14.50	23.87	37.90
	Onset GI8c	<b>38,220</b>	66.95	66.87	67.05	47.59	18.10	26.02	40.95
	End GI9	<b>39,900</b>	69.15	69.50	69.36	49.63	20.65		42.35
	Onset GI9	<b>40,160</b>	70.65	70.57	70.46	50.02	21.20		42.55
	DWT top		71.14	71.11	70.91		21.46		42.68
	DWT base	<b>40,370</b>	71.19	71.16	70.93		21.50		42.70
	End GI10	<b>40,800</b>	71.75	71.94	71.84		21.75		
	Onset GI10	<b>41,460</b>	73.15	72.77	72.60	51.01	22.50		
	End GI11	<b>42,240</b>	75.30	76.05	75.38		22.75	27.50	
	Onset GI11	<b>43,340</b>	77.15	76.42	76.46	53.54	23.55		43.60
	ACE top	<b>43,500</b>	77.20	76.60	76.62	53.60	24.08	28.00	43.61
	ACE base		77.94	77.10	76.94	56.97	24.33	29.00	44.00
	End GI12	<b>44,280</b>		77.49	77.07			30.02	
	Onset GI12c	<b>46,860</b>	78.35	78.20	77.87	56.99		30.80	46.40
MMT top		81.60	81.74	81.16	57.58	28.07	31.94	47.43	
MMT base	<b>47,340</b>	81.63	81.78	81.17	57.63	28.14	31.95	47.45	
End GI13	<b>48,340</b>		88.02	87.77	58.28	29.80	35.60	47.80	
LEZ 8 Spruce & hornbeam forest	Onset GI13c	<b>49,280</b>	88.30	89.92	89.61	59.72	32.55	36.18	48.45
	End GI14	<b>49,600</b>		90.87	90.50	60.07	33.20	36.33	49.10
	Onset GI14a	<b>51,500</b>		91.75	91.59	61.18			
	Onset GI14b	<b>51,660</b>		91.91	91.72	61.98			
	Onset GI14e	<b>54,220</b>	93.25	93.52	93.44	67.05	37.15	38.64	51.90
	End GI15.1	<b>54,900</b>		93.83	93.68				
	Onset GI15.1	<b>55,000</b>		93.85	93.70				
	End GI15.2	<b>55,400</b>	93.95	93.97	93.78	69.25		38.84	52.35
Onset GI15.2	<b>55,800</b>	95.10	96.31	95.13	69.56		38.95	52.80	
LEZ 9 Spruce forest	End GI16	<b>56,500</b>	97.75	100.42	99.70	70.32		39.06	53.15
	Onset GI16.1c	<b>58,040</b>		101.28	101.17		38.80		
	End GI16.2	<b>58,160</b>		101.37	101.19				
	Onset GI16.2	<b>58,280</b>	100.95	101.45	101.31	73.81			53.80
	End GI17	<b>58,560</b>	101.70	101.65	101.64				
	Onset GI17.2	<b>59,080</b>	102.15	101.96	102.31				
	AUT top		102.33		102.38	76.24	39.80	39.42	56.39
	AUT base	<b>59,130</b>				76.30	39.86	39.58	56.58
End GI18	<b>63,840</b>				78.35	46.35		62.40	
Onset GI18	<b>64,100</b>				78.43	46.65		62.80	

**Table 3.2 Stratigraphic tie-points of presented cores.** Core depths of tie-points to the NGRIP Greenland Interstadial (GI) succession (Rasmussen et al. 2014) are listed in cores' respective columns. Highlighted are identified marker tephra layers (red) and the Auel Cooling Event (ACE — grey), a massive slumping event during GS12. Additionally, Landscape Evolution zones (LEZ) 3 – 9 (Sirocko et al. 2016) and their characteristic landscapes are shown.

In core DE3, the ACE has a total thickness of 3.37 m (Fig. 3.21c). In the lower 3 m, it is characterised by well-developed, massive folds within the slumped sediment. Clearly visible fine laminations, even if in part extensively folded and tilted, indicate that the transported material has preserved most of its structural integrity. Overlying this folded segment is a breccia of unconsolidated, fine-grained sediments (Fig. 3.21d) as described in the Auel cores. However, in core DE3 fractured fragments only reach diameters of a few centimeters at the slump's base and several millimeters at its top.

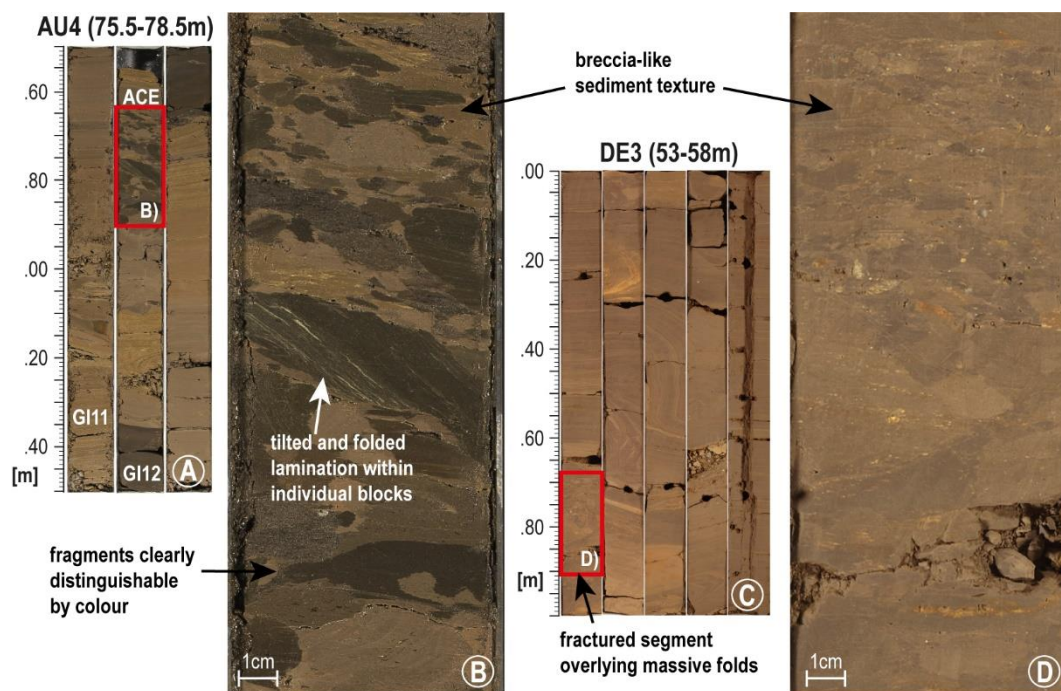


**Fig. 3.21 The Auel Cooling Event (ACE).** a) ACE sediment slump in core AU4. b) Enlarged segment showing a distinct breccia-like sediment texture within the slump with individual fragments clearly distinguishable. c) ACE sediment slump in core DE3 and d) enlarged segment of its breccia-like texture.

Due to a lack of lamination, the ACE is hardly visible in cores MS1 and RM2 (Supplementary Figs. 12, 18). Instead, the slumped segment is characterised by stained or spotted, clayey to silty sediments. However, a sediment texture similar to the Auel cores and DE3, even though faintly developed, is present in core RM2. ACE thickness is 0.25 m and 0.39 m in cores MS1 and RM2, respectively. In core OW1, a massive fold across an entire core meter (28 – 29 m; Supplementary Fig. 15) representing the ACE shows that the transported sediment has maintained its structural integrity on a large scale.

## Discussion

Phases of increased and supra-local flood activity in the Eifel region match Heinrich Events in marine sediment records (Fig. 3.20; Naafs et al. 2013). Variations in flood dynamics are climatically driven, either directly or indirectly via vegetation and/or permafrost. Shifts in flood frequency represent climate responses within the catchment area and elevated flood activity mainly reflects climate transitions into colder periods when a decline in vegetation cover decreases soil stability and therefore elevates the erosion potential (Vandenberghe 2003; Brunck et al. 2016). Heinrich events are generally associated with increased aeolian dust flux (Fuhrmann et al. 2020) and extensive glacial advances into the North Atlantic (e.g., Broecker et al. 1992; Hemming 2004). Accumulating flood layers during Heinrich events suggest a vegetation response within the catchment area to emerging cold climate conditions.

A prominent slump layer during GS12 (ACE), which is not associated with Heinrich Event times, stands out in the presented maar records. Slumped segments with distinctive fine-grained sediment fragments and a breccia-like texture in the Auel sediment records and other maars (Fig. 3.21) indicate that the sediment must have been frozen during time of the slumping event. This suggests that the region was exposed to deep frost at around 43,500 yr b2k and rapid thawing then caused solifluction of the lake sediments. Other authors indeed portray this stadial as a severe cooling step across Europe with deep frost or permafrost conditions (e.g., Antoine et al. 2016; Staubwasser et al. 2018). A loess-paleosol sequence at the archaeological site Willendorf II (Austria) features a well-developed frost layer, confined by two palaeosols representing GI11 and 12, respectively (Nigst et al. 2014). Further evidence can be found in a loess-palaeosol record in Northern France, where a distinct permafrost horizon was dated to 43 – 44 ka calBP (Antoine et al. 2016). Vandenberghe and van der Plicht (2016) propose that the Hasselo stadial, which is represented by ice-wedge cast horizons in silty sediment deposits at its type localities in Eastern (Van Huissteden 1990) and Northern Netherlands (Kasse et al. 1995) and was dated to 43,220 – 42,290 calBP, likely corresponds to GS12. In the East and South Carpathians, a hiatus and a very prominent  $\delta^{13}\text{C}$  maximum (dated to 43.3 – 44 ka<sub>U-Th</sub>) in two speleothem stable isotope records, respectively, indicate that a rapid shift towards cold and arid stadial conditions occurred within a few decades in Eastern Europe, at least in higher altitudes (Staubwasser et al. 2018).



The fact that such an extreme slumping event occurred at a time when deep frost prevailed in the region, indicates that either a rapid, unstable climate shift that differs significantly from other D/O cycles or some other major geological phenomenon occurred during GS12. If we look at potential triggers that took place around that time, one good candidate is the onset of the Laschamp geomagnetic excursion, during which the Earth's magnetic field strength was significantly reduced and reversed (Fig. 3.20; e.g., Laj et al. 2004; Nowaczyk et al. 2013). This caused a considerable enhanced flux of high-energy protons from the sun into the atmosphere (Muscheler et al. 2004), affecting ozone levels globally (Cooper et al. 2021). UV-B radiation levels in Europe increased 10 – 20% due to significant ozone depletion down to latitudes of 40 – 45° (Vogt et al. 2007; Winkler et al. 2008). Although the reversed polarity phase occurred between 40 – 41 ka (e.g., Singer et al. 2009; Channell et al. 2012), an initial short-termed, yet distinctive increase can be observed in the <sup>10</sup>Be flux record during GS12 (Muscheler et al. 2004). Albeit direct impacts of geomagnetic excursions and reversals and their underlying mechanisms are still debated in the literature, a connection to geological and ecological phenomena such as increased volcanism, major global climate shifts, long-term sea level changes and species extinctions have been proposed (e.g., Raup 1985; Böhnelt et al. 1987; Marzocchi et al. 1992; Meert et al. 2016; Pavlov et al. 2019; Herndon 2020, 2021). Cooper et al. (2021) suggest that the weakening of the geomagnetic field directly preceding the reversed state of the Laschamp event promoted major climate changes, extinction events and shifts in the archaeological record on a global scale.

The climate deteriorations during the GS12 permafrost period and Heinrich Event 4 likely forced European populations to track their preferred habitats or change their subsistence strategies in order to survive (Rendu et al. 2019). The environmental impacts caused by the Laschamp excursion and the Campanian Ignimbrite eruption, a massive volcanic eruption in South Italy approximately 40,000 years ago (Giaccio et al. 2017; Wulf et al. 2018), could have then taken further toll on stricken regional populations (Fig. 3.22; Norval et al. 2007; Fedele et al. 2008; Valet and Valladas 2010; Fitzsimmons et al. 2013). Several archaeological sites in the upper and middle Danube Valley propose a widespread Neanderthal depopulation across Europe during this time period and a subsequent repopulation by anatomically modern humans (e.g., Conard and Bolus 2003; Higham et al. 2012). During these major ecological challenges modern humans probably had the advantage of innovative technologies and

improved sociality over the Neanderthals, which might have helped them to better adapt to their changing environment (Conard et al. 2006; Staubwasser et al. 2018). The latest directly dated Neanderthal remains of central Europe range from 40.66 – 41.95 ka calBP (Semal et al. 2009; Hublin et al. 2012), which coincides exactly with the age of the Laschamp geomagnetic event.

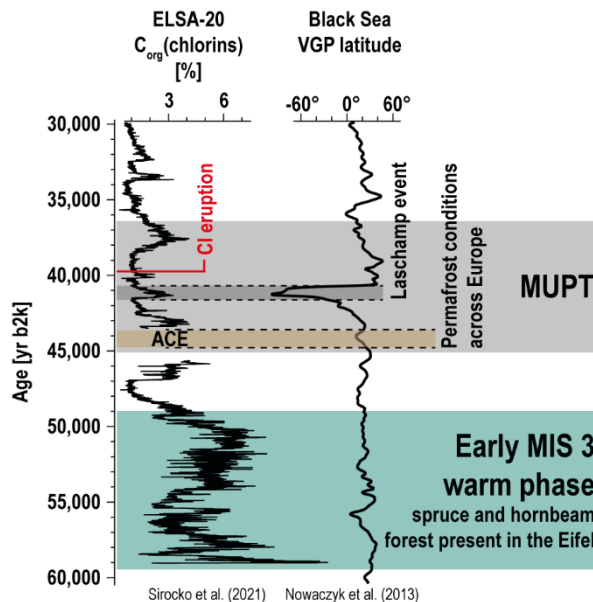


**Fig. 3.22 The Middle-Upper Paleolithic transition (MUPT).** Severely cold and arid climate conditions during Greenland Stadial 12 (Nigst et al. 2014; Staubwasser et al. 2018), as well as the environmental impacts of the Laschamp geomagnetic event (Norval et al. 2007; Valet and Valladas 2010) and the Campanian Ignimbrite volcanic eruption (Fedele et al. 2008; Fitzsimmons et al. 2013) affected the transition from Neanderthals to modern humans as the dominant species in Europe.

## Conclusion

During the early MIS3 warm phase a thermophilous spruce and hornbeam forest dominated the Eifel region (Fig. 3.18; Sirocko et al. 2016). Subsequently, Europe’s climate shifted towards colder and more arid conditions (e.g., Fuhrmann et al. 2020). Increasingly cold and arid climate and decline in vegetation during Heinrich events resulted in frequent flood deposition in the Eifel maars. The climate deteriorations culminated in the formation of deep frost and permafrost across Continental Europe during GS12 (Figs. 3.21 – 3.22; e.g., Vandenberghe and van der Plicht 2016; Staubwasser et al. 2018). However, the onset of the Laschamp geomagnetic excursion, which affected ecosystems worldwide (Cooper et al. 2021), yielded massive slumping activity in several Eifel maar lakes while the sediments were frozen.

The transition interval from Neanderthals to anatomically modern humans as the dominant species in Europe (Middle-Upper Pleistocene transition) was strongly influenced by the severe cold during GS12 (Nigst et al. 2014; Staubwasser et al. 2018), as well as the environmental impacts of the Laschamp and Campanian Ignimbrite events (Fig. 3.22; Norval et al. 2007; Fedele et al. 2008; Valet and Valladas 2010; Fitzsimmons et al. 2013). These hostile conditions must have presented major challenges for European populations and are quite likely responsible for the demise of the Neanderthals and the subsequent domination of the anatomically modern humans.

## 4 Conclusion

The last glacial cycle had an enormous impact on the environment of the central European continent. With increasingly cold climate conditions, the forests in the Eifel gradually retreated. Although the vegetation was able to recover to some extent during warmer and more humid interstadial periods, dry and cold environments eventually prevailed and the vegetation cover progressively declined. Interstadials were characterised by distinct multidecadal climate oscillations with a periodicity of around 20 to 150 years. However, a weakening of the AMOC and an expansion of North Atlantic sea ice cover during stadial periods caused these climate signals to remain essentially muted. The decline in vegetation cover resulted in soil stability to decrease, which led to an increase in flooding activity in the catchments of the maar lakes during particularly cold Heinrich layer times.

The increasingly deteriorating climate conditions resulted in the formation of permafrost and deep frost across Continental Europe during GS12. However, a rapid climate shift or a major geological event around 43,500 yr b2k ago caused massive, supra-local slumping activity in several Eifel maar lakes while the sediments were partially frozen. One potential trigger for this Auel Cooling Event (ACE — named after its type locality of Auel) is the onset of the Laschamp geomagnetic excursion, when Earth's magnetic field strength began to significantly decline.

During the LGM extensive glaciers repeatedly advanced into central Europe from Scandinavia, which is known as the Weichselian glaciation. The Weichselian ice sheets eroded considerable amounts of Scandinavian bedrock material and redeposited it in Northern Germany as alternating sequences of glacial till and glaciofluvial sands. These granitic and porphyritic sediment deposits are characterised by high uranium levels due to its large proportion of potassium-bearing minerals, which consequently causes increased radon concentrations in the glacial sediments of Northern Germany, as radon is a progeny isotope of uranium. Because of its relatively long half-life of 3.82 days, radon can migrate considerable distances in permeable strata or along structural pathways, if transported by a carrier such as CH<sub>4</sub> or CO<sub>2</sub>. This can lead to the formation of Local Radon Flux Maxima (LRFM), i.e., areas of significantly increased levels of radon release from the soil into the atmosphere. Mineralogical LRFM

occur above accumulations of radionuclide-rich sediment deposits. Sedimentary LRFM are caused by diverted migration paths of radon gas due to clay-rich, impermeable soil layers. However, highest levels of radon exhalation occur above active, deep-reaching tectonic or halokinetic faults (Structural LRFM). This can lead to a serious risk to human health in inhabited areas, because radon can easily enter the human body through the lungs, where it potentially causes lung cancer due to its radioactive nature.

The flux of radon from the soil into the atmosphere is not constant, but shows considerable temporal fluctuations. Distinct daily outgassing patterns vary greatly depending on the prevailing season with air pressure and temperature acting as the main driving forces. Four different exhalation modes could be identified in our specific monitoring setup:

- No periodic gas flux pattern during periods of minimal temperature gradients between soil and atmosphere (winter months) with air pressure variations as the sole driving force (exhalation mode I),
- Maximum radon outgassing during spring nights when the air temperature drops below the groundwater temperature (exhalation mode II),
- Maximum radon release from the soil during sunny summer afternoons when the sun stops heating the ground and the soil temperature is warmer than the surrounding air (exhalation mode III),
- Primary radon flux maxima with a periodicity of around three days following atmospheric pressure variations with secondary radon flux maxima during each afternoon and night (exhalation mode IV). This represents an interplay between modes II and III during the transition period from summer to autumn.

## **5 Acknowledgements**

## 6 References

- Abramowitz M, Stegun IA (1965) Handbook of Mathematical Functions: with Formulas, Graphs and Mathematical Tables. Dover Publications, New York.
- Al Hseinat M, Hübscher C, Lang J, Lüdmann T, Ott I, Polom U (2016) Triassic to recent tectonic evolution of a crestal collapse graben above a salt-cored anticline in the Glückstadt Graben/North German Basin. *Tectonophysics* 680:50–66. doi: 10.1016/j.tecto.2016.05.008.
- Al Hseinat M, Hübscher C (2017) Late Cretaceous to recent tectonic evolution of the North German Basin and the transition zone to the Baltic Shield/southwest Baltic Sea. *Tectonophysics* 708:28–55. doi: 10.1016/j.tecto.2017.04.021.
- Al-Zoughool M, Krewski D (2009) Health effects of radon: a review of the literature. *Int J Radiat Biol* 85(1):57–69. doi: 10.1080/09553000802635054.
- Ampel L, Wohlfarth B, Risberg J, Veres D (2008) Paleolimnological response to millennial and centennial scale climate variability during MIS 3 and 2 as suggested by the diatom record in Les Echets. *Quat Sci Rev* 27(15–16):1493–1504. doi: 10.1016/j.quascirev.2008.04.014.
- Andersen KK, Svensson A, Johnsen SJ, Rasmussen SO, Bigler M, Röthlisberger R, et al. (2006) The Greenland Ice Core Chronology 2005, 15–42 ka. Part 1: constructing the time scale. *Quat Sci Rev* 25(23–24):3246–3257. doi: 10.1016/j.quascirev.2006.08.002.
- Antoine P, Coutard S, Guerin G, Deschodt L, Goval E, Lochet J-L, Paris C (2016) Upper Pleistocene loess-paleosol records from Northern France in the European context: Environmental background and dating of the Middle Palaeolithic. *Quat Int* 411(Part A):4–24. doi: 10.1016/j.quaint.2015.11.036.
- AON (Application-Oriented Networking) (2016) Annual global climate and catastrophe report. Aon Benfield, London. <https://fundacionaon.es/wp-content/uploads/2020/07/20170117-ab-if-annual-climate-catastrophe-report.pdf>. Accessed 27 October 2022.
- Appleton JD (2007) Radon: Sources, health risks, and hazard mapping. *Ambio* 36(1):85–89. doi: 10.1579/0044-7447(2007)36[85:rshrah]2.0.co;2.

Atkinson TC, Lawson TJ, Smart PL, Harmon RS, Hess JW (1986) New data on speleothem deposition and palaeoclimate in Britain over the last forty thousand years. *J Quat Sci* 1(1):67–72. doi: 10.1002/jqs.3390010108.

Attallah MF, Awwad NS, Aly HF (2012) Environmental radioactivity of TENORM waste produced from petroleum industry in Egypt: review on characterization and treatment. In: Gupta S (ed) *Natural Gas: Extraction to End Use*. In Tech, Croatia, pp. 75–98. doi: 10.5772/CHAPTERDOI.

Baker VR, Webb RH, House PK (2002) The scientific and societal value of paleoflood hydrology. In: House PK, Webb RH, Baker VR, Levish DR (eds), *Ancient Floods, Modern Hazards: Principles and Applications of Paleoflood Hydrology*, Water Science and Application Series, vol. 5, American Geophysical Union, Washington, DC, pp. 127–146. doi: 10.1029/WS005p0001.

Ballesteros-Cánovas JA, Stoffel M, St George S, Hirschboek K (2015) A review of flood records from tree rings. *Prog Phys Geogr* 39(6):794–816. doi: 10.1177/0309133315608758.

Bayer U, Scheck M, Rabbel W, Krawczyk C M, Götze H-J, Stiller M, Beilecke T, Marotta A-M, Barrio-Alvers L, Kuder J (1999) An integrated study of the NE German Basin. *Tectonophys* 314(1–3):285–307. doi: 10.1016/S0040-1951(99)00249-8.

Beck TR (2017) Risks and radiation doses due to residential radon in Germany. *Radiat Prot Dosimetry* 2017, 175(4):466–472. doi: 10.1093/rpd/ncw374.

Bell B (1970) The oldest records of the Nile floods. *Geogr J* 136(4):569–573. doi: 10.2307/1796184.

Berglund BE, Ralska-Jasiewiczowa M (1986) Pollen analysis and pollen diagrams. In: Berglund BE (ed) *Handbook of Holocene Palaeoecology and Palaeohydrology*. John Wiley and Sons, New York, pp. 455–484.

Beyer W (1964) Zur Bestimmung der Wasserdurchlässigkeit von Kiesen und Sanden aus der Kornverteilungskurve. *Wasserwirtsch Wassertech* 14:165–169.

Birke M, Rauch U, Lorenz H (2009) Uranium in stream and mineral water of the Federal Republic of Germany. *Environ Geochem Health* 31:693–703. doi: 10.1007/s10653-009-9247-4.



- Bjorkholm P, Golub L, Gorenstein P (1973) Detection of a nonuniform distribution of polonium-210 on the Moon with the Apollo 16 Alpha Particle Spectrometer. *Sci* 180(4089):957–959. doi: 10.1126/science.180.4089.957.
- Binkley GE (1938) Results of Raiation Therapy in Primary Operable Rectal and Anal Cancer. *Radiology* 31(6):724–728. doi: 10.1148/31.6.724.
- Böhm E, Lippold J, Gutjahr M, Frank M, Blaser P, Antz B, et al. (2015) Strong and deep Atlantic meridional overturning circulation during the last glacial cycle. *Nat* 517:73–76. <https://doi.org/10.1038/nature14059>.
- Böhm H, Reismann N, Jäger G, Haverkamp U, Negendank JFW, Schmincke H-U (1987) Paleomagnetic investigation of the Quaternary West Eifel volcanics (Germany): indication for increased volcanic activity during geomagnetic excursion/event? *J Geophys* 62(1):50–61.
- Böse M, Lüthgens C, Lee J R, Rose J (2012) Quaternary glaciations of northern Europe. *Quat Sci Rev* 44:1–25. doi: 10.1016/j.quascirev.2012.04.017.
- Bossew P, Lettner H (2007) Investigations on indoor radon in Austria, Part 1: Seasonality of indoor radon concentration. *J Environ Radioact* 98(3):329–345. doi: 10.1016/j.jenvrad.2007.06.006.
- Brauer A, Endres C, Negendank JFW (1999) Lateglacial calendar year chronology based on annually laminated sediments from Lake Meerfelder Maar, Germany. *Quat Int* 61(1):17–25. doi: 10.1016/S1040-6182(99)00014-2.
- Brauer A, Litt T, Negendank JFW, Zolitschka B (2001) Lateglacial varve chronology and biostratigraphy of lakes Holzmaar and Meerfelder Maar, Germany. *Boreas* 30:83–88. doi: 10.1111/j.1502-3885.2001.tb00991.x.
- Brauer A, Allen JRM, Mingram J, Huntley B (2007) Evidence for the last interglacial chronology and environment change from Southern Europe. *Earth Atmos Planet Sci* 104(2):450–455. doi: 10.1073/pnas.0603321104.

Breitner D, Arvela H, Hellmuth KH, Renvall T (2010) Effect of moisture content on emanation at different grain size fractions – A pilot study on granitic esker sand sample. *J Environ Radioact* 101(11):1002–1006. doi: 10.1016/j.jenvrad.2010.07.008.

Broecker W, Bond G, Klas M, Clark E, McManus J (1992) Origin of the northern Atlantic's Heinrich events. *Clim Dyn* 6:265–273. doi: 10.1007/BF00193540.

Bronk Ramsey C, Staff RA, Bryant CL, Brock F, Kitagawa H, Van der Plicht J, et al. (2012) A complete terrestrial radiocarbon record for 11.2 to 52.8 kyr B.P. *Sci* 338(6105):370–374. doi: 10.1126/science.1226660.

Bruce M (1993) William Duane and the radium cow: An American contribution to an emerging atomic age. *Med Phys* 20(6):1601–1605. doi: 10.1118/1.596947.

Brüchmann C, Negendank JFW (2004) Indication of climatically induced natural eutrophication during the early Holocene period, based on annually laminated sediment from Lake Holzmaar, Germany. *Quat Int* 123–125:117–134. doi: 10.1016/j.quaint.2004.02.013.

Brunck H, Sirocko F, Albert J (2016) The ELSA-Flood-Stack: A reconstruction from the laminated sediments of Eifel maar structures during the last 60 000 years. *Glob Planet Change* 142:136–146. doi: 10.1016/j.gloplacha.2015.12.003.

Büchel G (1994) *Vulkanologische Karte der West- und Hocheifel*. Landesvermessungsamt Rheinland-Pfalz, Koblenz.

Bundesamt für Strahlenschutz (2019) *Radon-Handbuch Deutschland*. <https://www.bfs.de/SharedDocs/Downloads/BfS/DE/broschueren/ion/radon-handbuch.pdf>. Accessed 27 October 2022.

Bundesamt für Strahlenschutz (2020) *Karte Radon-Potential*. <https://www.bfs.de/DE/themen/ion/umwelt/radon/karten/boden>. Accessed 27 October 2022.

- Butz C, Grosjean M, Fischer D, Wunderle S, Tylmann W, Rein B (2015) Hyperspectral imaging spectroscopy: a promising method for the biogeochemical analysis of lake sediments. *J Appl Remote Sens* 9(1):096031. doi: 10.1117/1.JRS.9.096031.
- Caesar L, Rahmstorf S, Robinson A, Feulner G, Saba V (2018) Observed fingerprint of a weakening Atlantic Ocean overturning circulation. *Nat* 556:191–196. doi: 10.1038/s41586-018-0006-5.
- Cannariato KG, Kennet JP, Behl RJ (1999) Biotic response to late Quaternary rapid climate switches in Santa Barbara basin: ecology and evolutionary implications. *Geol* 27(1):63–66. doi: 10.1130/0091-7613(1999)027<0063:BRTLQR>2.3.CO;2.
- Chambers SD, Podstawczyńska A, Pawlak W, Fortuniak K, Williams AG, Griffiths AD (2019) Characterising the state of the urban surface layer using Radon-222. *J Geophys Res Atmos* 124:770–788. doi: 10.1029/2018JD029507.
- Channell JET, Hodell DA, Curtis JA (2012) ODP Site 1063 (Bermuda Rise) revisited: oxygen isotopes, excursions, and paleointensity in the Brunhes chron. *Geochem Geophys Geosyst* 13:Q02001. doi: 10.1029/2011GC003897.
- Chen Z, Li Y, Liu Z, Wang J, Zhou X, Du J (2018) Radon emission from soil gases in the active fault zones in the Capital of China and its environmental effects. *Sci Rep* 8:1–12. doi: 10.1038/s41598-018-35262-1.
- Cheng H, Lawrence Edwards R, Sinha A, Spötl C, Yi L, Chen S, et al. (2016) The Asian monsoon over the past 640,000 years and ice age terminations. *Nat* 534:640–646. doi: 10.1038/nature18591.
- Chmeleff J, von Blanckenburg F, Kossert K, Jakob D (2010) Determination of the  $^{10}\text{Be}$  half-life by multicollector ICP-MS and liquid scintillation counting. *Nucl Instrum Methods Phys Res B* 268(2):192–199. doi: 10.1016/j.nimb.2009.09.012.
- Christiansen HH, Gilbert GL, Neumann U, Demidov N, Guglielmin M, Isaksen K, et al. (2021) Ground ice content, drilling methods and equipment and permafrost dynamics in Svalbard 2016-2019 (PermaSval). doi: 10.5281/zenodo.4294095.

- Christl M, Vockenhuber C, Kubik PW, Wacker L, Lachner J, Alfimov V, et al. (2013) The ETH Zurich AMS facilities: performance parameters and reference materials. *Nucl Instrum Methods Phys Res B* 294:29–38. doi: 10.1016/j.nimb.2012.03.004.
- Chyi LL, Quick TJ, Yang TF, Chen CH (2010) The experimental investigation of soil gas radon migration mechanisms and its implication in earthquake forecast. *Geofluids* 10(4):556–563. doi: 10.1111/j.1468-8123.2010.00308.x.
- Clement CH, Tirmarche M, Harrison JD, Laurier D, Paquet F, Blanchardon E, et al. (2010) Lung cancer risk from radon and progeny and statement on radon. *Ann ICRP* 40(1):1–64. doi: 10.1016/j.icrp.2011.08.011.
- Collier CG, Strong JC, Humphreys JA, Timpson N, Baker ST, Eldred T, et al. (2005) Carcinogenicity of radon/radon decay product inhalation in rats – effect of dose, dose rate and unattached fraction. *Int J Radiat Bio* 81(9):631–647. doi: 10.1080/09553000500368404.
- Conard NJ, Bolus M (2003) Radiocarbon dating the appearance of modern humans and timing of cultural innovations in Europe: new results and new challenges. *J Hum Evol* 44(3):331–371. doi: 10.1016/S0047-2484(02)00202-6.
- Conard NJ, Bolus M, Goldberg P, Münzel S (2006) The last Neanderthals and first modern humans in the Swabian Jura. In: Conard NJ (ed). *When Neanderthals and Modern Human Met*. Kerns Verlag, Tübingen, pp. 305–342.
- Conard NJ, Bolus M (2008) Radiocarbon dating in the late Middle Paleolithic and the Aurignacian of the Swabian Jura. *J Hum Evol* 55(5):886–897. doi: 10.1016/j.jhevol.2008.08.006.
- Cooper A, Turney CSM, Palmer J, Hogg A, McGlone M, Wilmhurst J, et al. (2021) A global environmental crisis 42,000 years ago. *Sci* 371(6531):811–818. doi: 10.1126/science.abb8677.
- Correa-Metrio A, Bush MB, Hodell DA, Brenner M, Escobar J, Guilderson T (2011) The influence of abrupt climate change on the ice-age vegetation of the Central American lowlands. *J Biogeogr* 39(3):497–509. doi: 10.1111/j.1365-2699.2011.02618.x.

Croudace IW, Rindby A, Rothwell RG (2006) ITRAX: description and evaluation of a new multi-function X-ray core scanner. In: Rothwell RG (ed), *New Techniques in Sediment Core Analysis*. Geological Society of London Special Publications 267, pp. 51–63. doi: 10.1144/GSL.SP.2006.267.01.04.

Das B, Vinebrooke RD, Sanchez-Azofeifa A, Rivard B, Wolfe AP (2005) Inferring sedimentary chlorophyll concentrations with reflectance spectroscopy: a novel approach to reconstructing historical changes in the trophic status of mountain lakes. *Can J Fish Aquat Sci* 62(5):1067–1078. doi: 10.1139/f05-016.

Dean WE (1974) Determination of carbonate and organic matter in calcareous sediments and sedimentary rocks by loss on ignition; comparison with other methods. *J Sediment Petrol* 44(1):242–248. doi: 10.1306/74D729D2-2B21-11D7-8648000102C1865D.

Denniston RF, Lutscher M (2017) Speleothems as high-resolution paleoflood archives. *Quat Eci Rev* 170:1–13. doi: 10.1016/j.quascirev.2017.05.006.

Deplazes G, Lückge A, Peterson LC, Timmermann A, Hamann Y, Hughen KA, et al. (2013) Links between tropical rainfall and North Atlantic climate during the last glacial period. *Nat Geosci* 6:213–217. doi: 10.1038/ngeo1712.

Discamps E, Jaubert J, Bachellerie F (2011) Human choices and environmental constraints: deciphering the variability of large game procurement from Mousterian to Aurignacian times (MIS 5–3) in southwestern France. *Quat Sci Rev* 30(19–20):2755–2775. doi: 10.1016/j.quascirev.2011.06.009.

Dong B, Sutton RT, Scaife AA (2006) Multidecadal modulation of El Niño–Southern Oscillation (ENSO) variance by Atlantic Ocean sea surface temperatures. *Geophys Res Lett* 33(8):L08705. doi: 10.1029/2006GL025766.

Dubois G, Bossew P, Tollefsen T, De Cort M (2010) First steps towards a European atlas of natural datiation: status of the European indoor radon map. *J Environ Radioact* 101(10):786–798. doi: 10.1016/j.jenvrad.2010.03.007.

Ehlers J, Eißmann L, Lippstreu L, Stephan H-J, Wansa S (2004) Pleistocene glaciations of North Germany. In: Ehlers J, Gibbard P L (eds) *Quaternary Glaciations—Extent and Chronology, Part I: Europe*, 1st edn. Elsevier, Amsterdam, pp. 135–146.

Ehlers J, Grube A, Stephan H-J, Wansa S (2011) Pleistocene Glaciations of North Germany—New Results. *Dev Quat Sci* 15:149–162. doi: 10.1016/B978-0-444-53447-7.00013-1.

Ehlers J (2020) *Das Eiszeitalter*, 2nd edn. Springer Berlin, Heidelberg. doi: 10.1007/978-3-662-60582-0.

Elío J, Cinelli G, Bossew P, Gutiérrez-Villanueva JL, Tollefsen T, De Cort M, et al. (2019) The first version of the Pan-European indoor radon map. *Nat Hazards Earth Syst Sci* 19:2451–2464. doi: 10.5194/nhess-19-2451-2019.

Engels S, Bohncke SJP, Heiri O, Schaber K, Sirocko F (2008) The lacustrine sediment record of Oberwinkler Maar (Eifel, Germany): Chironomid and macro-remain-based inferences of environmental changes during Oxygen Isotope Stage 3. *Boreas* 37(3):414–425. doi: 10.1111/j.1502-3885.2008.00033.x.

Enker WE (2010) The Natural History of Rectal Cancer 1908-2008: The Evolving Treatment of Rectal Cancer into the Twenty-First Century. *Semin Colon Rectal Surg* 21(2):56–74. doi: 10.1053/j.scrs.2010.01.002.

Etiop G, Lombardi S (1995) Evidence for radon transport by carrier gas through faulted clays in Italy. *J Radioanal Nucl Chem* 193(2):291–300. doi: 10.1007/bf02039886.

Etiop G, Martinelli G (2002) Migration of carrier and trace gases in the geosphere: an overview. *Phys Earth Planet Inter* 129(3–4):185–204. doi: 10.1016/S0031-9201(01)00292-8.

Fægri K, Iversen J (1989) *Textbook of Pollen Analysis*. John Wiley and Sons, Chichester.

Fedele FG, Giaccio B, Hajdas I (2008) Timescales and cultural process at 40,000 BP in the light of the Campanian Ignimbrite eruption, Western Eurasia. *J Hum Evolut* 55(5):834–857. doi: 10.1016/j.jhevol.2008.08.012.

- Finne IE, Kolstad T, Larsson M, Olsen B, Prendergast J, Rudjord AL (2019) Significant reduction in indoor radon in newly built houses. *J Environ Radioact* 196:259–263. doi: 10.1016/j.jenvrad.2018.01.013.
- Fitzsimmons KE, Hambach U, Veres D, Iovita R (2013) The Campanian Ignimbrite Eruption: New Data on Volcanic Ash Dispersal and Its Potential Impact on Human Evolution. *PLOS ONE* 8(6):e65839. doi: 10.1371/journal.pone.0065839.
- Fleitmann D, Burns SJ, Mudelsee M, Neff U, Kramers J, Mangini A, et al. (2003) Holocene forcing of the Indian monsoon recorded in a stalagmite from southern Oman. *Sci* 300(5626):1737–1739. doi: 10.1126/science.1083130.
- Fleitmann D, Cheng H, Badertscher S, Edwards RL, Mudelsee M, Göktürk OM, et al. (2009) Timig and climatic impact of Greenland Interstadials recorded in stalagmites from northern Turkey. *Geophys Res Lett* 36(19):L197007. doi: 10.1029/2009GL040050.
- Fletcher WJ, Sánchez Goñi MF, Allen JRM, Cheddadi R, Combourieu-Nebout N, Huntley B, et al. (2010) Millennial-scale variability during last glacial in vegetation records from Europe. *Quat Sci Rev* 29(21–22):2839–2864. doi: 10.1016/j.quascirev.2009.11.015.
- Förster MW, Sirocko F (2016) Volcanic activity in the Eifel during the last 500,000 years: The ELSA-Tephra-Stack. *Glob Planet Chang* 142:100–107. doi: 10.1016/j.gloplacha.2015.07.012.
- Förster MW, Zemplinskaya A, Otter L, Buhre S, Sirocko F (2019) Late Pleistocene Eifel eruptions: insights from clinopyroxene and glass geochemistry of tephra layers from Eifel Laminated Sediment Archive sediment cores. *J Quat Sci* 35(1–2):186–198. doi: 10.1002/jqs.3134.
- Fuhrmann F, Diensberg B, Gong X, Lohmann G, Sirocko F (2020) Aridity synthesis for eight selected key regions of the global climate system during the last 60 000 years. *Clim Past* 16(6):2221–2238. doi: 10.5194/cp-16-2221-2020.
- Galmarini S (2006) One year of  $^{222}\text{Rn}$  concentration in the atmospheric surface layer. *Atmos Chem Phys* 6(10):2865–2886. doi: 10.5194/acp-6-2865-2006.

George AC (2008) World history of radon research and measurement from the early 1900's to today. *The Natural Radiation Environment – 8th International Symposium, AIP Conference Proceedings* 1034(1):20–33. doi: 10.1063/1.2991210.

Geotektonischer Atlas von Nordwest-Deutschland und dem deutschen Nordsee-Sektor (2001). In: Baldschuhn R, Binot F, Fleig S, Kockel F (eds) *Geologisches Jahrbuch Reihe A, Band A 153*. Schweizerbart'sche, Stuttgart.

Giaccio B, Hajdas I, Isaia R, Deino A, Nomade S (2017) High-precision  $^{14}\text{C}$  and  $^{40}\text{Ar}/^{39}\text{Ar}$  dating of the Campanian Ignimbrite (Y-5) reconciles the time-scales of climatic-cultural processes at 40 ka. *Sci Rep* 7:45940. doi: 10.1038/srep45940.

Giammanco S, Immè G, Mangano G, Morelli D, Neri M (2009) Comparison between different methodologies for detecting radon in soil along an active fault: The case of the Pernicana fault system, Mt. Etna (Italy). *Appl Radiat Isot* 67(1):178–185. doi: 10.1016/j.apradiso.2008.09.007.

Gilli A, Anselmetti FS, Glur L, Wirth SB (2013) Lake sediments as archives of recurrence rates and intensities of past flood events. In: Schneuwly-Bollschweiler M, Stoffel M, Rudolf-Miklau F (eds), *Dating torrential processes on fans and cones – Methods and their application for hazard and risk assessment Advances in global change research*. Springer, Heidelberg, pp. 225–242. doi: 10.1007/978-94-007-4336-6.

Glaser R, Riemann D, Schönbein J, Barreindos M, Brázdil R, Bertolin C, et al. (2010) The variability of European floods since AD 1500. *Clim Chang* 101:235–256. doi: 10.1007/s10584-010-9816-7.

Goldenberg SB, Landsea CW, Mestas-Nuñez AM, Gray WM (2001) The recent increase in Atlantic hurricane activity: causes and implications. *Science* 293(5529):474–479. doi: 10.1126/science.1060040.

Gorenstein P, Bjorkholm P (1972) Observation of lunar radon emanation with the Apollo 15 alpha particle spectrometer. *Geochim Cosmochim Acta* 3(Suppl 3):2179–2187.

Gregorič A, Vaupotič J, Šebela S (2014) The role of cave ventilation in governing cave air temperature and radon levels (Postojna Cave, Slovenia). *Int J Climatol* 34 (5):1488–1500. doi: 10.1002/joc.3778.



Griffiths AD, Zahorowski W, Element A, Werczynski S (2010) A map of radon flux at the Australian land surface. *Atmos Chem Phys* 10(18):8969–8982. doi: 10.5194/acp-10-8969-2010.

Grootes PM, Stuiver M, White JWC, Johnsen S, Jouzel J (1993) Comparison of oxygen isotope records from the GISP2 and GRIP Greenland ice cores. *Nat* 366:552–554. doi: 10.1038/366552a0.

Grzywa-Celińska A, Krusiński A, Mazur J, Szewczyk K, Kozak K (2020) Radon — The element of risk. The impact of radon exposure on human health. *Toxics* 8(4):120. doi: 10.3390/toxics8040120.

Hajdas I, Zolitschka B, Ivy-Ochs SD, Beer J, Bonani G, Leroy SAG, et al. (1995) AMS radiocarbon dating of annually laminated sediments from Lake Holzmaar, Germany. *Quat Sci Rev* 14(2):137–143. doi: 10.1016/0277-3791(94)00123-S.

Haslett J, Parnell A (2008) A simple monotone process with application to radiocarbon-dated depth chronologies. *J R Stat Soc Ser C (Appl Stat)* 57:399–418. doi: 10.1111/j.1467-9876.2008.00623.x.

Hassan NM, Hosoda M, Ishikawa T, Sorimachi A, Sashoo SK, Tokonami S, Fukushi M (2009) Radon migration process and its influence factors; Review. *Jpn J Health Phys* 44(2):218–231. doi: 10.5453/jhps.44.218.

Haug GH, Pedersen TF, Sigman DM, Calvert SE, Nielsen B, Peterson LC (1998) Glacial/interglacial variations in production and nitrogen fixation in the Cariaco Basin during the last 580 kyr. *Paleoceanography* 13(5):427–432. doi: 10.1029/98PA01976.

Haug GH, Hughen K, Sigman DM, Peterson LC, Röhl U (2001) Southward migration of the intertropical convergence zone through the holocene. *Sci* 293(5533):1304–1308. doi: 10.1126/science.1059725.

Hemming SR (2004) Heinrich events: Massive late Pleistocene detritus layers of the North Atlantic and their global climate imprint. *Rev Geophys* 42(1):RG1005. doi: 10.1029/2003RG000128.

Herndon JM (2020) Causes and consequences of geomagnetic field collapse. *J Geog Environ Earth Sci Int* 24(9):60–76. doi: 10.9734/JGEESI/2020/v24i930256.

- Herndon JM (2021) Scientific basis and geophysical consequences of geomagnetic reversals and excursions: a fundamental statement. *J Geog Environ Earth Sci Int* 25(3):59–69. doi: 10.9734/JGEESI/2021/v25i330277.
- Hersbach H, Bell B, Berrisford P, Hirahara S, Horányi A, Muñoz-Sabater J, et al. (2020) The ERA5 global reanalysis. *Q J R Meteorol Soc* 146(730):1999–2049. doi: 10.1002/qj.3803.
- Higham T, Basell L, Jacobi R, Wood R, Bronk Ramsey C, Conard NJ (2012) Testing models for the beginning of the Aurignacian and the advent of figurative art and music: The radiocarbon chronology of Geißenklösterle. *J Hum Evolut* 62(6):664–676. doi: 10.1016/j.jhevol.2012.03.003.
- Hirabayashi Y, Mahendran R, Koirala S, Konoshima L, Yamazaki D, Watanabe S, et al. (2013) Global flood risk under climate change. *Nat Clim Chang* 3:816–821. doi: 10.1038/nclimate1911.
- Hodell DA, Curtis JH, Brenner M (1995) Possible role of climate in the collapse of Classic Maya civilization. *Nat* 375:391–394. doi: 10.1038/375391a0.
- Hoffecker JF (2009) The spread of modern humans in Europe. *PNAS* 106(38):16040–16045. doi: 10.1073/pnas.0903446106.
- Hublin J-J, Talamo S, Julien M, David F, Connet N, Bodu P, et al. (2012) Radiocarbon dates from the Grotte du Renne and Saint-Césaire support a Neandertal origin for the Châtelperronian. *PNAS* 109(46):18743–18748. doi: 10.1073/pnas.1212924109.
- Hublin JJ (2015) The modern human colonization of western Eurasia: When and where? *Quat Sci Rev* 118:194–210. doi: 10.1016/j.quascirev.2014.08.011.
- Huntington TG (2006) Evidence for intensification of the global water cycle: Review and synthesis. *J Hydrol* 319(1–4):83–95. doi: 10.1016/j.jhydrol.2005.07.003.
- Iakovleva VS, Karataev VD (2005) Factors determining the formation of radon levels inside buildings. *Radiat Biol Radioecol* 45(3):333–337.

Igarashi G, Saeki Sm Takahata N, Sumikawa K, Tasaka S, Sasaki Y, Takahashi M, Sano Y (1995) Ground-Water Radon Anomaly Before the Kobe Earthquake in Japan. *Sci* 269:60–61. doi: 10.1126/science.269.5220.60.

International Agency for Research on Cancer (2001) IARC monographs on the evaluation of carcinogenic risk to humans. Vol 78. Ionizing radiation. Part 2: Some internally deposited radionuclides. Lyon, France.

Iovine G, Guagliardi I, Bruno C, Greco R, Tallarico A, Falcone G, Lucà F, Buttafuoco G (2018) Soil-gas radon anomalies in three study areas of Central-Northern Calabria (Southern Italy). *Nat Hazards* 91:193–219. doi: 10.1007/s11069-017-2839-x.

Irwin WP, Barnes I (1980) Tectonic relations of carbon dioxide discharges and earthquakes. *J Geophys Res* 85(B6):3115–3121. doi: 10.1029/JB085iB06p03115.

Jones AF, Lewin J, Macklin MG (2010) Flood series data for the later Holocene: Available approaches, potential and limitations from UK alluvial sediments. *Holocene* 20(7):1123–1135. doi: 10.1177/0959683610369501.

Justino F, Peltier WR (2005) The glacial North Atlantic oscillation. *Geophys Res Lett* 32(21):L21803. doi: 10.1029/2005GL023822.

Karstens U, Schwingshackl C, Schmithüsen D, Levin I (2015) A process-based  $^{222}\text{Rn}$  flux map for Europe and its comparison to long-term observations. *Atmos Chem and Phys* 15(22):12845–12865. doi: 10.5194/acp-15-12845-2015.

Kasse C, Vandenberghe J, Bohncke SJP (1995) Climate change and fluvial dynamics of the Maas during the Late Weichselian and Early Holocene. In: Frenzel B, Vandenberghe J, Kasse C, Bohncke S, Gläser B (eds) European river activity and climate change during the Lateglacial and early Holocene. *Paleoclim Res* 14:123–150.

Kemski J, Klingel R, Siehl A (1996) Classification and mapping of radon-affected areas in Germany. *Environ Int* 22(Suppl 1):789–798. doi: 10.1016/S0160-4120(96)00185-7.

- Kemski J, Siehl A, Stegemann R, Valdivia-Manchego M (2001) Mapping the geogenic radon potential in Germany. *Sci. Total Environ* 272(1–3):217–230. doi: 10.1016/S0048-9697(01)00696-9.
- Kemski J, Klingel R, Siehl A, Stegemann R (2005) Radon transfer from ground to houses and prediction of indoor radon in Germany based on geological information. *Radioact in the Environ* 7:820–832. doi: 10.1016/S1569-4860(04)07103-7.
- Kerr RA (2000) A North Atlantic climate pacemaker for the centuries. *Sci* 288(5473):1984–1985.
- Kliem P, Enters D, Hahn A, Ohlendorf C, Lisé-Pronovost A, St-Onge G, et al. (2013) Lithology, radiocarbon chronology and sedimentological interpretation of the lacustrine record from Laguna Potrok Aike, southern Patagonia. *Quat Sci Rev* 71:54–69. doi: 10.1016/j.quascirev.2012.07.019.
- Knight JR, Folland CK, Scaife AA (2006) Climate impacts of the Atlantic multidecadal oscillation. *Geophys Res Lett* 33(17):L02706.
- Knudsen MF, Seidenkrantz M-S, Jacobsen BH, Kuijpers A (2011) Tracking the Atlantic multidecadal oscillation through the last 8,000 years. *Nat Commun* 2:178. doi: 10.1038/ncomms1186.
- Köhn D, Thorwart M, De Nil D, Rabbel W, Sirocko F (2019) Charakterisierung einer Störungszone östlich des großen Plöner Sees (Schleswig-Holstein) mittels 2D SH Full Waveform Inversion. 79th annual meeting of the German Geophysical Society, Braunschweig.
- Korschinek G, Bergmaier A, Faesermann T, Gerstmann UC, Knie K, Rugel G, et al. (2010) A new value for the half-life of  $^{10}\text{Be}$  by heavy-ion elastic recoil detection and liquid scintillation counting. *Nucl Instrum Methods Phys Res Sec B* 268(2):187–191. doi: 10.1016/j.nimb.2009.09.020.
- Kreienbrock L, Kreuzer M, Gerken M, Dingerkus G, Wellmann J, Keller G, Wichmann HE (2001) Case-Control study on lung cancer and residential radon in Western Germany. *Am J Epidemiol* 153(1):42–52. doi: 10.1093/aje/153.1.42.
- Kropat G, Bochud F, Murith C, Palacios (Gruson) M, Baechler S (2017) Modeling of geogenic radon in Switzerland based on ordered logistic regression. *J Environ Radioact* 166(2):376–381. doi: 10.1016/j.jenvrad.2016.06.007.

- Künze N, Koroleva M, Reuther CD (2012)  $^{222}\text{Rn}$  activity in soil gas across selected fault segments in the Cantabrian Mountains, NW Spain. *Radiat Meas* 47(5):389–399. doi: 10.1016/j.radmeas.2012.02.013.
- Künze N, Koroleva M, Reuther CD (2013) Soil gas  $^{222}\text{Rn}$  concentration in northern Germany and its relationship with geological subsurface structures. *J Environ Radioact* 115:83–96. doi: 10.1016/j.jenvrad.2012.07.009.
- Laj C, Kissel C, Beer J (2004) High Resolution Global Paleointensity Stack Since 75 kyr (GLOPIS-75) Calibrated to Absolute Values. In: Channell JET, Kent DV, Lowrie W, Meert JG (eds) *Timescales of the Paleomagnetic Field*. Am Geophys Union, Washington, DC, pp. 255–265. doi: 10.1029/145GM19.
- Lawson SL, Feldman WC, Lawrence DJ, Moore KR, Elphic RC, Belian RD, et al. (2005) Recent outgassing from the lunar surface: The Lunar Prospector Alpha Particle Spectrometer. *J Geophys Res* 110(E9):E09009. doi: 10.1029/2005JE002433.
- Lean JL (2017) *Sun-climate connections*. Oxford Res Encycl Clim Sci (Oxford Univ. Press). doi: 10.1093/acrefore/9780190228620.013.9.
- Lehné R, Sirocko F (2005) Quantification of recent movement potentials in Schleswig-Holstein (Germany) by GIS-based calculation of correlation coefficients. *Int J Earth Sci* 94:1094–1102. doi: 10.1007/s00531-005-0043-9.
- Lehné R, Sirocko F (2010) Recent vertical crustal movements and resulting surface deformation within the North German Basin (Schleswig-Holstein) derived by GIS-based analysis of repeated precise leveling data. *Z Dtsch Ges Geowiss* 162(2):175–188. doi: 10.1127/1860-1804/2010/0161-0175.
- Levine AFZ, McPhaden MJ, Frierson DMW (2017) The impact of the AMO on multidecadal ENSO variability. *Geophys Res Lett* 44(8):3877–3886. doi: 10.1002/2017GL072524.
- Li C, Battisti DS, Bitz CM (2010) Can North Atlantic sea ice anomalies account for Dansgaard-Oeschger climate signals? *J Clim* 23(20):5457–5475. doi: 10.1175/2010JCLI3409.1.

- Li C, Born A (2019) Coupled atmosphere-ice-ocean dynamics in Dansgaard-Oeschger events. *Quat Sci Rev* 203:1–20. doi: 10.1016/j.quascirev.2018.10.031.
- Li F, Orsolini YJ, Wang H, Gao Y, He S (2018) Atlantic multidecadal oscillation modulates the impacts of Arctic sea ice decline. *Geophys Res Lett* 45(5):2497–2506. doi: 10.1002/2017GL076210.
- Litt T, Brauer A, Goslar T, Merkt J, Balaga K, Müller H, et al. (2001) Correlation and synchronisation of Lateglacial continental sequences in northern central Europe based on annually laminated lacustrine sediments. *Quat Sci Rev* 20(11):1233–1249. doi: 10.1016/S0277-3791(00)00149-9.
- Litt T, Schölzel C, Kühl N, Brauer A (2009) Vegetation and climate history in the Westeifel Volcanic Field (Germany) during the past 11,000 years based on annually laminated lacustrine maar sediments. *Boreas* 38(4):679–690. doi: 10.1111/j.1502-3885.2009.00096.x.
- López-Abente G, Núñez O, Fernández-Navarro P, Barros-Dios JM, Martín-Méndez I, Bel-Lan A, et al. (2018) Residential radon and cancer mortality in Galicia, Spain. *Sci Total Environ* 610–611:1125–1132. doi: 10.1016/j.scitotenv.2017.08.144.
- Lorenz E (1944) Radioactivity and Lung Cancer; A Critical Review of Lung Cancer in the Miners of Schneeberg and Joachimsthal. *J Natl Cancer Inst* 5(1):1–15. doi: 10.1093/jnci/5.1.1.
- Louda JW, Baker EW (1986) The biochemistry of chlorophyll. In: Sohn ML (ed) *Organic Marine Geochemistry* Vol. 305:107–126, American Chemical Society, Washington, DC. doi: 10.1021/bk-1986-0305.ch007.
- Lowe JJ, Walker MJC (2014) *Reconstructing Quaternary Environments* (3rd ed.), Routledge, London. doi: 10.4324/9781315797496.
- Lowe DJ (2011) Tephrochronology and its application: A review. *Quat Geochron* 6(2):107–153. doi: 10.1016/j.quageo.2010.08.003.
- Lücke A, Schleser GH, Zolitschka B, Negendank JFW (2003) A Lateglacial and Holocene organic carbon isotope record of lacustrine palaeoproductivity and climate change derived from varved lake

sediments of Lake Holzmaar, Germany. *Quat Sci Rev* 22(5–7):269–580. doi: 10.1016/S0277-3791(02)00187-7.

Macklin MG (1999) Holocene River Environments in Prehistoric Britain: Human Interaction and Impact. *J Quat Sci* 14(6):521–530. doi: 10.1002/(SICI)1099-1417(199910)14:6<521::AID-JQS487>3.0.CO;2-G.

Mann ME, Park J, Bradley RS (1995) Global interdecadal and century-scale climate oscillations during the past five centuries. *Nat* 378:266–270. doi: 10.1038/378266a0.

Martens CS, Shay TJ, Mendlovitz HP, Matross DM, Saleska SR, Wofsy SC, et al. (2004) Radon fluxes in tropical forest ecosystems of Brazilian Amazonia: night-time CO<sub>2</sub> net ecosystem exchange derived from radon and eddy covariance methods. *Glob Chang Biol* 10(5):618–629.

Martrat B, Grimalt JO, Shackleton NJ, de Abreu L, Hutterli MA, Stocker TF (2007) Four climate cycles of recurring deep and surface water destabilizations on the Iberian margin. *Sci* 317(5837):502–507.

Marzocchi W, Mulargia F, Paruolo P (1992) The correlation of geomagnetic reversals and mean sea level in the last 150 m.y. *Earth Planet Sci Lett* 111(2–4):383–393. doi: 10.1016/0012-821X(92)90191-W.

Masson-Delmotte V (2005) GRIP deuterium excess reveals rapid and orbital-scale changes in Greenland moisture origin. *Sci* 309(5731):118–121. doi: 10.1126/science.1108575.

Maystrenko Y, Bayer U, Scheck-Wenderoth M (2005) Structure and evolution of the Glueckstadt Graben due to salt movements. *Int J Earth Sci (Geol Rundsch)* 94:799–814. doi: 10.1007/s00531-005-0003-4.

Maystrenko Y, Bayer U, Brink H-J, Littke R (2008) The Central European Basin System – an Overview. In: Littke R, Bayer U, Gajewski D, Nelskamp S (2008) *Dynamics of Complex Intracontinental Basins*. 1st edn. Springer, Berlin Heidelberg. doi: 10.1007/978-3-540-85085-4\_2.

Mc Laughlin J (2012) An historical overview of radon and its progeny: applications and health effects. *Radiat Prot Dosimetry* 152(1–3):2–8. doi: 10.1093/rpd/ncs189.

Meert JG, Levashova NM, Bazhenov ML, Landing E (2016) Rapid changes of magnetic Field polarity in the late Ediacaran: Linking the Cambrian evolutionary radiation and increased UV-B radiation. *Gondwana Res* 34:149–157. doi: 10.1016/j.gr.2016.01.001.

Meier G (2003) Ingenieurgeologische Ergebnisse bei der Standsicherheitsanalyse der „Kalkberghöhle“ in Bad Segeberg. Tagung f Ing.-Geol 14, Kiel.

Méléder V, Jesus B, Barnett A, Barillé L, Lavaud J (2018) Microphytobenthos primary production estimated by hyperspectral reflectance. *PLOS ONE* 13:e0197093. doi: 10.1371/journal.pone.0197093.

Menzler S, Piller G, Gruson M, Schaffrath-Rosario A, Wichmann HE, Kreienbrock L (2008) Population attributable fraction for lung cancer due to residential radon in Switzerland and Germany. *Health Phys* 95(2):179–189. doi: 10.1097/01.HP.0000309769.55126.03.

Meslin P-Y, Sabroux J-C, Berger L, Pineau J-F, Chassefière E (2006) Evidence of <sup>210</sup>Po on Martian dust at Meridiani Planum. *J Geophys Res* 111(E9):E09012. doi: 10.1029/2006JE002692.

Michelutti N, Smol JP (2016) Visible spectroscopy reliably tracks trends in paleo-production. *J Paleolimnol* 56:253–265. doi: 10.1007/s10933-016-9921-3.

Milly PCD, Wetherald RT, Dunne KA, Delworth TL (2002) Increasing risk of great floods in the changing climate. *Nat* 415:514–517. doi: 10.1038/415514a.

Mingram J, Stebich M, Schlettler G, Hu Y, Rioual P, Nowaczyk N, et al. (2018) Millennial-scale East Asian monsoon variability of the last glacial deduced from annually laminated sediments from Lake Sihailongwan, N.E. China. *Quat Sci Rev* 201:57–76. doi: 10.1016/j.quascirev.2018.09.023.

Ministerium für Energiewende, Landwirtschaft, Umwelt, Natur und Digitalisierung (2020) Pressemitteilung „Untersuchungsprogramm abgeschlossen: Radon-Belastung in Schleswig-Holstein liegt unterhalb der Schwellenwerte“. [https://www.schleswig-holstein.de/DE/landesregierung/ministerien-behoerden/V/Presse/PI/2020/1220/201207\\_Radon.html](https://www.schleswig-holstein.de/DE/landesregierung/ministerien-behoerden/V/Presse/PI/2020/1220/201207_Radon.html).

Accessed 27 October 2022.



Monnin MM, Seidel JL (1992) Radon in soil-air and in groundwater related to major geophysical events: A survey. *Nucl Instrum Methods Phys Res Sec A* 314(2):316–330. doi: 10.1016/0168-9002(92)90975-A.

Moreno A, Svensson A, Brooks SJ, Connor S, Engels S, Fletcher W, et al. (2014) A compilation of Western European terrestrial records 60-8 ka BP: towards an understanding of latitudinal climatic gradients. *Quat Sci Rev* 106:167–185. doi: 10.1016/j.quascirev.2014.06.030.

Morin E (2008) Evidence for declines in human population densities during the early Upper Paleolithic in western Europe. *PNAS* 105(1):48–53. doi: 10.1073/pnas.0709372104.

Mudelsee M (2000) Ramp function regression: a tool for quantifying climate transitions. *Comput Geosci* 26(3):293–307. doi: 10.1016/S0098-3004(99)00141-7.

Mudelsee M (2009) Break function regression. *Eur Phys J Spec Top* 174:49–63. doi: 10.1140/epjst/e2009-01089-3.

Mudelsee M (2014) *Climate Time Series Analysis: Classical Statistical and Bootstrap Methods*. Springer, Basel.

Mudelsee M, Albert J, Sirocko F (2020) Weather control in radon flux time series from Schleswig-Holstein, Germany. *Int J Geomath* 11:23. doi: 10.1007/s13137-020-00156-w.

Mulder T, Syvitski JPM, Migeon S, Faugères J-C, Savoye B (2003) Marine hyperpycnal flows: initiation, behavior and related deposits. A review. *Mar Petroleum Geol* 20(6–8):861–882. doi: 10.1016/j.marpetgeo.2003.01.003.

Muscheler R, Beer J, Wagner G, Laj C, Kissel C, Raisbeck GM, et al. (2004) Changes in the carbon cycle during the last deglaciation as indicated by the comparison of  $^{10}\text{Be}$  and  $^{14}\text{C}$  records. *Earth Planet Sci Lett* 219(3–4):325–340. doi: 10.1016/S0012-821X(03)00722-2.

Muscheler R, Beer J, Kubik PW, Synal H-A (2005) Geomagnetic field intensity during the last 60,000 years based on  $^{10}\text{Be}$  and  $^{36}\text{Cl}$  from the Summit ice cores and  $^{14}\text{C}$ . *Quat Sci Rev* 24(16–17):1849–1860. doi: 10.1016/j.quascirev.2005.01.012.

Muscheler R, Beer J (2006) Solar forced Dansgaard/Oeschger events? *Geophys Res Lett* 33(20):L20706. doi: 10.1029/2006GL026779.

Naafs BDA, Hefter J, Grützner J, Stein R (2013) Warming of surface waters in the mid-latitude North Atlantic during Heinrich events. *Paleoceanogr* 28(1):153–163. doi: 10.1029/2012PA002354.

National Research Council (US) (1999a) Committee on Health risks of exposure to radon (BEIR VI) Health effects of exposure to radon. National Academy Press, Washington, DC. doi: 10.17226/5499.

National Research Council (US) (1999b) Committee on risk assessment of exposure to radon in drinking water. National Academy Press, Washington, DC. doi: 10.17226/6287.

Nazaroff WW (1992) Radon transport from soil to air. *Rev Geophys* 30(2):137–160. doi: 10.1029/92RG00055.

Neri M, Ferrera E, Giammanco S, Currenti G, Cirrincione R, Patanè G, Zanon V (2016) Soil radon measurements as a potential tracer of tectonic and volcanic activity. *Sci Rep* 6:1–12. doi: 10.1038/srep24581.

Nigst PR, Haesaerts P, Damblon F, Frank-Fellner C, Mallol C, Viola B, et al. (2014) Early modern human settlement of Europe north of the Alps occurred 43,500 years ago in a cold steppe-type environment. *PNAS* 111(40):14394–14399. doi: 10.1073/pnas.1412201111.

Nishiizumi K, Imamura M, Caffee MW, Southon JR, Finkel RC, McAninch J (2007) Absolute calibration of  $^{10}\text{Be}$  AMS standards. *Nucl Instrum Methods Phys Res B* 258(2):403–413.

North Greenland Ice Core Project Members (2004) High-resolution record of Northern Hemisphere climate extending into the last interglacial period. *Nat* 431:147–151. doi: 10.1038/nature02805.

Norval M, Cullen AP, de Gruijl FR, Longstreth J, Takizawa Y, Lucas RM, et al. (2007) The effects on human health from stratospheric ozone depletion and its interactions with climate change. *Photochem Photobio Sci* 6(3):232–251. doi: 10.1039/B700018A.

Nowaczyk NR, Frank U, Kind J, Arz HW (2013) A high-resolution paleointensity stack of the past 14 to 68 ka from Black Sea sediments. *Earth Planet Sci Lett* 384:1–16. doi: 10.1016/j.epsl.2013.09.028.

- Obreht I, Hambach U, Veres D, Zeeden C, Böskén J, Stevens T, et al. (2017) Shift of large-scale atmospheric systems over Europe during late MIS 3 and implications for Modern Human dispersal. *Sci Rep* 7:5848. doi: 10.1038/s41598-017-06285-x.
- Obreht I, Wörmer L, Brauer A, Wendt J, Alfken S, De Vleeschouwer D, et al. (2020) An annually resolved record of Western European vegetation response to Younger Dryas cooling. *Quat Sci Rev* 231:106198. doi: 10.1016/j.quascirev.2020.106198.
- Otterå OH, Bentsen M, Drange H, Sui L (2010) External forcing as a metronome for Atlantic multidecadal variability. *Nat Geosci* 3:688–694. doi: 10.1038/ngeo955.
- Pausata FSR, Li C, Wettstein JJ, Kageyama M, Nisancioglu KH (2011) The key role of topography in altering North Atlantic atmospheric circulation during the last glacial period. *Clim Past* 7(4):1089–1101. doi: 10.5194/cp-7-1089-2011.
- Pavlov VE, Fluteau F, Latyshev AV, Fetisova AM, Elkins-Tanton LT, Black BA, et al. (2019) Geomagnetic secular variations at the Permian-Triassic boundary and pulsed magmatism during the eruption of the Siberian Traps. *Geochem Geophys Geosyst* 20(2):773–791. doi: 10.1029/2018GC007950.
- Perrier F, Richon P, Byrdina S et al (2009) A direct evidence for high carbon dioxide and radon-222 discharge in Central Nepal. *Earth Planet Sci Let* 278(3–4):198–207. doi: 10.1016/j.epsl.2008.12.008.
- Peterson LC, Haug GH, Hughen KA, Röhl U (2000) Rapid changes in the hydrological cycle of the tropical Atlantic during the last glacial. *Sci* 290(5498):1947–1951. doi: 10.1126/science.290.5498.1947.
- Pickarski N, Kwiecien O, Langgut D, Litt T (2015) Abrupt climate and vegetation variability of eastern Anatolia during the last glacial. *Clim Past* 11:1491–1505. doi: 10.5194/cp-11-1491-2015.
- Raaschou-Nielsen O (2008) Indoor radon and childhood leukaemia. *Radiat Prot Dosimetry* 132(2):175–181. doi: 10.1093/rpd/ncn288.
- Rach O, Braue, A, Wilkes H, Sachse D (2014) Delayed hydrological response to Greenland cooling at the onset of the Younger Dryas in western Europe. *Nat Geosci* 7:109–112. doi: 10.1038/ngeo2053.

- Rahmstorf S (2002) Ocean circulation and climate during the past 120,000 years. *Nat* 419:207–214.
- Rasmussen SO, Andersen KK, Svensson AM, Steffensen JP, Vinther BM, Clausen HB, et al. (2006) A new Greenland ice core chronology for the last glacial. *J Geophys Res* 111(D6):D06102. doi: 10.1029/2005JD006079.
- Rasmussen SO, Bigler M, Blockley SP, Blunier T, Buchardt SL, Clausen HB, et al. (2014) A stratigraphic framework for abrupt climatic changes during the Last Glacial period based on three synchronized Greenland ice-core records: refining and extending the INTIMATE event stratigraphy. *Quat Sci Rev* 106:14–28.
- Raup DM (1985) Magnetic reversals and mass extinctions. *Nat* 314:341–343. doi: 10.1038/314341a0.
- Rein B, Sirocko F (2002) In-situ reflectance spectroscopy — analysing techniques for high resolution pigment 300 logging in sediment cores. *Int J Earth Sci* 91:950–954. doi: 10.1007/s00531-002-0264-0.
- Reinig F, Wacker L, Jöris O, Oppenheimer C, Guidobaldi G, Nievergelt D, et al. (2021) Precise date for the Laacher See eruption synchronizes the Younger Dryas. *Nat* 595:66–69. doi: 10.1038/s41586-021-03608-x.
- Rendu W, Renou S, Soulier M-C, Rigaud S, Roussel M, Soressi M (2019) Subsistence strategy changes during Middle to Upper Paleolithic transition of Human Populations to their environment. *Sci Rep* 9:15817. doi: 10.1038/s41598-019-50647-6.
- Richon P, Sabroux JC, Halbwachs M, Vandemeulebrouck J, Poussielgue N, Tabbagh J, Punongbayan R (2003) Radon anomaly in the soil of Taal volcano, the Philippines: A likely precursor of the M 7.1 Mindoro earthquake (1994). *Geophys Res Lett* 30(9):1–4. doi: 10.1029/2003GL016902.
- Richter TO, van der Gaast S, Koster B, Vaars A, Gieles R, de Stigter HC, et al. (2006) The Avaatech XRF Core Scanner: technical description and applications to NE Atlantic sediments. *Geol Soc Lond Spec Publ* 267:39–50.
- Rose AW, Hutter AR, Washington JW (1990) Sampling variability of radon in soil gases. *J Geochem Explor* 38(1–2):173–191. doi: 10.1016/0375-6742(90)90100-O.

- Rosell-Melé A, Maslin MA, Maxwell JR, Schaeffer P (1997) Biomarker evidence for “Heinrich” events. *Geochim Cosmochim Acta* 61(8):1671–1678. doi: 10.1016/S0016-7037(97)00046-X.
- Ross P-H (1998) Salzaufstieg und Geländemorphologie in Schleswig-Holstein – der Segeberger Salzstock und seine schutzwürdige Karstlandschaft. *Jahrbuch für den Kreis Segeberg*. C H Wäser, Bad Segeberg.
- Sadatzki H, Dokke TM, Berben SM, Muschitiello F, Stein R, Fahl K, et al. (2019) Sea ice variability in the southern Norwegian sea during glacial Dansgaard-Oeschger climate cycles. *Sci Adv* 5(3):eaau6174. doi: 10.1126/sciadv.aau6174.
- Sainz Fernández S, Quindós Poncela LS, Fernández Villar A et al (2017) Spanish experience on the design of radon surveys based on the use of geogenic information. *J Environ Radioact* 166(2):390–397. doi: 10.1016/j.jenvrad.2016.07.007.
- Sánchez Goñi MF, Landais A, Cacho I, Duprat J, Rossignol L (2009) Contrasting intrainterstadial climatic evolution between high and middle North Atlantic latitudes: a close-up of Greenland Interstadial 8 and 12. *Geochem Geophys Geosyst* 10(4):1–16. doi: 10.1029/2008GC002369.
- Sanchini A, Grosjean M (2020) Quantification of chlorophyll *a*, chlorophyll *b* and pheopigments *a* in lake sediments through deconvolution of bulk UV-VIS absorption spectra. *J Paleolimnol* 64:243–256. doi: 10.1007/s10933-020-00135-z.
- Schery SD, Huang S (2004) An estimate of the global distribution of radon emissions from the ocean. *Geophys Res Lett* 34(19):L19104. doi: 10.1029/2004GL021051.
- Schillereff DN, Chiverrell RC, Macdonald N, Hooke JM (2014) Flood stratigraphies in lake sediments: A review. *Earth Sci Rev* 135:17–37. doi: 10.1016/j.earscirev.2014.03.011.
- Schlesinger ME, Ramankutty N (1994) An oscillation in the global climate system of period 65–70 years. *Nat* 367:723–726. doi: 10.1038/367723a0.

- Schlolaut G, Brauer A, Marshall MH, Nakagawa T, Staff RA, Bronk Ramsey C, et al. (2014) Event layers in the Japanese Lake Suigetsu ‘SG06’ sediment core: description, interpretation and climatic implications. *Quat Sci Rev* 83: 157–170. doi: 10.1016/j.quascirev.2013.10.026.
- Schnellmann M, Anselmetti FS, Giardini D, McKenzie JA (2005) Mass movement induced fold-and-thrust belt structures in unconsolidated sediments in Lake Lucerne (Switzerland). *Sedimentol* 52(2):271–289. doi: 10.1111/j.1365-3091.2004.00694.x.
- Schubert M, Schulz H (2002) Diurnal radon variations in the upper soil layers and at the soil-air interface related to meteorological parameters. *Health Phys* 83(1):91–96. doi: 10.1097/00004032-200207000-00010.
- Schulz M, Mudelsee M (2002) REDFIT: estimating red-noise spectra directly from unevenly spaced paleoclimatic time series. *Comput Geosci* 28(3):421–426. doi: 10.1016/S0098-3004(01)00044-9.
- Sciarra A, Mazzini A, Inguaggiato S, Vita F, Lupi M, Hadi S (2018) Radon and carbon gas anomalies along the Watukosek Fault System and Lusi mud eruption, Indonesia. *Mar Pet Geol* 90:77–90. doi: 10.1016/j.marpetgeo.2017.09.031.
- Seelos K, Sirocko F (2007) Abrupt cooling events at the very end of the last interglacial. *Dev Quat Sci* 7:207–229. doi: 10.1016/S1571-0866(07)80039-X.
- Seelos K, Sirocko F, Dietrich S (2009) A continuous high-resolution dust record for the reconstruction of wind systems in central Europe (Eifel, Western Germany) over the past 133 ka. *Geophys Res Lett* 36(20):L20712. doi: 10.1029/2009GL039716.
- Seib N, Kley J, Büchel G (2013) Identification of maars and similar volcanic landforms in the West Eifel Volcanic Field through image processing of DTM data: efficiency of different methods depending on preservation state. *Int J Earth Sci* 102:875–901. doi: 10.1007/s00531-012-0829-5.
- Seidenglanz A, Prange M, Varma V, Schulz M (2012) Ocean temperature response to idealized Gleissberg and de Vries solar cycles in a comprehensive climate model. *Geophys Res Lett* 39(22):L22602. doi: 10.1029/2012GL053624.

Seiler KP (1973) Durchlässigkeit, Porosität und Kornverteilung quartärer Kies-Sand-Ablagerungen des bayerischen Alpenvorlandes. *GWF Wasser Abwasser* 114(8):353–400.

Semal P, Rougier H, Crevecoeur I, Jungels C, Flas D, Hauzeur A, et al. (2009) New data on the late Neanderthals: Direct dating of the Belgian Spy fossils. *Am J Phys Anthropol* 138(4):421–428. doi: 10.1002/ajpa.20954.

Semkow TM (1990) Recoil-emanation theory applied to radon release from mineral grains. *Geochimica et Cosmochimica Acta* 54(2):425–440. doi: 10.1016/0016-7037(90)90331-E.

Shmuel M, Mordechai S, Agnon A, Ron H (1996) Long-term earthquake clustering: A 50,000-year paleoseismic record in the Dead Sea Graben. *J Geophys Res* 101(B3):6179–6191. doi: 10.1029/95JB01587.

Siino M, Scudero S, Cannelli V, Piersanti A, D'Alessandro A (2019) Multiple seasonality in soil radon time series. *Sci Rep* 9:8610. doi: 10.1038/s41598-019-44875-z.

Singer BS, Guillou H, Jicha BR, Laj C, Kissel C, Beard BL, et al. (2009)  $^{40}\text{Ar}/^{39}\text{Ar}$ , K-Ar and  $^{230}\text{Th}$ – $^{238}\text{U}$  dating of the Laschamp excursion: a radioisotopic tie-point for ice core and climate chronologies. *Earth Planet Sci Lett* 286(1–2):80–88. doi: 10.1016/j.epsl.2009.06.030.

Sirocko F, Szeder T, Seelos C, Lehné R, Rein B, Schneider WM, Dimke M (2002) Young tectonic and halokinetic movements in the North-German-Basin: its effect on formation of modern rivers and surface morphology. *Neth J Geosci* 81(3–4):431–441. doi: 10.1017/S0016774600022708.

Sirocko F, Seelos K, Schaber K, Rein B, Dreher F, Diehl M, et al. (2005) A late Eemian aridity pulse in central Europe during the last glacial interception. *Nat* 436:833–836. doi: 10.1038/nature03905.

Sirocko F, Reicherter K, Lehné R, Hübscher C, Winsemann J, Stackebrandt W (2008) Glaciation, salt and the present landscape. In: Littke R, Bayer U, Gajewski D, Nelskamp S (eds) *Dynamics of Complex Intracontinental Basins*. 1st edn. Springer, Berlin Heidelberg, pp. 233–246.

Sirocko F (2009) *Wetter – Klima – Menschheitsentwicklung. Von der Eiszeit bis ins 21. Jahrhundert*. Theiss Verlag, Stuttgart.

Sirocko F (2012) Lüneburg und das Salz. <https://www.klimaundsedimente.geowissenschaften.uni-mainz.de/projekt-lueneburg>. Accessed 27 October 2022.

Sirocko F, Dietrich S, Veres D, Grootes P, Schaber-Mohr K, Seelos K, et al. (2013) Multi-Proxy-Dating of Holocene maar lakes and Pleistocene dry maar sediments in the Eifel, Germany. *Quat Sci Rev* 62:56–72. doi: 10.1016/j.quascirev.2012.09.011.

Sirocko F, Knapp H, Dreher F, Förster MW, Albert J, Brunck H, et al. (2016) The ELSA-Vegetation-Stack: Reconstruction of Landscape Evolution Zones (LEZ) from laminated Eifel maar sediments of the last 60,000 years. *Glob Planet Chang* 142:108–135. doi: 10.1016/j.gloplacha.2016.03.005.

Sirocko F, Martínez-García A, Mudelsee M, Albert J, Britzius S, Christl M, et al. (2021) Multidecadal climate variability in central Europe over the past 60,000 years. *Nat Geosci* 14:651–658. doi: 10.1038/s41561-021-00786-1.

Sirocko F, Albert J, Britzius S, Dreher F, Martínez-García A, Dosseto A, et al. (submitted) Threshold for the presence of glacial megafauna in central Europe during the last 60,000 years. Submitted to *Nat Sci Rep*.

Skeppström K, Olofsson B (2007) Uranium and radon in groundwater: an overview of the problem. *Eur Water* 17(18):51–62.

Srokosz MA, Bryden HL (2015) Observing the Atlantic meridional overturning circulation yields a decade of inevitable surprises. *Sci* 348(6241):1255575. doi: 10.1126/science.1255575.

Staubwasser M, Drăgușin V, Onac BP, Assonov S, Ersek V, Hoffmann DL, et al. (2018) Impact of climate change on the transition of Neanderthals to modern humans in Europe. *PNAS* 115(37):9116–9121.

Stein R (1985) Rapid grain-size analyses of clay and silt fraction by Sedigraph 5000D: comparison with Counter and Atterberg methods. *J Sediment Petrol* 55(4):590–615. doi: 10.2110/55.4.590.



Steinhilber F, Abreu JA, Beer J, Brunner I, Christl M, Fischer H, et al. (2012) 9,400 years of cosmic radiation and solar activity from ice cores and tree rings. *PNAS* 109(16):5967–5971. doi: 10.1073/pnas.1118965109.

Steinitz G, Begin ZB, Gazit-Yaari N (2003) Statistically significant relation between radon flux and weak earthquakes in the Dead Sea rift valley. *Geol* 31(6):505–508. doi: 10.1130/0091-7613(2003)031<0505:SSRBRF>2.0.CO;2.

Stow DAV, Shanmugam G (1980) Sequence of structures in fine-grained turbidites: Comparison of recent deep-sea and ancient flysch sediments. *Sediment Geol* 25(1–2):23–42.

Strong K P, Levins D M (1982) Effect of moisture content on radon emanation from uranium ore and tailings. *Health Phys* 42(1):27–32. doi: 10.1097/00004032-198201000-00003.

Sun Y, Wang X, Liu Q, Clemens SC (2010) Impacts of post-depositional processes on rapid monsoon signals recorded by the last glacial loess deposits of northern China. *Earth Planet Sci Lett* 289(1–2):171–179. doi: 10.1016/j.epsl.2009.10.038.

Sutton RT, Hodson DLR (2005) Atlantic Ocean forcing of North American and European summer climate. *Sci* 309(5731):115–118.

Svensson A, Andersen KK, Bigler M, Clausen HB, Dahl-Jensen D, Davies SM, et al. (2008) A 60,000 year Greenland stratigraphic ice core chronology. *Clim Past* 4(1): 47–57.

Tanner AB (1964) Radon migration in the ground: a review. In: Adams JAS, Lowder WM (ed) *Natural Radiation Environment*. University of Chicago Press, Chicago, pp. 161–190.

Tanner AB (1980) Radon migration in the ground: A supplementary review. In: Gesell, Lowder WM (ed) *Proceedings of the Symposium on Third Natural Radiation Environment 1*, Houston, pp. 5–56.

Tareen ADK, Rafique M, Basharat M (2019) Study of diurnal and seasonal variations in the time series data of soil  $^{222}\text{Rn}$  gas. *Int J Environ Anal Chem* 101:337–350. doi: 10.1080/03067319.2019.1666834.

Tatzber M, Stemmer M, Spiegel H, Katzlberger C, Haberhauer G, Gerzabek MH (2007) An alternative method to measure carbonate in soils by FT-IR spectroscopy. *Environ Chem Let* 5:9–12. doi: 10.1007/s10311-006-0079-5.

Thornalley DJR, Oppo DW, Ortega P, Robson JI, Brierley CM, Davis R, et al. (2018) Anomalously weak Labrador Sea convection and Atlantic overturing during the past 150 years. *Nat* 556:227–230.

Thorndycraft VR, Benito G, Rico M, Sopena A, Sánchez-Moya Y, Casas A (2005) A long-term flood discharge record derived from slackwater flood deposits of the Llobregat River, NE Spain. *J Hydro* 313(1–2):16–31. doi: 10.1016/j.jhydrol.2005.02.003.

Tirmarache M, Harrison J, Laurier D, Blanchardon E, Paquet F, Marsh J (2012) Risk of lung cancer from radon exposure: contribution of recently published studies of uranium miners. *Ann ICRP* 41:368–377. doi: 10.1016/j.icrp.2012.06.033.

Tollefsen T, Cinelli G, Bossew P, Gruber V, De Cort M (2014) From the European indoor radon map towards an atlas of natural radiation. *Radiat Prot Dosimetry* 162(1–2):129–134. doi: 10.1093/rpd/ncu244.

Torrence C, Compo GP (1998) A practical guide to wavelet analysis. *Bull Am Meteor Soc* 79(1):61–78.

Tuccimei P, Soligo M (2008) Correction for CO<sub>2</sub> interference in soil radon flux measurements. *Radiation Measurements* 43(1):102–105. doi: 10.1016/j.radmeas.2007.05.056.

Turekian KK, Graustein WC (2003) Natural Radionuclides in the Atmosphere. In: Keeling RF, Holland HD, Turekian KK (ed) *Treatise on Geochemistry Vol. 4 The Atmosphere*, Elsevier, Amsterdam, pp. 261–279. doi: 10.1016/B0-08-043751-6/04042-1.

UNISDR CRED (2015) *The human cost of natural disasters. A global perspective*. Centre for research on the epidemiology of disasters. Brussels, Belgium.

UNSCEAR (1982) *Ionizing radiation: Sources and biological effects*. UNSCEAR 1982 Report, New York.

- Valet J-P, Valladas H (2010) The Laschamp-Mono lake geomagnetic events and the extinction of Neanderthal: a causal link or a coincidence? *Quat Sci Lett* 29(27–28):3887–3893. doi: 10.1016/j.quascirev.2010.09.010.
- Van Geel B, Bos J, Van Huissteden J, Pals J, Schatz H, Van Mourik J, et al. (2010) Palaeoecological study of a Weichselian wetland site in the Netherlands suggests a link with Dansgaard-Oeschger climate oscillation. *Neth J Geosci* 89(3–4):187–201. doi: 10.1017/S001677460000069X.
- Van Huissteden J (1990) Tundra rivers of the last glacial: sedimentation and geomorphological processes during the Middle Pleniglacial (Eastern Netherlands). *Meded Rijks Geol Dienst* 44(3):1–138.
- Van Kreveld S, Sarnthein M, Erlenkeuser H, Grootes P, Jung S, Nadeau MJ, Pflaumann U, et al. (2004) Potential links between surging ice sheets, circulation changes and the Dansgaard-Oeschger cycles in the Irminger Sea, 60-19 Kyr. *Paleoceanography* 15(4):425–442. doi: 10.1029/1999PA000464.
- Vandenbergh J (2003) Climate forcing of fluvial system development: an evolution of ideas. *Quat Sci Rev* 22(20):2053–2060. doi: 10.1016/S0277-3791(03)00213-0.
- Vandenbergh J, van der Plicht J (2016) The age of the Hengelo interstadial revisited. *Quat Geochro* 32:21–28. doi: 10.1016/j.quageo.2015.12.004.
- Verpaelst M, Fortier D, Kanevskiy M, Paquette M, Shur Y (2017) Syngenetic dynamic of permafrost of a polar desert solifluction lobe, Ward Hunt Island, Nunavut. *Arctic Sci* 3(2):301–319. doi: 10.1139/as-2016-0018.
- Vinther BM, Clausen HB, Johnsen SJ, Rasmussen SO, Andersen KK, Buchardt SL, et al. (2006) A synchronized dating of three Greenland ice cores throughout the Holocene. *J Geophys Res Atmospheres* 111(D13):D13102. doi: 10.1029/2005JD006921.
- Vogt J, Zieger B, Glassmeier K-H, Stadelmann A, Kallenrode M-B, Sinnhuber M, et al. (2007) Energetic particles in the paleomagnetosphere: Reduced dipole configurations and quadrupolar contributions. *J Geophys Res* 112(A6):A06216.

von Storch H, Zwiers FW (2001) *Statistical Analysis in Climate Research*. Cambridge Univ. Press, Cambridge.

Wagner G, Beer J, Masarik J, Muscheler R, Kubik PW, Mende W, et al. (2001) Presence of the solar de Vries cycle (~205 years) during the last Ice Age. *Geophys Res Lett* 28(2):303–306. doi: 10.1029/2000GL006116.

Walker M, Johnsen S, Rasmussen SO, Popp T, Steffensen J-P, Gibbard P, et al. (2009) Formal definition and dating of the GSSP (Global Stratotype Section and Point) for the base of the Holocene using the Greenland NGRIP ice core, and selected auxiliary records. *J Quat Sci* 24(1):3–17.

Wang Y, Cheng H, Edwards RL, He Y, Kong X, An Z, et al. (2005) The Holocene Asian monsoon: links to solar changes and North Atlantic climate. *Sci* 308(5723):854–857.

Wernli H, Pfahl S (2009) Grundlage des Klimas und extremer Wettersituationen. In Sirocko F (ed) *Wetter, Klima, Menschheitsentwicklung. Von der Eiszeit bis ins 21. Jahrhundert*. Theiss, Stuttgart, pp. 44–52.

Wiederhold H, Agster G, Binot F, Kirsch R (2003) Geophysical investigations on the connection between salt structures and aquifers in Schleswig-Holstein. In: Mares S, Pospisil L (ed) *Proceedings 9th Meeting Environmental and Engineering Geophysics: P-065*, Prague. doi: 10.3997/2214-4609.201414638.

Wilhelm B, Arnaud F, Enters D, Allignol F, Legaz A, Magand O, et al. (2012) Does global warming favour the occurrence of extreme floods in European Alps? First evidence from a NW Alps proglacial lake sediment record. *Clim Chang* 113:563–581. doi: 10.1007/s10584-011-0376-2.

Williams AG, Zahorowski W, Chambers S, Griffiths A, Hacker JM, Element A, et al. (2011) The Vertical Distribution of Radon in Clear and Cloudy Daytime Terrestrial Boundary Layers. *J Atmos Sci* 68(1):155–174. doi: 10.1175/2010JAS3576.1.

- Winkler R, Ruckerbauer F, Bunzl K (2001) Radon concentration in soil gas: a comparison of the variability resulting from different methods, spatial heterogeneity and seasonal fluctuations. *Sci Total Environ* 272(1–3):273–282. doi: 10.1016/S0048-9697(01)00704-5.
- Winkler H, Sinnhuber M, Notholt J, Kallenrode M-B, Steinhilber F, Vogt J, et al. (2008) Modeling impacts of geomagnetic field variations on middle atmospheric ozone responses to solar proton events on long timescales. *J Geophys Res* 113(D2):D02302. doi: 10.1029/2007JD008574.
- Wirth SB, Girardclos S, Rellstab C, Anselmetti FS (2001) The sedimentary response to a pioneer geo-engineering project: Tracking the Kander River deviation in the sediments of Lake Thun (Switzerland). *Sedimentol* 58(7):1737–1761. doi: 10.1111/j.1365-3091.2011.01237.x.
- Wohlfarth B, Björck S, Funder S, Houmark-Nielsen M, Ingólfsson Ó, Lunkka J-P, et al. (2008a) Quaternary of Norden. *Episodes* 31(1):73–81. doi: 10.18814/epiiugs/2008/v31i1/011.
- Wohlfarth B, Veres D, Ampel L, Lacourse T, Blaauw M, Preusser F, et al. (2008b) Rapid ecosystem response to abrupt climate changes during the last glacial period in western Europe, 40 – 16 ka. *Geology* 36(5):407–410. doi: 10.1130/G24600A.1.
- Woith H (2015) Radon earthquake precursor: A short review. *Eur Phys J Special Top* 224:611–627. doi: 10.1140/epjst/e2015-02395-9.
- Wolfe AP, Vinebrooke RD, Michelutti N, Rivard B, Das B (2006) Experimental calibration of lake-sediment spectral reflectance to chlorophyll *a* concentrations: methodology and paleolimnological validation. *J Paleolimnol* 36:91–100. doi: 10.1007/s10933-006-0006-6.
- World Health Organisation (2009) WHO Handbook on Indoor radon: A Public Health Perspective. Geneva.
- Woźniak PP, Czubla P (2015) The Late Weichselian glacial record in northern Poland: A new look at debris transport routes by the Fennoscandian Ice Sheet. *Quat Int* 386:3–17. doi: 10.1016/j.quaint.2015.01.014.

Wulf S, Hardiman MJ, Staff RA, Koutsodendris A, Appelt O, Blockley SPE, et al. (2018) The marine isotope stage 1–5 cryptotephra record of Tenaghi Philippon, Greece: Towards a detailed tephrostratigraphic framework for the Eastern Mediterranean region. *Quat Sci Rev* 186:236–262. doi: 10.1016/j.quascirev.2018.03.011.

Yan R, Woith H, Wang R, Wang G (2017) Decadal radon cycles in a hot spring. *Sci Rep* 7:1–12. doi: 10.1038/s41598-017-12441-0.

Yang J, Busen H, Scherb H, Hürkamp K, Guo Q, Tschiersch J (2019) Modeling of radon exhalation from soil influenced by environmental parameters. *Sci Total Environ* 656:1304–1311. doi: 10.1016/j.scitotenv.2018.11.464.

Ye Y, Chen G, Dai X, Huang C, Yang R, Kearfott KJ (2019) Experimental study of the effect of water level and wind speed on radon exhalation of uranium tailings from heap leaching uranium mines. *Environ Sci Pollut Res* 26:25702–25711. doi: 10.1007/s11356-019-05788-6.

Zhang R, Sutton R, Danabasoglu G, Kwon Y-O, Marsh R, Yeager SG, et al. (2019) A review of the role of the Atlantic meridional overturning circulation in Atlantic multidecadal variability and associated climate impacts. *Rev Geophys* 57(2):316–375.

## 7 Supplements

Profile: BS1		Date: 04.04.2019		Profile length: 3.37km		Sampling time: 2h		Temp.: 13.9°C		Atm. pressure: 997.7hPa		Air moisture: 60%	
Sampling point	<sup>222</sup> Rn flux	<sup>222</sup> Rn-Index	Water content	Bulk density wet	Bulk density dry	Permeability (k <sub>r</sub> value) Seiler	Permeability (k <sub>r</sub> value) Bayer	Mean grain size	LOI	Carbonate cont.			
	[mBq/m <sup>2</sup> s]	[-]	[wt%]	[g/cm <sup>3</sup> ]	[g/cm <sup>3</sup> ]	[m/s]	[m/s]	[µm]	[%]	[%]			
1	1.68	0.98	15.11	1.23	1.05	5.53E-05	2.13E-05	347	7.00	0.04			
2	1.20	0.70	11.43	1.20	1.07	1.00E-04	4.72E-05	434	6.33	0.02			
3	0.65	0.38	14.45	1.16	0.99	1.12E-04	5.96E-05	541	8.33	0.03			
4	1.07	0.63	9.87	1.28	1.15	9.52E-05	4.01E-05	387	5.67	0.02			
5	1.48	0.87	9.95	1.37	1.24	3.75E-05	2.00E-05	331	7.00	0.02			
6	2.43	1.42	15.71	1.29	1.07	4.17E-05	2.22E-05	380	9.00	0.09			
7	2.02	1.19	11.92	1.39	1.23	1.20E-05	8.97E-06	423	8.00	0.07			
8	1.78	1.04	11.23	1.19	1.05	7.60E-05	4.05E-05	535	10.00	0.08			
9	3.82	2.24	10.39	1.35	1.21	-	8.82E-06	634	7.33	0.09			
10	2.37	1.39	14.14	1.51	1.30	4.38E-06	4.57E-06	428	8.33	0.08			
11	1.98	1.16	15.22	1.22	1.03	1.75E-05	9.07E-06	354	7.67	0.08			
12	0.48	0.28	13.06	1.65	1.43	3.38E-06	2.26E-06	265	7.33	0.07			
13	1.22	0.71	23.97	1.19	0.90	-	-	-	-	-			

**Supplementary Table 1 Radon flux values, radon indices and physical properties of soil samples of profile BS1.**

Profile: BS2		Date: 16.07.2019		Profile length: 3.69km		Sampling time: 2h		Temp.: 19.5°C		Atm. pressure: 1012.0hPa		Air moisture: 60%	
Sampling point	<sup>222</sup> Rn flux	<sup>222</sup> Rn-Index	Water content	Bulk density wet	Bulk density dry	Permeability (k <sub>r</sub> value) Seiler	Permeability (k <sub>r</sub> value) Bayer	Mean grain size	LOI	Carbonate cont.			
	[mBq/m <sup>2</sup> s]	[-]	[wt%]	[g/cm <sup>3</sup> ]	[g/cm <sup>3</sup> ]	[m/s]	[m/s]	[µm]	[%]	[%]			
1	1.10	0.43	13.50	1.47	1.27	2.85E-05	1.52E-05	316	8.33	0.11			
2	0.98	0.38	12.05	1.19	1.04	7.12E-05	2.65E-05	271	8.67	0.01			
3	0.69	0.27	5.88	1.44	1.35	3.23E-05	1.35E-05	181	3.33	0			
4	1.76	0.68	8.50	1.14	1.05	-	4.09E-05	223	8.67	0			
5	2.78	1.08	7.98	1.29	1.19	3.46E-05	1.29E-05	215	9.67	0.01			
6	2.83	1.10	9.40	1.18	1.07	5.03E-05	2.12E-05	243	10.00	0.06			
7	2.48	0.96	10.45	1.23	1.11	2.18E-05	1.03E-05	270	9.00	0.09			
8	2.87	1.11	12.71	1.20	1.05	1.48E-05	8.80E-06	295	7.67	0.06			
9	3.02	1.17	9.91	1.12	1.01	1.44E-05	8.52E-06	309	8.67	0.07			
10	2.99	2.32	12.44	1.06	0.93	2.07E-05	1.22E-05	313	7.33	0.06			
11	3.11	1.20	9.31	1.12	1.02	1.33E-05	7.10E-06	274	10.00	0.04			
12	4.77	1.85	2.85	1.26	1.22	-	2.23E-04	424	1.33	0.73			
13	1.16	0.45	13.31	1.45	1.26	6.10E-06	3.61E-06	236	-	0.04			

**Supplementary Table 2 Radon flux values, radon indices and physical properties of soil samples of profile BS2.**

Profile: BS3		Date: 16.07.2019		Profile length: 3.69km		Sampling time: 2h		Temp.: 17.5°C		Atm. pressure: 1013.0hPa		Air moisture: 67%	
Sampling point	<sup>222</sup> Rn flux	<sup>222</sup> Rn-Index	Water content	Bulk density wet	Bulk density dry	Permeability (k <sub>r</sub> value) Seiler	Permeability (k <sub>r</sub> value) Bayer	Mean grain size	LOI	Carbonate cont.			
	[mBq/m <sup>2</sup> s]	[-]	[wt%]	[g/cm <sup>3</sup> ]	[g/cm <sup>3</sup> ]	[m/s]	[m/s]	[µm]	[%]	[%]			
1	1.30	0.64	13.50	1.47	1.27	2.85E-05	1.52E-05	316	8.33	0.11			
2	0.88	0.43	12.05	1.19	1.04	7.12E-05	2.65E-05	271	8.67	0.01			
3	1.00	0.49	5.88	1.44	1.35	3.23E-05	1.35E-05	181	3.33	0			
4	1.60	0.78	8.50	1.14	1.05	-	4.09E-04	223	8.67	0			
5	2.45	1.20	7.98	1.29	1.19	3.46E-05	1.29E-05	215	9.67	0.01			
6	2.18	1.07	10.45	1.23	1.11	2.18E-05	1.03E-05	270	9.00	0.09			
7	3.42	1.67	9.91	1.12	1.01	1.44E-05	8.52E-06	309	8.67	0.07			
8	3.64	1.78	12.44	1.06	0.93	2.07E-05	1.22E-05	313	7.33	0.06			
9	3.03	1.48	9.31	1.12	1.02	1.33E-05	7.10E-06	274	10.00	0.04			
10	2.31	1.13	2.85	1.26	1.22	-	2.23E-04	424	1.33	0.73			
11	0.67	0.33	13.31	1.45	1.26	6.10E-06	3.61E-06	236	-	0.04			

**Supplementary Table 3 Radon flux values, radon indices and physical properties of soil samples of profile BS3.**

Profile: BS4		Date: 17.07.2019		Profile length: 3.69km		Sampling time: 2h		Temp.: 15.7°C		Atm. pressure: 1013.9hPa		Air moisture: 77%	
Sampling point	<sup>222</sup> Rn flux	<sup>222</sup> Rn-Index	Water content	Bulk density wet	Bulk density dry	Permeability (k <sub>r</sub> value) Seiler	Permeability (k <sub>r</sub> value) Bayer	Mean grain size	LOI	Carbonate cont.			
	[mBq/m <sup>2</sup> s]	[-]	[wt%]	[g/cm <sup>3</sup> ]	[g/cm <sup>3</sup> ]	[m/s]	[m/s]	[µm]	[%]	[%]			
1	1.42	0.68	13.50	1.47	1.27	2.85E-05	1.52E-05	316	8.33	0.11			
2	0.98	0.47	12.05	1.19	1.04	7.12E-05	2.65E-05	271	8.67	0.01			
3	1.21	0.58	5.88	1.44	1.35	3.23E-05	1.35E-05	181	3.33	0			
4	2.26	1.08	8.50	1.14	1.05	-	4.09E-05	223	8.67	0			
5	1.69	0.81	7.98	1.29	1.19	3.46E-05	1.29E-05	215	9.67	0.01			
6	2.23	1.07	9.40	1.18	1.07	5.03E-05	2.12E-05	243	10.00	0.06			
7	2.54	1.21	10.45	1.23	1.11	2.18E-05	1.03E-05	270	9.00	0.09			
8	2.72	1.30	12.71	1.20	1.05	1.48E-05	8.80E-06	295	7.67	0.06			
9	2.91	1.39	9.91	1.12	1.01	1.44E-05	8.52E-06	309	8.67	0.07			
10	4.18	2.00	12.44	1.06	0.93	2.07E-05	1.22E-05	313	7.33	0.06			
11	2.59	1.24	9.31	1.12	1.02	1.33E-05	7.10E-06	274	10.00	0.04			
12	1.64	0.78	2.85	1.26	1.22	-	2.23E-04	424	1.33	0.73			
13	0.83	0.40	13.31	1.45	1.26	6.10E-06	3.61E-06	236	-	0.04			

**Supplementary Table 4 Radon flux values, radon indices and physical properties of soil samples of profile BS4.**



Profile: BS5	Date: 14.08.2018	Profile length: 495m	Sampling time: 1h
Temp.: 23.2°C	Atm. pressure: 1007.0hPa	Air moisture: 65%	
Sampling point	<sup>222</sup> Rn flux	<sup>222</sup> Rn- Index	
	[mBq/m <sup>2</sup> s]	[-]	
1	0.59	0.57	
2	1.06	1.03	
3	0.67	0.65	
4	0.70	0.68	
5	1.17	1.14	
6	0.85	0.82	
7	0.58	0.56	
8	0.42	0.41	
9	0.64	0.62	
10	0.47	0.46	
11	2.42	2.35	
12	1.75	1.70	
13	1.00	0.97	
14	2.08	2.02	

**Supplementary Table 5 Radon flux values and radon indices of profile BS5.**

Profile: BS6	Date: 03.04.2019	Profile length: 495m	Sampling time: 2h
Temp.: 10.8°C	Atm. pressure: 1002.5hPa	Air moisture: 89%	
Sampling point	<sup>222</sup> Rn flux	<sup>222</sup> Rn- Index	
	[mBq/m <sup>2</sup> s]	[-]	
1	1.77	0.74	
2	2.71	1.13	
3	3.28	1.37	
4	2.31	0.97	
5	1.81	0.76	
6	3.39	1.42	
7	2.17	0.91	
8	1.00	0.42	
9	1.93	0.81	
10	1.98	0.83	
11	3.63	1.52	
12	2.59	1.08	
13	3.41	1.43	
14	2.29	0.96	
15	1.20	0.50	
16	2.77	1.16	

**Supplementary Table 6 Radon flux values and radon indices of profile BS6.**

Profile: EC1		Date: 08.04.2019		Profile length: 11.76km		Sampling time: 2h		Temp.: 8.1°C		Atm. pressure: 1011.8hPa		Air moisture: 65%	
Sampling point	<sup>222</sup> Rn flux	<sup>222</sup> Rn-Index	Water content	Bulk density wet	Bulk density dry	Permeability (k <sub>r</sub> value) Seiler	Permeability (k <sub>r</sub> value) Bayer	Mean grain size	LOI	Carbonate cont.			
	[mBq/m <sup>2</sup> s]	[-]	[wt%]	[g/cm <sup>3</sup> ]	[g/cm <sup>3</sup> ]	[m/s]	[m/s]	[µm]	[%]	[%]			
1	0.27	0.13	15.38	1.09	0.92	1.12E-05	4.70E-06	154	6.33	0			
2	2.27	1.14	16.69	1.39	1.16	1.02E-05	4.81E-06	193	7.33	0			
3	0.43	0.22	16.18	1.46	1.22	4.49E-06	2.99E-06	288	6.33	0.01			
4	6.67	3.34	13.72	1.53	1.32	4.28E-06	2.28E-06	197	4.67	0			
5	2.42	1.21	13.05	1.37	1.19	4.28E-06	1.80E-06	198	4.33	0			
6	1.33	0.66	12.98	1.51	1.32	7.50E-06	3.53E-06	162	4.67	0			
7	0.88	0.44	15.85	1.16	0.97	5.19E-05	2.19E-05	300	5.33	0			
8	1.86	0.93	13.84	1.24	1.07	4.23E-06	2.51E-06	226	5.67	0			
9	1.49	0.74	12.59	1.61	1.41	3.91E-06	2.32E-06	220	3.67	0			
10	>7.85	>3.93	11.79	1.62	1.43	4.59E-06	2.45E-06	187	3.67	0.03			
11	0.68	0.34	13.98	1.60	1.37	4.13E-06	2.20E-06	188	5.33	0			
12	1.33	0.67	16.33	1.71	1.43	4.13E-06	2.45E-06	207	7.67	0			
13	2.16	1.08	12.61	1.48	1.29	4.64E-06	2.75E-06	212	4.00	0			
14	0.35	0.17	11.09	1.30	1.16	1.53E-05	7.20E-06	226	4.33	0			
15	0.94	0.47	16.05	1.54	1.29	9.79E-06	4.61E-06	181	3.00	0			
16	1.04	0.52	8.24	1.67	1.53	8.04E-05	2.99E-05	253	1.67	0.06			

**Supplementary Table 7 Radon flux values, radon indices and physical properties of soil samples of profile EC1.**

Profile: EC2		Date: 09.04.2019		Profile length: 4.70km		Sampling time: 2h		Temp.: 5.5°C		Atm. pressure: 1015.7hPa		Air moisture: 51%	
Sampling point	<sup>222</sup> Rn flux	<sup>222</sup> Rn-Index	Water content	Bulk density wet	Bulk density dry	Mean grain size	LOI	Carbonate cont.					
	[mBq/m <sup>2</sup> s]	[-]	[wt%]	[g/cm <sup>3</sup> ]	[g/cm <sup>3</sup> ]	[µm]	[%]	[%]					
1	3.06	1.52	36.38	1.83	1.16	271	5.00	0					
2	2.82	1.40	10.93	1.74	1.55	265	4.33	0					
3	1.11	0.55	12.93	1.39	1.21	201	5.67	0					
4	1.93	0.96	13.90	1.61	1.38	274	5.00	0					
5	0.92	0.46	14.98	1.54	1.31	349	6.67	0.01					
6	1.47	0.73	14.45	1.44	1.23	367	5.00	0					
7	0.59	0.29	11.96	1.40	1.23	422	5.33	0					
8	3.53	1.75	13.75	1.23	1.06	196	5.00	0					
9	1.13	0.56	12.56	1.45	1.27	230	5.00	0					
10	0.48	0.24	13.97	1.71	1.47	221	5.00	0					
11	>7.85	>3.89	11.64	1.58	1.39	185	2.00	0.03					
12	1.14	0.57	18.56	1.27	1.04	381	5.67	0					
13	1.61	0.80	12.54	1.45	1.27	373	3.67	0					
14	2.55	1.27	14.66	1.39	1.19	212	4.33	0					
15	1.25	0.62	19.83	1.47	1.18	217	3.67	0					
16	0.82	0.41	12.43	1.55	1.36	319	4.33	0					

**Supplementary Table 8 Radon flux values, radon indices and physical properties of soil samples of profile EC2.**

Profile: EC3	Date: 17.07.2019	Profile length: 11.76km	Sampling time: 2h	Temp.: 18.6°C	Atm. pressure: 1010.9hPa	Air moisture: 72%	
Sampling point	<sup>222</sup> Rn flux	<sup>222</sup> Rn- Index	Water content	Bulk density wet	Bulk density dry	Mean grain size	LOI
	[mBq/m <sup>2</sup> s]	[-]	[wt%]	[g/cm <sup>3</sup> ]	[g/cm <sup>3</sup> ]	[µm]	[%]
1	1.17	0.62	12.89	1.18	1.03	166	6.67
2	2.40	1.27	11.30	1.13	1.01	190	7.67
3	0.83	0.44	16.13	1.36	1.14	210	5.33
4	4.63	2.45	10.70	1.03	0.92	196	6.67
5	3.49	1.85	18.75	1.17	0.95	193	8.33
6	1.66	0.88	5.82	1.39	1.31	184	4.00
7	0.77	0.41	5.05	1.35	1.28	179	3.00
8	0.91	0.48	6.10	1.35	1.27	145	3.67
9	1.15	0.61	6.94	1.29	1.20	181	4.33
10	1.13	0.60	10.64	1.44	1.28	175	4.67
11	2.69	1.57	6.12	0.97	0.91	286	4.00
12	1.26	0.67	10.77	1.15	1.02	182	4.33
13	1.48	0.78	19.21	1.32	1.07	254	4.33
14	2.64	1.40	15.75	0.75	0.63	210	10.33

**Supplementary Table 9 Radon flux values, radon indices and physical properties of soil samples of profile EC3.**

Profile: EC4	Date: 18.07.2019	Profile length: 4.89km	Sampling time: 2h	Temp.: 18.2°C	Atm. pressure: 1009.4hPa	Air moisture: 77%		
Sampling point	<sup>222</sup> Rn flux	<sup>222</sup> Rn- Index	Water content	Bulk density wet	Bulk density dry	Mean grain size	LOI	Carbonate cont.
	[mBq/m <sup>2</sup> s]	[-]	[wt%]	[g/cm <sup>3</sup> ]	[g/cm <sup>3</sup> ]	[µm]	[%]	[%]
1	0.84	0.57	14.83	1.33	1.13	314	6.67	0
2	0.67	0.45	10.82	1.56	1.39	496	5.33	0
3	1.47	1.00	9.50	1.35	1.23	249	7.33	0
4	1.73	1.17	7.73	1.32	1.22	237	6.67	0
5	1.20	0.81	21.13	1.17	0.92	264	6.33	0.03
6	1.27	0.86	7.35	1.58	1.47	207	4.33	0
7	1.93	1.31	9.49	1.16	1.50	243	7.00	0.01
8	3.15	2.13	5.82	1.27	1.20	226	4.67	0
9	1.77	1.20	7.80	1.20	1.11	249	5.33	0.01
10	0.81	0.55	5.46	1.37	1.30	233	5.67	0
11	0.49	0.33	4.71	1.11	1.06	268	5.33	0
12	0.98	0.67	8.39	1.20	1.10	332	4.67	0
13	2.49	1.68	16.93	0.82	0.68	205	6.00	0
14	1.89	1.28	18.68	1.50	1.22	267	7.00	0

**Supplementary Table 10 Radon flux values, radon indices and physical properties of soil samples of profile EC4.**

Profile: EC5	Date: 18.07.2019	Profile length: 2.79km	Sampling time: 2h	Temp.: 19.1°C	Atm. pressure: 1007.9hPa	Air moisture: 77%		
Sampling point	<sup>222</sup> Rn flux	<sup>222</sup> Rn- Index	Water content	Bulk density wet	Bulk density dry	Mean grain size	LOI	Carbonate cont.
	[mBq/m <sup>2</sup> s]	[-]	[wt%]	[g/cm <sup>3</sup> ]	[g/cm <sup>3</sup> ]	[µm]	[%]	[%]
1	0.27	0.18	19.84	1.43	1.14	274	7.33	0.01
2	0.14	0.10	7.43	1.26	1.16	270	6.33	0.08
3	0.64	0.43	5.86	1.24	1.17	184	3.67	0
4	1.38	0.92	6.24	1.15	1.08	183	5.00	0
5	1.40	0.94	5.51	1.14	1.08	224	5.33	0
6	1.43	0.95	7.90	1.11	1.02	205	3.33	0
7	0.95	0.64	7.48	1.07	0.99	259	6.67	1.01
8	2.60	1.74	16.60	1.15	0.96	205	5.33	0
9	2.55	1.71	7.96	1.12	1.03	233	6.00	0
10	1.40	0.94	9.63	1.51	1.37	275	7.00	0
11	1.30	0.87	12.94	1.36	1.18	227	4.33	0.04
12	1.77	1.18	12.79	1.53	1.33	235	4.67	0
13	3.73	2.50	6.14	1.38	1.29	287	6.00	0
14	1.37	0.91	14.68	1.03	0.88	206	7.67	0

**Supplementary Table 11 Radon flux values, radon indices and physical properties of soil samples of profile EC5.**

Profile: EC6	Date: 19.07.2019	Profile length: 10.17km	Sampling time: 2h	Temp.: 19.9°C	Atm. pressure: 1009.4hPa	Air moisture: 78%		
Sampling point	<sup>222</sup> Rn flux	<sup>222</sup> Rn- Index	Water content	Bulk density wet	Bulk density dry	Mean grain size	LOI	Carbonate cont.
	[mBq/m <sup>2</sup> s]	[-]	[wt%]	[g/cm <sup>3</sup> ]	[g/cm <sup>3</sup> ]	[µm]	[%]	[%]
1	0.76	0.36	10.85	1.14	1.02	240	5.33	0
2	0.81	0.38	8.55	1.25	1.14	291	5.33	0.07
3	4.40	2.07	11.39	1.07	0.95	212	5.67	0
4	1.51	0.71	12.29	1.53	1.34	223	2.67	0
5	1.30	0.61	9.68	1.38	1.25	283	3.67	0.01
6	2.93	1.38	18.11	1.00	0.82	363	6.00	0
7	4.11	1.94	5.65	1.04	0.98	188	3.33	0.01
8	1.13	0.53	5.38	1.02	0.97	206	3.00	0
9	2.53	1.19	17.68	1.20	0.98	247	4.67	0
10	2.16	1.02	8.14	1.02	0.94	225	2.67	0
11	0.76	0.36	9.35	1.50	1.36	376	0.67	0
12	0.96	0.45	10.34	1.13	1.01	204	2.33	0
13	2.91	1.37	11.24	1.82	1.61	344	2.00	0
14	3.43	1.62	18.71	1.64	1.34	346	3.33	0

**Supplementary Table 12 Radon flux values, radon indices and physical properties of soil samples of profile EC6.**

Profile:	Date:	Profile length:	Sampling time:	Temp.:	Atm. pressure:	Air moisture:	
EC7	19.07.2019	263m	2h	20.3°C	1010.5hPa	71%	
Sampling point	<sup>222</sup> Rn flux	<sup>222</sup> Rn-Index	Water content	Bulk density wet	Bulk density dry	Mean grain size	LOI
	[mBq/m <sup>2</sup> s]	[-]	[wt%]	[g/cm <sup>3</sup> ]	[g/cm <sup>3</sup> ]	[µm]	[%]
1	>7.85	>5.05	19.69	1.42	1.14	247	7.67
2	2.12	1.36	18.13	1.64	1.34	184	6.00
3	1.30	0.84	14.27	1.56	1.33	235	4.67
4	0.62	0.40	29.36	1.35	0.95	391	11.67
5	0.66	0.43	34.30	1.27	0.83	521	16.33
6	1.12	0.72	18.66	1.31	1.07	274	8.67
7	0.71	0.46	16.86	1.28	1.07	214	8.00
8	1.00	0.64	15.35	1.41	1.20	249	5.00
9	0.37	0.23	20.14	1.43	1.15	227	8.33
10	1.04	0.67	6.99	1.20	1.12	244	3.33
11	1.20	0.77	14.25	1.54	1.32	225	5.33
12	0.81	0.52	12.38	1.41	1.23	287	7.33
13	1.94	1.25	8.69	1.18	1.08	265	4.67
14	1.02	0.66	12.27	1.54	1.35	211	5.67

**Supplementary Table 13 Radon flux values, radon indices and physical properties of soil samples of profile EC7.**

Profile:	Date:	Profile length:	Sampling time:	Temp.:	Atm. pressure:	Air moisture:	
EC8	20.07.2019	263m	2h	22.9°C	1008.9hPa	56%	
Sampling point	<sup>222</sup> Rn flux	<sup>222</sup> Rn-Index	Water content	Bulk density wet	Bulk density dry	Mean grain size	LOI
	[mBq/m <sup>2</sup> s]	[-]	[wt%]	[g/cm <sup>3</sup> ]	[g/cm <sup>3</sup> ]	[µm]	[%]
1	5.57	3.69	19.69	1.42	1.14	247	7.67
2	2.45	1.62	18.13	1.64	1.34	184	6.00
3	1.42	0.94	14.27	1.56	1.33	235	4.67
4	2.43	1.61	29.36	1.35	0.95	391	11.67
5	0.61	0.40	34.30	1.27	0.83	521	16.33
6	1.08	0.71	18.66	1.31	1.07	274	8.67
7	0.85	0.56	16.86	1.28	1.07	214	8.00
8	0.92	0.61	15.35	1.41	1.20	249	5.00
9	0.84	0.55	20.14	1.43	1.15	227	8.33
10	0.73	0.48	6.99	1.20	1.12	244	3.33
11	1.35	0.89	14.25	1.54	1.32	225	5.33
12	0.42	0.28	12.38	1.41	1.23	287	7.33
13	1.47	0.97	8.69	1.18	1.08	265	4.67
14	1.01	0.67	12.27	1.54	1.35	211	5.67

**Supplementary Table 14 Radon flux values, radon indices and physical properties of soil samples of profile EC8.**

Profile:	Date:	Profile length:	Sampling time:	Temp.:	Atm. pressure:	Air moisture:
KN1	23.03.2018	2.45km	1h	3.1 °C	1007.0hPa	85%
Sampling point	<sup>222</sup> Rn flux	<sup>222</sup> Rn-Index	Water content	Bulk density wet	Bulk density dry	
	[mBq/m <sup>2</sup> s]	[-]	[wt%]	[g/cm <sup>3</sup> ]	[g/cm <sup>3</sup> ]	
1	0.30	0.46	26.04	1.32	0.98	
2	0.19	0.29	31.51	0.92	0.63	
3	0.06	0.09	17.31	1.72	1.42	
4	0.10	0.15	14.09	1.58	1.35	
5	1.76	2.27	19.06	1.59	1.29	
6	3.45	5.32	18.75	1.69	1.37	
7	0.87	1.34	18.57	1.57	1.28	
8	0.09	0.14	27.53	1.24	0.90	
9	0.03	0.05	27.52	1.80	1.31	
10	0.16	0.24	23.20	1.79	1.37	
11	0.13	0.20	20.86	1.38	1.09	

**Supplementary Table 15 Radon flux values, radon indices and physical properties of soil samples of profile KN1.**

Profile:	Date:	Profile length:	Sampling time:	Temp.:	Atm. pressure:	Air moisture:			
KN2	05.04.2019	2.35km	2h	9.9 °C	1005.6	81%			
Sampling point	<sup>222</sup> Rn flux	<sup>222</sup> Rn-Index	Water content	Bulk density wet	Bulk density dry	Permeability (kr value) Seiler	Permeability (kr value) Bayer	Mean grain size	LOI
	[mBq/m <sup>2</sup> s]	[-]	[wt%]	[g/cm <sup>3</sup> ]	[g/cm <sup>3</sup> ]	[m/s]	[m/s]	[µm]	[%]
1	2.23	0.63	9.28	1.28	1.17	1.29E-04	5.43E-05	268	2.67
2	0.78	0.22	13.11	1.17	1.01	2.12E-05	9.96E-06	244	4.33
4	0.91	0.26	12.73	1.31	1.14	7.10E-06	3.79E-06	324	4.67
5	>7.85	>2.90	12.90	1.80	1.57	7.88E-06	3.32E-06	373	3.00
6	0.71	0.20	-	1.51	-	-	-	-	3.33
7	1.32	0.37	-	1.41	-	8.78E-06	3.70E-06	397	4.67
8	1.44	0.41	14.58	1.64	1.40	3.92E-06	2.32E-06	335	3.33
9	0.41	0.11	14.51	1.40	1.19	6.07E-06	3.60E-06	290	4.33
10	>7.85	2.54	16.47	1.29	1.07	8.02E-06	3.38E-06	245	6.33
11	2.26	0.64	17.48	1.51	1.25	4.85E-06	2.28E-06	300	5.67
12	>7.85	>2.90	14.77	1.60	1.36	3.93E-06	2.62E-06	326	4.00
13	>7.85	>2.90	16.16	1.50	1.26	3.78E-06	2.01E-06	348	4.67
14	2.50	0.71	11.68	1.08	0.96	-	-	315	4.00
15	1.36	0.38	15.10	0.93	0.79	5.31E-06	2.50E-06	268	6.33
16	0.45	0.13	12.59	1.00	0.87	1.61E-05	6.77E-06	234	2.67

**Supplementary Table 16 Radon flux values, radon indices and physical properties of soil samples of profile KN2.**

Profile: KN3	Date: 06&10.04.2019	Profile length: 2.91km	Sampling time: 1h
Temp.: 12.8°C	Atm. pressure: 1008.4hPa	Air moisture: 69%	
Sampling point	<sup>222</sup> Rn flux	<sup>222</sup> Rn- Index	
	[mBq/m <sup>2</sup> s]	[-]	
1	1.94	0.48	
2	0.78	0.19	
3	3.93	0.98	
4	1.13	0.28	
5	14.27	3.56	
6	0.35	0.09	
7	1.14	0.28	
8	4.52	1.13	
9	0.54	0.14	
10	7.04	1.75	
11	2.84	0.71	
12	>15.71	>3.91	
13	11.65	2.90	
14	1.24	0.31	
15	3.60	0.90	
16	1.18	0.30	
17	2.23	0.56	
18	0.88	0.22	
19	1.27	0.32	

**Supplementary Table 17 Radon flux values and radon indices of profile KN3.**

Profile: KN4	Date: 21.03.2018	Profile length: 198m	Sampling time: 1h	Temp.: 4.9°C	Atm. pressure: 1023.7hPa	Air moisture: 75%
Sampling point	<sup>222</sup> Rn flux	<sup>222</sup> Rn- Index	Water content	Bulk density wet	Bulk density dry	
	[mBq/m <sup>2</sup> s]	[-]	[wt%]	[g/cm <sup>3</sup> ]	[g/cm <sup>3</sup> ]	
1	0.37	0.52	37.20	1.31	0.82	
2	0.17	0.23	-	-	-	
3	3.74	5.20	-	-	-	
4	0.22	0.30	50.97	1.68	0.82	
5	0.23	0.32	-	-	-	
6	1.50	2.09	-	-	-	
7	0.55	0.76	-	-	-	
8	0.98	1.36	22.45	1.85	1.43	
9	0.54	0.74	21.81	1.60	1.25	
10	0.11	0.16	33.05	1.29	0.86	
11	0.01	0.02	31.02	1.39	0.96	
12	0.22	0.30	27.23	1.47	1.07	
13	0.72	1.00	22.78	1.72	1.33	

**Supplementary Table 18 Radon flux values, radon indices and physical properties of soil samples of profile KN4.**

Profile: KN5	Date: 22.03.2018	Profile length: 161m	Sampling time: 1h	Temp.: 5.6°C	Atm. pressure: 1008.2hPa	Air moisture: 89%
Sampling point	<sup>222</sup> Rn flux	<sup>222</sup> Rn-Index	Water content	Bulk density wet	Bulk density dry	
	[mBq/m <sup>2</sup> s]	[-]	[wt%]	[g/cm <sup>3</sup> ]	[g/cm <sup>3</sup> ]	
1	1.01	0.86	17.23	1.89	1.57	
2	0.71	0.61	17.22	1.83	1.51	
3	0.27	0.23	13.91	1.76	1.52	
4	1.08	0.92	42.80	0.92	0.53	
5	0.64	0.54	32.95	1.43	0.96	
6	7.49	6.36	16.72	1.70	1.42	
7	0.50	0.42	19.82	1.53	1.22	
8	0.37	0.31	33.81	1.60	1.06	
9	0.65	0.55	42.84	1.34	0.77	
10	0.51	0.44	35.60	1.38	0.89	
11	0.65	0.55	17.67	1.69	1.39	
12	0.85	0.72	11.52	1.69	1.49	
13	0.59	0.50	13.90	1.93	1.66	

**Supplementary Table 19 Radon flux values, radon indices and physical properties of soil samples of profile KN5.**

Profile: KN6	Date: 07.04.2019	Profile length: 103m	Sampling time: 2h	Temp.: 9.5°C	Atm. pressure: 1009.6hPa	Air moisture: 73%				
Sampling point	<sup>222</sup> Rn flux	<sup>222</sup> Rn-Index	Water content	Bulk density wet	Bulk density dry	Permeability (k <sub>r</sub> value) Seiler	Permeability (k <sub>r</sub> value) Bayer	Mean grain size	LOI	Carbonate cont.
	[mBq/m <sup>2</sup> s]	[-]	[wt%]	[g/cm <sup>3</sup> ]	[g/cm <sup>3</sup> ]	[m/s]	[m/s]	[µm]	[%]	[%]
1	>7.85	>2.88	11.32	1.70	1.51	3.00E-06	2.50E-06	328	2.67	0.06
2	2.21	0.81	10.12	1.24	1.11	5.85E-06	3.90E-06	256	3.67	0.02
3	5.21	1.91	13.47	1.73	1.50	1.83E-06	1.52E-06	312	6.67	0.01
4	3.67	1.35	14.03	1.68	1.45	2.37E-06	1.76E-06	306	5.33	0.04
5	1.11	0.41	14.44	1.71	1.46	1.97E-06	1.47E-06	264	5.33	0.02
6	0.88	0.32	17.86	1.70	1.40	4.11E-06	2.74E-06	273	6.00	0.03
7	2.28	0.84	13.67	1.62	1.40	3.34E-06	2.49E-06	300	4.33	0.02
8	2.82	1.03	12.51	1.60	1.40	4.47E-06	2.98E-06	247	3.67	-
9	0.71	0.26	16.74	1.70	1.41	3.30E-06	2.46E-06	260	3.67	0.02
10	1.91	0.70	11.60	1.47	1.30	4.53E-06	2.68E-06	226	4.33	0.04
11	2.86	1.05	13.80	1.66	1.43	5.10E-06	3.02E-06	218	3.67	0.03
12	2.26	0.83	14.54	1.50	1.28	3.40E-06	2.27E-06	250	4.67	0.05
13	3.45	1.26	16.26	1.74	1.46	3.27E-06	2.43E-06	285	5.33	0.02
14	0.72	0.26	15.07	1.78	1.52	2.60E-06	1.93E-06	271	5.33	0.02
15	3.94	1.45	12.07	1.69	1.48	2.36E-06	1.58E-06	254	4.33	0.04
16	1.77	0.65	13.18	1.57	1.36	3.33E-06	2.48E-06	277	3.33	0.02

**Supplementary Table 20 Radon flux values, radon indices and physical properties of soil samples of profile KN6.**

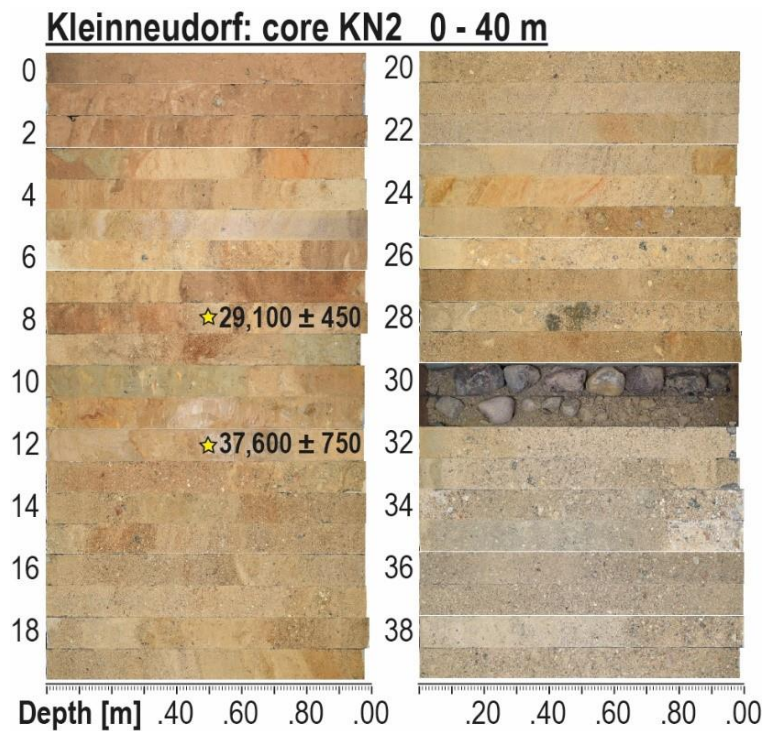


Profile: LK1		Date: 07.&08.08.2019		Profile length: 2.57km		Sampling time: 2h		Temp.: 18.8°C		Atm. pressure: 1004.9hPa		Air moisture: 81%	
Sampling point	<sup>222</sup> Rn flux	<sup>222</sup> Rn-Index	Water content	Bulk density wet	Bulk density dry	Permeability (k <sub>r</sub> value) Seiler	Permeability (k <sub>r</sub> value) Bayer	Mean grain size	LOI	Carbonate cont.			
	[mBq/m <sup>2</sup> s]	[-]	[wt%]	[g/cm <sup>3</sup> ]	[g/cm <sup>3</sup> ]	[m/s]	[m/s]	[µm]	[%]	[%]			
1	1.11	0.79	7.14	1.17	1.09	-	2.48E-04	294	11.00	0.28			
2	1.32	0.94	6.17	1.16	1.08	6.37E-06	3.77E-06	223	12.00	1.15			
3	1.75	1.25	7.35	1.14	1.05	9.56E-06	5.10E-06	223	6.00	0.06			
4	1.08	0.77	-	-	-	1.07E-05	6.33E-06	253	5.00	0.07			
5	2.10	1.49	10.91	0.91	0.81	4.21E-06	2.49E-06	203	6.00	0.11			
6	1.11	0.79	15.33	0.86	0.73	1.67E-05	7.03E-06	207	11.67	0.04			
7	3.85	2.73	8.17	1.48	1.36	6.41E-06	4.28E-06	260	7.00	0.02			
8	1.87	1.33	3.95	1.52	1.46	4.52E-06	2.68E-06	214	5.00	0.02			
9	3.01	2.14	6.38	1.04	0.97	2.55E-05	1.07E-05	207	18.67	-			
10	1.63	1.16	5.18	1.16	1.10	-	1.28E-05	156	8.00	0.02			
11	0.39	0.28	7.57	1.10	1.02	6.91E-05	4.03E-05	729	-	0.02			
12	1.10	0.78	5.69	1.22	1.15	2.02E-05	8.52E-06	177	8.00	0.03			
13	2.43	1.73	-	1.22	-	7.35E-06	4.35E-06	243	6.00	0.03			
14	0.53	0.38	-	-	-	6.71E-05	2.83E-05	304	4.67	0.02			
15	0.17	0.12	2.49	1.47	1.44	1.94E-05	9.13E-06	266	7.00	0.45			
16	0.71	0.50	7.69	1.46	1.34	8.48E-06	4.52E-06	228	4.00	0.01			
17	0.51	0.36	7.75	1.45	1.33	5.33E-06	3.55E-06	284	9.00	0.01			
18	3.46	2.46	7.43	1.51	1.40	-	-	-	4.33	-			
19	1.91	1.36	6.59	1.70	1.59	4.01E-06	2.34E-06	258	5.33	-			
20	2.50	1.77	-	-	-	-	-	216	5.67	0.02			
21	0.35	0.25	7.69	1.32	1.22	1.04E-05	5.56E-06	254	8.67	0.19			
22	0.90	0.64	11.49	1.36	1.21	8.35E-06	4.46E-06	220	7.33	0.01			
23	0.14	0.10	6.04	1.13	1.06	7.26E-06	4.84E-06	306	15.67	-			
24	0.27	0.19	18.60	1.31	1.07	6.61E-06	3.11E-06	187	6.67	0.01			
25	0.98	0.69	6.91	1.28	1.19	-	-	-	15.33	-			

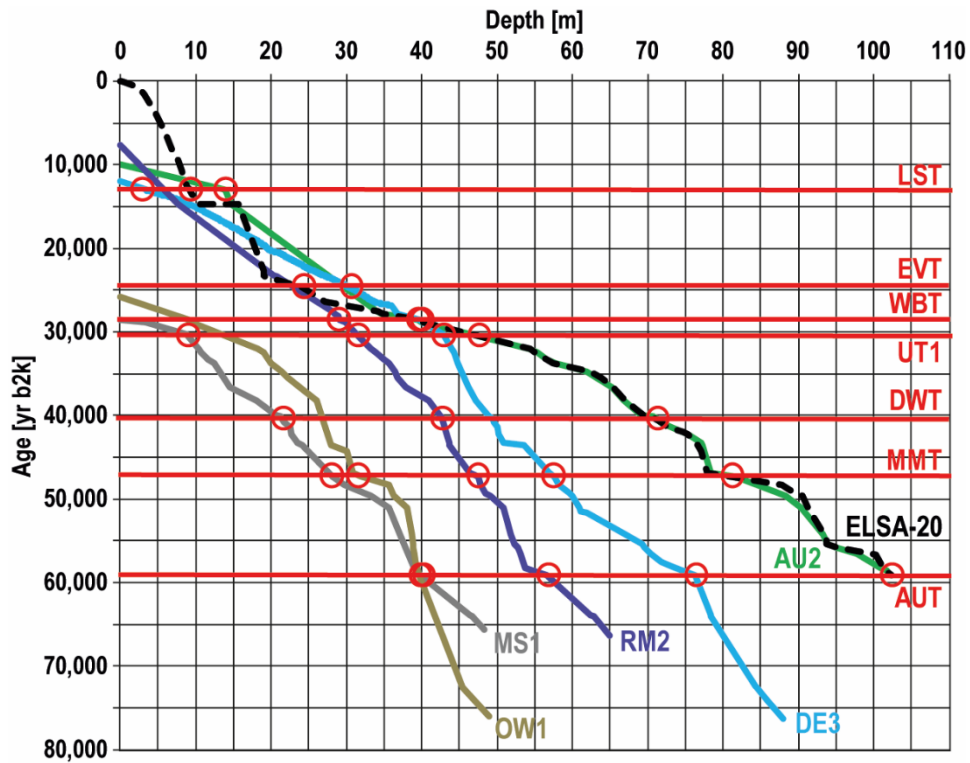
**Supplementary Table 21 Radon flux values, radon indices and physical properties of soil samples of profile LK1.**

Profile: LK2	Date: 09.08.2019	Profile length: 221m	Sampling time: 2h
Temp.: 20.3°C	Atm. pressure: 1011.2hPa	Air moisture: 69%	
Sampling point	<sup>222</sup> Rn flux	<sup>222</sup> Rn- Index	
	[mBq/m <sup>2</sup> s]	[-]	
1	1.95	0.68	
2	4.56	1.59	
3	4.04	1.41	
4	2.38	0.83	
5	2.03	0.71	
6	5.49	1.91	
7	7.67	2.67	
8	0.59	0.21	
9	0.32	0.11	
10	1.03	0.36	
11	2.84	0.99	
12	1.48	0.51	
13	1.94	0.67	
14	3.89	1.35	

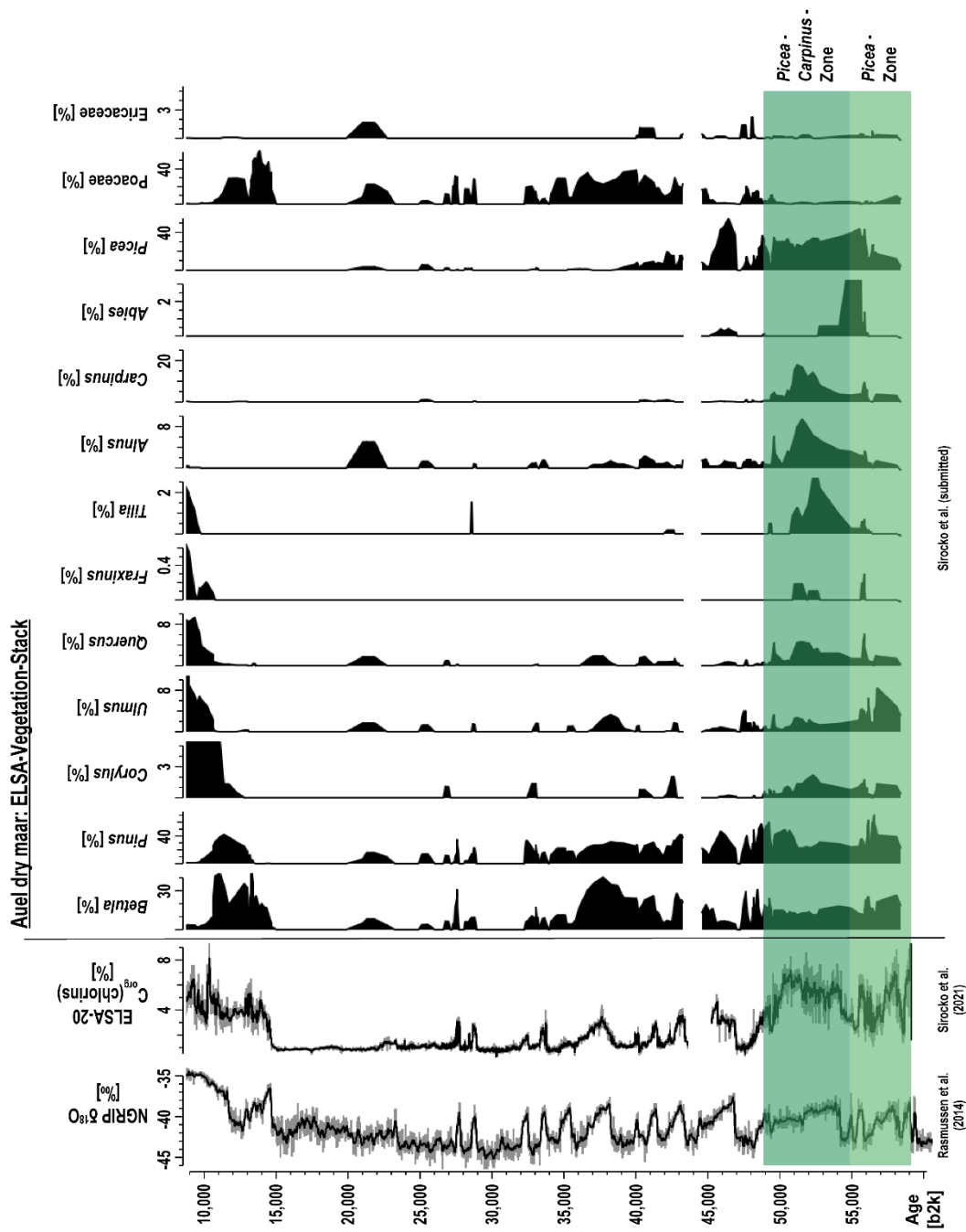
**Supplementary Table 22 Radon flux values and radon indices of profile LK2.**



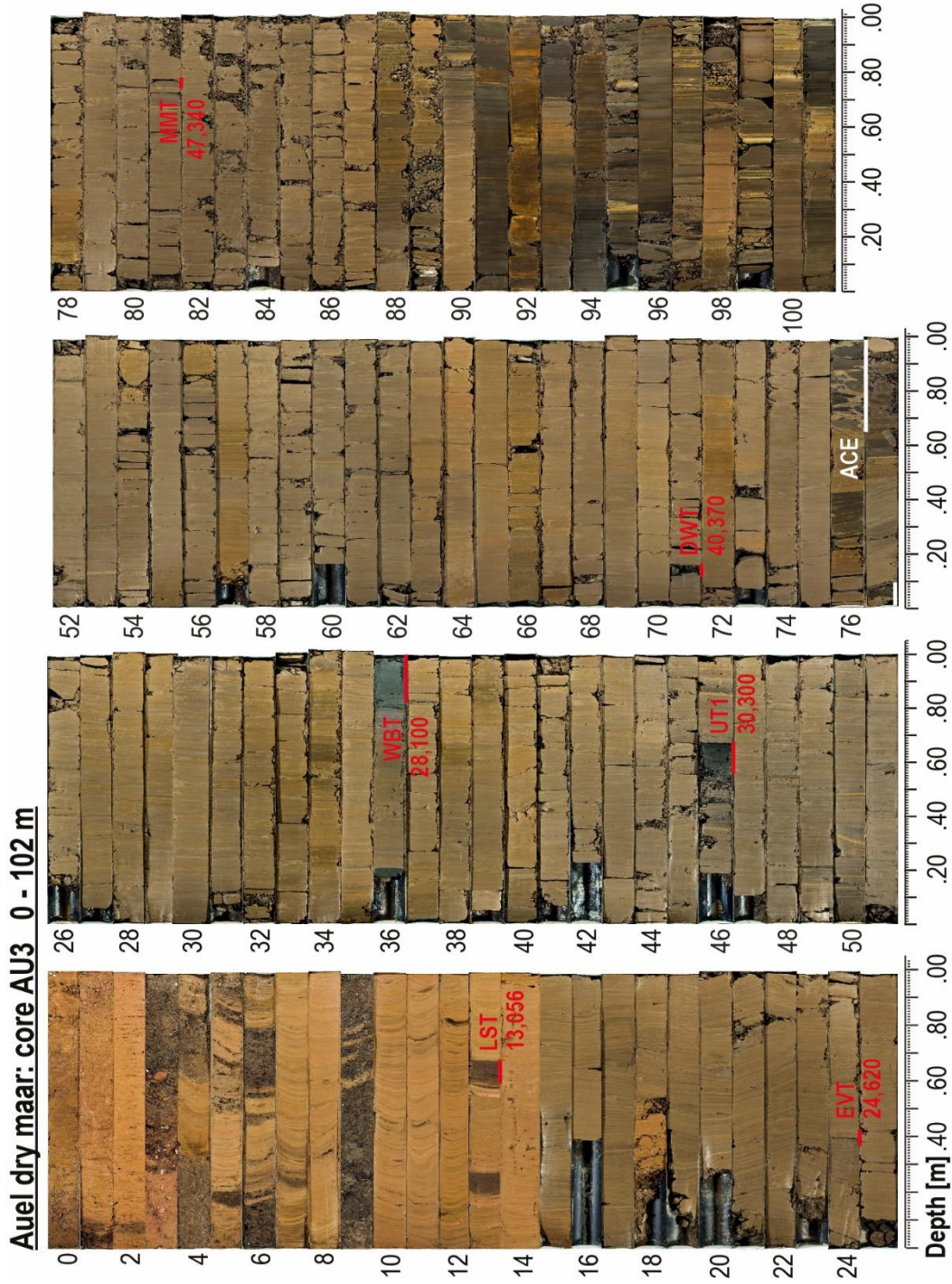
**Supplementary Fig. 1 Core photo of sediment record KN2 (Kleinneudorf). Radiocarbon dates are given in the yr b2k notation.**



**Supplementary Fig. 2** Age/depth models of cores AU2, DE3, MS1, OW1 and RM2 on basis of the ELSA-20 stratigraphy (Sirocko et al. 2021). Red circles represent exposed marker tephra layers in each core (LST — Laacher See Tephra; EVT — Eltville Tephra; WBT — Wartgesberg Tephra; UT1 — Unknown Tephra 1; DWT — Dreiser Weiher Tephra; MMT — Meerfelder Maar Tephra; AUT — Aueler Maar Tephra).



**Supplementary Fig. 3 The ELSA-20 Vegetation Stack (Sirocko et al. submitted), ELSA-20  $C_{org}$  (chlorins) record (Sirocko et al. 2021) and pollen percentages of the ELSA-20 Vegetation Stack comprised of cores HM4, AU3 and AU4 together with NGRIP temperature index (Rasmussen et al. 2014). Pollen data were smoothed using a three-point running mean. Pollen counts were performed by Frank Dreher and Sarah Britzius.**



**Supplementary Fig. 4** Core photo of sediment core AU3 with the Auel Cooling Event (ACE) and ages of marker tephra layers (Sirocko et al. 2016, 2021, Reing et al. 2021). Ages of marker layers are given in the yr b2k notation.

AU3		Ager
Sirocko et. al. 2021		
[m]	[yr b2k]	
Depth	Age	Comment
0.000	10000	Coretop (extrapolated)
13.690	13056	LST
14.680	14692	GI1 onset
18.310	23220	GI2 end
18.393	23340	GI2 onset
24.440	24620	EVT
34.450	27540	GI3 end / onset GS3
35.040	27780	GI3 onset
37.020	28100	WBT
39.820	28600	GI4 end / onset GS4
40.170	28900	GI4 onset
46.680	30300	UT1
54.310	32040	GI5.2 end / onset GS5.2
55.150	32500	GI5.2 onset
56.830	33360	GI6 end / onset GS6
57.730	33740	GI6 onset
62.105	34740	GI7 end / onset GS7
63.320	35480	GI7c onset
65.430	36580	GI8 end / onset GS8
66.870	38220	GI8c onset
69.500	39900	GI9 end / onset GS9
70.570	40160	GI9 onset
71.160	40370	DWT
71.940	40800	GI10 end / onset GS10
72.770	41460	GI10 onset
76.050	42240	GI11 end / onset GS11
76.417	43340	GI11 onset
76.600	43500	ACE top (to 77.10m)
77.485	44280	GI12 end / onset GS12 (by core photo)
78.200	46860	GI12c onset (by core photo)
81.780	47340	MMT
88.020	48340	GI13 end / onset GS13
89.920	49280	GI13c onset
90.870	49600	GI14 end / onset GS14QS
91.750	51500	GI14a onset
91.910	51660	GI14b onset
93.520	54220	GI14e onset
93.830	54900	GI15.1 end
93.850	55000	GI15.1 onset
93.970	55400	GI15.2 end / onset GS15.2
96.310	55800	GI15.2 onset
100.420	56500	GI16 end / onset GS16
100.522	56700	GI16 Corg max
101.280	58040	GI16.1c onset
101.370	58160	GI16.2 end
101.450	58280	GI16.2 onset
101.650	58560	GI17 end / onset GS17
101.960	59080	GI17.1c onset
102.000	59120	Corebase (extrapolated)

AU3 Events		
	[m]	[m]
Depth top	Depth base	Comment
0.000	6.410	Debris
7.220	7.256	Flood
9.000	10.000	Debris
10.452	10.462	Flood
10.965	10.975	Flood
11.445	11.453	Flood
11.755	11.764	Flood
11.928	11.940	Flood
12.705	12.714	Flood
12.731	12.744	Flood
13.200	13.280	LST Flood
13.590	13.690	LST
15.283	15.292	Flood
15.316	15.328	Flood
15.469	15.490	Flood
15.732	15.744	Flood
16.781	16.792	Flood
16.823	16.832	Flood
16.845	16.853	Flood
16.902	16.911	Flood
17.157	17.170	Flood
17.268	17.279	Flood
17.471	17.482	Flood
17.536	17.549	Flood
17.658	17.670	Flood
17.702	17.713	Flood
17.829	17.844	Flood
17.858	17.885	Flood
17.911	17.920	Flood
17.927	17.936	Flood
17.942	17.953	Flood
18.274	18.283	Flood
18.538	18.555	Flood
18.788	18.800	Flood
19.297	19.317	Flood
19.406	19.415	Flood
19.562	19.576	Flood
19.597	19.609	Flood
20.523	20.533	Flood
20.573	20.581	Flood
20.613	20.628	Flood
20.641	20.657	Flood
20.773	20.790	Flood
20.795	20.811	Flood
21.244	21.257	Flood
21.264	21.272	Flood
21.283	21.293	Flood
21.298	21.307	Flood
21.314	21.322	Flood

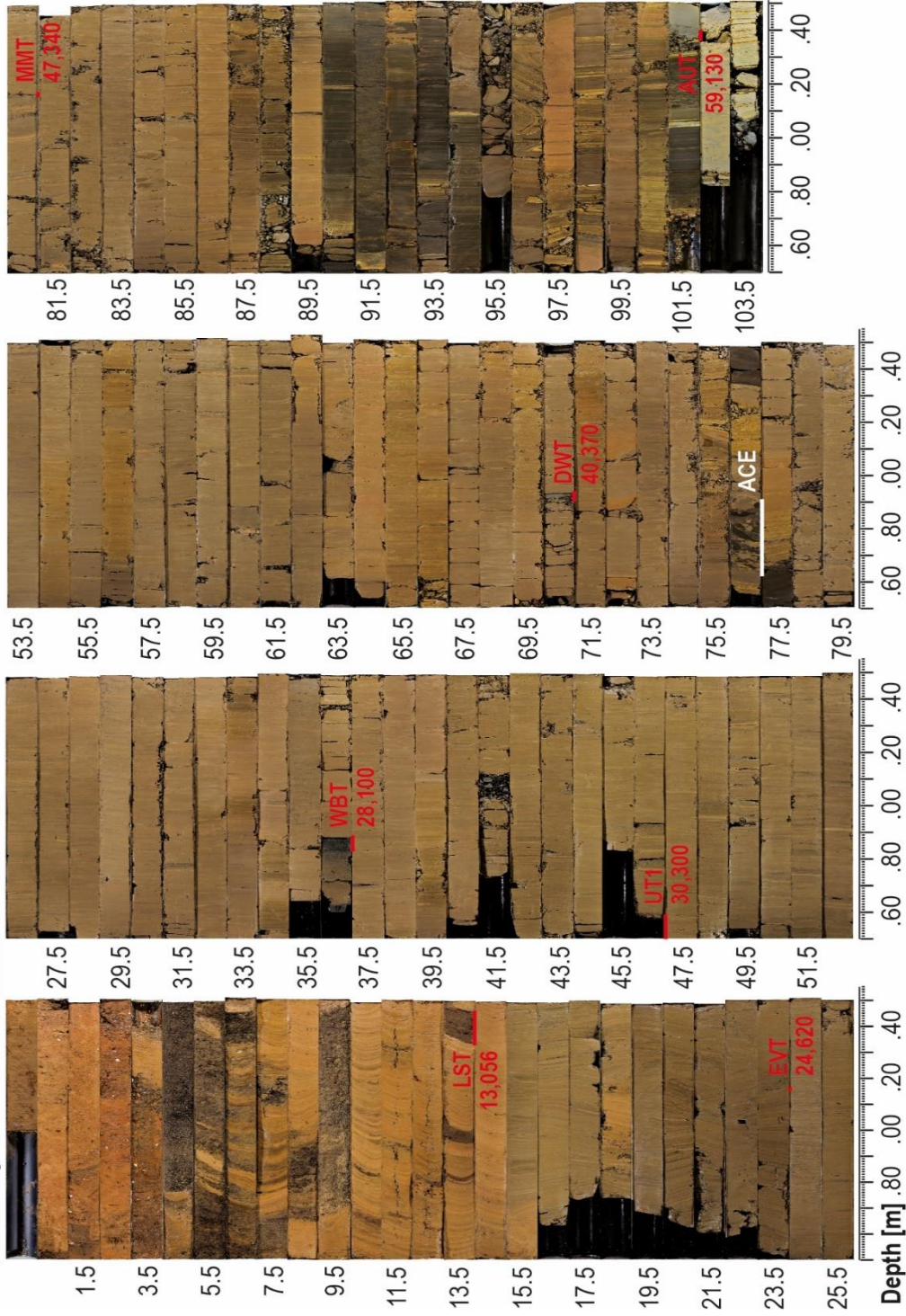
**Supplementary Table 23** Ager marker points of core AU3. Depths of event layers (floods, slumps, tephra and drilling artefacts) were subtracted from the age/depth model.

AU3 Events		
[m]	[m]	
Depth top	Depth base	Comment
21.329	21.339	Flood
21.372	21.384	Flood
21.555	21.567	Flood
21.605	21.613	Flood
21.717	21.729	Flood
21.737	21.751	Flood
21.758	21.772	Flood
21.860	21.868	Flood
22.098	22.107	Flood
22.111	22.120	Flood
22.252	22.261	Flood
22.338	22.347	Flood
22.351	22.361	Flood
22.382	22.390	Flood
22.400	22.411	Flood
22.487	22.496	Flood
22.562	22.583	Flood
22.663	22.673	Flood
22.952	22.961	Flood
23.231	23.242	Flood
23.248	23.261	Flood
23.298	23.319	Flood
24.360	24.440	<b>EVT</b>
24.640	24.649	Flood
25.310	25.336	Flood
25.423	25.431	Flood
26.264	26.274	Flood
26.404	26.416	Flood
26.576	26.586	Flood
27.325	27.333	Flood
27.394	27.403	Flood
36.000	36.210	<b>WBT</b>
36.800	37.020	<b>WBT (main eruption)</b>
37.810	37.820	<b>WBT</b>
41.873	41.888	Flood
42.620	42.631	Flood
42.948	42.956	Flood
43.586	43.598	Flood
44.378	44.386	Flood
44.601	44.610	Flood
44.777	44.787	Flood
46.357	46.393	Flood
46.550	46.680	<b>UT1</b>
46.860	46.881	Flood
48.501	48.518	Flood

AU3 Events		
[m]	[m]	
Depth top	Depth base	Comment
48.538	48.550	Flood
49.151	49.210	Flood
50.094	50.102	Flood
50.127	50.142	Flood
50.172	50.190	Flood
50.318	50.351	Flood
50.839	50.851	Flood
52.831	52.851	Flood
53.292	53.302	Flood
55.807	55.835	Flood
56.822	56.831	Flood
57.465	57.478	Flood
58.147	58.158	Flood
60.396	60.404	Flood
60.540	60.580	Flood
60.675	60.682	Flood
61.485	61.516	Flood
61.618	61.626	Flood
63.981	64.221	Slump
71.110	71.160	<b>DWT</b>
73.190	73.220	Slump
76.270	76.410	Slump
78.490	78.560	Slump
81.282	81.294	Flood
81.573	81.581	Flood
81.695	81.724	Flood
81.740	81.780	<b>MMT</b>
82.268	82.293	Flood
82.518	82.533	Flood
83.415	83.423	Flood
84.808	84.822	Flood
85.160	85.210	Slump
85.340	85.400	Slump
85.894	85.902	Flood
86.327	86.363	Flood
86.640	86.651	Flood
88.110	88.160	Slump
91.430	91.440	Slump
91.910	91.930	Slump
92.050	92.070	Slump
93.894	93.968	Slump
95.285	96.280	Slump
96.973	97.420	Slump
98.600	98.842	Slump
100.580	100.660	Slump

**Supplementary Table 23 cont. Ager marker points of core AU3.** Depths of event layers (floods, slumps, tephra and drilling artefacts) were subtracted from the age/depth model.

**Auel dry maar: core AU4 0 - 104.5 m**



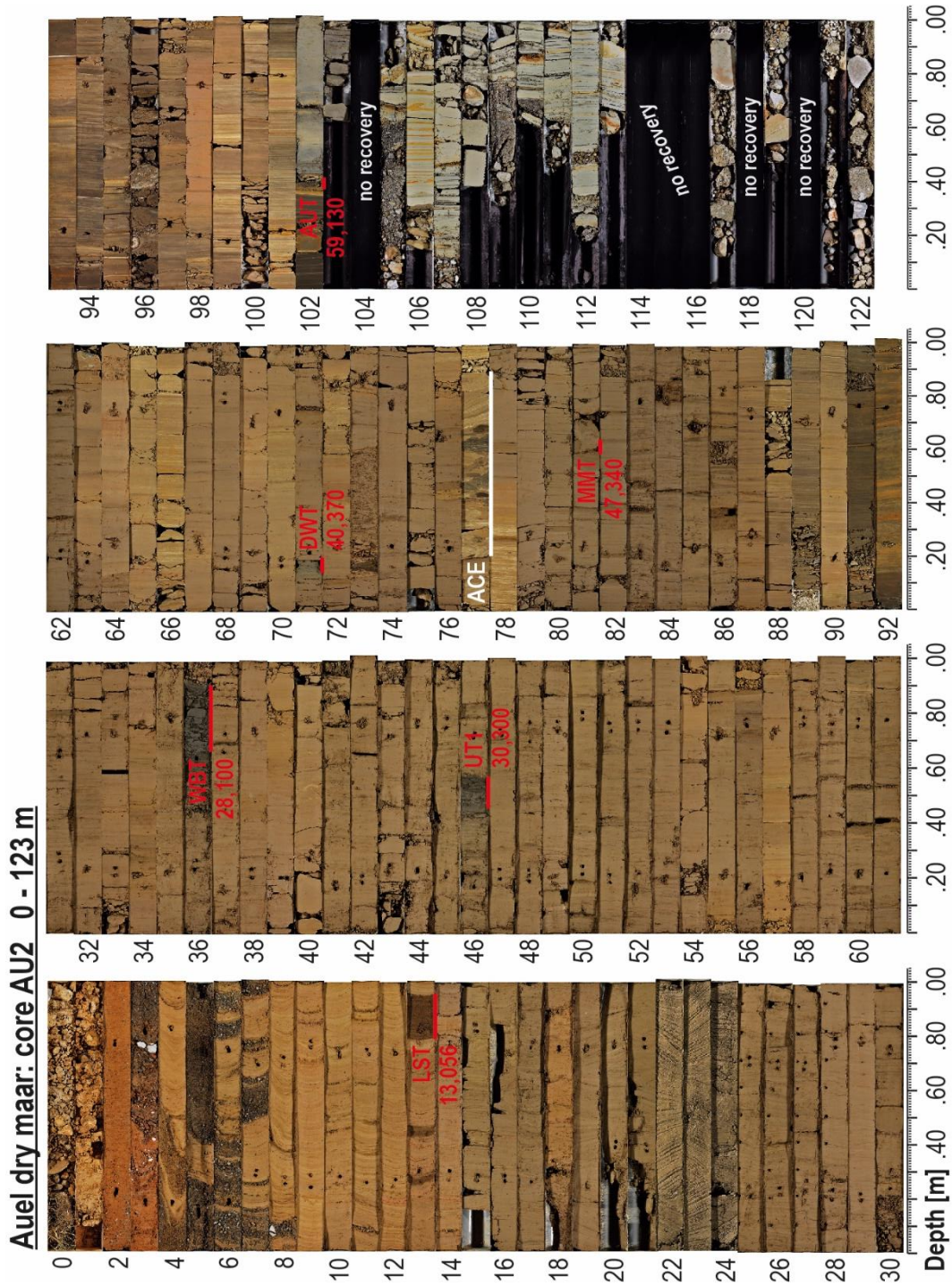
**Supplementary Fig. 5** Core photo of sediment core AU4 with the Auel Cooling Event (ACE) and ages of marker tephra layers (Sirocko et al. 2016, 2021; Reinig et al. 2021). Ages of marker layers are given in the yr b2k notation.



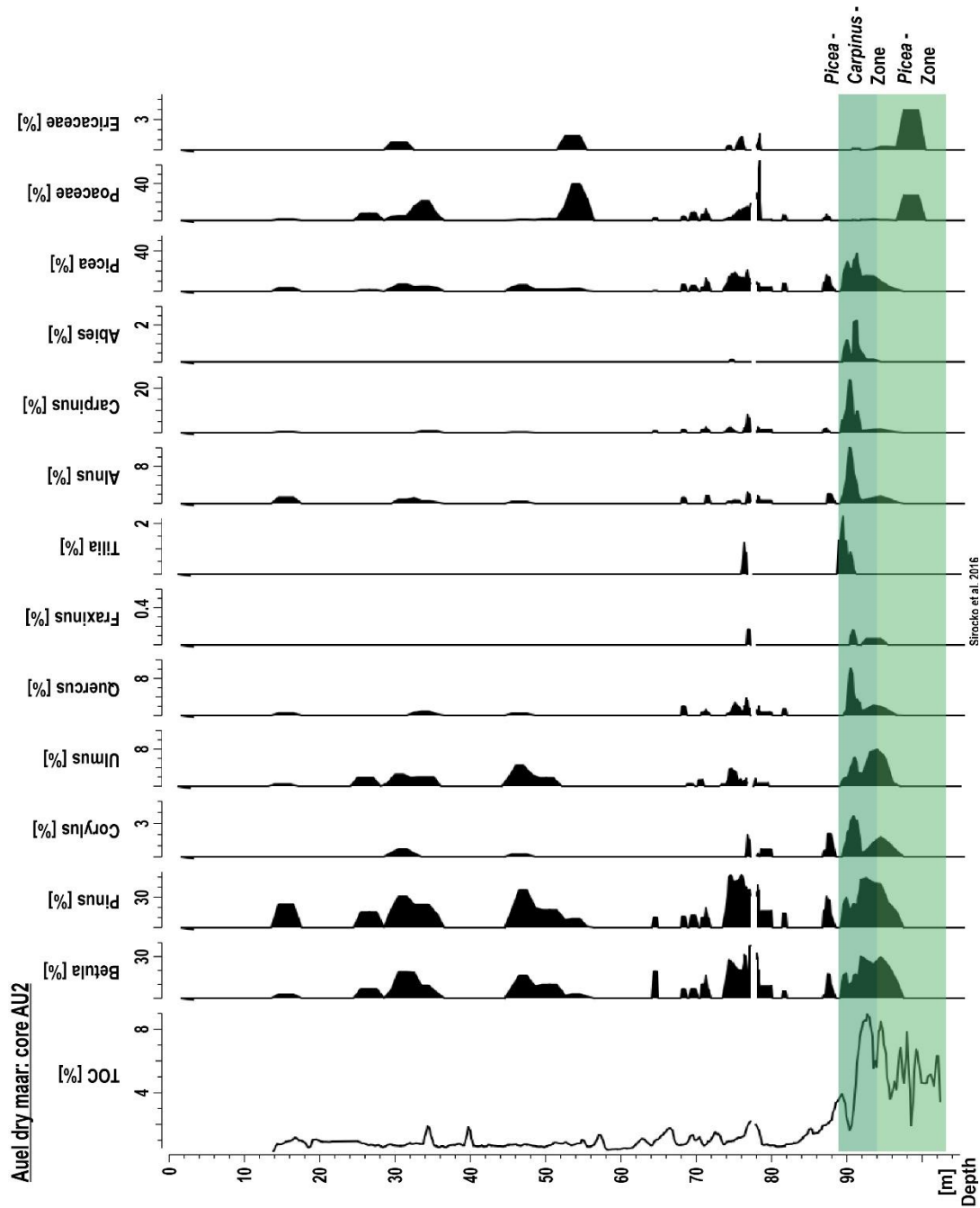
AU4		Ager
Sirocko et al. 2021		
[m]	[yr b2k]	
Depth	Age	Comment
0.000	10000	Coretop (extrapolated)
14.500	13056	<b>LST</b>
15.610	14692	<b>GI1</b> onset
18.987	22700	GS2 Corg min
19.090	23220	<b>GI2.2</b> end
19.190	23340	<b>GI2.2</b> onset
24.160	24619	<b>EVT</b>
27.200	26430	dust intensification
34.250	27540	<b>GI3</b> end / onset GS3
34.950	27780	<b>GI3</b> onset
39.630	28600	<b>GI4</b> end / onset GS4
40.100	28900	<b>GI4</b> onset
54.443	32040	<b>GI5.2</b> end / onset GS5.2
55.030	32500	<b>GI5.2</b> onset
56.680	33360	<b>GI6</b> end / onset GS6
57.407	33740	<b>GI6</b> onset
62.370	34740	<b>GI7</b> end / onset GS7
63.842	35480	<b>GI7c</b> onset
65.470	36580	<b>GI8</b> end / onset GS8
67.050	38220	<b>GI8c</b> onset
69.360	39900	<b>GI9</b> end / onset GS9
70.460	40160	<b>GI9</b> onset
71.840	40800	<b>GI10</b> end / onset GS10
71.950	41000	<sup>10</sup> Be <b>Laschamp</b> end
72.600	41460	<b>GI10</b> onset
74.750	42000	<sup>10</sup> Be <b>Laschamp</b> start
75.380	42240	<b>GI11</b> end / onset GS11
76.459	43340	<b>GI11</b> onset
76.620	43500	<b>ACE</b> top (to 76.94m)
77.070	44280	<b>GI12</b> end
77.865	46860	<b>GI12c</b> onset
87.770	48340	<b>GI13</b> end / onset GS13
89.613	49280	<b>GI13c</b> onset
90.500	49600	<b>GI14</b> end / onset GS14QS
91.590	51500	<b>GI14a</b> onset
91.720	51660	<b>GI14b</b> onset
93.440	54220	<b>GI14e</b> onset
93.684	54900	<b>GI15.1</b> end
93.704	55000	<b>GI15.1</b> onset
93.780	55400	<b>GI15.2</b> end / onset GS15.2
95.130	55800	<b>GI15.2</b> onset
99.700	56500	<b>GI16</b> end / onset GS16
100.310	56700	<b>GI16</b> Corg max
101.170	58040	<b>GI16.1c</b> onset
101.190	58160	<b>GI16.2</b> end
101.310	58280	<b>GI16.2</b> onset
101.640	58560	<b>GI17</b> end / onset GS17.1
102.310	59080	<b>GI17.1c</b> onset
102.380	59130	<b>AUT</b> (top)

AU4 Events		
[m]	[m]	
Depth Top	Depth Base	Comment
0.000	7.700	Debris
12.780	12.800	LST Flood
13.950	14.000	LST Flood
14.400	14.500	<b>LST</b>
24.150	24.160	<b>EVT</b>
36.500	36.630	<b>WBT</b>
36.830	36.890	<b>WBT</b> (main eruption)
37.700	37.710	<b>WBT</b>
41.810	41.910	Drilling artefact
46.520	46.590	<b>UT1</b>
70.910	70.930	<b>DWT</b>
76.020	76.200	Slump
78.690	78.910	Slump
79.400	79.420	Slump
81.150	81.170	<b>MMT</b>
84.810	84.950	Slump
88.310	88.330	Slump
92.280	92.360	Slump
93.380	93.430	Slump
95.080	95.110	Slump
95.190	95.270	Slump
96.930	97.340	Slump
98.310	98.430	Slump
98.500	98.600	Slump
98.630	98.680	Slump
101.000	101.030	Slump
102.110	102.210	Slump

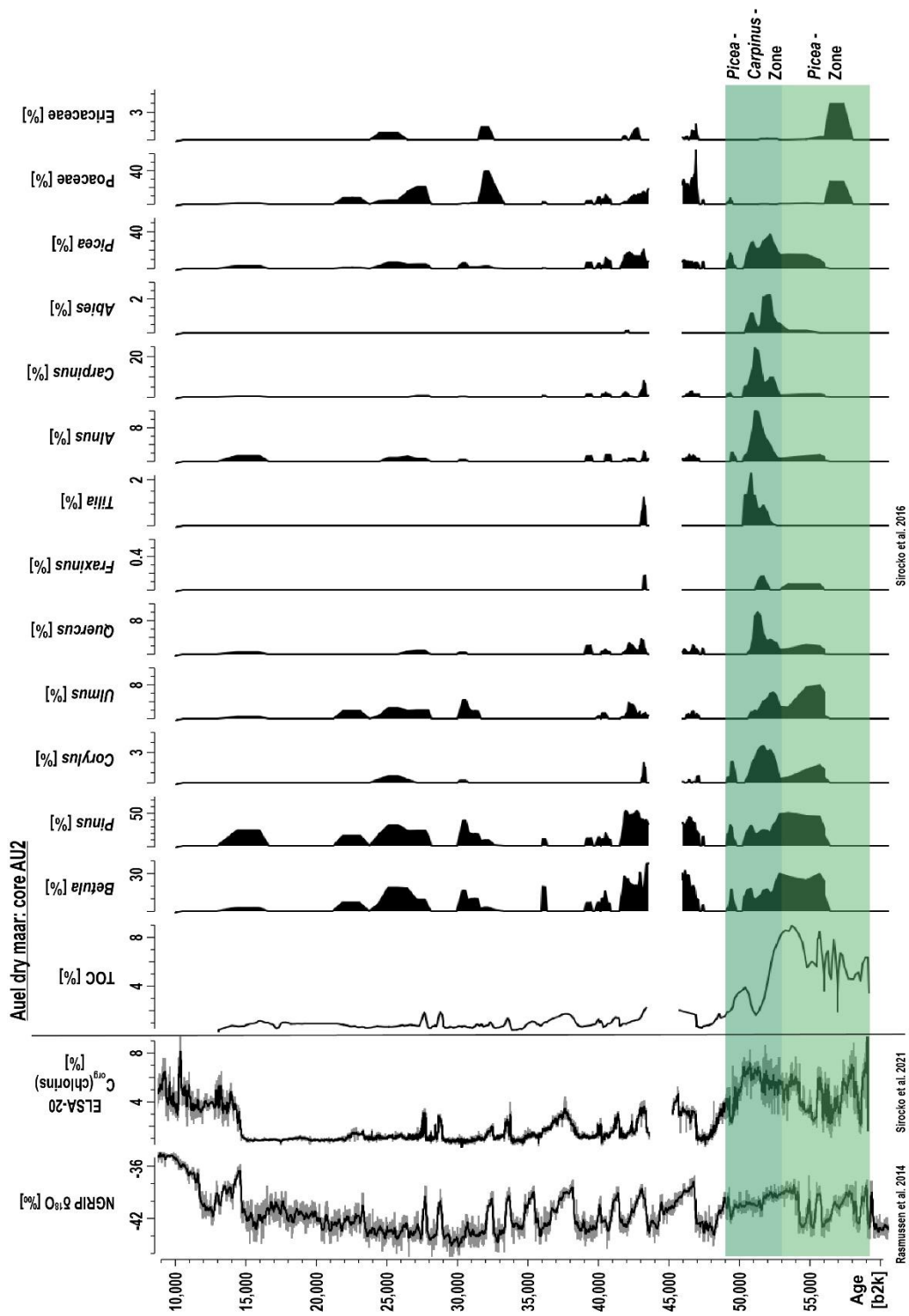
**Supplementary Table 24** Ager marker points of core AU4. Depths of event layers (floods, slumps, tephra and drilling artefacts) were subtracted from the age/depth model.



**Supplementary Fig. 6** Core photo of sediment record AU2 with Auel Cooling Event (ACE) and ages of marker tephra layers (Sirocko et al. 2016, 2021; Reing et al. 2021). Ages of marker layers are given in the yr b2k notation.



**Supplementary Fig. 7 Pollen percentages and  $C_{org}$  (chlorins) record of core AU2 versus depth (Sirocko et al. 2016).** Pollen data were smoothed using a three-point running mean. Pollen counts were performed by Frank Dreher.



**Supplementary Fig. 8** Pollen percentages and Total Organic Carbon (TOC) record of core AU2 versus age (Sirocko et al. 2016) together with ELSA-20  $C_{org}$ (chlorins) (Sirocko et al. 2021) and NGRIP  $\delta^{18}O$  (Rasmussen et al. 2014) records. Pollen data were smoothed using a three-point running mean. Pollen counts were performed by Frank Dreher.

AU2		Ager	
Sirocko et al. 2016			
Update ELSA-20 strat.			
[m]	[yr b2k]		
Depth	Age	Comment	
0.000	10000	Coretop (extrapolated)	
13.950	13056	<b>LST</b>	
14.650	14690	<b>G11</b> onset	
34.150	27540	<b>G13</b> end / onset GS3	
34.750	27780	<b>G13</b> onset	
36.900	28100	<b>WBT</b>	
39.550	28600	<b>G14</b> end / onset GS4	
39.950	28900	<b>G14</b> onset	
46.590	30300	<b>UT1</b>	
54.250	32040	<b>G15.2</b> end / onset GS5.2	
55.400	32500	<b>G15.2</b> onset	
56.650	33360	<b>G16</b> end / onset GS6	
57.700	33740	<b>G16</b> onset	
61.950	34740	<b>G17</b> end / onset GS7	
63.150	35480	<b>G17c</b> onset	
65.350	36580	<b>G18</b> end / onset GS8	
66.950	38220	<b>G18c</b> onset	
69.150	39900	<b>G19</b> end / onset GS9	
70.650	40160	<b>G19</b> onset	
71.190	40370	<b>DWT</b>	
71.750	40800	<b>G110</b> end / onset GS10	
73.150	41460	<b>G110</b> onset	
75.300	42240	<b>G111</b> end / onset GS11	
77.150	43340	<b>G111</b> onset	
77.200	43500	<b>ACE</b> (to 77.94m)	
78.350	46860	<b>G112c</b> onset	
81.630	47340	<b>MMT</b>	
88.300	49600	<b>G114</b> end / onset GS14QS	
90.400	51100	Carpinus Peak	
93.250	54220	<b>G114e</b> onset	
93.950	55400	<b>G115.2</b> end / onset GS15.2	
95.100	55800	<b>G115.2</b> onset	
97.750	56500	<b>G116</b> end / onset GS16	
100.950	58280	<b>G116.2</b> onset	
101.700	58560	<b>G117</b> end / onset GS17.1	
102.150	59080	<b>G117.1c</b> onset	
102.330	59130	<b>AUT (top)</b>	

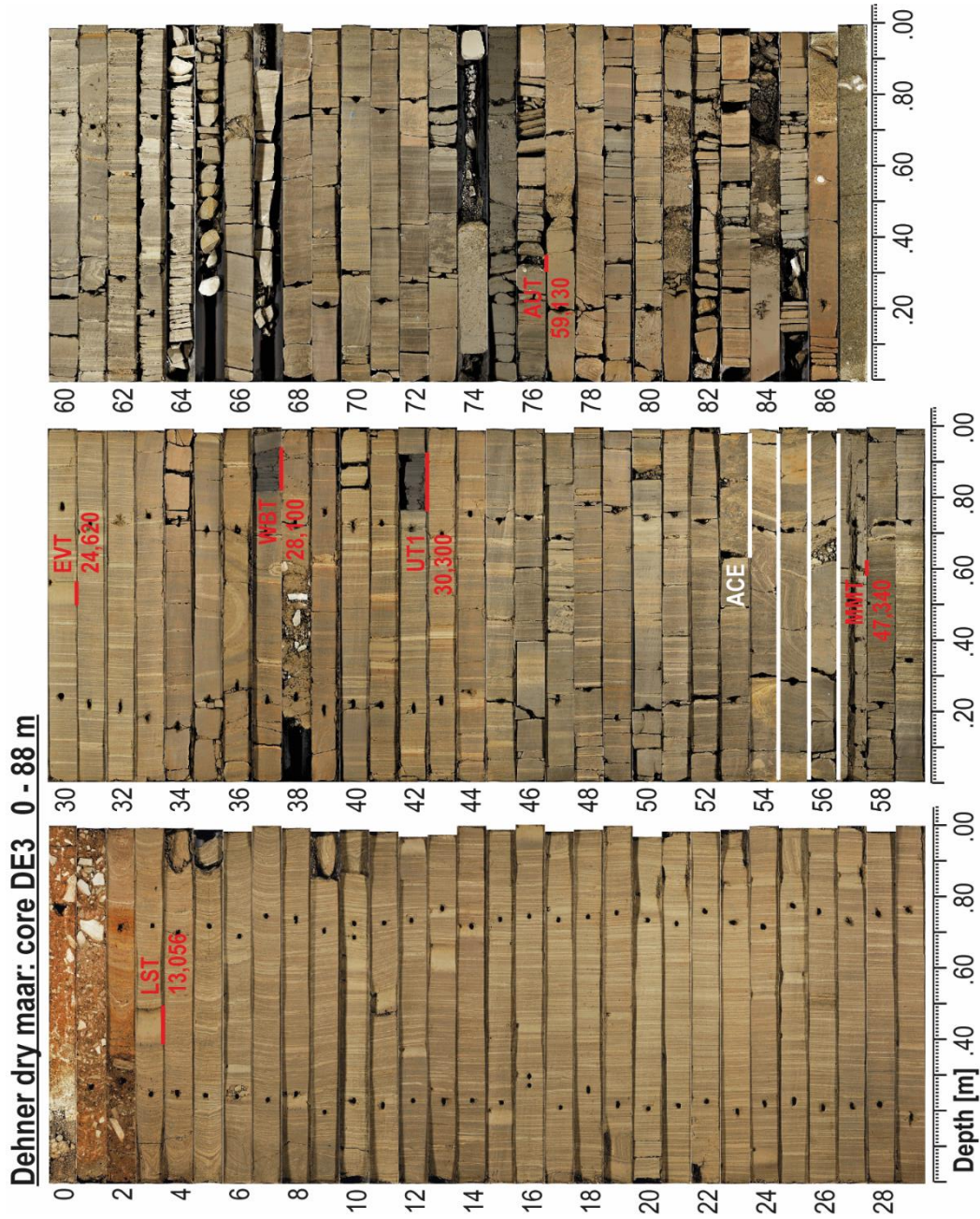
AU2 Events		
[m]	[m]	
Depth top	Depth base	Comment
0.000	6.410	Debris
8.051	8.110	Flood
8.355	8.379	Flood
9.696	9.720	Flood
9.833	9.850	Flood
9.875	9.884	Flood
10.439	10.449	Flood
10.476	10.515	Flood
10.614	10.622	Flood
11.070	11.092	Flood
11.618	11.628	Flood
11.852	11.900	Flood
12.197	12.220	Flood
13.240	13.280	<b>LST Flood</b>
13.420	13.480	<b>LST Flood</b>
13.800	13.950	<b>LST</b>
14.138	14.152	Flood
15.385	15.443	Flood
15.622	15.634	Flood
15.698	15.709	Flood
15.770	15.789	Flood
16.305	16.313	Flood
17.027	17.043	Flood
17.420	17.433	Flood
17.506	17.517	Flood
17.575	17.608	Flood
18.402	18.424	Flood
18.457	18.478	Flood
18.513	18.539	Flood
18.622	18.646	Flood
19.717	19.732	Flood
19.807	19.837	Flood
19.853	19.863	Flood
24.347	24.370	Flood
24.585	24.597	Flood
26.360	26.378	Flood
26.391	26.406	Flood
26.577	26.592	Flood
26.697	26.705	Flood
26.740	26.774	Flood
26.896	26.929	Flood
27.236	27.261	Flood
27.340	27.351	Flood
27.509	27.517	Flood
27.789	27.814	Flood
28.043	28.052	Flood
35.960	36.040	<b>WBT</b>
36.660	36.900	<b>WBT</b> (main eruption)
37.036	37.046	Flood
37.670	37.730	<b>WBT</b>

**Supplementary Table 25 Ager marker points of core AU2.** Depths of event layers (floods, slumps, tephra and drilling artefacts) were subtracted from the age/depth model.

AU2 Events		
[m]	[m]	
Depth top	Depth base	Comment
41.599	41.621	Flood
42.096	42.106	Flood
42.643	42.660	Flood
42.822	42.838	Flood
43.738	43.747	Flood
44.345	44.361	Flood
44.613	44.621	Flood
44.837	44.846	Flood
46.270	46.321	Flood
46.430	46.590	<b>UT1</b>
46.777	46.834	Flood
47.688	47.706	Flood
48.296	48.330	Flood
48.490	48.510	Flood
48.720	48.736	Flood
49.097	49.161	Flood
50.061	50.078	Flood
50.165	50.192	Flood
50.335	50.394	Flood
50.603	50.617	Flood
50.858	50.868	Flood
51.386	51.420	Flood
52.818	52.837	Flood
53.193	53.202	Flood
54.620	54.634	Flood
55.875	55.886	Flood
58.488	58.503	Flood
59.558	59.574	Flood

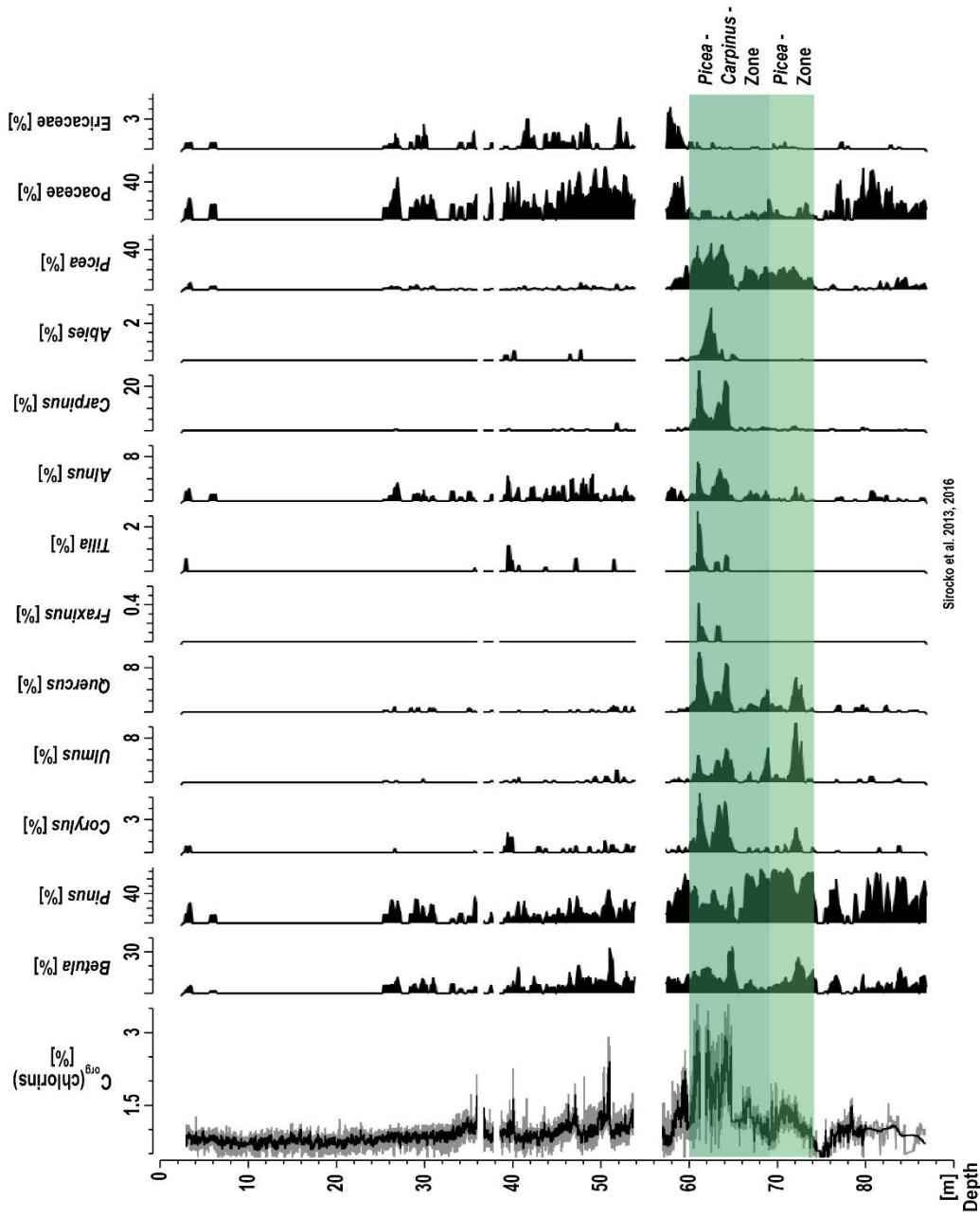
AU2 Events		
[m]	[m]	
Depth top	Depth base	Comment
59.686	59.697	Flood
60.378	60.407	Flood
60.520	60.542	Flood
61.393	61.420	Flood
61.524	61.539	Flood
62.344	62.362	Flood
62.818	62.834	Flood
63.860	64.140	Slump
71.140	71.190	<b>DWT</b>
73.160	73.610	Slump
78.740	78.920	Slump
79.400	79.470	Slump
81.510	81.750	Slump (81.60-.63m <b>MMT</b> )
82.400	82.409	Flood
83.373	83.396	Flood
83.467	83.495	Flood
84.447	84.457	Flood
84.785	84.848	Flood
85.120	85.220	Slump
86.355	86.390	Flood
86.684	86.692	Flood
86.737	86.749	Flood
92.280	92.360	Slump
95.420	96.730	Slump
97.600	97.630	Slump
98.310	98.860	Slump
102.330	102.370	<b>AUT</b> (eruption)

**Supplementary Table 25 cont. Ager marker points of core AU2.** Depths of event layers (floods, slumps, tephra and drilling artefacts) were subtracted from the age/depth model.



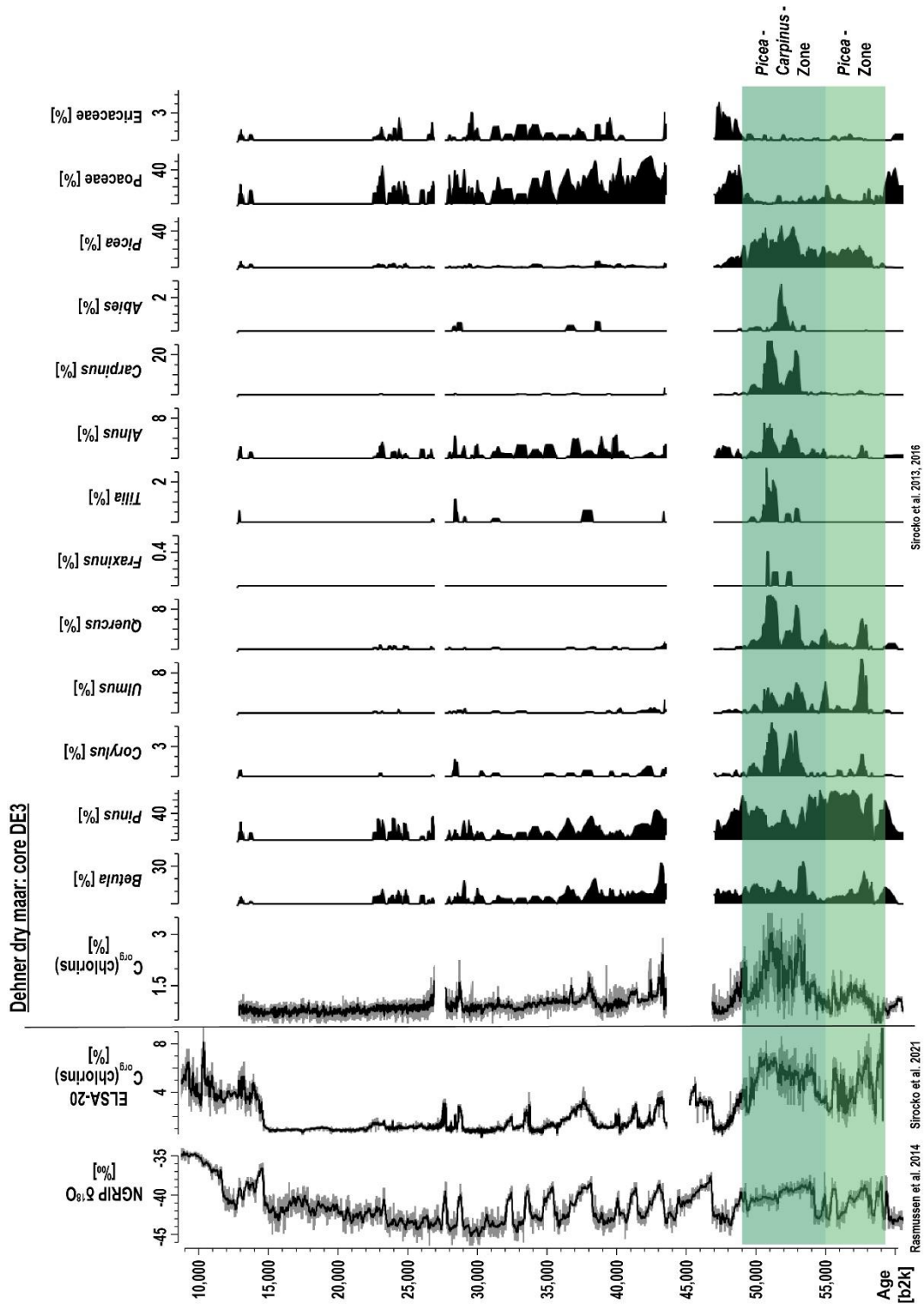
**Supplementary Fig. 9** Core photo of sediment core DE3 with the Auel Cooling Event (ACE) and ages of marker tephra layers (Sirocko et al. 2016, 2021; Reinig et al. 2021). Ages of marker layers are given in the yr b2k notation.

Dehner dry maar: core DE3



Supplementary Fig. 10 Pollen percentages (Sirocko et al. 2013, 2016) and C<sub>org</sub>(chlorins) record of core DE3 versus depth. Pollen data were smoothed using a three-point running mean. Pollen counts were performed by Frank Dreher.





**Supplementary Fig. 11** Pollen percentages (Sirocko et al. 2013, 2016) and  $C_{org}$ (chlorins) record of core DE3 versus age together with ELSA-20  $C_{org}$ (chlorins) (Sirocko et al. 2021) and NGRIP  $\delta^{18}O$  (Rasmussen et al. 2014) records. Pollen data were smoothed using a three-point running mean. Pollen counts were performed by Frank Dreher.

DE3		Ager
Sirocko et al. 2013, 2016		
Update ELSA-20 strat.		
[m]	[yr b2k]	
Depth	Age	Comment
0.000	12000	Coretop (extrapolated)
3.475	13056	<b>LST</b>
10.001	15036	<b>GI1</b> onset (nach P); 14692 b2k
27.158	23309	<b>GI2</b> onset (Diatomeen)
30.565	24720	<b>EVT</b>
36.730	27780	<b>GI3</b> onset
37.920	28100	<b>WBT</b>
39.880	28600	<b>GI4</b> end / onset GS4
40.180	28900	<b>GI4</b> onset
42.910	30300	<b>UT1</b>
43.921	32040	<b>GI5.2</b> end / onset GS5.2
44.270	32500	<b>GI5.2</b> onset
44.570	33360	<b>GI6</b> end / onset GS6
44.810	33740	<b>GI6</b> begin
46.260	36580	<b>GI8</b> end / onset GS8
47.590	38220	<b>GI8c</b> onset
49.630	39900	<b>GI9</b> end / onset GS9
50.020	40160	<b>GI9</b> onset
51.010	41460	<b>GI10</b> onset
53.540	43340	<b>GI11</b> onset
53.600	43500	<b>ACE</b> top (to 56.97m)
56.992	46860	<b>GI12c</b> onset
57.630	47340	<b>MMT</b>
58.280	48340	<b>GI13</b> end / onset GS13
59.720	49280	<b>GI13c</b> onset
60.070	49600	<b>GI14</b> end / onset GS14QS
60.950	51100	<i>Carpinus</i> peak
61.180	51500	<b>GI14a</b> onset
61.980	51660	<b>GI14b</b> onset
67.050	54220	<b>GI14e</b> onset
69.250	55400	<b>GI15.2</b> end / onset GS15.2
69.560	55800	<b>GI15.2</b> onset
70.320	56500	<b>GI16</b> end / onset GS16
71.800	57600	small <i>Carpinus</i> peak
73.810	58280	<b>GI16.2</b> onset
76.300	59130	<b>AUT</b>
78.350	63840	<b>GI18</b> end
78.425	64100	<b>GI18</b> onset
84.350	72340	<b>GI19.2</b> onset
84.530	72590	<b>SMT</b> (by DE3)
85.850	74100	<b>GI20</b> end
88.000	76250	<b>DET</b> (eruption)

DE3 Events		
[m]	[m]	
Depth Top	Depth Base	Comment
3.400	3.475	<b>LST</b>
3.499	3.571	Drilling artefact
3.994	4.017	Drilling artefact
4.857	4.906	Drilling artefact
4.941	5.006	Drilling artefact
5.858	6.006	Drilling artefact
6.233	6.280	Drilling artefact
6.990	7.007	Drilling artefact
7.992	8.009	Drilling artefact
8.992	9.007	Drilling artefact
9.848	10.030	Drilling artefact
10.873	10.887	Drilling artefact
10.996	11.015	Drilling artefact
11.472	11.486	Drilling artefact
11.500	11.540	Flood
11.997	12.009	Drilling artefact
13.570	13.670	Flood
13.750	13.770	Flood
13.990	14.011	Drilling artefact
14.680	14.710	Flood
14.996	15.004	Drilling artefact
15.120	15.280	Flood
15.994	16.004	Drilling artefact
16.300	16.310	Flood
16.420	16.450	Flood
16.996	17.007	Drilling artefact
17.992	18.017	Drilling artefact
18.988	19.005	Drilling artefact
19.989	20.025	Drilling artefact
20.991	21.006	Drilling artefact
21.987	22.010	Drilling artefact
22.993	23.002	Drilling artefact
23.992	24.009	Drilling artefact
24.060	24.100	Flood
24.520	24.540	Flood
24.840	24.870	Flood
25.400	25.420	Flood
25.570	25.610	Flood
25.990	26.002	Drilling artefact
26.994	27.000	Drilling artefact
27.820	27.860	Flood
27.991	28.008	Drilling artefact
28.989	29.000	Drilling artefact
29.190	29.200	Flood
29.380	29.390	Flood
29.670	29.680	Flood
29.994	30.005	Drilling artefact
30.330	30.340	Flood
30.480	30.565	<b>EVT</b>

**Supplementary Table 26** Ager marker points of core DE3. Depths of event layers (floods, slumps, tephra and drilling artefacts) were subtracted from the age/depth model.

DE3 Events		
[m]	[m]	
Depth Top	Depth Base	Comment
30.989	31.010	Drilling artefact
31.210	31.220	Flood
31.680	31.710	Flood
31.992	32.002	Drilling artefact
32.380	32.390	Flood
32.610	32.620	Flood
32.996	33.006	Drilling artefact
33.996	34.005	Drilling artefact
34.139	34.162	Drilling artefact
34.733	34.753	Drilling artefact
34.861	34.880	Drilling artefact
34.943	34.954	Drilling artefact
34.990	35.001	Drilling artefact
36.000	36.600	Slump
36.991	37.010	Drilling artefact
37.099	37.111	Drilling artefact
37.559	37.580	<b>WBT</b>
37.799	37.920	<b>WBT (main eruption)</b>
37.920	38.601	<b>WBT</b>
38.992	39.013	Drilling artefact
39.991	40.013	Drilling artefact
40.822	40.836	Drilling artefact
40.882	40.901	Drilling artefact
40.988	41.015	Drilling artefact
41.986	42.009	Drilling artefact
42.410	42.420	Flood
42.760	42.910	<b>UT1</b>
42.996	43.008	Drilling artefact
43.989	44.004	Drilling artefact
44.994	45.009	Drilling artefact
45.461	45.469	Drilling artefact
45.999	46.010	Drilling artefact
46.997	47.009	Drilling artefact
47.550	47.560	Flood
47.610	47.630	Slump
47.659	47.670	Drilling artefact
47.999	48.010	Drilling artefact
48.030	48.040	Flood
48.130	48.140	Flood
48.380	48.400	Flood
48.520	48.530	Flood
48.790	48.810	Flood
48.995	49.007	Drilling artefact
49.260	49.270	Flood
49.999	50.020	Drilling artefact
50.204	50.212	Drilling artefact
50.440	50.450	Flood
50.480	50.490	Flood
50.669	50.680	Drilling artefact
50.853	50.879	Tephra
50.981	51.006	Drilling artefact
51.213	51.232	Drilling artefact

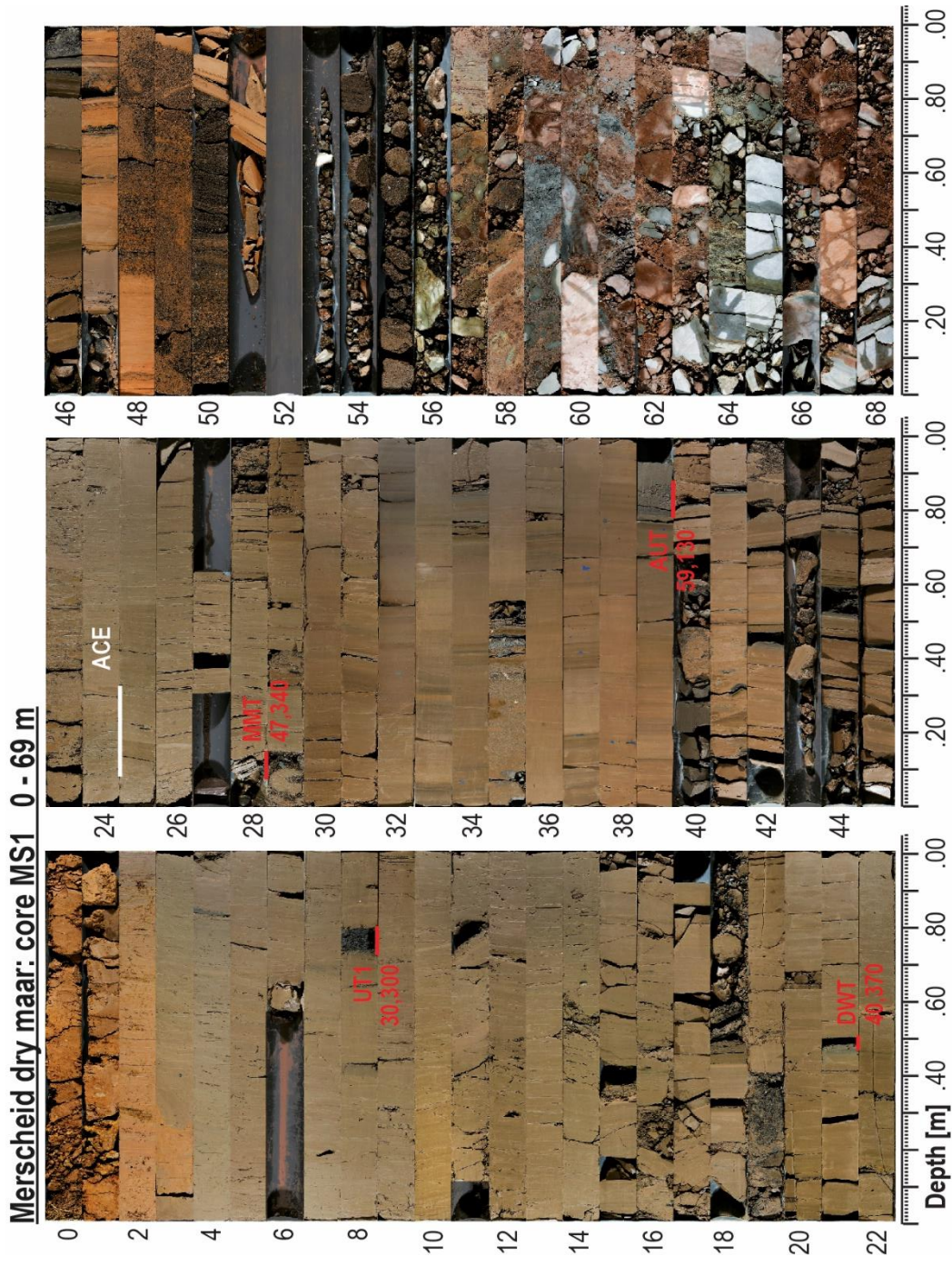
DE3 Events		
[m]	[m]	
Depth Top	Depth Base	Comment
51.400	51.410	Flood
51.999	52.009	Drilling artefact
52.230	52.248	Drilling artefact
52.320	52.330	Flood
52.984	53.008	Drilling artefact
57.580	57.630	<b>MMT</b>
57.999	58.011	Drilling artefact
58.223	58.231	Drilling artefact
58.500	58.510	Flood
58.678	58.734	Drilling artefact
58.992	59.001	Drilling artefact
59.325	59.344	Drilling artefact
59.820	59.830	Flood
59.890	59.900	Flood
59.993	60.006	Drilling artefact
60.070	60.130	Flood
60.229	60.248	Drilling artefact
60.289	60.350	Slump
60.748	60.773	Drilling artefact
60.995	61.006	Drilling artefact
61.175	61.183	Drilling artefact
61.239	61.264	Drilling artefact
61.269	61.861	Slump
61.980	61.992	Drilling artefact
61.999	62.006	Drilling artefact
62.025	62.040	Drilling artefact
62.070	62.079	Drilling artefact
62.280	62.321	Drilling artefact
62.723	62.739	Drilling artefact
63.350	63.380	Flood
63.640	63.690	Flood
63.990	64.000	Drilling artefact
64.829	65.235	Drilling artefact
65.252	65.287	Drilling artefact
65.301	65.550	Drilling artefact
65.582	65.595	Drilling artefact
65.603	65.670	Drilling artefact
65.715	65.875	Drilling artefact
65.890	65.960	Drilling artefact
65.988	66.016	Drilling artefact
66.042	66.054	Drilling artefact
66.365	66.375	Drilling artefact
66.446	66.455	Drilling artefact
66.678	66.740	Drilling artefact
66.971	67.235	Drilling artefact
67.280	67.300	Drilling artefact
67.408	67.430	Drilling artefact
67.528	67.635	Drilling artefact
67.804	68.030	Drilling artefact
68.275	68.295	Drilling artefact
68.754	68.769	Drilling artefact
68.999	69.005	Drilling artefact

**Supplementary Table 26 cont. Ager marker points of core DE3.** Depths of event layers (floods, slumps, tephra and drilling artefacts) were subtracted from the age/depth model.

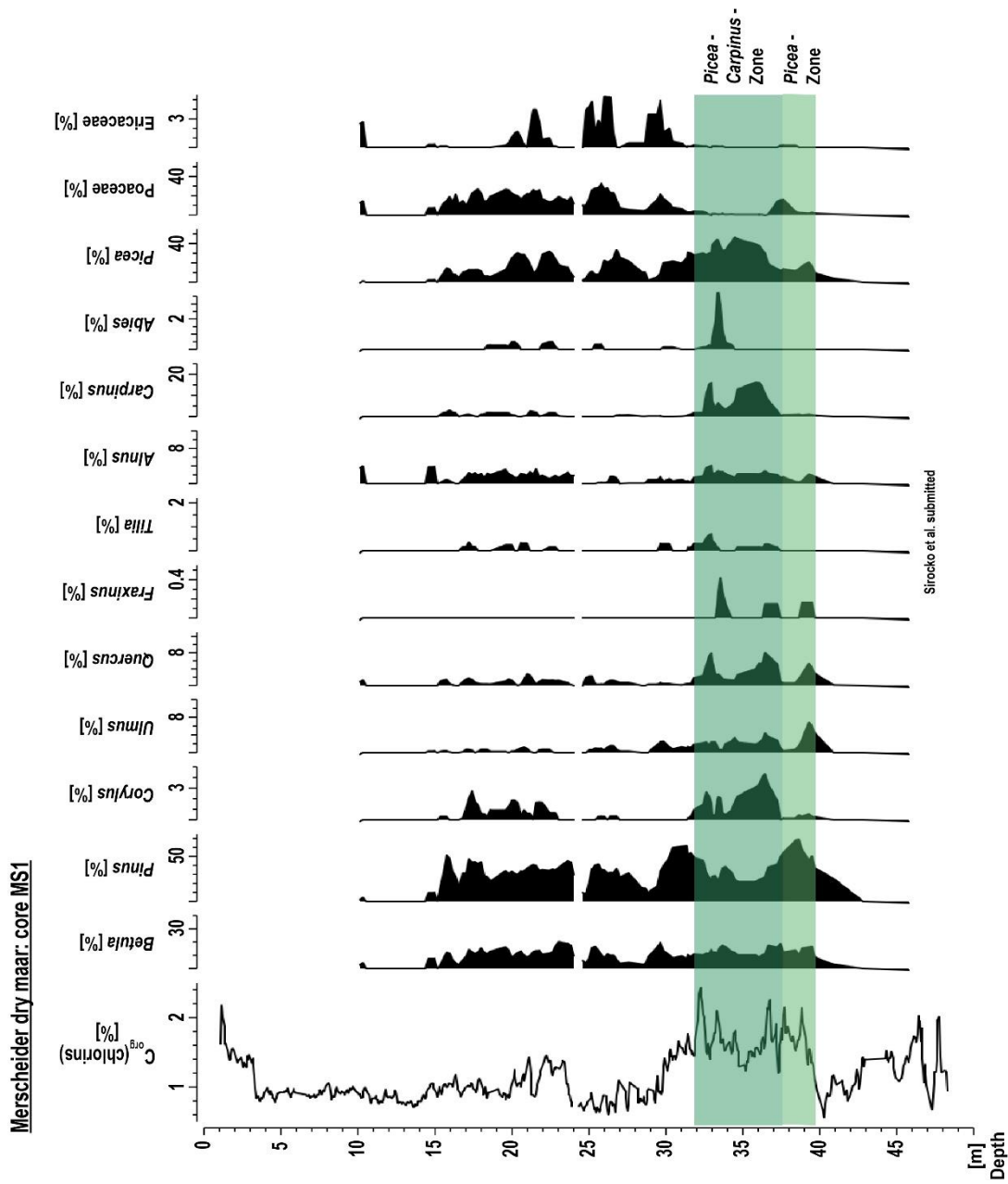
DE3 Events		
[m]	[m]	
Depth Top	Depth Base	Comment
69.205	69.222	Drilling artefact
69.401	69.410	Drilling artefact
69.550	69.561	Drilling artefact
69.754	69.760	Drilling artefact
69.770	69.780	Drilling artefact
69.900	69.908	Drilling artefact
70.050	70.058	Drilling artefact
70.060	70.067	Drilling artefact
70.072	70.080	Drilling artefact
70.189	70.281	Slump
70.300	70.320	Drilling artefact
70.757	70.764	Drilling artefact
70.809	70.816	Drilling artefact
70.999	71.008	Drilling artefact
71.015	71.040	Drilling artefact
71.230	71.240	Drilling artefact
71.775	71.780	Drilling artefact
71.940	71.949	Drilling artefact
72.080	72.090	Drilling artefact
72.275	72.285	Drilling artefact
72.295	72.303	Drilling artefact
72.694	72.702	Drilling artefact
72.790	72.800	Drilling artefact
72.996	73.005	Drilling artefact
73.026	73.071	Drilling artefact
73.289	73.471	Slump
73.473	73.479	Drilling artefact
73.649	73.680	Drilling artefact
73.710	73.725	Drilling artefact
73.750	73.780	Drilling artefact
73.819	74.085	Slump
74.230	74.242	Drilling artefact
74.419	74.900	Drilling artefact
74.908	74.925	Drilling artefact
74.950	75.010	Drilling artefact
75.051	75.058	Drilling artefact
75.104	75.110	Drilling artefact

DE3 Events		
[m]	[m]	
Depth top	Depth base	Comment
75.294	75.307	Drilling artefact
75.350	75.370	Drilling artefact
75.504	75.514	Drilling artefact
75.780	75.798	Drilling artefact
75.998	76.029	Drilling artefact
76.223	76.240	Drilling artefact
76.240	76.300	<b>AUT</b>
76.309	76.375	Drilling artefact
76.385	76.399	Drilling artefact
76.405	76.415	Drilling artefact
76.425	76.432	Drilling artefact
76.535	76.550	Drilling artefact
76.620	76.635	Drilling artefact
76.664	76.670	Drilling artefact
76.695	76.790	Drilling artefact
76.821	76.830	Drilling artefact
76.845	76.868	Drilling artefact
76.999	77.013	Drilling artefact
77.195	77.210	Drilling artefact
77.419	77.471	Drilling artefact
77.522	77.532	Drilling artefact
77.690	77.705	Drilling artefact
77.999	78.012	Drilling artefact
78.060	78.090	Drilling artefact
78.185	78.205	Drilling artefact
78.760	78.781	Drilling artefact
78.997	79.073	Slump
79.233	79.250	Drilling artefact
79.330	79.346	Drilling artefact
79.523	79.531	Drilling artefact
79.570	79.579	Drilling artefact
79.600	79.610	Tephra
79.710	79.725	Drilling artefact
79.888	79.895	Drilling artefact
84.450	84.530	<b>SMT</b>
84.660	85.370	Drilling artefact
86.710	88.000	<b>DET</b> (eruption)

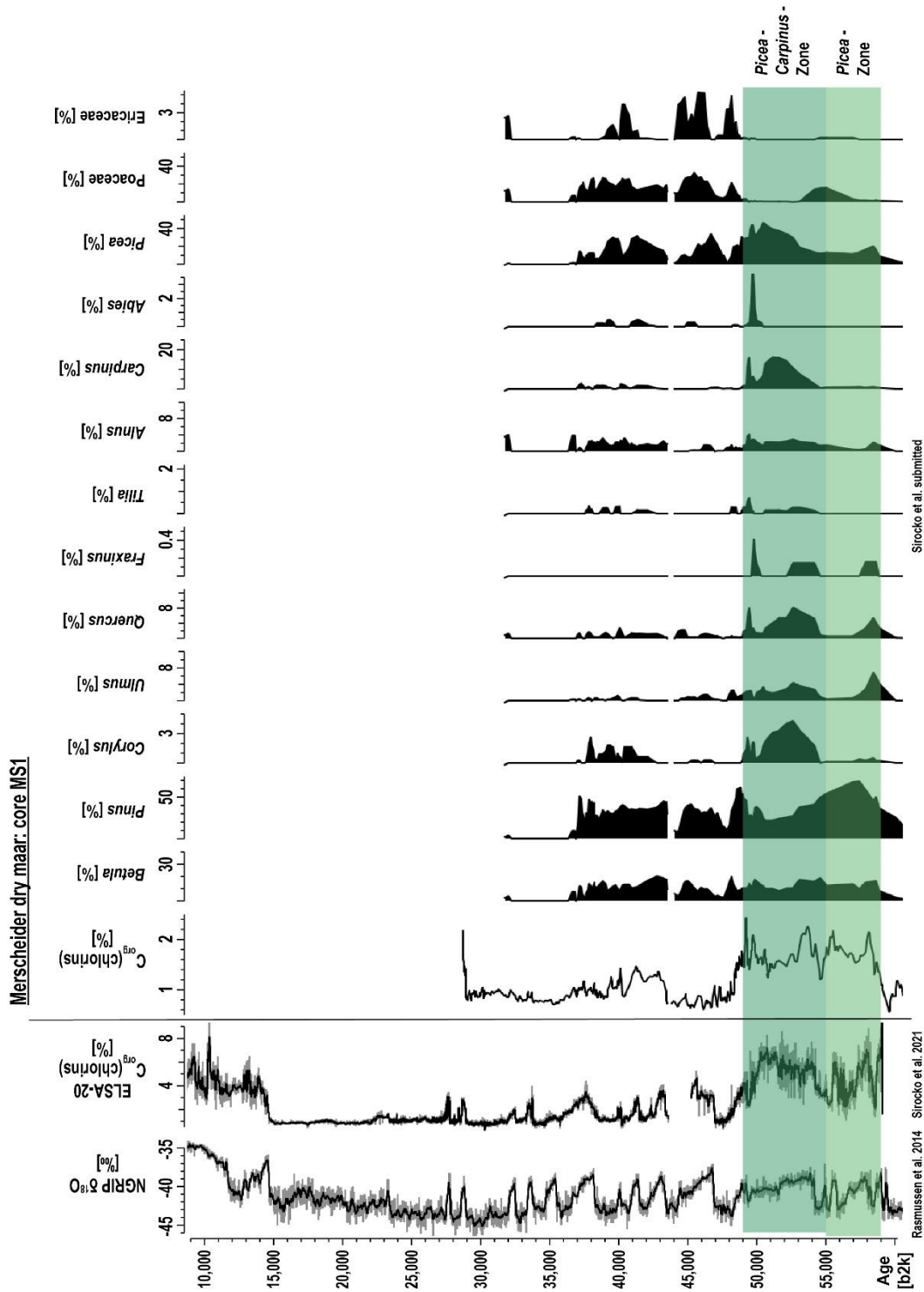
**Supplementary Table 26 cont. Ager marker points of core DE3.** Depths of event layers (floods, slumps, tephra and drilling artefacts) were subtracted from the age/depth model.



**Supplementary Fig. 12** Core photo of sediment core MS1 with the Auel Cooling Event (ACE) and ages of marker tephra layers (Sirocko et al. 2016, 2021). Ages of marker layers are given in the yr b2k notation.



**Supplementary Fig. 13** Pollen percentages and  $C_{org}$ (chlorins) record of core MS1 versus depth (Sirocko et al. submitted). Pollen data were smoothed using a three-point running mean. Pollen counts were performed by Frank Dreher.



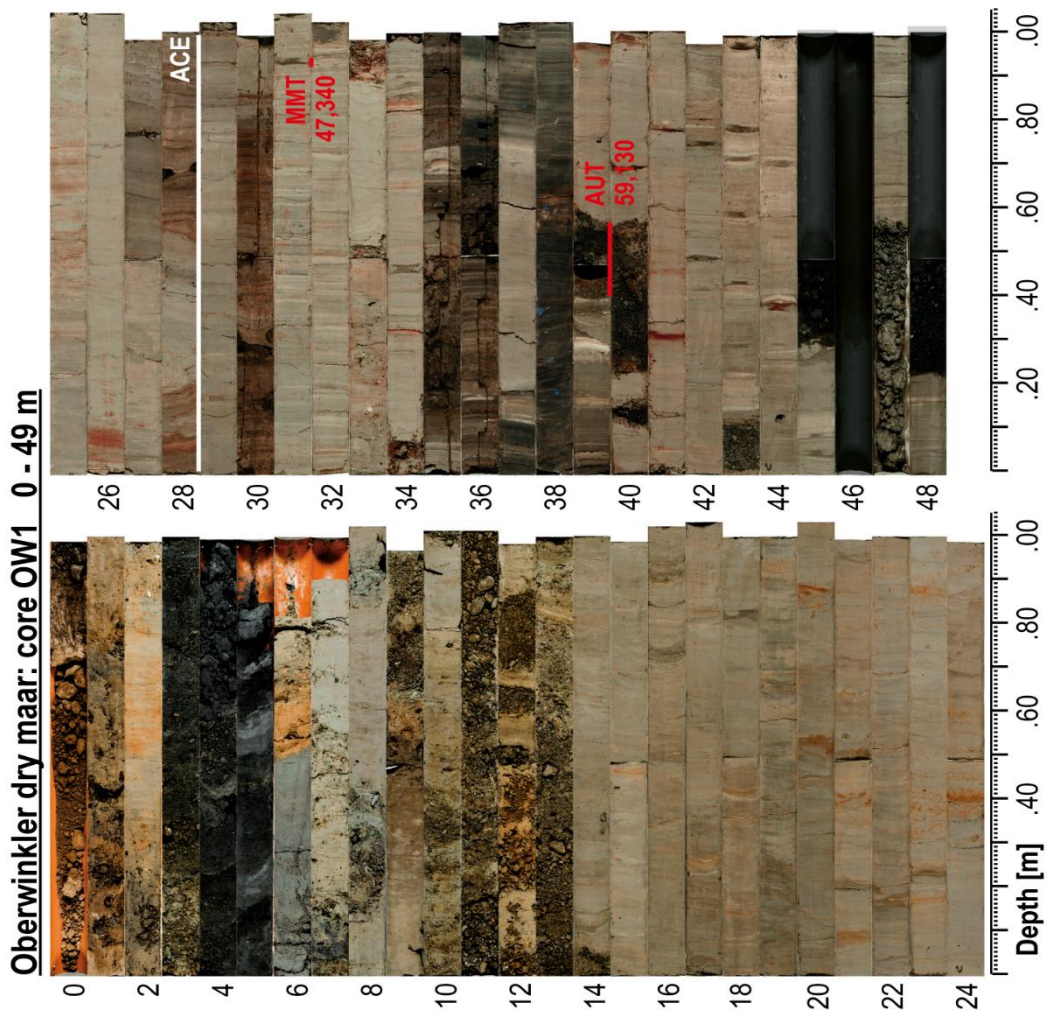
**Supplementary Fig. 14** Pollen percentages and  $\text{C}_{\text{org}}$ (chlorins) record of core MS1 versus age (Sirocko et al. submitted) together with ELSA-20  $\text{C}_{\text{org}}$ (chlorins) (Sirocko et al. 2021) and NGRIP  $\delta^{18}\text{O}$  (Rasmussen et al. 2014) records. Pollen data were smoothed using a three-point running mean. Pollen counts were performed by Frank Dreher.

<b>MS1</b>		<b>Ager</b>	
Sirocko et al. 2016			
Update ELSA-20 strat.			
<b>[m]</b>	<b>[yr b2k]</b>		
<b>Depth</b>	<b>Age</b>	<b>Comment</b>	
0.000	28600	Coretop (extrapolated)	
3.300	28900	<b>G14</b> onset	
8.800	30300	<b>UT1</b>	
10.350	32040	<b>G15.2</b> end / onset GS5.2	
10.700	32500	<b>G15.2</b> onset	
11.650	33360	<b>G16</b> end / onset GS6	
12.550	33740	<b>G16</b> onset	
14.500	36580	<b>G18</b> end / onset GS8	
18.100	38220	<b>G18c</b> onset	
20.650	39900	<b>G19</b> end / onset GS9	
21.200	40160	<b>G19</b> onset	
21.500	40370	<b>DWT</b>	
21.750	40800	<b>G110</b> end / onset GS10	
22.500	41460	<b>G110</b> onset	
22.750	42240	<b>G111</b> end / onset GS11	
23.550	43340	<b>G111</b> onset	
24.080	43500	<b>ACE</b> to (to 24.33m)	
28.140	47340	<b>MMT</b>	
29.800	48340	<b>G113</b> end / onset GS13	
32.550	49280	<b>G113c</b> onset	
33.200	49600	<b>G114</b> end / onset GS14QS	
35.700	51100	<i>Carpinus</i> peak	
37.150	54220	<b>G114e</b> onset	
38.800	58040	<b>G116.1c</b> onset	
39.860	59130	<b>AUT</b>	
46.350	63840	<b>G118</b> end	
46.650	64100	<b>G118</b> onset	
48.250	65700	Corebase (extrapolated)	

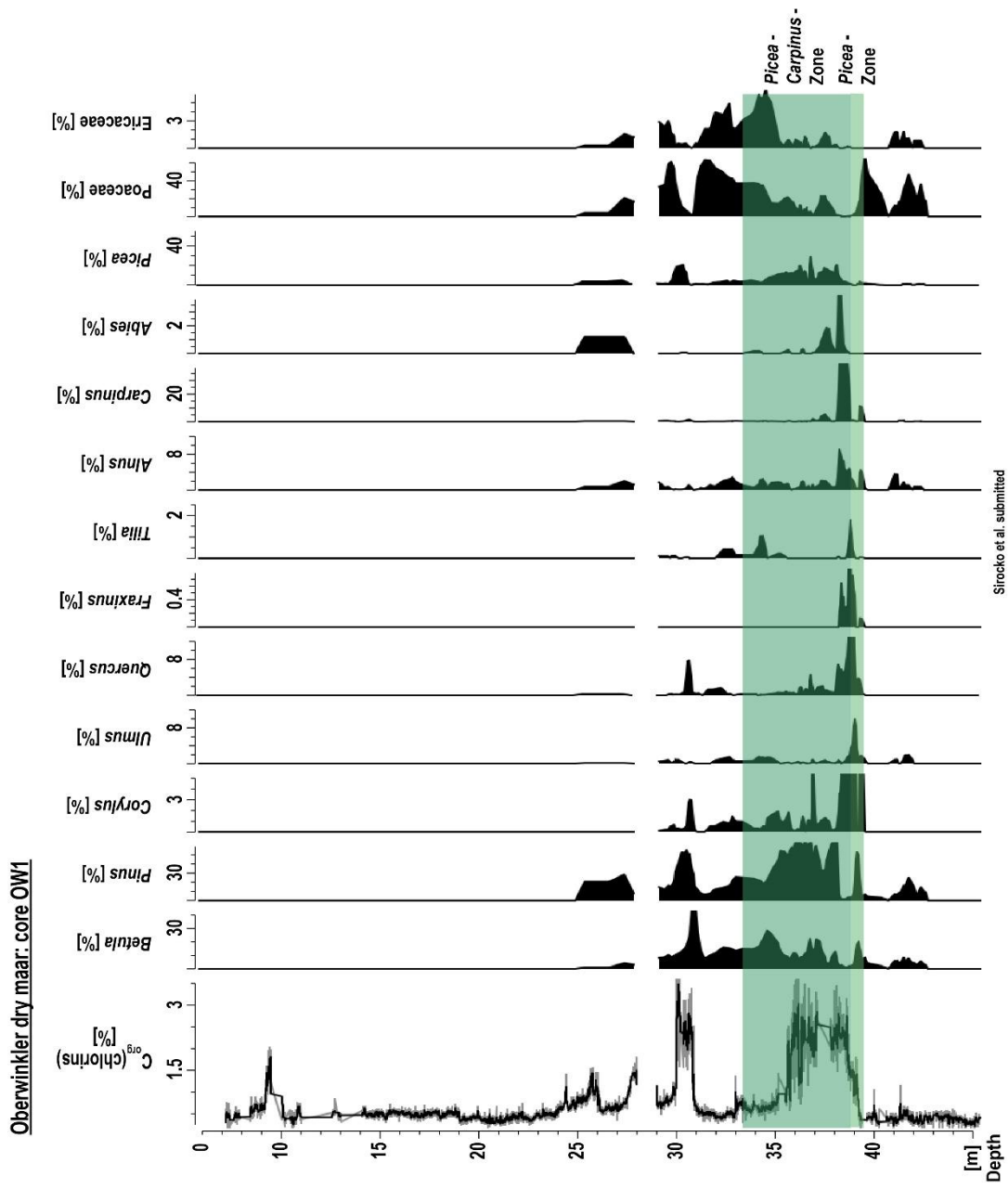
<b>MS1 Events</b>		
<b>[m]</b>	<b>[m]</b>	
<b>Depth top</b>	<b>Depth base</b>	<b>Comment</b>
4.970	4.988	Flood
5.738	5.749	Flood
5.950	6.600	Drilling artefact
8.390	8.420	Tephra
8.720	8.800	<b>UT1</b>
9.428	9.4370	Flood
10.950	11.090	Drilling artefact
11.767	11.811	Flood
14.527	14.538	Flood
15.363	15.419	Flood
16.455	16.468	Flood
17.910	18.090	Drilling artefact
18.304	18.328	Flood
18.500	19.090	Drilling artefact
19.220	19.400	Tephra
20.950	21.050	Drilling artefact
21.460	21.500	<b>DWT</b>
22.128	22.138	Flood
22.327	22.341	Flood
22.900	23.100	Drilling artefact
23.120	23.390	Slump
25.981	26.000	Flood
26.910	27.340	Drilling artefact
27.710	28.070	Drilling artefact
28.070	28.140	<b>MMT</b>
28.706	28.720	Flood
28.860	29.140	Slump
29.391	29.428	Flood
29.543	29.555	Flood
30.069	30.078	Flood
34.760	35.140	Slump
34.871	34.898	Flood
35.404	35.415	Flood
35.448	35.463	Flood
36.910	37.090	Drilling artefact
39.800	39.860	<b>AUT</b>
40.816	40.828	Flood
41.130	41.450	Slump
41.851	41.868	Flood
42.445	42.471	Flood
42.910	44.240	Drilling artefact
44.512	44.597	Flood
46.493	46.519	Flood
46.910	47.290	Drilling artefact
48.250	69.000	Eruption

**Supplementary Table 27 Ager marker points of core MS1.** Depths of event layers (floods, slumps, tephra and drilling artefacts) were subtracted from the age/depth model.

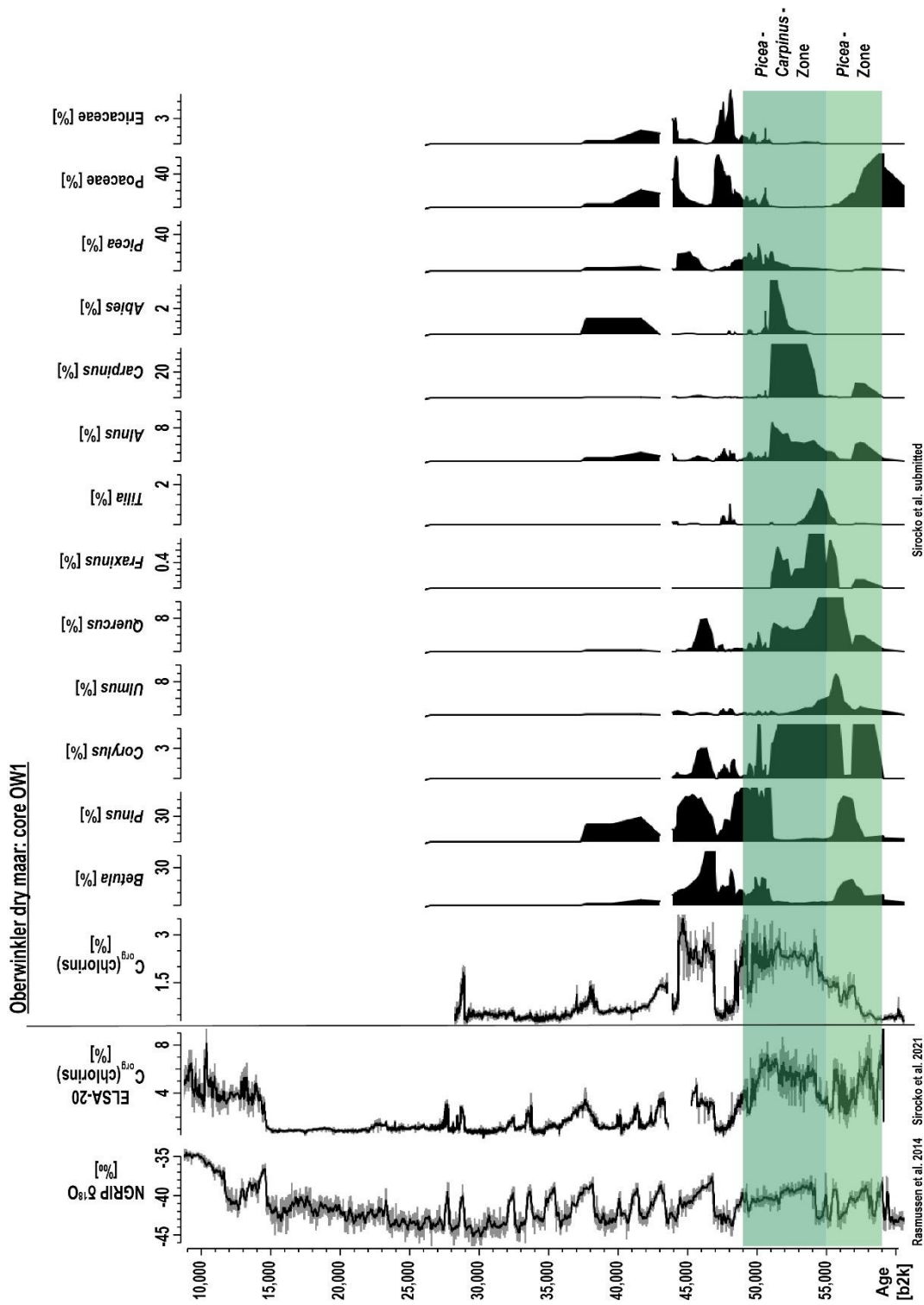




**Supplementary Fig. 15** Core photo of sediment core OW1 with the Auel Cooling Event (ACE) and ages of marker tephra layers (Sirocko et al. 2016, 2021). Ages of marker layers are given in the yr b2k notation.



**Supplementary Fig. 16** Pollen percentages and C<sub>org</sub>(chlorins) record of core OW1 versus depth (Sirocko et al. submitted). Pollen data were smoothed using a three-point running mean. Pollen counts were performed by Frank Dreher.



Supplementary Fig. 17 Pollen percentages and  $C_{org}$ (chlorins) record of core OW1 versus age (Sirocko et al. submitted) together with ELSA-20  $C_{org}$ (chlorins) (Sirocko et al. 2021) and NGRIP  $\delta^{18}O$  (Rasmussen et al. 2014) records. Pollen data were smoothed using a three-point running mean. Pollen counts were performed by Frank Dreher.

OW1		Ager
Albert et al. subm		
[m]	[yr b2k]	
Depth	Age	Comment
0.000	25800	Coretop (extrapolated)
9.190	28600	<b>G14</b> end / onset GS4
9.490	28900	<b>G14</b> onset
18.300	32040	<b>G15.2</b> end / onset GS5.2
19.000	32500	<b>G15.2</b> onset
19.650	33360	<b>G16</b> end / onset GS6
20.030	33740	<b>G16</b> onset
21.360	34740	<b>G17</b> end / onset GS7
22.220	35480	<b>G17c</b> onset
23.870	36580	<b>G18</b> end / onset GS8
26.020	38220	<b>G18c</b> onset
27.500	42240	<b>G111</b> end / onset GS11
28.000	43500	<b>ACE</b> top (to 29.00m)
30.020	44280	<b>G112</b> end
30.800	46860	<b>G112c</b> onset
31.950	47340	<b>MMT</b>
35.600	48340	<b>G113</b> end / onset GS13
36.180	49280	<b>G113c</b> onset
36.330	49600	<b>G114</b> end / onset GS14QS
38.150	51100	<i>Carpinus</i> peak
38.640	54220	<b>G114e</b> onset
38.840	55400	<b>G115.2</b> end / onset GS15.2
38.950	55800	<b>G115.2</b> onset
39.060	56500	<b>G116</b> end / onset GS16
39.250	57600	small <i>Carpinus</i> peak
39.610	59130	<b>AUT</b>
45.500	72590	<b>SMT</b>
49.000	76000	Corebase (extrapolated)

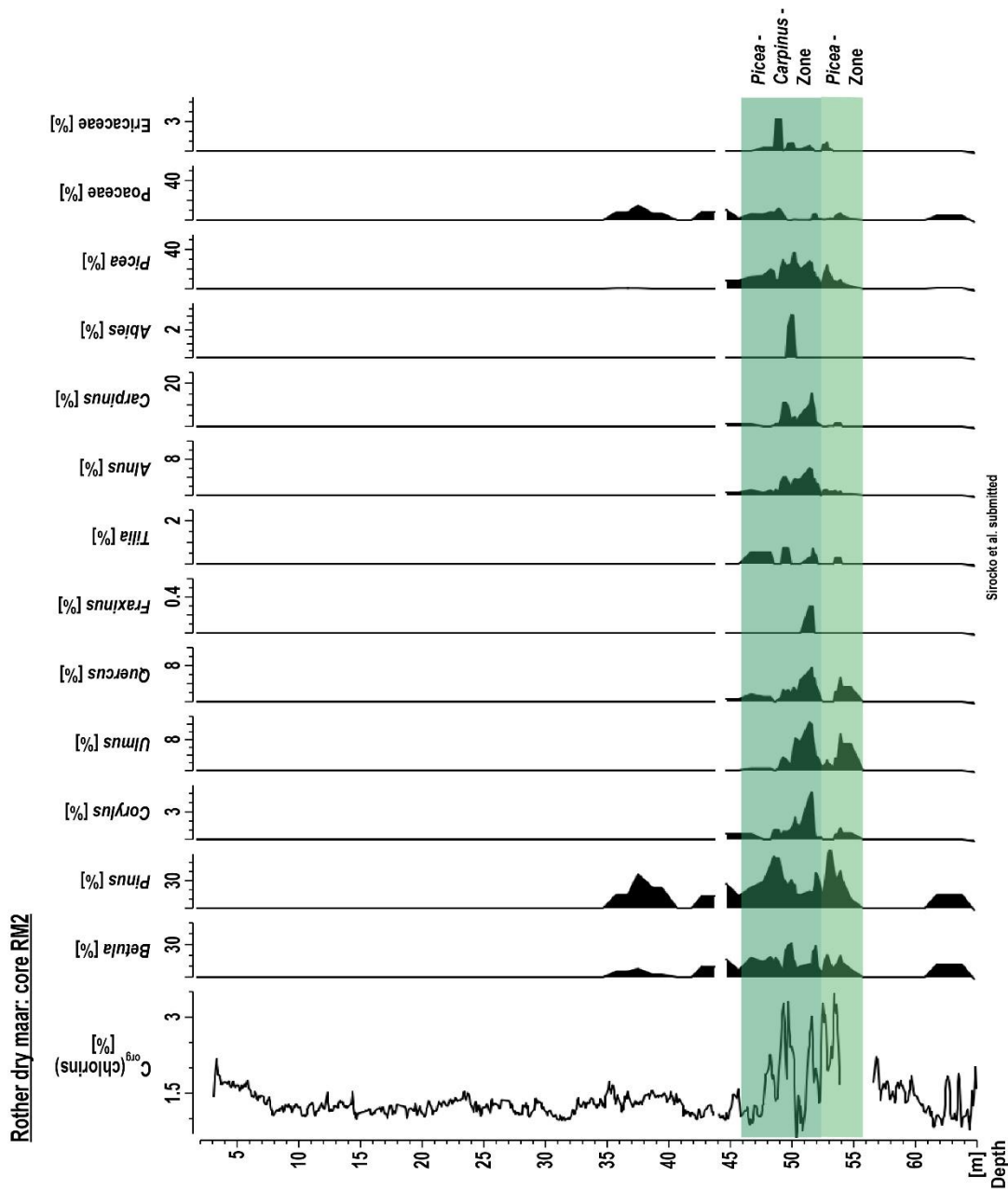
OW1 Events		
[m]	[m]	
Depth top	Depth base	Comment
7.410	7.600	Slump
7.900	8.410	Drilling artefact
8.830	8.920	Drilling artefact
9.477	10.043	Drilling artefact
10.073	10.145	Drilling artefact
10.240	10.430	Drilling artefact
10.997	12.547	Drilling artefact
12.607	12.679	Drilling artefact
12.707	12.893	Drilling artefact
12.999	14.070	Drilling artefact
27.760	27.780	Tephra
30.200	30.320	Tephra
31.944	31.950	<b>MMT</b>
33.930	34.090	Drilling artefact
35.170	35.510	Slump
36.500	36.630	Drilling artefact
37.130	37.780	Slump
39.363	39.605	<b>AUT</b>
40.119	40.173	Tephra / drilling artefact
40.260	40.590	Tephra / drilling artefact
42.985	43.120	Tephra
45.300	45.500	<b>SMT</b>
45.500	47.000	Drilling artefact
47.000	47.570	Drilling artefact

**Supplementary Table 28 Ager marker points of core OW1.** Depths of event layers (floods, slumps, tephra and drilling artefacts) were subtracted from the age/depth model.

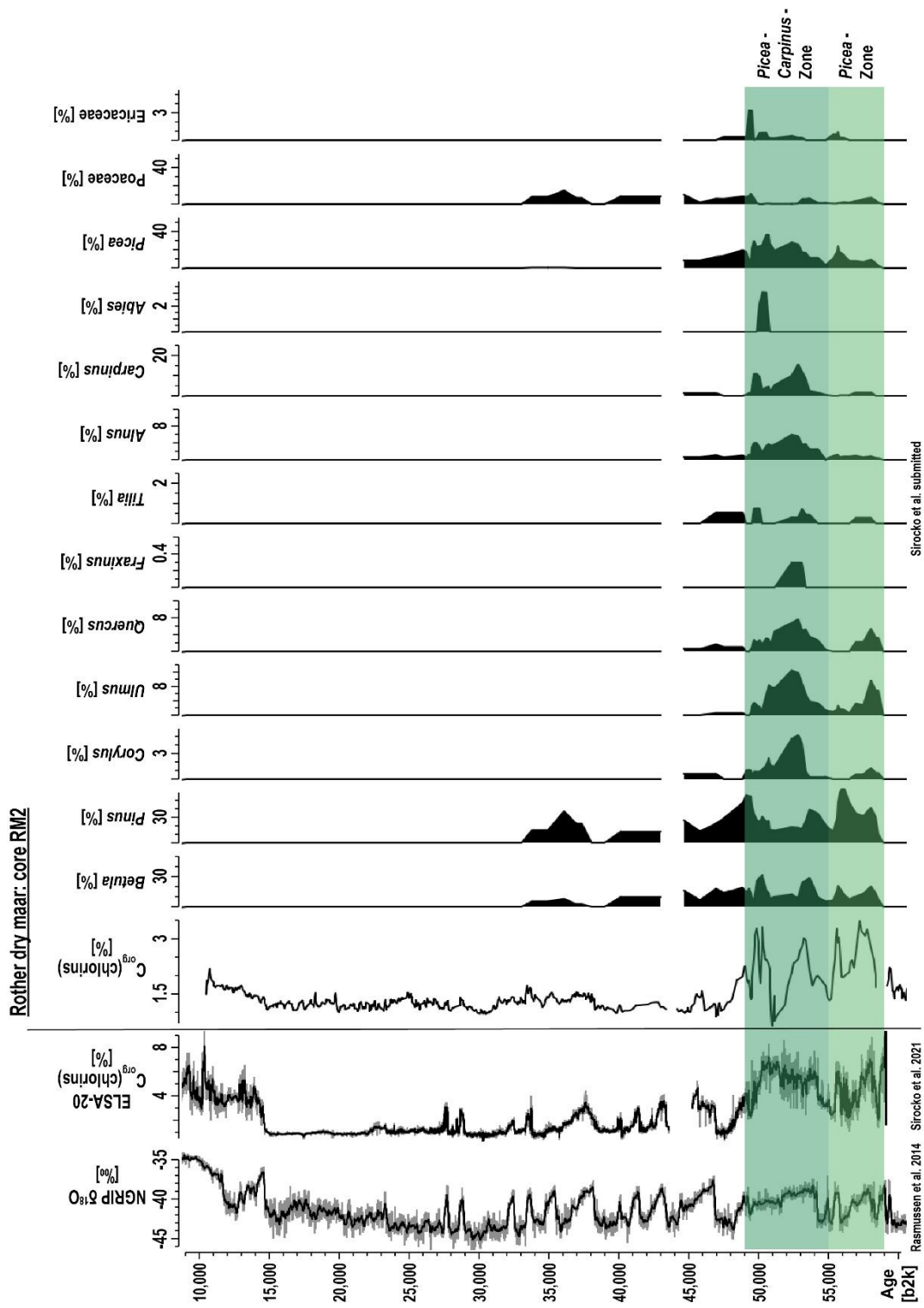
**Rother Maar dry maar: core RM2 0 - 65 m**



**Supplementary Fig. 18 Core photo of sediment core RM2 with the Auel Cooling Event (ACE) and ages of marker tephra layers (Sirocko et al. 2016, 2021). Ages of marker layers are given in the yr b2k notation.**



**Supplementary Fig. 19** Pollen percentages and  $C_{org}$ (chlorins) record of core RM2 versus depth (Sirocko et al. submitted). Pollen data were smoothed using a three-point running mean. Pollen counts were performed by Frank Dreher.



**Supplementary Fig. 20** Pollen percentages and  $C_{org}$ (chlorins) record of core RM2 versus age (Sirocko et al. submitted) together with ELSA-20  $C_{org}$ (chlorins) (Sirocko et al. 2021) and NGRIP  $\delta^{18}O$  (Rasmussen et al. 2014) records. Pollen data were smoothed using a three-point running mean. Pollen counts were performed by Frank Dreher.

RM2		Ager	
Sirocko et al. 2016			
Update ELSA-20 strat.			
[m]	[yr b2k]		
Depth	Age	Comment	
0.000	7700	Coretop	
7.700	14692	GI1 onset	
20.300	23220	GI2.2 end / onset GS2.2	
20.800	23340	GI2.2 onset	
28.150	27540	GI3 end / onset GS3	
28.550	27780	GI3 onset	
28.920	28100	WBT	
29.100	28600	GI4 end / onset GS4	
29.900	28900	GI4 onset	
31.410	30300	UT1	
33.350	32040	GI5.2 end / onset GS5.2	
33.900	32500	GI5.2 onset	
35.100	33360	GI6 end / onset GS6	
35.600	33740	GI6 onset	
36.400	34740	GI7 end / onset GS7	
36.850	35480	GI7c onset	
37.900	36580	GI8 end / onset GS8	
40.950	38220	GI8c onset	
42.350	39900	GI9 end / onset GS9	
42.550	40160	GI9 onset	
42.700	40370	DWT	
43.600	43340	GI11 onset	
43.610	43500	ACE top (to 44.00m)	
46.400	46860	GI12c onset	
47.450	47340	MMT	
47.800	48340	GI13 end / onset GS13	
48.450	49280	GI13c onset	
49.100	49600	GI14 end / onset GS14QS	
50.850	51100	Carpinus Peak	
51.900	54220	GI14e begin	
52.350	55400	GI15.2 end / onset GS15.2	
52.800	55800	GI15.2 onset	
53.150	56500	GI16 end / onset GS16	
53.80	58280	GI16.2 onset	
56.580	59130	AUT	
62.400	63840	GI18 end	
62.800	64100	GI18 onset	
65.000	66400	Corebase	

RM2 Events		
[m]	[m]	
Depth top	Depth base	Comment
4.630	4.646	Flood
4.667	4.675	Flood
6.467	6.481	Flood
6.846	6.857	Flood
7.065	7.082	Flood
8.568	8.579	Flood
9.642	9.650	Flood
9.693	9.701	Flood
10.907	10.946	Flood
12.083	12.112	Flood
13.726	13.741	Flood
14.000	14.250	Drilling artefact
14.800	15.400	Drilling artefact
15.913	15.921	Flood
16.261	16.271	Flood
16.330	16.550	Drilling artefact
18.000	18.500	Drilling artefact
19.000	19.250	Drilling artefact
22.273	22.298	Flood
22.647	22.659	Flood
26.450	26.900	Slump (GI3)
27.273	27.282	Flood
28.512	28.520	Flood
28.800	28.920	WBT
29.781	29.792	Flood
30.161	30.173	Flood
30.631	30.639	Flood
31.113	31.122	Flood
31.360	31.410	UT1
34.900	35.100	Drilling artefact
40.831	40.843	Flood
40.950	41.150	Drilling artefact
41.441	41.456	Flood
41.562	41.581	Flood
42.680	42.700	DWT
43.190	43.360	Slump
43.482	43.494	Flood
45.250	45.350	Drilling artefact
45.337	45.352	Flood
45.742	45.756	Flood
46.915	46.924	Flood
47.430	47.450	MMT
47.492	47.501	Flood
50.247	50.259	Flood
50.500	50.840	Slump
51.401	51.409	Flood
51.595	51.603	Flood
56.390	56.580	AUT
56.839	56.848	Flood

**Supplementary Table 29** Ager marker points of core RM2. Depths of event layers (floods, slumps, tephra and drilling artefacts) were subtracted from the age/depth model.



RM2 Events		
[m]	[m]	
Depth top	Depth base	Comment
56.913	56.922	Flood
57.247	57.262	Flood
58.000	58.180	Slump
58.527	58.535	Flood
58.671	58.681	Flood
59.458	59.469	Flood
59.503	59.514	Flood
64.000	64.200	Tephra

**Supplementary Table 29 cont.**  
**Age marker points of core RM2.** Depths of event layers (floods, slumps, tephra and drilling artefacts) were subtracted from the age/depth model.



# Weather control in radon flux time series from Schleswig-Holstein, Germany

Manfred Mudelsee<sup>1,2</sup> · Johannes Albert<sup>3</sup> · Frank Sirocko<sup>3</sup>

Received: 7 November 2019 / Accepted: 10 June 2020 / Published online: 31 July 2020  
© The Author(s) 2020

## Abstract

Indoor radon exposure is a serious hazard to human health. The radon concentration in surface air varies spatially as a result of the uranium content in the underlying rocks. However, there exist also considerable knowledge gaps about temporal variations. Here we document the high temporal variability of radon flux from exhalation in high-resolution (hourly) time series from a site near Kleinneudorf, Schleswig-Holstein, Germany. By means of advanced techniques of statistical time series analysis, we show a close association between radon and meteorological variables (air temperature and air pressure). We identify four principal weather regimes that lead to different radon exhalation modes. For each of the modes, we construct a statistical linear model for radon prediction via the meteorological variables and their derivatives or time-lagged versions. The model explains between 53 and 86 percent of the variance. Many model deviations consist in excessively high measured radon values and hint at nonlinear effects. Other model deviations hint at non-meteorological forcing.

**Keywords** Radon · Time series analysis · Cross-spectral analysis · Kernel trend and derivative estimation · Multiple linear regression · Prediction · Air temperature · Air pressure · Human health

**Mathematics Subject Classification** 62M10 · 62M15 · 62M20 · 62P12

---

This work received funding by the German Federal Ministry for Economic Affairs and Energy via the ANGUS II Project (<https://www.angus2.de/en>), Grant Number 03ET6122C.

---

✉ Manfred Mudelsee  
mudelsee@climate-risk-analysis.com

<sup>1</sup> Alfred Wegener Institute, Helmholtz Centre for Polar and Marine Research, 27570 Bremerhaven, Germany

<sup>2</sup> Climate Risk Analysis, Heckenbeck, 37581 Bad Gandersheim, Germany

<sup>3</sup> Institute of Geosciences, Johannes Gutenberg University Mainz, 55128 Mainz, Germany

## 1 Introduction

The noble gas radon (Rn) has only radioactive isotopes, of which  $^{222}\text{Rn}$  has the longest half-life (3.8 days, alpha decay).  $^{222}\text{Rn}$  is part of the decay chain of the uranium isotope  $^{238}\text{U}$ .

Inside the human body, the alpha radiation produced by  $^{222}\text{Rn}$  and its decay products may damage body cells. Hence,  $^{222}\text{Rn}$  is considered as one of the main causes of lung cancer (Yoon et al. 2016). Accordingly, the EU has launched an initiative to map Rn concentrations in natural soils and rocks (Elío et al. 2019). The purpose is to determine Rn risk areas, where newly built houses have to be protected against infiltration from the subsurface strata into the basement. The problem is particularly pressing for old houses without a baseplate, which were usually built directly on bare soil. If additionally a strong thermal insulation is installed, then the indoor Rn concentration for such houses can reach extremely high values, above  $10,000\text{ Bq/m}^3$  (Huber et al. 2001), a value otherwise observed only in mines. The WHO (Zeeb and Shannoun 2009, p. xi therein) proposed a “reference level of  $100\text{ Bq/m}^3$  to minimize health hazards due to indoor radon exposure” and, “if this level cannot be reached under the prevailing country-specific conditions, the chosen reference level should not exceed  $300\text{ Bq/m}^3$ .” See also the EU’s Council Directive 2013/59/Euratom.

As a result of these policies, the natural Rn concentrations in soils and rocks have to be analyzed. Pioneering work on this for Germany has been performed by Kemski et al. (2001, 2005, 2009). For Germany, a map (Fig. 1b) was constructed on basis of measurements done between 1992 and 2003, which is also available from the website of the Bundesamt für Strahlenschutz (<https://www.bfs.de/DE/themen/ion/umwelt/radon/karten/boden.html>, last access 15 October 2019). These maps show large regions of increased Rn content in the southern parts of Germany and also in all other regions where granite or metal ores (i.e., uranium) are found (Fig. 1b).

The noble gas Rn can be dissolved in groundwater or the open pore space of soils and subsurface strata. The rate of production and venting from the water will usually be in steady state, and accordingly the Rn content in the pore water (groundwater) will be mostly constant over time. The Rn flux from the pore water, however, may change when the water warms. This can mean up to several degrees between winter and summer at a given location. In addition to this slow groundwater-related process, the Rn can be released from the open pore space (often the upper metres of strata) to the surface by thermal convection in the sediments, in particular along faults and fractures. On the relation between Rn release from the groundwater and temperature, see Akawwi (2014). On the influence of thermal convection in sediments, see Mogro-Campero et al. (1980) and Burkhart and Huber (1993).

Rn concentrations in the Quaternary strata of Northern Germany are generally low or intermediate. This is the case, for example, in the region of moraines from the last ice age in Schleswig-Holstein. However, local maxima of Rn have been observed intermittently at practically all places in Northern Germany. Such local maxima are thought to be mainly caused by locally high concentration of Rn-bearing rocks (e.g. granites, in particular those with abundant K-feldspar); see, for example, Kemski et al. (2001).

The data for the mapping of the Rn risk areas are measured in distinct time windows. The “normal” exposition time of a commercial exposimeter (the cheapest and most effective Rn measurement device) is in the order of a month. However, this exposure duration appears to be one of the main obstacles towards a consistent map because, as long time series reveal, the seasonal structure of Rn concentration is rather complex. For example, at our measurement site (Sect. 2), the monthly average Rn concentrations in February 2019 is  $6183 \text{ Bq/m}^3$ , while that in June 2019 is just  $1343 \text{ Bq/m}^3$ .

The availability of high-resolution time series of soil Rn concentrations has increased over the past few years. This allows to study space-time variability for critical geographical regions. For example, Moreno et al. (2016) study the Amer fault zone in Spain at a resolution of one day (and higher) for a 4-year time span; Siino et al. (2019) examine nine Rn stations from the Italian Radon Monitoring Network at a resolution of 2 h (and higher) for time intervals between 1 and 5 years; and Tareen et al. (2019) analyse a series from Muzaffarabad, a town sitting on top of a fault zone in Iran, at 40-min resolution (and downscaled) for a time span of 1 year. What distinguishes the present study is the fact that our measurements directly reflect the outgassing Rn (not the Rn in the soil), which makes it relevant from a health perspective.

The regular structure and the superimposed variations in the time series (Sect. 2) hint at a meteorological (co-)explanation of the causes of the temporal variability. Therefore, we measured surface-air temperature and surface-air pressure in the same device as the Rn concentrations. This allows us to compare selected time windows from the series by means of statistical methods (Sect. 3). The analytical results (Sect. 4) feed into the discussion (Sect. 5) of the separation of the weather regimes (i.e., Rn exhalation modes) with the purpose of predicting the Rn concentrations over time.

This paper is about ongoing work within the project ANGUS II. The aims of this paper are (1) to explore the above mentioned exhalation modes by means of an advanced high-resolution, direct measurement technique and (2) to compare the different modes by means of statistical time series analysis. The obtained results are the basis for a successful prediction of the Rn exhalation. There are two companion papers to be published elsewhere (Albert et al., manuscript in preparation; Sirocko et al., manuscript in preparation), to which we briefly refer to in the text.

## 2 Data

We have monitored the Rn flux above a well, which was drilled into last glacial meltwater sand and till down to a depth of 40 m. The location is near to the village of Kleinneudorf, east of lake Plön, Schleswig-Holstein, Germany (Fig. 1).

The drilling at Kleinneudorf is located in a small depression of active subsidence and highly permeable Quaternary sediments in the uppermost 40 m, which facilitates high permeability and causes a local “hotspot” of Rn flux (Albert et al., manuscript in preparation). To understand the role of this specific geological process at Kleinneudorf, we developed a fluxbox measurement system directly in the subsidence center. The fluxbox presents a novel approach to measure continuously Rn concentrations in a chamber, which allows a controlled gas flux from the soil to the air in a system of two boxes (Fig. 2).

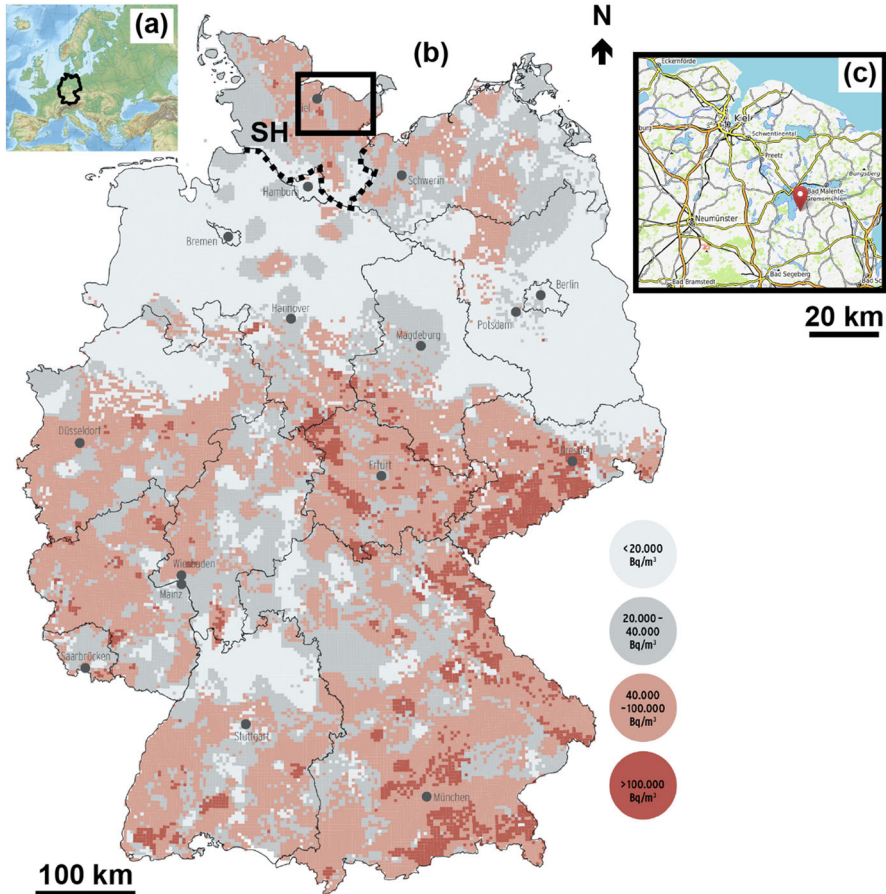


**Fig. 1** Study site and Rn map. **a** Map of Europe, with Germany indicated; **b** Rn map for Germany with concentration levels (shaded) and indicated study area (inset box); also indicated is the Bundesland Schleswig-Holstein (SH, north of the dashed boundary); **c** study area, with study site (red marker) indicated. Modified and reproduced with permission (**a** Wikipedia; **b** Bundesamt für Strahlenschutz (German Federal Office for Radiation Protection); **c** OpenStreetMap) (color figure online)

The schematic drill section (Fig. 2) shows that the groundwater level is at 8 m. The surface of the well is open, but covered with two boxes, which protect against rain, direct sun and wind. The casing of the well is solid plastic, so that the inner space of the casing is filled with gas exhaled only from the groundwater. The gas exhaled from the soil is trapped in the outer box, intrudes into the inner box, where it is shielded from direct venting by wind, which is a serious methodological problem in studies of Rn in houses, tunnels or direct air measurements.

We measured the Rn concentration in the inner box next to the bore hole. The two boxes are closed, but allow slow convection to the outside. Thus, our measurements reflect the Rn exhalation and not the soil Rn concentration. That means, the absolute values of Rn concentration are a function of this setting and cannot be used directly

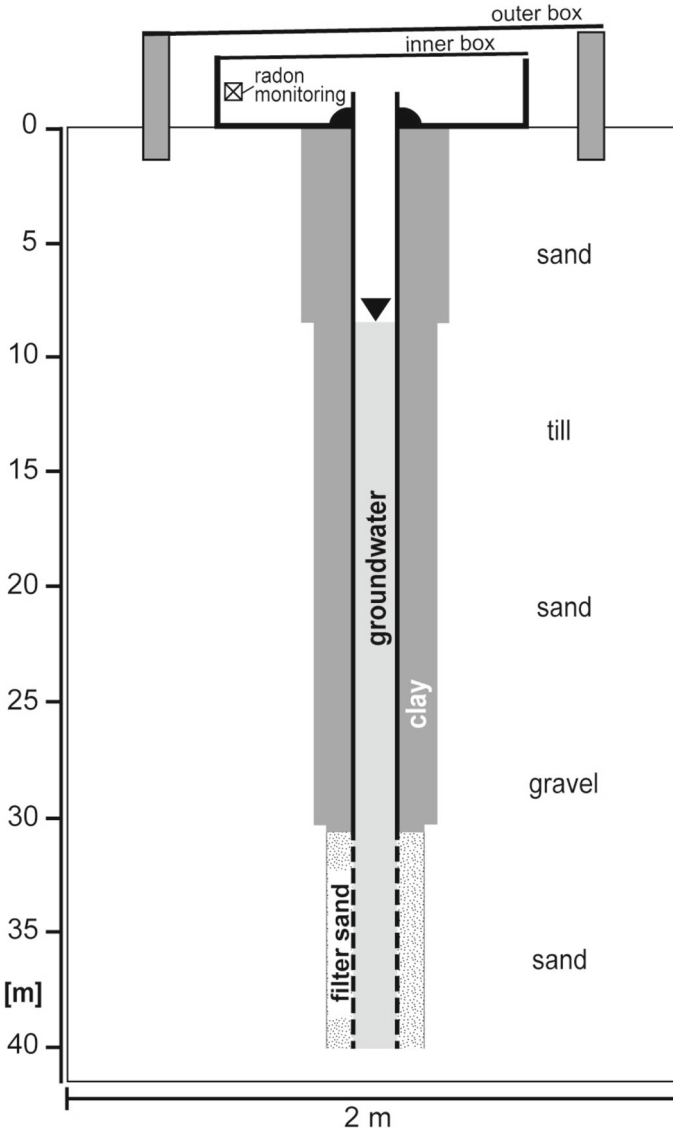


**Fig. 2** Schematic profile of well. Also shown are the two boxes for the detection of the exhalation flux

to compare to soil concentrations (as used for the mapping of the Rn risk areas). Accordingly, the absolute values in this study are arbitrary, and the variability structure of the time series (relative changes) is the main source of information. It was mandatory to keep the boundary conditions constant during the entire time of the experiment, which was run from April 2018 to September 2019.

The Rn measurements are done with a Canary Pro monitor (manufactured in 2017 by Corentium) (Radon Analytics 2020), modified for scientific use. The measurement

principle of the Canary device is based on a Si photodiode. When  $^{222}\text{Rn}$  and its progeny isotopes  $^{218}\text{Po}$  and  $^{214}\text{Po}$  decay within the instrument's dome, a few of the released alpha particles hit the open photodiode and the event, where the energy is released during the impact, is counted. This allows the number of decays to be measured. This measuring principle can be used to detect both Rn and its daughter isotopes. However, only Rn can enter the measuring chamber, because the daughters are electrically charged and get caught in the filters of the device. The modified Canary monitor has an application range from zero to  $100000 \text{ Bq/m}^3$ . The efficiency for Rn sampling specified by the manufacturer is one count per hour at a concentration of  $33 \text{ Bq/m}^3$ . Additionally to hourly Rn sampling, the device can record temperature, air pressure and humidity. However, due to repeated technical failure of the humidity sensor, this variable was not considered in this survey.

The full series for the variables Rn concentration, air temperature and air pressure are shown in Fig. 3. The nominal time spacing is  $d(i) = t(i) - t(i - 1) = d = 1$  hour, however, there exist two major gaps for Rn and a few other, minor gaps.

The time series (Fig. 3) shows pronounced Rn maxima for June 2018 and January 2019, that means, during rather different seasons. The processes controlling the Rn flux are best visible in shorter (about one week) series. Four different modes can be deciphered. Mode II (Fig. 4) is characterized by a Rn maximum during the night. Mode III (Fig. 5) exhibits two maxima, one during the night and one in the afternoon. Mode IV (Fig. 6) has the maximum in the late afternoon. Mode I (Fig. 7) has no relation to temperature but to decreasing surface air pressure. Apparently, surface air temperature and surface air pressure are the main control variables for the Rn flux in our monitoring system.

Hence, we selected four time intervals (Table 1) as representatives of the different weather regimes (i.e.. Rn exhalation modes)

### 3 Methods of data analysis

The general aim of climate data analysis is to make an inference about the data generating system (i.e., the climate) on basis of a set of data values. The data for the Rn project are in the form of time series. Let  $t(i)$  denote the time value and  $x(i)$  denote the value of a climate parameter (e.g., Rn concentration). The time values may in principle be unevenly spaced, although here in the project the case is even spacing (Table 1). Let  $n$  denote the sample size. The compact notation for a univariate time series is  $\{t(i), x(i)\}_{i=1}^n$ . Even spacing means that  $t(i) - t(i - 1) = d(i) = d = \text{constant}$  for  $i = 2, \dots, n$ . For multivariate time series, we have additional time series, and we write either  $x(i), y(i)$  (bivariate) or  $x_1(i), x_2(i), \dots, x_p(i)$  ( $p$ -dimensional). The inference consists (1) in the estimation of values of parameters of a statistical model for the climate and (2) in the testing of hypotheses about the climate. The models relevant for the project (cross-spectra, trend and regression) are detailed in the following subsections.

Since  $n < \infty$  and the data are affected by measurement noise (Sect. 2), the inference shows uncertainties. For parameter estimation, the uncertainties are expressed as error bars, confidence intervals, and so forth. For hypothesis testing, the uncertainty is

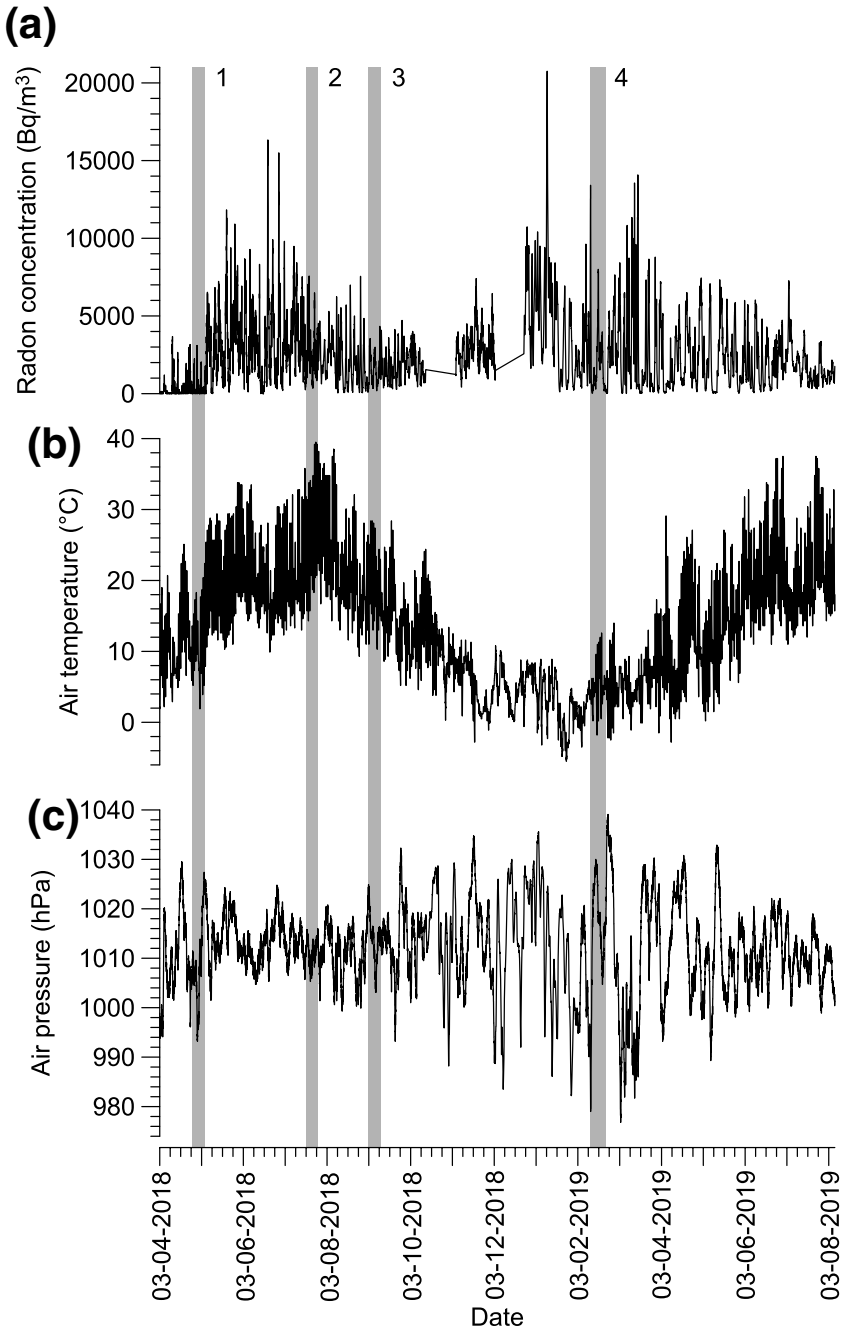


**Fig. 3** Data, time series of **a** Rn concentration, **b** air temperature and **c** air pressure for the full time interval (03-04-2018 02:16 to 07-08-2019 10:47). Also indicated (shaded) and numbered are the four intervals used for statistical analysis (Table 1)



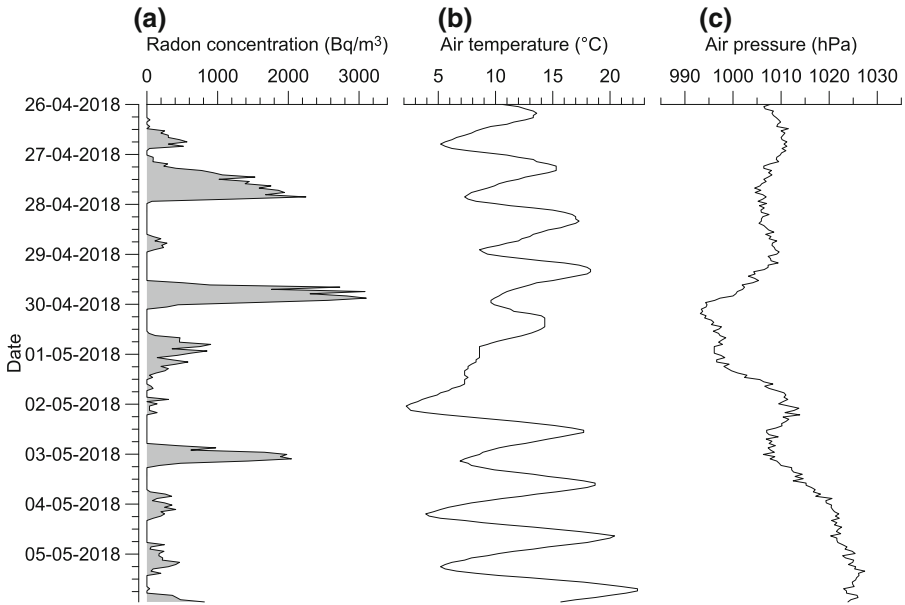


**Fig. 4** Data, time series of **a** Rn concentration, **b** air temperature and **c** air pressure for the time interval 1 (Table 1). This series represents exhalation mode II (“night mode”); see Sect. 5

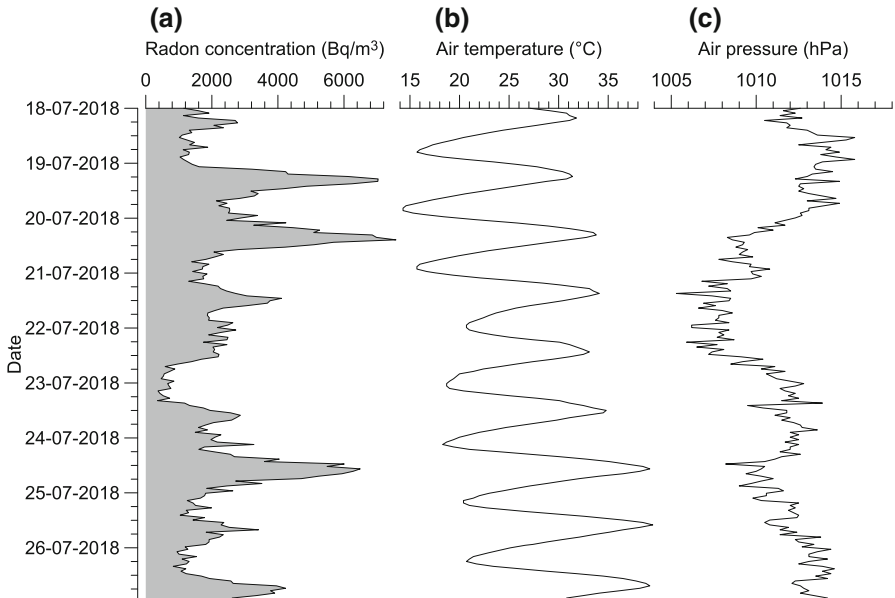


**Fig. 5** Data, time series of **a** Rn concentration, **b** air temperature and **c** air pressure for the time interval 2 (Table 1). This series represents exhalation mode III (“day mode”); see Sect. 5

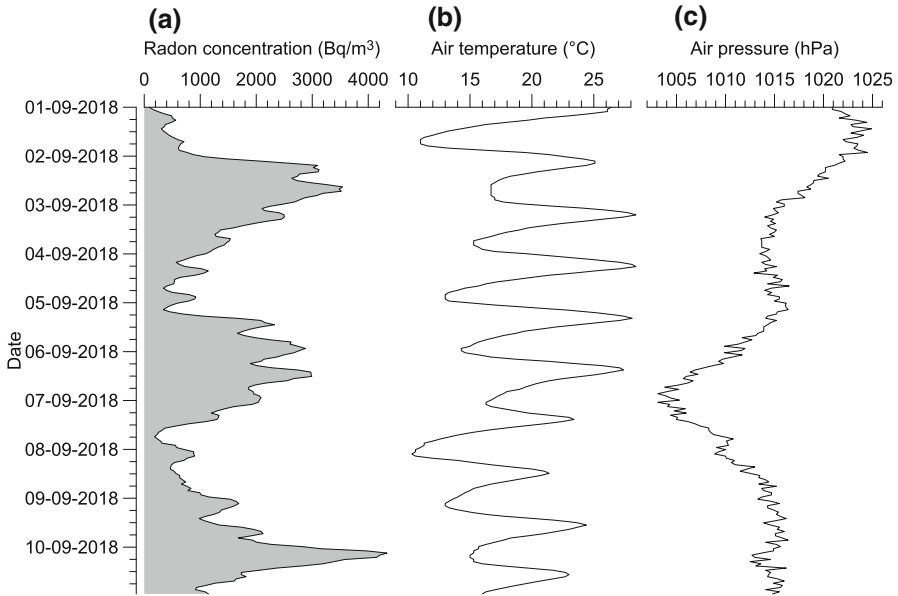


**Fig. 6** Data, time series of **a** Rn concentration, **b** air temperature and **c** air pressure for the time interval 3 (Table 1). This series represents exhalation mode IV (“day + night + air pressure mode”); see Sect. 5

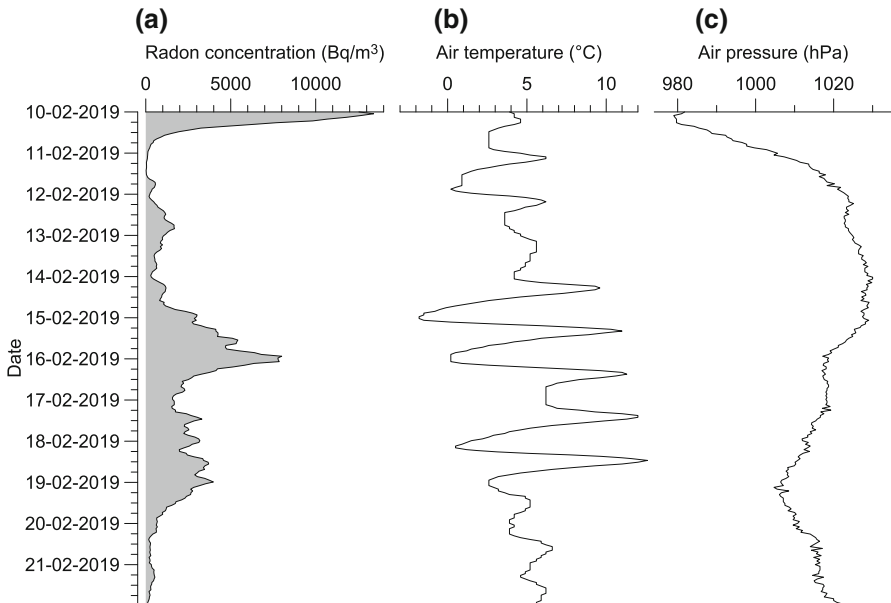


**Fig. 7** Data, time series of **a** Rn concentration, **b** air temperature and **c** air pressure for the time interval 4 (Table 1) This series represents exhalation mode I (“air pressure mode”); see Sect. 5

**Table 1** Database, selected time intervals. Also shown (roman numbers) are the corresponding Rn exhalation modes

Interval	Mode	Start	End	<i>n</i>	<i>d</i> (h)
<i>Air measurement data</i>					
Interval 1	II	26-04-2018 02:16	06-05-2018 01:16	240	1
Interval 2	III	18-07-2018 02:16	27-07-2018 01:16	216	1
Interval 3	IV	01-09-2018 02:51	11-09-2018 01:51	240	1
Interval 4	I	10-02-2019 01:55	22-02-2019 00:55	288	1
<i>Groundwater measurement data</i>					
Interval 1	II	26-04-2018 08:00:00	06-05-2018 00:00:00	117	2
Interval 2	III	18-07-2018 13:58:59	26-07-2018 23:58:59	102	2
Interval 3	IV	01-09-2018 09:23:42	11-09-2018 01:23:42	117	2
Interval 4	I	10-02-2019 08:33:29	22-02-2019 00:33:29	141	2
<i>Rn regression model data</i>					
Interval 1	II	26-04-2018 14:16	06-05-2018 00:16	114	2
Interval 2	III	18-07-2018 14:16	27-07-2018 00:16	102	2
Interval 3	IV	01-09-2018 15:51	11-09-2018 01:51	114	2
Interval 4	I	10-02-2019 14:55	22-02-2019 00:55	138	2

*h* hour

expressed as *P*-value, also denoted as false-alarm probability. To allow the assessment and climatological interpretation of the inferential results, the uncertainties have to be reported. Estimates without error bars are useless. For more background on climate and statistical inference, see, for example, the textbooks by von Storch and Zwiers (1999) or Mudelsee (2014).

### 3.1 Cross-spectral analysis

Consider a stationary process in continuous time,  $X(T)$ , which has a spectral representation (Priestley 1981). This means,

$$X_{T'}(T) = (2\pi)^{1/2} \int_{-\infty}^{\infty} G_{T'}(f) e^{2\pi ifT} df, \tag{1}$$

where  $X_{T'}(T)$  is the truncated process (i.e.,  $X_{T'}(T) = X(T)$  for  $-T' \leq T \leq T'$  and  $X_{T'}(T) = 0$  elsewhere),

$$G_{T'}(f) = (2\pi)^{-1/2} \int_{-\infty}^{\infty} X_{T'}(T) e^{-2\pi ifT} dT \tag{2}$$

and  $f$  is frequency. Then the one-sided nonnormalized power spectral density function—shortly denoted henceforth as autospectrum—is given by

$$h(f) = \lim_{T' \rightarrow \infty} \left\{ E \left[ 2\pi \left| G_{T'}(f) \right|^2 / T' \right] \right\}, \tag{3}$$

where  $E[\cdot]$  is the expectation operator. The autospectrum is the Fourier transform of the autocovariance function (Priestley 1981). It measures the variance contribution of a certain frequency to the overall variance,  $S^2$ , of the process. Other roads to the definition of a spectrum exist.

Given a discrete, possibly unevenly sampled time series of size  $n$ ,  $\{t(i), x(i)\}_{i=1}^n$ , the task is to estimate the autospectrum. The Lomb–Scargle periodogram (Lomb 1976; Scargle 1982) is given by

$$I_{LS}(f_j) = \bar{d} \cdot \left\{ \frac{\left[ \sum_{i=1}^n X(i) \cos(2\pi f_j [T(i) - \tau_{Lomb}]) \right]^2}{\sum_{i=1}^n [\cos(2\pi f_j [T(i) - \tau_{Lomb}])]^2} + \frac{\left[ \sum_{i=1}^n X(i) \sin(2\pi f_j [T(i) - \tau_{Lomb}]) \right]^2}{\sum_{i=1}^n [\sin(2\pi f_j [T(i) - \tau_{Lomb}])]^2} \right\}, \tag{4}$$

where

$$\tan(4\pi f_j \tau_{Lomb}) = \frac{\sum_{i=1}^n \sin(4\pi f_j T(i))}{\sum_{i=1}^n \cos(4\pi f_j T(i))}, \tag{5}$$

the search frequencies are  $f_j = 1/(n\bar{d}), \dots, 1/(2\bar{d})$  and the average temporal spacing is given by  $\bar{d} = [t(n) - t(1)]/(n - 1)$ . In the case of even spacing, where  $d(i) = t(i) - t(i - 1) = d = \bar{d} = \text{const.}$ , the Lomb–Scargle periodogram corresponds to the usual periodogram (Mudelsee 2014). The frequencies  $f_j$  are employed to search for peaks of  $I_{LS}(f_j)$ . One drawback of the periodogram is that it is an inconsistent autospectrum estimator (Bartlett 1955), which means that with increasing  $n$  the estimation variance of the autospectrum does not decrease.

For autospectrum estimation, we therefore followed the common practice (Schulz and Mudelsee 2002) and employed time series segments (with 50% overlap), segment-wise linear detrending, segment-wise tapering and averaging of the Lomb–Scargle periodograms for the segments. We also corrected for autospectrum estimation bias via Monte Carlo simulations of an AR(1) noise process. The idea is to compare the theoretical AR(1) spectrum (Priestley 1981) with the average autospectrum over the simulations in order to obtain a frequency-dependent bias correction factor (Schulz and Mudelsee 2002). The existence of peaks in the spectrum was tested via the upper 95th percentile of the distribution for the AR(1) red-noise alternative (Schulz and Mudelsee 2002), which was determined by means of 1000 Monte Carlo simulations. We additionally assessed peaks by means of Siegel’s test at the 95% confidence level on the Lomb-Scargle periodogram (Schulz and Stattegger 1997). In the case of a strongly dominating peak in the estimated autospectrum, Schulz and Stattegger (1997) recom-

mended to first subtract this spectral component by means of a filter (Ferraz-Mello 1981) and only then to estimate the AR(1) parameter. We followed this recommendation since Rn concentration and air temperature exhibit strong daily components (Sect. 4.1). Multitaper estimation may for even spacing provide a superior estimation since it employs optimal tapers (Mudelsee 2014).

Next, consider two stationary processes,  $X(T)$  and  $Y(T)$ , with autospectra  $h_X(f)$  and  $h_Y(f)$ . The coherency (Schulz and Stattegger 1997) is defined as

$$c_{XY}^2 = \frac{|h_{XY}(f)|^2}{h_X(f) \cdot h_Y(f)}, \quad (6)$$

where  $h_{XY}(f)$  is the cross-spectrum, that is, the Fourier transform of the cross-covariance function (Priestley 1981). The coherency is a dimensionless measure between 0 and 1, which quantifies the degree of the linear relation between two processes in dependence on frequency.

Given two discrete, possibly unevenly sampled time series,  $\{t_X(i), x(i)\}_{i=1}^{n_X}$  and  $\{t_Y(i), y(i)\}_{i=1}^{n_Y}$ , the task is to estimate the coherency. Note that the set of time values,  $\{t_X(i)\}_{i=1}^{n_X}$ , needs not to be equal to  $\{t_Y(i)\}_{i=1}^{n_Y}$ . The Lomb–Scargle periodogram can also be used for the estimation of the cross-spectrum (Schulz and Stattegger 1997).

For coherency estimation, we employed segmenting (50% overlap), segment-wise linear detrending, segment-wise tapering, averaging of periodograms and tests against the AR(1) red-noise alternative (Ólafsdóttir et al. 2016). The upper percentile for the red-noise alternative was determined by means of 1000 Monte Carlo simulations. The interpretation of coherency estimates is only meaningful for frequencies where both  $X(T)$  and  $Y(T)$  have a significant peak in the autospectrum.

In the case of a meaningful and significant coherency estimate at a certain frequency, the estimate of the phase may shed light on lead–lag behaviour between the two processes at that frequency. We estimated also the phase via the Lomb–Scargle periodogram and the estimated cross-spectrum (Ólafsdóttir et al. 2016, Eq. (9) therein). The 95% confidence interval for the phase estimate was determined by means of 1000 Monte Carlo simulations.

For tapering in the estimations, we consistently employed the Welch I type, a number of seven overlapping segments and an oversampling factor (which corresponds to interpolation in the frequency domain in order to better visualize spectrum curves) of 16. The resulting spectral bandwidths (which determine the frequency resolution) for the Rn concentration and air temperature spectra (Sect. 4.1) is between  $2.21 \cdot 10^{-2} \text{ h}^{-1}$  ( $n = 288$ ) and  $2.94 \cdot 10^{-2} \text{ h}^{-1}$  ( $n = 216$ ). See Schulz and Mudelsee (2002) for more detailed technical explanation.

We used the software REDFIT-X (Ólafsdóttir et al. 2016) for autospectrum, coherency and phase estimation. We used the software TAUEST (Mudelsee 2002) for the estimation of the AR(1) parameter in the presence of uneven spacing, which includes a bias correction after Kendall (1954).

### 3.2 Kernel trend and derivative estimation

Consider a nonstationary process in continuous time,  $X(T)$ , which can be decomposed into trend, extremes and noise components,

$$X(T) = X_{\text{trend}}(T) + X_{\text{ext}}(T) + S(T) \cdot X_{\text{noise}}(T). \quad (7)$$

Mudelsee (2014) calls this the climate equation. The noise,  $X_{\text{noise}}(T)$ , is a zero-mean, unit-standard deviation process, which may have a spectral representation (Sect. 3.1). The noise may also describe the memory (i.e., autocorrelation, red noise) of the climate. The climate variability,  $S(T)$ , is a positive function. The trend component,  $X_{\text{trend}}(T)$ , is the long-term, possibly time-dependent climate mean. The terms  $X_{\text{trend}}(T)$  and  $S(T) \cdot X_{\text{noise}}(T)$  represent the definition of climate in terms of mean and variability (Brückner 1890; Hann 1901; Köppen 1923). The extreme component,  $X_{\text{ext}}(T)$ , was added by Mudelsee (2014) to allow for a separate analysis of climate extremes and related parameters (e.g., risk).

Given a discrete, possibly unevenly sampled time series,  $\{t(i), x(i)\}_{i=1}^n$ , the task is to estimate the trend component. In many situations, the data analyst aims for trend-model flexibility and avoids the restriction imposed by parametric models (e.g., linear) by means of a kernel smoothing technique. The approach by Gasser and Müller (1979, 1984) is:

$$\hat{X}_{\text{trend}}^{\text{GM}}(T) = h^{-1} \sum_{i=1}^n \left[ \int_{s(i-1)}^{s(i)} K\left(\frac{T-y}{h}\right) dy \right] X(i), \quad (8)$$

where  $T(i-1) \leq s(i-1) \leq T(i)$ . (The integration bounds,  $s(i)$ , are described in a subsequent paragraph.)

The kernel is a continuous and usually positive and symmetric function, it integrates as  $\int K(y)dy = 1$ . The kernel function employed by us is the Epanechnikov kernel,  $K(y) = 0.75 \cdot (1 - y^2)$ . Another common choice is the Gaussian,  $K(y) = (2\pi)^{-1/2} \exp(-y^2/2)$ .

Whereas the choice of  $K$  (Epanechnikov, Gaussian, and so forth), is more of “cosmetic” (Diggle 1985) interest, the bandwidth parameter,  $h$ , is crucial because it determines the uncertainty measures for the trend estimate. Although there exist bandwidth selectors for optimal smoothing (Mudelsee 2014), we prescribed  $h = 1$  day in order to smooth over the daily cycle.

Note that the selection of the sequence  $s(i)$  in particular, and the Gasser–Müller smoothing procedure in general, can be performed on unevenly spaced time series. The trend can be estimated for all time points within the observation interval,  $[t(1); t(n)]$ . The kernel functions are modified near the interval boundaries (Gasser and Müller 1979, 1984), so that the trend can be estimated also there.

KERNEL (<https://www.manfredmudelsee.com/soft/kernel/index.htm>, 30 August 2019) is a Fortran software based on routines originally developed by Theo Gasser. It places the integration bound,  $s(i)$ , in the middle between two time points. KERNEL further sets

$$s(0) = 1.5 \cdot t(1) - 0.5 \cdot t(2) \quad (9)$$

and

$$s(n) = 1.5 \cdot t(n) - 0.5 \cdot t(n - 1). \quad (10)$$

Also the first derivative of the variable,  $dX(T)/dT$ , and its long-term time dependence, can be studied by means of the kernel technique. This goes via the first derivative of the kernel function (Gasser and Müller 1984).

An uncertainty measure for the estimated trend or derivative curves is essential for assessing the significance of the ups and downs in the estimate, whether these variations constitute real features or are generated by noise.

Let  $\hat{x}_{\text{trend}}^{\text{GM}}(i)$  be the estimate (sample level) at time  $t(i)$ . Date minus trend estimate define the unweighted nonparametric regression residuals,  $e(i) = x(i) - \hat{x}_{\text{trend}}^{\text{GM}}(i)$ . The time series of residuals is  $\{t(i), e(i)\}_{i=1}^n$ .

The moving block bootstrap (MBB) resampling procedure (Künsch 1989) draws random blocks of length  $l$  ( $0 < l < n$ ) from the residuals. Mudelsee (2014) presents  $l$ -selectors, which are based on the autocorrelation properties of the data. The MBB then concatenates the blocks until a series of size  $n$  is obtained. The random series, denoted as  $\{t(i), e^*(i)\}_{i=1}^n$ , preserves the statistical properties of the random component of the data generating process. These are distributional shape and serial dependence (over  $l$ ).

The so-called replication of the trend estimate is obtained via re-application of the kernel technique. This procedure resampling–estimation is repeated  $B$  times (we use  $B = 400$ ). The bootstrap standard error,  $\text{se}(T')$ , of the trend estimate at a certain time point,  $T'$ , is defined as the standard deviation over the  $B$  replications at  $T'$ .

A pointwise standard-error band can be constructed from the standard-error intervals for the trend estimate as follows. The standard-error interval for the time value  $T'$  is given by  $[\hat{X}_{\text{trend}}^{\text{GM}}(T') - \text{se}(T'); \hat{X}_{\text{trend}}^{\text{GM}}(T') + \text{se}(T')]$ . The band is obtained by concatenating the upper bounds,  $\hat{X}_{\text{trend}}^{\text{GM}}(T') + \text{se}(T')$ , for the full time interval,  $t(1) \leq T' \leq t(n)$ , and by concatenating the lower bounds,  $\hat{X}_{\text{trend}}^{\text{GM}}(T') - \text{se}(T')$ . For the Rn project, we show in a conservative approach the wider two-standard-errors bands, which are obtained from the interval  $[\hat{X}_{\text{trend}}^{\text{GM}}(T') - 2 \text{se}(T'); \hat{X}_{\text{trend}}^{\text{GM}}(T') + 2 \text{se}(T')]$ .

The book by Mudelsee (2014) contains more details about kernel estimation, MBB resampling, block length selection and the construction of uncertainty measures.

### 3.3 Multiple linear regression model

Let  $Y(i)$  denote Rn concentration in discrete time. Let  $X_1(i), X_2(i), \dots, X_p(i)$  denote a number of  $p$  air and groundwater variables. Assume that there exists a simple linear relation,

$$Y(i) = \beta_0 + \beta_1 \cdot X_1(i) + \beta_2 \cdot X_2(i) + \dots + \beta_p \cdot X_p(i) + S_Y(i) \cdot Y_{\text{noise}}(i) \quad (11)$$

for  $i = 1, \dots, n$ . This is a multiple linear regression model (Montgomery and Peck 1992), where  $Y(i)$  is the response variable and  $X_1(i), X_2(i), \dots, X_p(i)$  are the predictor variables. The term  $S_Y(i) \cdot Y_{\text{noise}}(i)$  is the noise component. The model can be used to predict unobserved Rn concentrations on basis of observed air and groundwater data.

In order to derive theoretical properties of estimates obtained by means of the regression model, the assumptions are often made that  $S_Y(i) = S_Y$  is constant (homoscedasticity) and  $Y_{\text{noise}}(i)$  is a purely random Gaussian stochastic process. However, in practice the model may be useful also in the presence of (1) heteroscedasticity, (2) autocorrelation and (3) non-Gaussian distributions. Indeed, for practical purposes the linearity of the model may also be sufficiently accurate in the presence of mild forms of nonlinear dependence. To quote Box and Draper (1987, p. 424 therein): “Essentially, all models are wrong, but some are useful. However, the approximate nature of the model must always be borne in mind.”

Given a discrete, possibly unevenly sampled time series of size  $n$ ,  $\{t(i), y(i), x_1(i), x_2(i), \dots, x_p(i))\}_{i=1}^n$ , the task is to estimate the regression parameters,  $\beta_0, \beta_1, \beta_2, \dots, \beta_p$ . This can be achieved by minimizing the sum of squares of deviations between data and linear fit. The formulas for this least-squares estimation (Montgomery and Peck 1992) are as follows. Let

$$y = \begin{bmatrix} y(1) \\ y(2) \\ \vdots \\ y(n) \end{bmatrix} \text{ (response vector),} \tag{12}$$

$$x = \begin{bmatrix} x_1(1) & x_2(1) & \cdots & x_p(1) \\ x_1(2) & x_2(2) & \cdots & x_p(2) \\ \vdots & \vdots & \ddots & \vdots \\ x_1(n) & x_2(n) & \cdots & x_p(n) \end{bmatrix} \text{ (data matrix),} \tag{13}$$

then

$$\hat{\beta} = \begin{bmatrix} \hat{\beta}_1 \\ \hat{\beta}_2 \\ \vdots \\ \hat{\beta}_p \end{bmatrix} \text{ (parameter estimate vector)} \tag{14}$$

is given by

$$\hat{\beta} = (x'x)^{-1} x'y. \tag{15}$$

In this matrix notation (Dahlquist and Björck 2008, Appendix A therein), if  $A$  is a matrix, then  $A'$  is its transpose and  $A^{-1}$  is its inverse. We used the `lm` function within the R computing environment (Dalggaard 2008) for the calculations.

The “classical” uncertainty measures (Montgomery and Peck 1992) for the parameter estimates are based on assumptions such as a purely random Gaussian noise. In case of autocorrelated noise, the estimates can be obtained via the effective data size Mudelsee (2014, Chapter 2 therein), the determination of which can be achieved via the time series of the residuals and AR(1) fits (Mudelsee 2002). If there are indications



that also the distributional assumption is violated, then bootstrap uncertainty measures (via the MBB) can be determined.

However, the actual parameter estimates (and their uncertainties) are less of interest in the present paper. The focus is on a strategy for prediction and the selection of predictors. For this, a measure of the quality of the fit of the model (Eq. 11) to the data is relevant. Literature (Montgomery and Peck 1992) recommends to calculate the adjusted coefficient of multiple determination,  $R_{\text{adj}}^2$ , as follows. Let

$$\bar{y} = \sum_{i=1}^n y(i)/n, \quad (16)$$

$$S_{yy} = \sum_{i=1}^n y(i)^2 - n \cdot \bar{y}^2, \quad (17)$$

$$y_{\text{fit}}(i) = \hat{\beta}_0 + \hat{\beta}_1 \cdot x_1(i) + \hat{\beta}_2 \cdot x_2(i) + \dots + \hat{\beta}_p \cdot x_p(i), \quad i = 1, \dots, n, \quad (18)$$

$$SSE = \sum_{i=1}^n [y(i) - y_{\text{fit}}(i)]^2, \quad (19)$$

$$R^2 = 1 - SSE/S_{yy}, \quad (20)$$

then

$$R_{\text{adj}}^2 = 1 - (1 - R^2) \cdot (n - 1) / (n - p - 1). \quad (21)$$

The advantage of using the adjusted measure,  $R_{\text{adj}}^2$ , instead of  $R^2$  is that this penalizes overfitting with too many predictors.  $R_{\text{adj}}^2$  and  $R^2$  are both between 0 and 1. The values can be used as a measure of the data variance explained by the model.

We made an extension of the model to take into account prior knowledge, namely that the Rn concentration cannot be less than zero. Hence, we augmented the model (Eq. 11) as follows: if  $y_{\text{fit}}(i) < 0$ , then set  $y_{\text{fit}}(i) = 0$ . This augmented model has one extra parameter (which has a value of zero). The calculation of  $R_{\text{adj}}^2$  in Eq. (21) has to take this into account by an increase of  $p$  by one.

## 4 Results

### 4.1 Cross-spectra

The results of the cross-spectral analyses for Rn concentration and air temperature in the various intervals are presented in numerical form (Table 2) and as plots (Figs. 8, 9, 10 and 11). The phase estimate for the relation between Rn concentration and air temperature for the daily cycle ( $T_{\text{period}} = 1.0$  days) can be used to support the regression model (Sect. 4.3) via the inclusion of lagged predictor variables. The other air or groundwater variables do not exhibit strong daily cycles (results not shown).

For interval 1, both Rn concentration and air temperature show a clear, highly significant daily cycle (Fig. 8a, b). The coherency for that cycle is also significant (Fig. 8c).

**Table 2** Results, cross-spectral analyses.  $T_{\text{period}}$ , period (one over frequency) of the major spectral peak;  $\hat{a}'$ , bias-corrected AR(1) parameter estimate;  $\hat{\phi}$ , phase estimate with 95% confidence interval ( $\hat{\phi} > 0$  means that air temperature leads over Rn concentration)

Interval	Mode	Rn concentration		Air temperature		$\hat{\phi}$
		$T_{\text{period}}$	$\hat{a}'$	$T_{\text{period}}(d)$	$\hat{a}'$	
Interval 1	II	1.0 d	0.44	1.0	0.61	141°[96°; 183°]
Interval 2	III	1.0 d	0.13	1.0	0.69	19°[-4°; 44°]
Interval 3	IV	8.0 h	0.66	1.0	0.54	NA
Interval 4	I	7.2 h	0.56	1.0	0.08	NA

Also shown (roman numbers) are the corresponding Rn exhalation modes. Units: *d* day; *h* hour. NA not applicable

This allows to study the phase, which is estimated (with 95% confidence interval) as 141°[96°; 183°] (Fig. 8d). This means that for the daily cycle, air temperature leads over Rn concentration by an estimated time lag (with 95% confidence interval) of  $(141/360) \cdot 24 \text{ h} = 9.0 \text{ h}$  [6.4 h; 12.2 h].

Also for interval 2, both Rn concentration and air temperature show a clear, highly significant daily cycle (Fig. 9a, b). The coherency for that cycle is also significant (Fig. 9c). The phase is estimated as 19°[-4°; 44°] (Fig. 9d). This means that for the daily cycle, air temperature leads over Rn concentration by an estimated time lag of 1.3 h [-0.3 h; 2.9 h]. Since the confidence interval includes zero, the time lag is not statistically significant.

For interval 3 (Fig. 10) and interval 4 (Fig. 11), Rn concentrations do not show a significant daily cycle. Hence, phase estimation is not applicable here.

On basis of the phase estimates, we included lagged temperature as predictor variable. To accommodate for estimation uncertainties in the phase, and perhaps also of the peak period, a liberal approach (i.e., many time lags and for all intervals) was taken. That means, air temperature before 0 h, 1 h, 2 h, . . . , 12 h were used as predictors for Rn concentrations.

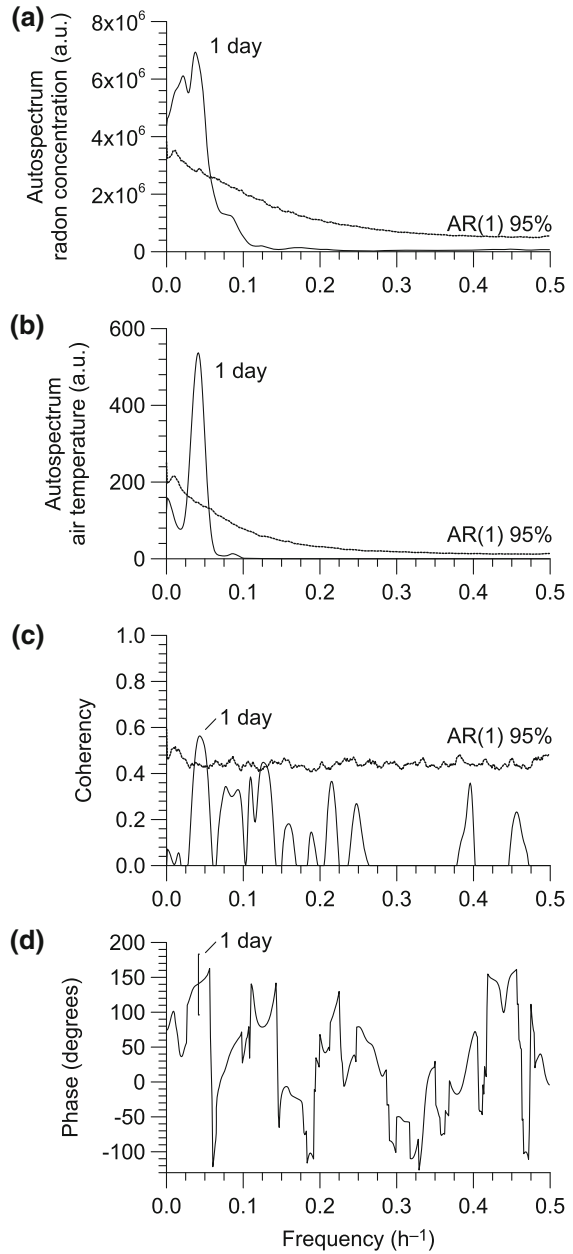
### 4.2 Trends and derivatives

The results of the analyses of time-dependent trends and time-dependent first derivatives of the air pressure are shown as plots (Figs. 12, 13, 14 and 15). Air pressure and its changes may constitute relevant meteorological control variables of Rn concentration. Therefore, they are included as predictors in the regression model (Sect. 4.3).

The shown time intervals in the plots are those for the Rn regression model data (Table 1). Note that the predictors include air temperature lagged by up to 12 h (Sect. 4.1). This means that the air-pressure data that are available for trend and derivative estimation (shown as filled symbols in Figs. 12a, 13a, 14a and 15a) extend somewhat beyond the shown interval boundaries. This explains, for example, the trend estimate at the earlier interval boundary (10-02-2019 08:55) for interval 4 (Fig. 15a).

The estimated persistence times,  $\hat{\tau}$ , with standard errors for the fits of an AR(1) autocorrelation model under uneven spacing (Mudelsee 2002), obtained on the resid-

**Fig. 8** Cross-spectra, interval 1 (mode II). See Sect. 3.1 for methodical details and Table 2 for result numbers. The vertical bar in panel (d) shows the 95% confidence interval for the phase estimate at the daily cycle



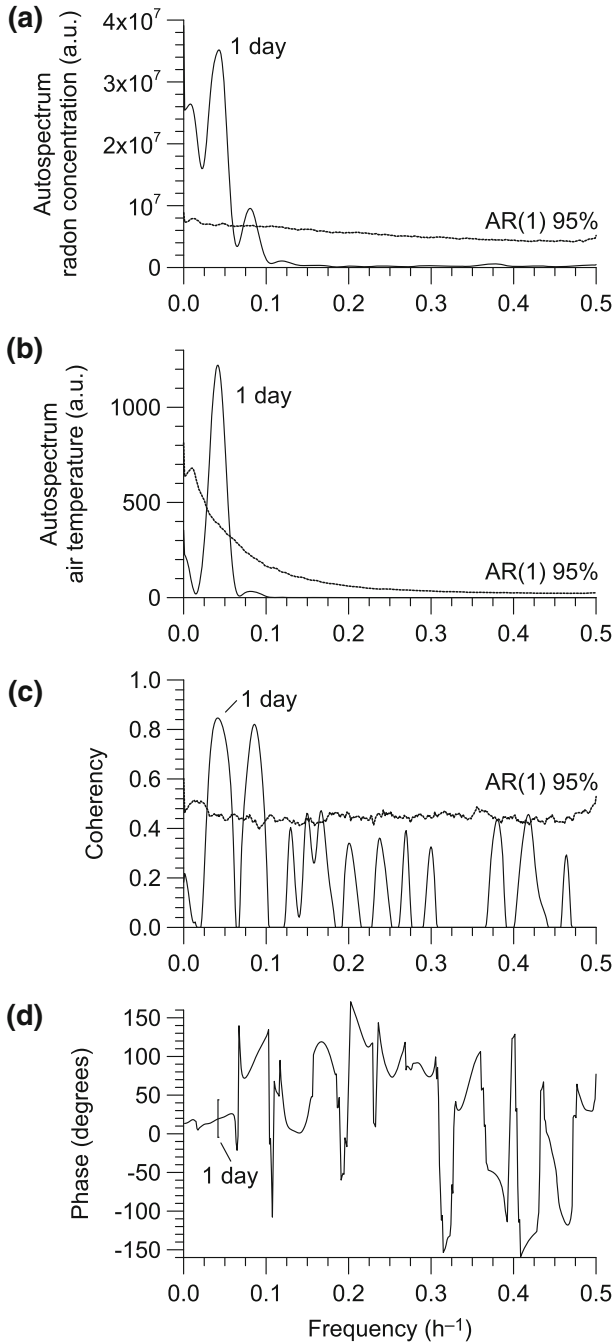


**Fig. 9** Cross-spectra, interval 2 (mode III). See Sect. 3.1 for methodical details and Table 2 for result numbers. The vertical bar in panel (d) shows the 95% confidence interval for the phase estimate at the daily cycle

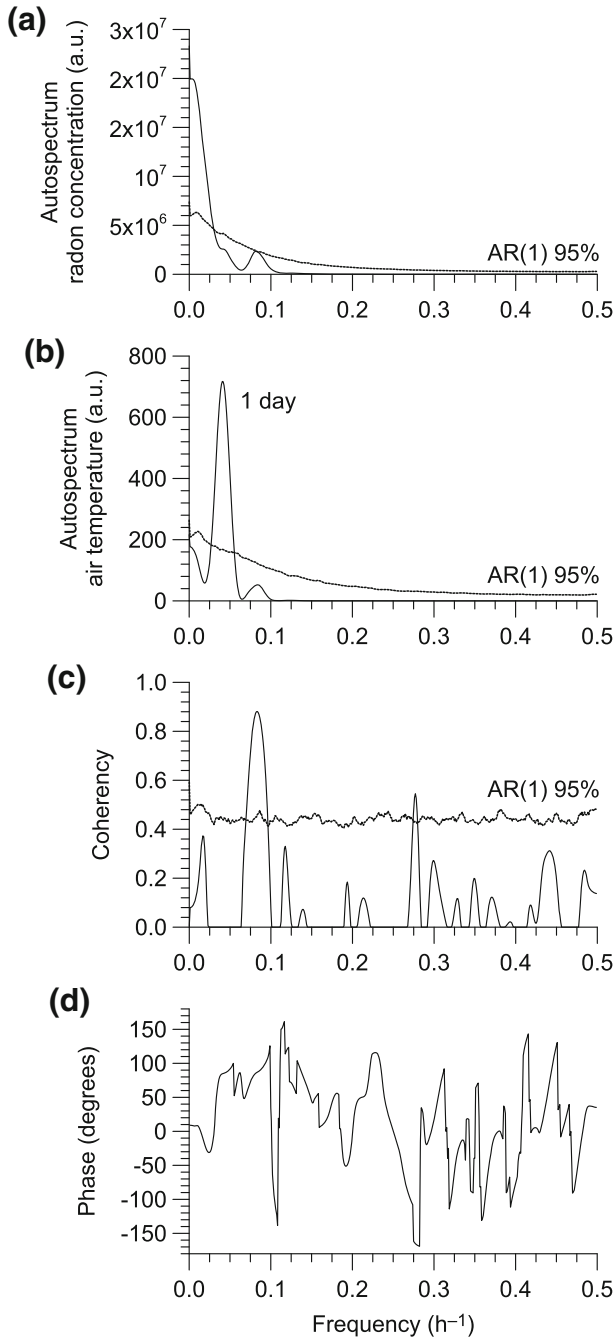


**Fig. 10** Cross-spectra, interval 3 (mode IV). See Sect. 3.1 for methodical details and Table 2 for result numbers

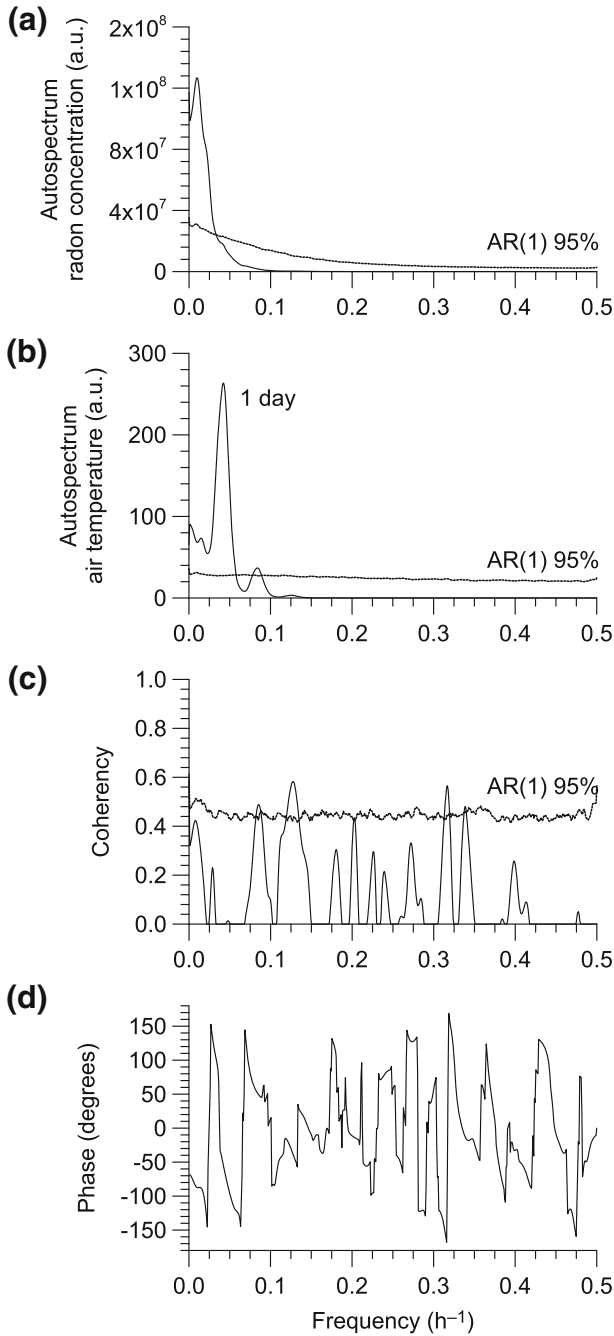
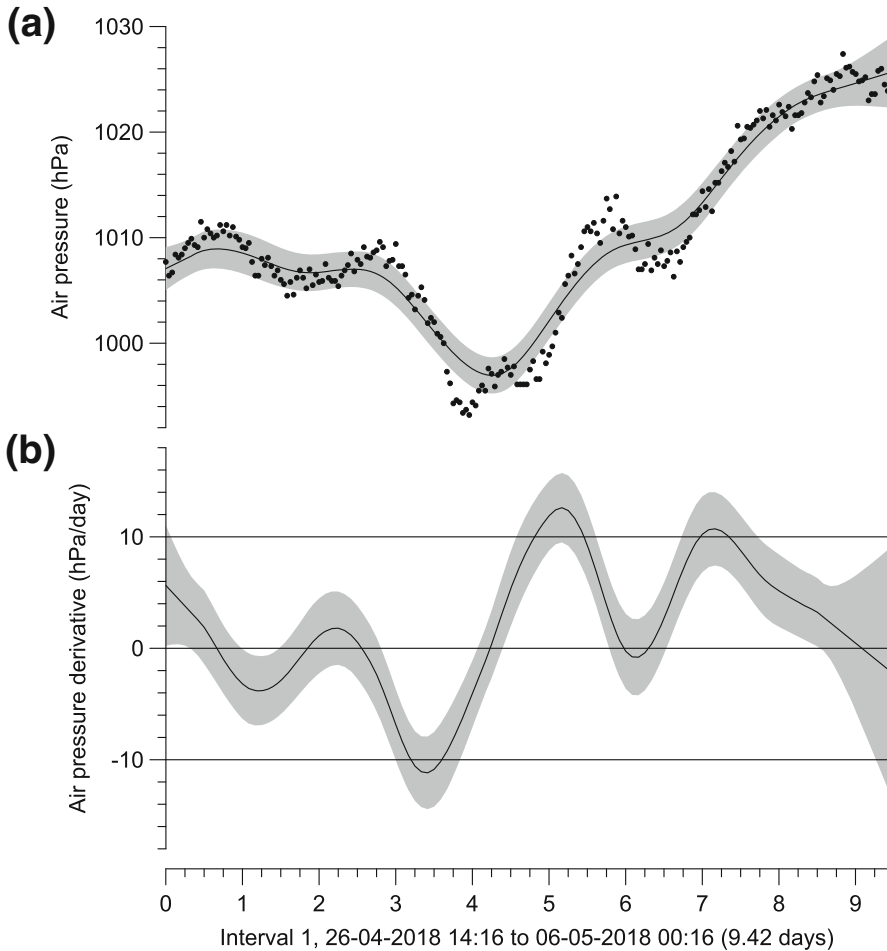


Fig. 11 Cross-spectra, interval 4 (mode I). See Sect. 3.1 for methodical details and Table 2 for result numbers



**Fig. 12** Kernel trend and derivative estimation, interval 1 (mode II). Shown are data (**a**; filled symbols), estimation curves (**a**, **b** solid, wiggly lines) and two-standard-errors bands (**a**, **b**; shaded). See Sect. 3.2 for methodical details

uals,  $e(i)$ , are: interval 1,  $\hat{\tau} = 4.8 \pm 1.0$  h; interval 2,  $\hat{\tau} = 1.1 \pm 0.2$  h; interval 3,  $\hat{\tau} = 2.1 \pm 0.3$  h and interval 4,  $\hat{\tau} = 19.8 \pm 5.4$  h. The variations among these numbers indicate that the memory of air-pressure fluctuations depends on the general weather situation. The persistence time estimates, together with samples sizes (Table 1), translate after Mudelsee (2014, Eq. 3.28 therein) into following block lengths,  $l$ , for the MBB: interval 1,  $l = 20$ ; interval 2,  $l = 7$ ; interval 3,  $l = 11$  and interval 4,  $l = 55$ .

The MBB confidence bands attest that there occurred significant changes in air-pressure trends and derivatives on daily and longer timescales (Figs. 12, 13, 14 and 15). This features are taken into account for the regression model of Rn concentrations. In addition to the smoothed series ( $h = 1$  day) of trend and first derivative, we employ

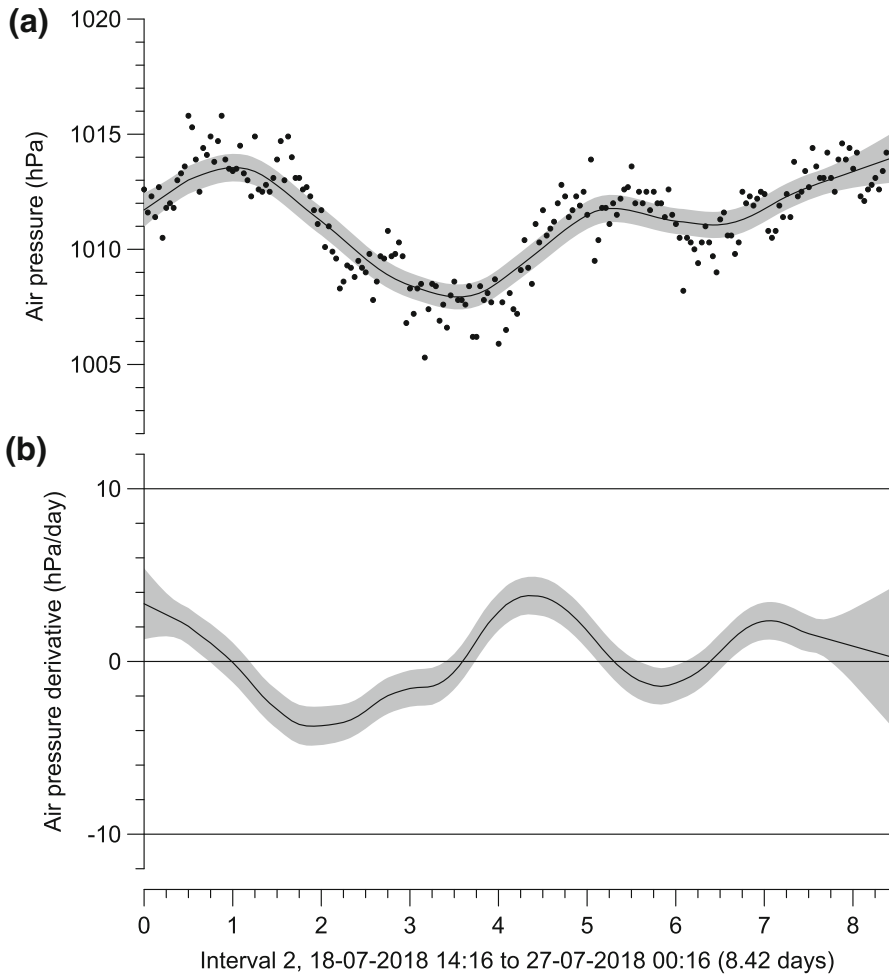


**Fig. 13** Kernel trend and derivative estimation, interval 2 (mode III). Shown are data (**a** filled symbols), estimation curves (**a, b** solid, wiggly lines) and two-standard-errors bands (**a, b** shaded). See Sect. 3.2 for methodical details

as predictors also the original air-pressure data,  $x(i)$ , and the first differences,  $x(i) - x(i - 1)$ , that means, versus before 1 h.

### 4.3 Regression model

Table 3 shows the description of the 19 predictors for Rn concentration. Since the model is constrained to  $y_{fit}(i) \geq 0$ , the calculation of  $R_{adj}^2$  in Eq. (21) employs a value of  $p = 20$ . The results of the regression model fits are shown as plots (Figs. 16, 17, 18 and 19).



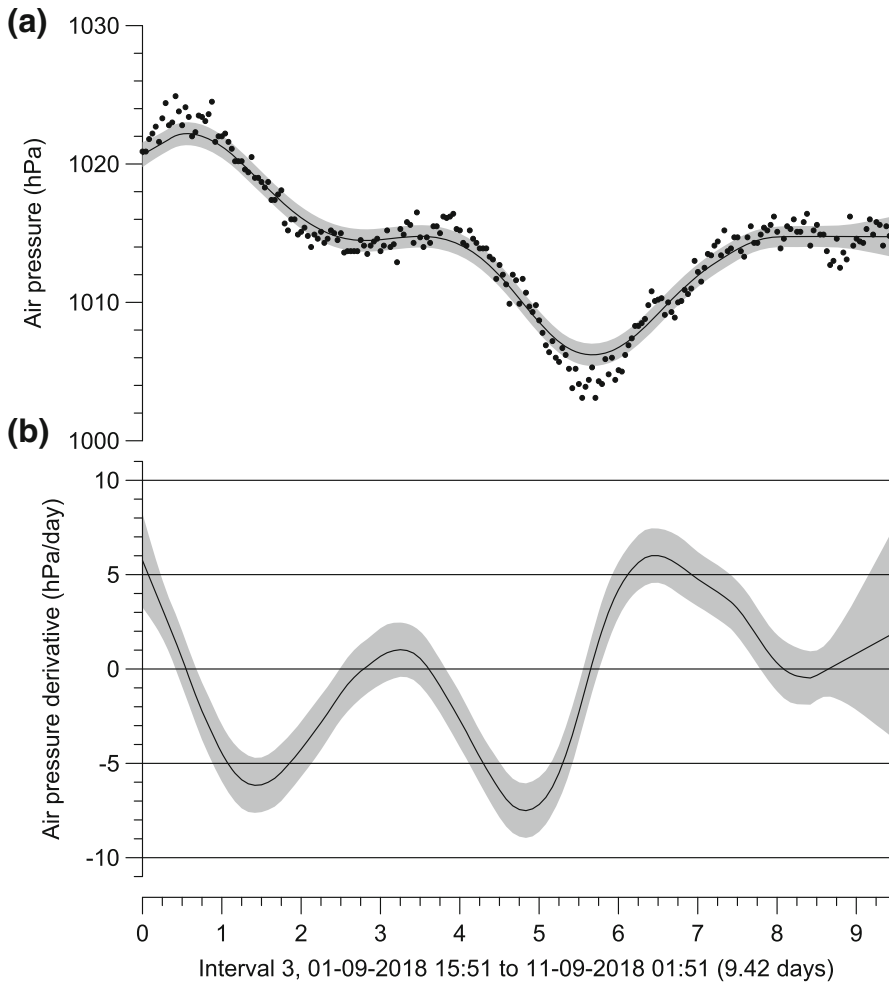


**Fig. 14** Kernel trend and derivative estimation, interval 3 (mode IV). Shown are data (**a** filled symbols), estimation curves (**a**, **b**; solid, wiggly lines) and two-standard-errors bands (**a**, **b**; shaded). See Sect. 3.2 for methodical details

The overall visual appearances of the fits for the four intervals is good. This is reflected in the high numerical values of  $R_{\text{adj}}^2$ , which are not very much smaller than the theoretical maximum of one. The constraint  $y_{\text{fit}}(i) \geq 0$  brought a slight improvement of fit quality (in terms of  $R_{\text{adj}}^2$ ) for intervals 1 and 4. It is remarkable that the rather simple linear regression model yields such good fits for the four different weather situations reflected in the four intervals.

Still, there are deviations between data and model. These deviations appear especially prominent in cases where the data exceed the model fits. One example of such a prominent peak is between days 8 and 9 for interval 3 (Fig. 18). These peaks of “excess

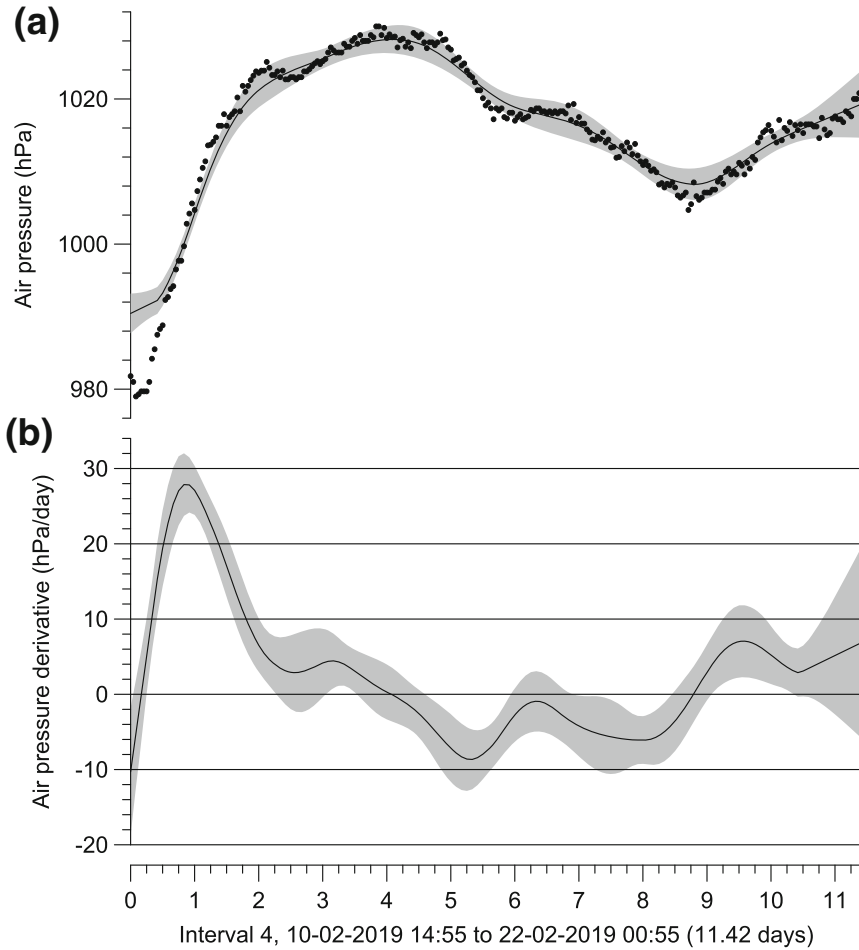


**Fig. 15** Kernel trend and derivative estimation, interval 4 (mode I). Shown are data (**a**; filled symbols), estimation curves (**a**, **b**; solid, wiggly lines) and two-standard-errors bands (**a**, **b**; shaded). See Sect. 3.2 for methodical details

Rn” (i.e., higher Rn than assumed on basis of the weather conditions) are subjected to further consideration (Sect. 5).

Another point for further discussion is the separation of the different weather regimes. This is important for “out-of-sample” prediction. This point is further pursued in Sect. 5.

## 5 Discussion

The fits of the relatively simple regression model to the Rn concentration data for the four time intervals (Figs. 16, 17, 18 and 19) enjoy rather high  $R_{\text{adj}}^2$  values, between 0.53

**Table 3** Regression model predictors for Rn concentration (in units of Bq/m<sup>3</sup>)

Number	Description	Unit
1	Air temperature	°C
2	Air temperature before 1 h	°C
3	Air temperature before 2 h	°C
4	Air temperature before 3 h	°C
5	Air temperature before 4 h	°C
6	Air temperature before 5 h	°C
7	Air temperature before 6 h	°C
8	Air temperature before 7 h	°C
9	Air temperature before 8 h	°C
10	Air temperature before 9 h	°C
11	Air temperature before 10 h	°C
12	Air temperature before 11 h	°C
13	Air temperature before 12 h	°C
14	Air pressure	hPa
15	Air pressure, first difference	hPa
16	Air pressure, trend	hPa
17	Air pressure, first derivative	hPa/d
18	Groundwater level	m
19	Groundwater temperature	°C

*d* day

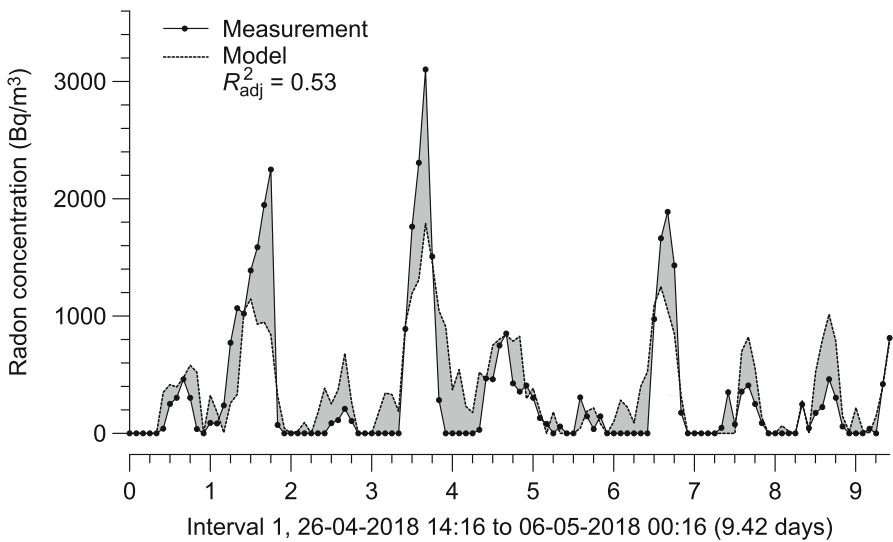


**Fig. 16** Rn concentration data and regression model fit, interval 1 (mode II). Also shown (shaded) are the deviations between data and fit. See Sect. 3.3 for methodical details

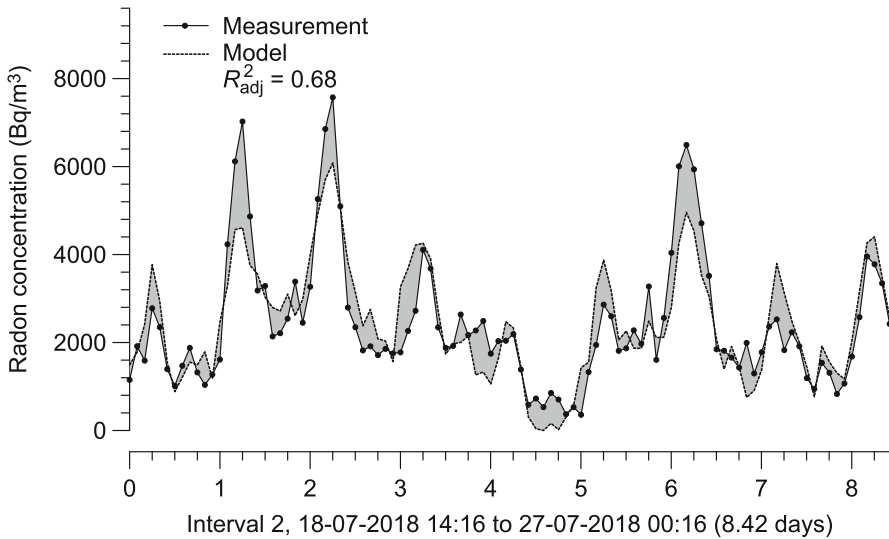


**Fig. 17** Rn concentration data and regression model fit, interval 2 (mode III). Also shown (shaded) are the deviations between data and fit. See Sect. 3.3 for methodical details

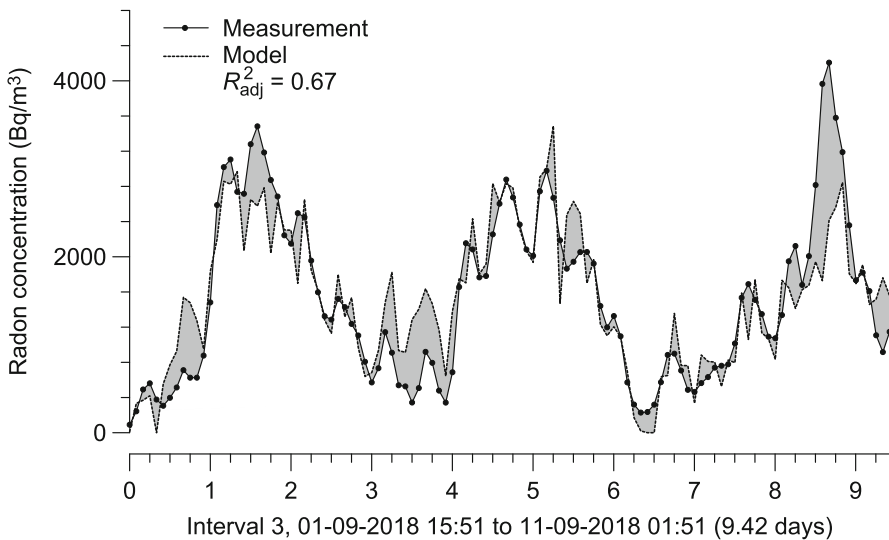


**Fig. 18** Rn concentration data and regression model fit, interval 3 (mode IV). Also shown (shaded) are the deviations between data and fit. See Sect. 3.3 for methodical details

and 0.86. Also if judged per eye, the fitted models appear to have a good descriptive power. An interesting methodical extension would be to consider fit measures other than  $R^2_{adj}$ , that means, measures that take into account the persistence in the time series data. This can be achieved by means of the effective data size Mudelsee (2014). For the present paper, however, this extension seems to be beyond the scope, and we believe that the fit assessments would not strongly change.

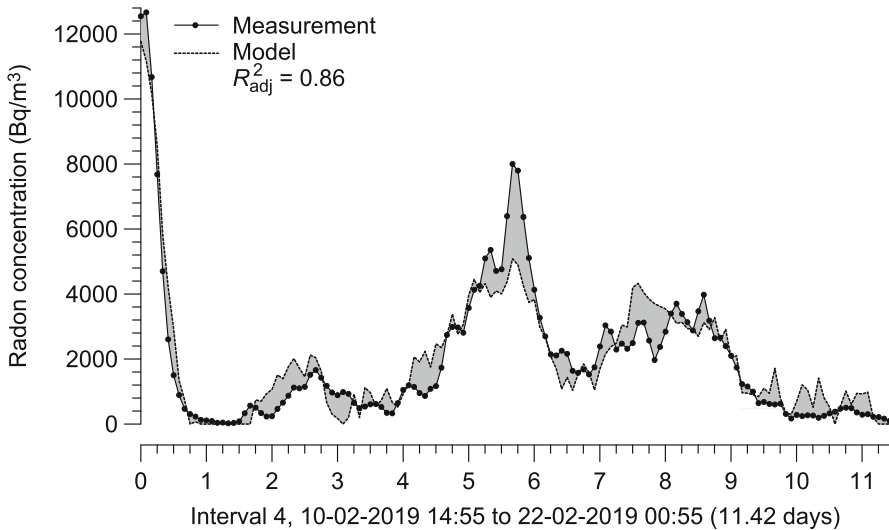


**Fig. 19** Rn concentration data and regression model fit, interval 4 (mode I). Also shown (shaded) are the deviations between data and fit. See Sect. 3.3 for methodical details

The largest deviations between model and data (indicated by the shaded areas in Figs. 16, 17, 18 and 19), are the excess Rn peaks, for which the Rn measurement values clearly exceed those of the weather-derived model fits. Many of those measurement peaks appear at times when also the model has a peak (but not so high), as, for example, around day 8.75 in Fig. 18. This hints at amplifying mechanisms, which may be taken into account by means of adding nonlinear terms to the regression model. However, some of the excess Rn measurement peaks may have no counterpart in the model, as, for example, around day 5.5 in Fig. 18. An explanation of such excess Rn peaks may be the occurrence of sporadic events affecting the ground, where a kind of “bypass” is formed to Rn stored in the depth. Microearthquakes can be one type of such an event (Al-Hilal et al. 1998; Steinitz et al. 2003; Walia et al. 2010). Therefore it would be interesting to compare the series of excess Rn peaks to seismic time series for the region. This will be done in a future paper. Other driving factors may be events of high precipitation and high wind speed (Schumann and Gundersen 1996; Martin et al. 2004; Gregorič et al. 2014). Furthermore, the series of excess Rn peaks may also be analysed by means of statistical tools from climate risk analysis (Mudelsee 2014, Chapter 6 therein). One typical inference would be the estimation of the return period of excess peaks, and another inference the analysis of the time-dependence in the occurrence rate of such events.

A hint for the reader who searches for literature on nonlinear models and data analysis. Standard references on nonlinear time series analysis are provided by Priestley (1988) from a statistical viewpoint and Kantz and Schreiber (1997) from a nonlinear dynamical system viewpoint. Tong (1990, 1992) took the notable approach to build a bridge between the two areas. Although these research areas are in development, it is probably a good learning strategy to start with the mentioned works.

The four time intervals (Table 1) have been selected as representatives of the different weather regimes (i.e., Rn exhalation modes). The “in-sample” model fits (Figs. 16, 17, 18 and 19) were on the one hand “necessarily good.” On the other, the good descriptive power of weather has a root in physics. The Rn flux is to a large extent controlled by only two weather parameters, the surface air pressure and surface air temperature, which explain a large fraction of the Rn variance (indicated by the  $R_{adj}^2$  values). The physical processes that govern these patterns are likely related to convective meteorological processes. These may influence the partial pressure of a gas above a liquid (Henry’s law), see, for example, Westphal (1970, p. 245 therein). In particular, it is the thermal convection in the open pore space in the loose Quaternary sediments above the groundwater level, from which the Rn is released.

For the practice of prediction, however, it has to be decided on basis of the weather data which regime, which Rn exhalation mode prevails. What are the defining weather properties for our site (Fig. 1)?

Exhalation mode I. The effect of the air pressure becomes best visible during the weeks of reduced temperature variations, that means, during days of minimal temperature gradients between day and night in October or March. However, particularly the October is associated with strong air-pressure gradients. This situation leads to increased flux from the strata into the air during times of rapid pressure reduction (as the opening the cover of a pot with hot water). The weather regression model for this exhalation mode explains 86% of the variance.

Exhalation mode II. The maximum of Rn is during the night, when air temperature falls below the temperature in the borehole, that is, when air temperature is below the groundwater temperature. This process (called chimney effect) dominates the Rn flux during winter and can be used as an indirect measure of groundwater temperature. This process works perfectly in a borehole chimney, but is less effective in normal soil/strata. Despite this limitation, the Rn maximum during the night is a typical feature at many other locations outside a borehole (Sirocko et al., manuscript in preparation). The weather regression model for this exhalation mode explains 53% of the variance.

Exhalation mode III. This regime is a mixture between mode II and mode IV. It characterizes the transition between these two primary modes. The transition time is in the order of a few weeks. The weather regression model for this exhalation mode explains 68% of the variance.

Exhalation mode IV. The precise synchronicity between (1) the maximum Rn flux during the late afternoon and (2) the beginning of the decrease of air temperature is typical for the months from May to August (Fig. 17). It can be best explained by the warming of the subsurface strata during a sunny day, and the onset of thermal convection/expansion of the soil gas in the open pore space of the upper subsurface strata. The daily warming of the upper soil strata must lead to convective processes in the sediments as soon as the direct insolation begins to cease, that is, when the soil at about 2 m depth is warmer than at the surface. This is the same process as the formation of fog in a cold air overlying a heated substrate. This explains the Rn maximum in the late summer afternoon. The weather regression model for this exhalation mode explains 67% of the variance.

The variations of the Rn concentration in the fluxbox system are apparently strongly related to changes in air pressure and air temperature, which explain 53–86% of the

total measured Rn variance. Accordingly, the largest proportions of degassed Rn is related to meteorological processes. Our fluxbox system, however, shows that this is not caused by venting of the detection system (as often occurs in measurement systems within houses or tunnels), but is indeed related to thermal convective gas flux from the permeable sediment pore space.

Ongoing work on a 2-year-long time series indicates that the majority of the unexplained variance is due to changes in the speed of the wind, which can “suck” gas out of the ground at high velocities. This third meteorological process will be presented in an ongoing project, and will likely explain most of the—yet—unexplained variance.

In the statistical area, we are currently experimenting with more or less direct implementations of the weather regime segmentation via the temperature–air pressure–season approach described above (Sirocko et al., manuscript in preparation). More advanced options via machine learning (Breiman 2001; Deloncle et al. 2007) will eventually also be explored in the future.

## 6 Conclusions

The flux of Rn from soil to air exhibits considerable time-dependent variability during the course of a year. This is documented by our new high-resolution measurement series from a well drilled near Kleinneudorf in the Bundesland Schleswig-Holstein, Germany.

Statistical time series analysis reveals that the variability is dominated by the daily cycle and weather variations (temperature and air pressure). It is possible to construct a Rn prediction model on the basis of weather variables and a segmentation into four principally different weather regimes (Rn exhalation modes). Still, there remains additional Rn variability, mainly in the form of excess Rn peaks. This will be pursued in future papers. Certainly the presented statistical approach can also be applied to other observed series that record a system with high variability and nonlinear interactions.

Since high Rn concentrations in the surface air are dangerous to human health, risk analyses of the excess Rn peaks have a high socioeconomic relevance. This type of analysis can deliver information about the return period of the excess peaks and the time-dependent occurrence rate of such dangerous events. This allows to better assess health impacts for a study site.

Our conclusions are based on fundamental process from geology, physics and meteorology. Therefore, we expect that the time-dependent variability of Rn is observable not only at our site but also at other places in Germany and the EU.

The current programmes for spatially mapping the long-term Rn concentrations in high resolution across the EU are important. However, this endeavour should be augmented by plans to also monitor the Rn concentrations over time. Such high-quality spatiotemporal Rn data, analysed by state-of-the-art statistical methods, will provide a basis for making better Rn risk predictions.

**Acknowledgements** Open Access funding provided by Projekt DEAL. We are grateful to the referees (Muhammad Rafique and two anonymous persons) and the Issue Editor István Hatvani for constructive review comments. MM thanks István Hatvani for his generous hospitality on the conference tour through

Hungary in May 2019. The ANGUS II project's title is "Impacts of the use of the geological subsurface for thermal, electrical or material energy storage in the context of the transition to renewable energy sources – Integration of subsurface storage technologies into the energy system transformation using the example of Schleswig-Holstein as a model area."

**Author contributions** FS conceived the idea of the relation between Rn concentration and meteorological control variables. FS and JA measured the data. MM designed the data analysis strategy and carried it out. MM wrote the manuscript with input from FS. All authors contributed to the interpretation of results and the final version of the paper.

## Compliance with ethical standards

**Conflict of interest** The authors declare that they have no conflict of interest.

**Open Access** This article is licensed under a Creative Commons Attribution 4.0 International License, which permits use, sharing, adaptation, distribution and reproduction in any medium or format, as long as you give appropriate credit to the original author(s) and the source, provide a link to the Creative Commons licence, and indicate if changes were made. The images or other third party material in this article are included in the article's Creative Commons licence, unless indicated otherwise in a credit line to the material. If material is not included in the article's Creative Commons licence and your intended use is not permitted by statutory regulation or exceeds the permitted use, you will need to obtain permission directly from the copyright holder. To view a copy of this licence, visit <http://creativecommons.org/licenses/by/4.0/>.

## References

- Akawwi, E.: Radon-222 concentrations in the groundwater along eastern Jordan Rift. *J. Appl. Sci.* **14**(4), 309–316 (2014)
- Al-Hilal, M., Sbeinati, M., Darawcheh, R.: Radon variations and microearthquakes in western Syria. *Appl. Radiat. Isot.* **49**(1–2), 117–123 (1998)
- Bartlett, M.: *An Introduction to Stochastic Processes with Special Reference to Methods and Applications*. Cambridge University Press, Cambridge (1955)
- Box, G., Draper, N.: *Empirical Model-Building and Response Surfaces*. Wiley, New York (1987)
- Breiman, L.: Statistical modeling: the two cultures (with discussion). *Statistical Science* **16**(3), 199–231 (2001)
- Brückner, E.: Klimaschwankungen seit 1700 nebst Bemerkungen über die Klimaschwankungen der Diluvialzeit. *Geographische Abhandlungen* **4**(2), 153–484 (1890)
- Burkhart, J., Huber, T.: Correlation of indoor radon concentration to commonly available geologic data. *Environ. Manag* **17**(2), 249–256 (1993)
- Dahlquist, G., Björck, Å.: *Numerical Methods in Scientific Computing*, vol. 1. SIAM, Philadelphia (2008)
- Dalgaard, P.: *Introductory Statistics with R*, 2nd edn. Springer, New York (2008)
- Deloncle, A., Berk, R., D'Andrea, F., Ghil, M.: Weather regime prediction using statistical learning. *J. Atmos. Sci.* **64**(5), 1619–1635 (2007)
- Diggle, P.: A kernel method for smoothing point process data. *Appl. Stat.* **34**(2), 138–147 (1985)
- Elfo, J., Cinelli, G., Bossew, P., Gutiérrez-Villanueva, J., Tollefsen, T., De Cort, M., Nogarotto, A., Braga, R.: The first version of the pan-European indoor radon map. *Natural Hazards Earth Syst. Sci.* **19**(11), 2451–2464 (2019)
- Ferraz-Mello, S.: Estimation of periods from unequally spaced observations. *Astron. J.* **86**(4), 619–624 (1981)
- Gasser, T., Müller, H.: Kernel estimation of regression functions. In: Gasser, T., Rosenblatt, M. (eds.) *Smoothing Techniques for Curve Estimation*, pp. 23–68. Springer, Berlin (1979)
- Gasser, T., Müller, H.: Estimating regression functions and their derivatives by the kernel method. *Scand. J. Stat.* **11**(3), 171–185 (1984)
- Gregorič, A., Vaupotič, J., Šebela, S.: The role of cave ventilation in governing cave air temperature and radon levels (Postojna Cave, Slovenia). *Int. J. Climatol.* **34**(5), 1488–1500 (2014)
- Hann, J.: *Lehrbuch der Meteorologie*. Tauchnitz, Leipzig (1901)



- Huber, J., Ennemoser, O., Schneider, P.: Quality control of mitigation methods for unusually high indoor radon concentrations. *Health Phys.* **81**(2), 156–162 (2001)
- Kantz, H., Schreiber, T.: *Nonlinear Time Series Analysis*. Cambridge University Press, Cambridge (1997)
- Kemski, J., Siehl, A., Stegemann, R., Valdivia-Manchego, M.: Mapping the geogenic radon potential in Germany. *Sci. Total Environ.* **272**(1–3), 217–230 (2001)
- Kemski, J., Klingel, R., Siehl, A., Stegemann, R.: Radon transfer from ground to houses and prediction of indoor radon in Germany based on geological information. *Radioact. Environ.* **7**, 820–832 (2005)
- Kemski, J., Klingel, R., Siehl, A., Valdivia-Manchego, M.: From radon hazard to risk prediction-based on geological maps, soil gas and indoor measurements in Germany. *Environ. Geol.* **56**(7), 1269–1279 (2009)
- Kendall, M.: Note on bias in the estimation of autocorrelation. *Biometrika* **41**(3–4), 403–404 (1954)
- Köppen, W.: *Die Klimate der Erde: Grundriss der Klimakunde*. de Gruyter, Berlin (1923)
- Künsch, H.: The jackknife and the bootstrap for general stationary observations. *Ann. Stat.* **17**(3), 1217–1241 (1989)
- Lomb, N.: Least-squares frequency analysis of unequally spaced data. *Astrophys. Space Sci.* **39**(2), 447–462 (1976)
- Martin, P., Tims, S., Ryan, B., Bollhöfer, A.: A radon and meteorological measurement network for the Alligator Rivers Region. Australia. *J. Environ. Radioact.* **76**(1–2), 35–49 (2004)
- Mogro-Campero, A., Fleischer, R.: Search for long-distance migration of subsurface radon (with discussion). In: Gesell, T., Lowder, W. (Eds.), *Natural Radiation Environment III*, vol 1, U.S. Department of Energy, Technical Information Center, Oak Ridge, TN, pp. 72–83 (1980)
- Montgomery, D., Peck, E.: *Introduction to Linear Regression Analysis*, 2nd edn. Wiley, New York (1992)
- Moreno, V., Bach, J., Font, L.L., Baixeras, C., Zarroca, M., Linares, R., Roqué, C.: Soil radon dynamics in the Amer fault zone: an example of very high seasonal variations. *J. Environ. Radioact.* **151**(1), 293–303 (2016)
- Mudelsee, M.: TAUEST: a computer program for estimating persistence in unevenly spaced weather/climate time series. *Comput. Geosci.* **28**(1), 69–72 (2002)
- Mudelsee, M.: *Climate Time Series Analysis: Classical Statistical and Bootstrap Methods*, 2nd edn. Springer, Cham (2014)
- Ólafsdóttir, K., Schulz, M., Mudelsee, M.: REDFIT-X: Cross-spectral analysis of unevenly spaced paleo-climate time series. *Comput. Geosci.* **91**, 11–18 (2016)
- Priestley, M.: *Spectral Analysis and Time Series*. Academic Press, London (1981)
- Priestley, M.: *Non-linear and Non-stationary Time Series Analysis*. Academic Press, London (1988)
- Radon Analytics.: Messgeräte für Radon. Radon Analytics (2020), <https://www.radon-analytics.com/>. Accessed 16 April 2020
- Scargle, J.: Studies in astronomical time series analysis. II. Statistical aspects of spectral analysis of unevenly spaced data. *Astrophys. J.* **263**(2), 835–853 (1982)
- Schulz, M., Mudelsee, M.: REDFIT: Estimating red-noise spectra directly from unevenly spaced paleoclimatic time series. *Comput. Geosci.* **28**(3), 421–426 (2002)
- Schulz, M., Stättegger, K.: SPECTRUM: spectral analysis of unevenly spaced paleoclimatic time series. *Comput. Geosci.* **23**(9), 929–945 (1997)
- Schumann, R., Gundersen, L.: Geologic and climatic controls on the radon emanation coefficient. *Environ. Int.* **22**(Supplement 1), S439–S446 (1996)
- Siino, M., Scudero, S., Cannelli, V., Piersanti, A., D’Alessandro, A.: Multiple seasonality in soil radon time series. *Sci. Rep.* **9**(1), 8610 (2019). <https://doi.org/10.1038/s41598-019-44875-z>
- Steinitz, G., Begin, Z., Gazit-Yaari, N.: Statistically significant relation between radon flux and weak earthquakes in the Dead Sea rift valley. *Geology* **31**(6), 505–508 (2003)
- Tareen, A., Rafique, M., Basharat, M.: Study of diurnal and seasonal variations in the time series data of soil  $^{222}\text{Rn}$  gas. *Int. J. Environ. Anal. Chem.* (2019). <https://doi.org/10.1080/03067319.2019.1666834>
- Tong, H.: *Non-linear Time Series*. Clarendon Press, Oxford (1990)
- Tong, H.: Some comments on a bridge between nonlinear dynamicists and statisticians. *Physica D* **58**(1–4), 299–303 (1992)
- von Storch, H., Zwiers, F.: *Statistical Analysis in Climate Research*. Cambridge University Press, Cambridge (1999)
- Walia, D., Lyngdoh, A., Saxena, A.: Seismotectonic zones demarcation in the Shillong Plateau using the microearthquakes and radon emanation rate. *Acta Geophys.* **58**(5), 893–907 (2010)
- Westphal, W.: *Physik*, 25th/26th edn. Springer, Berlin (1970)

Yoon, J., Lee, J.D., Joo, S., Kang, D.: Indoor radon exposure and lung cancer: a review of ecological studies. *Ann. Occup. Environ. Med.* **28**(1), 15 (2016). <https://doi.org/10.1186/s40557-016-0098-z>

Zeeb, H., Shannoun, F. (eds.): *WHO Handbook on Indoor Radon: A Public Health Perspective*. WHO, Geneva (2009)

**Publisher's Note** Springer Nature remains neutral with regard to jurisdictional claims in published maps and institutional affiliations.